Investigating electron transport in chemical vapor deposition graphene nanostructures

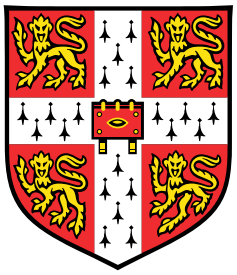

Jinggao Sui

Department of Physics
University of Cambridge

This dissertation is submitted for the degree of
Doctor of Philosophy

Christ's College

September 2019

Declaration

I hereby declare that except where specific reference is made to the work of others, the contents of this dissertation are original and have not been submitted in whole or in part for consideration for any other degree or qualification in this, or any other university. This dissertation is my own work and contains nothing which is the outcome of work done in collaboration with others, except as specified in the text and Acknowledgements. This dissertation contains fewer than 60,000 words including appendices, bibliography, footnotes, tables and equations and has fewer than 150 figures.

Jinggao Sui
September 2019

Acknowledgements

This thesis is the culmination of the efforts that I have made in the past five years at the Cavendish Laboratory of the University of Cambridge. Although it was such a long journey with countless days and nights working in the lab, I enjoyed every moment of my experience here in this beautiful university town. More importantly, I have received selfless help from many people and organizations during this period, and I would not have been able to complete this thesis without their support.

First and foremost, I would like to thank my supervisor, Professor Charles Smith, for all his guidance and support with great patience, Thank you for always being available when I had questions. I would also like to thank my secondary supervisor Dr. Malcolm Connolly, for all the advice and fruitful discussions during my PhD project. I am also grateful for the kind support from Professor David Ritchie, the head of Semiconductor Physics Group, and the wise advice Professor Chris Ford has offered. Many thanks to my college tutor, Dr. Helena Browne, for all her advice and support in my Cambridge life.

Second, I would like to thank my collaborators, Dr. Jack Alexander-Webber and Dr. Ye Fan, for supplying graphene material and generously sharing with me their inspiring insights. I would like to thank Dr. Vijay Narayan for the hours of cleanroom training. My lab experience especially in cryostat operation was definitely enhanced by my dear colleagues Dr. Joanna Waldie, Cassandra Chua, Carly Richardson, Dr. James Aldous and Dr. Chong Chen. I would also like to express my thanks to Melanie Tribble for all her help with solving cleanroom-related problems, and to Jonathan Griffiths and Thomas Mitchell for their splendid job with e-beam. Many thanks to Dan and Mariusz for making sure we always had a source of liquid helium through all the time, and even on holidays.

Third, I must thank Ziwei, Shu-Wei, Vivek, Gulzat, Yuqing, Binbin, Hangtian, Teng, Luke and other members of the Semiconductor Physics Group for their friendship and help in various aspects. They have made my time at the Cavendish a lot more enjoyable. I would also like to thank Linzhi, Zeyu, Chen, Kexin, Zhongyang, Huantao and other friends outside the lab for helping make Cambridge feel like a second home. Moreover, I gratefully acknowledge the National University of Defense Technology, Semiconductor Physics Group,

and Christ's College, Cambridge, for their financial support, which enabled my continued studies in Cambridge.

Finally, I would like to thank my family for their endless support. Despite being on the other side of the world, I know they are always there for me.

Abstract

This thesis investigates electron transport properties in chemical vapor deposition (CVD) graphene-related nanostructures. There are many potential electronic and optoelectronic applications envisioned for graphene, due to its two-dimensional character and exceptional properties. However, the lack of scalability of exfoliated graphene and the high cost of epitaxial graphene on silicon carbide remain the major obstacles for further commercialization of graphene devices. Different approaches to solve this problem have been proposed for different applications and graphene grown by CVD stands out as a useful alternative and proves to be one of the viable routes towards scalable high quality electronics.

This thesis presents a study of scalable nanostructured devices based on CVD graphene, with the purpose of understanding the quantum physics of electron transport and demonstrating the potential for nano-electronic applications. First, this thesis demonstrates a scalable approach towards encapsulating and passivating high quality CVD graphene field effect transistors (FETs), and electron scattering processes are explored by studying electrical characterisation and magnetotransport phenomena in encapsulated CVD AB stack and large twist angle (30°) bilayer graphene FETs, as well as monolayer graphene FETs for reference. The result has significant impact on the widespread implementation of graphene for its scalable device applications. Second, in order to enhance spin-orbit coupling (SOC) in graphene for spin transport study and spintronics applications, a graphene - transition metal dichalcogenide (TMD) heterostructure is investigated. Phase coherence length is reduced in the heterostructure and a special transition from weak localization (WL) to weak anti-localization (WAL) is found around a certain carrier concentration due to surface roughness induced patches. This result provides insight into fabrication and operation of scalable graphene spintronic devices. Moreover, to further elucidate single-electron behaviours as well as solve the lack of bandgap issues, graphene is studied by being patterned into various quantum dot structures, such as nanoribbon multiple quantum dots, quantum Hall antidots, and double quantum dots (DQDs). The presence of multiple quantum dots in series is exhibited in a bilayer SiC epitaxial graphene nanoribbon, due to the interplay between disorder and quantum confinement. As an alternative to etched quantum dots in graphene, antidots in the quantum Hall regime can take advantage of Landau gaps in graphene and are explored via

magnetotransport measurements at millikelvin temperature. Single-electron behaviors such as Aharonov-Bohm effect and Coulomb blockade effect are observed, whereas signatures of the effective antidots proved elusive, probably due to the disorder-broadening of the Landau levels. Finally, for the purpose of fast readout of charge and spin states, radio-frequency (RF) reflectometry technique is developed in GaAs antidots and graphene double quantum dots, corresponding to capacitive and resistive couplings to the devices respectively. This attempt paves a way for characterizing the time scale of the charge transfer and spin dephasing in graphene nanodevices. All the quantum dots studies in a scalable style lay the foundation for further quantum metrology and quantum computation applications.

The research in this thesis enable us to better understand the quantum physics in CVD graphene, and the fabrication and operature of CVD graphene nanostructures are highly promising for future electronics.

Table of contents

List of figures

List of tables

Nomenclature

Roman Symbols

$\hbar$	Reduced Planck constant, $\hbar = h/2\pi$
B	Magnetic field
D	Diffusion coefficient
E	Energy
e	Elementary charge
E_C	Charging energy of a quantum dot
f_0	Resonant frequency
G	Conductance
g_s	Degeneracy
h	Planck constant
I	Electric current
k	Momentum vector
k_B	Boltzmann constant
m	Orbital quantized number
m^*	Effective mass
n	Carrier density
P	Energy loss rate per carrier

R	Resistance
R_K	Resistance quantum
R_T	Tunnel barrier resistance
r_{AD}	Radius of the antidot
T	Temperature
t	Intra-layer hopping energy
$t_\perp$	Inter-layer hopping energy
T_e	Electron temperature
V_g	Gate voltage
V_{AD}	Antidot top gate voltage
V_{BG}	Back gate voltage
V_{PG}	Plunger gate voltage
V_{QPC}	QPC split gates voltage
V_{rf}	Reflected RF amplitude
V_{SD}	Source drain bias
V_{SG}	Side gate voltage
Z_0	Characteristic impedance of transmission line
Z_t	Transformed impedance

Greek Symbols

$\Delta\rho(B)$	Quantum resistance in resistance
$\Delta\sigma(B)$	Quantum resistance in conductance
ΔB	Resonance period of the Aharonov-Bohm oscillations
ΔR_{xx}	Weak localization peak height
Δ_g	Band gap

Δ_{1D}	Quantum confinement gap
Δ_{BL}	Bilayer graphene band gap
ε_0	Permittivity of free space
ε_r	Relative permittivity
Γ	Tunnelling rate
μ	Electrochemical potential
μ_i	Carrier mobility
ν	Filling factor
ω_c	Cyclotron frequency
ϕ	Magnetic flux quantum
ψ	Digamma function
ρ	Resistivity
ρ_{xx}	Longitudinal resistance
ρ_{xy}	Hall resistance
σ	Conductivity
σ_{xx}	Longitudinal conductance
σxy	Hall conductance
τ^{-1}	Electron scattering rate
τ_φ^{-1}	Dephasing rate
υ_F	Fermi velocity
L_φ	Phase coherence length

Acronyms / Abbreviations

1D	one dimensional
2D	two dimensional

2DEG	two dimensional electron gas
AFM	atomic force microscope
ALD	atomic layer deposition
BLG	bilayer graphene
CAPE	Centre for Advanced Photonics and Electronics
CVD	chemical vapor deposition
DAC	digital to analogue converter
DMM	digital multimeter
DQDs	double quantum dots
EBL	electron beam lithography
ESD	electrostatic discharge
FET	field effect transistor
FWHM	full width at half maximum
GADs	graphene antidots
GDQDs	graphene double quantum dots
Gr/WS_2	graphene/tungsten disulfide
HD	high doping
IPA	isopropanol
LCC	leaded chip carrier
LD	low doping
LI	lock-in
MD	medium doping
MLG	monolayer graphene
PCB	printed circuit board

PMMA	Polymethyl methacrylate
QHE	quantam Hall effect
QPC	quantum point contact
RF	radio-frequency
SdH	Shubniknov-de Hass
SET	single electron transistor
SMU	source measure unit
SOC	spin-orbit coupling
SP	semiconductor physics
TFM	thin film magnetism
TMA	trimethylaluminum
TMD	transition metal dichalcogenide
UHFLI	ultra high frequency lock-in
VRH	variable-range hopping
WAL	weak anti-localization
WL	weak localization

Chapter 1

Introduction

1.1 The Development of Graphene

In 1965, Gordon Moore, the CEO of Intel observed and predicted that the number of transistors in a dense integrated circuit doubles about every two years, which is known as Moore's law [133]. This trend evolved as predicted over the past few decades, as shown in figure 1.1(a). Accordingly, the performance speed of processors, which is strongly linked to Moore's law, has increased dramatically over this period. However, the rate of the progress in conventional transistor made from silicon may reach saturation when the transistor is manufactured extremely small. Because when the size of transistor is comparable to the wavelength of electrons, quantum mechanics comes into play and dominates the electron transport properties. Therefore, there is a growing interest in finding new promising materials with low resistance and high charge carrier mobility. Graphene, a two-dimensional allotrope of carbon stands out as one of the most promising candidates for its exotic electronic properties. Since its first isolation mechanically exfoliated from graphite by Geim and Novoselov in 2004 [141], the interest in graphene and its possible applications has drastically increased, which is apparent in the number of annual publications on graphene (see figure 1.1(b)). This extraordinary promise led to Geim and Novoselov winning the 2010 Nobel Prize in Physics for "groundbreaking experiments regarding the two-dimensional material graphene".

The discovery of two-dimensional graphene first and foremost yielded access to a large amount of interesting physics [67, 101]. Initial studies included observations of ambipolar field effects in graphene [141], measurements of extremely high charge carrier mobility [22, 51, 35, 14] and unconventional quantum Hall effect [198, 94]. In addition, graphene has a relatively large Landau level spacing between the zeroth and the first Landau levels as a consequence of its linear dispersion near the Dirac point and high Fermi velocity [142],

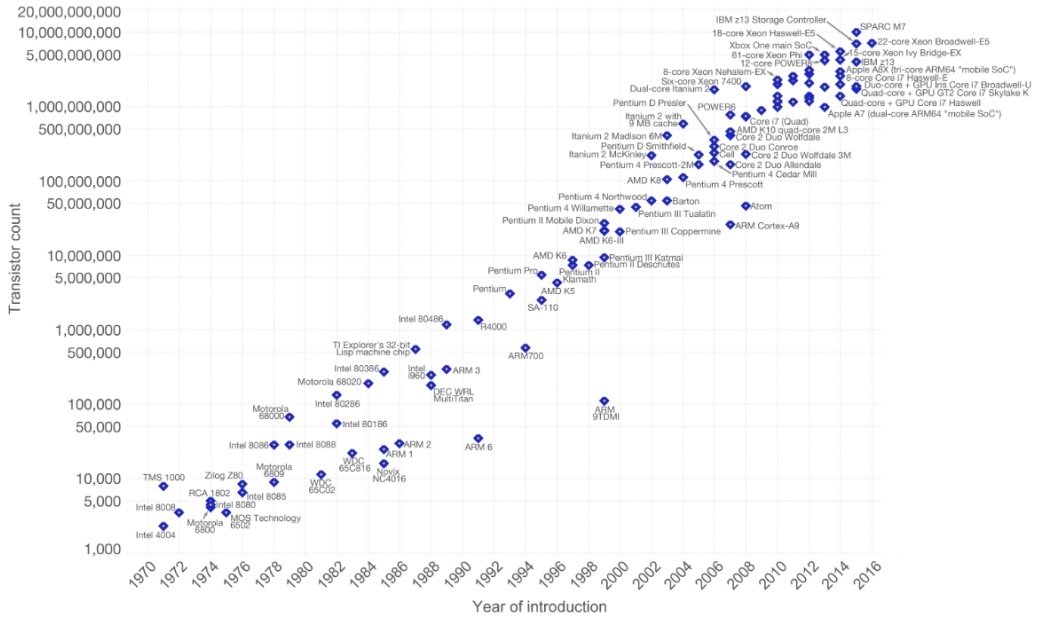

(a)

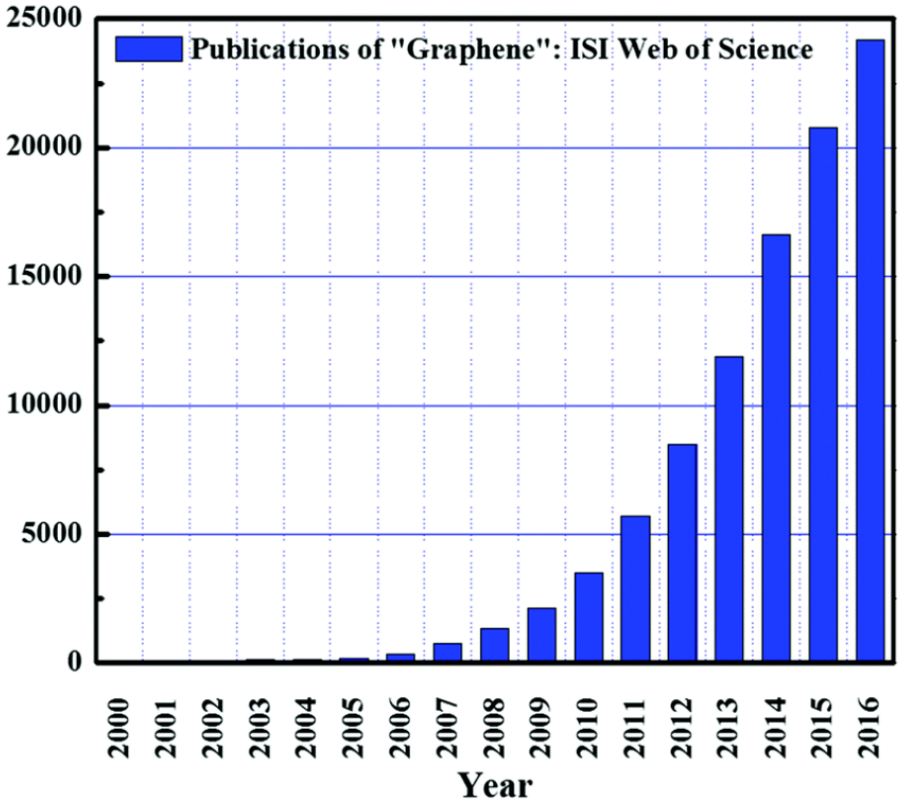

(b)

Fig. 1.1 (a) Number of transistors on integrated circuit chips from 1971 to 2016, demonstrating Moore's law. Source: https://en.wikipedia.org/wiki/Moore'law. (b) Publications on graphene from 2000 to 2016. Adapted from [153].

which allows for the observation of the quantum Hall effect at a higher temperature or lower magnetic fields compared to GaAs. Moreover, carbon is a light atom compared to most of the semiconductor materials, such as InAs and GaAs, so the spin-orbit coupling and hyperfine interaction are relatively weak in graphene, which enables long spin decoherence times. These properties attracted significant interest in the possible implementation of graphene in various devices [5], including future generations of high-speed and radio frequency logic transistors, quantum qubits, thermally and electrically conductive reinforced composites, sensors, and transparent electrodes for displays and solar cells. Another application for graphene is in single electron pumps or charge pumps [71, 149, 45], which can generate an amount of electric current ef, at a drive frequency f by controlled manipulation of single electrons. Thus, it allows the redefination of the ampere in terms of the fundamental elementary charge e and provides a powerful tool in the research of metrology [95]. Graphene has advantages compared to conventional semiconductors in terms of ease of fabrication and low capacitance of tunnel barriers, which makes it possible to transfer charge quickly and pump high currents at gigahertz frequency [45].

Despite intense interest in graphene, widespread implementation of graphene has not been achieved so far. This is primarily due to the difficulty of reliably producing high quality samples, especially in any scalable fashion at a reasonable cost. To date, various approaches, including mechanical exfoliation from graphite [141], chemical vapour deposition (CVD) [194, 84], as well as epitaxial growth on silicon carbide [16, 17] have been investigated for obtaining graphene layers. However, the lack of scalability and reproducibility of graphene devices fabricated from small exfoliated flakes and the high cost of epitaxial graphene on silicon carbide, remain the major obstacles for further commercialization of graphene electronics and optoelectronics. By contrast, due to its wafer-scale growth, CVD enables large scale production with a low cost [156, 84]. More recently, it has been shown to provide a scalable route towards high electronic quality graphene [47], and significant effort has been made to tailor the growth parameters to selectively obtain bilayer graphene [60].

This thesis is based on graphene grown by the CVD approach with the purpose towards scaling up graphene nanodevices for electronic applications. Figure 1.2 illustrates the scale-up progress of CVD graphene electronic nanodevices made in this thesis. The CVD graphene material is transferred onto a quarter of a SiO_2/Si wafer, which can be divided into ten 10 mm^2 chips, with each chip producing 36 nanodevices. A key limitation for the electronic applications of graphene is the lack of a natural band gap. Current methods to induce a gap include etching graphene to make use of the one-dimensional confinement gap [80], or applying perpendicular electric fields to bilayer graphene [145]. Therefore, the graphene used in this thesis is patterned into various nanostructures, not only just Hall

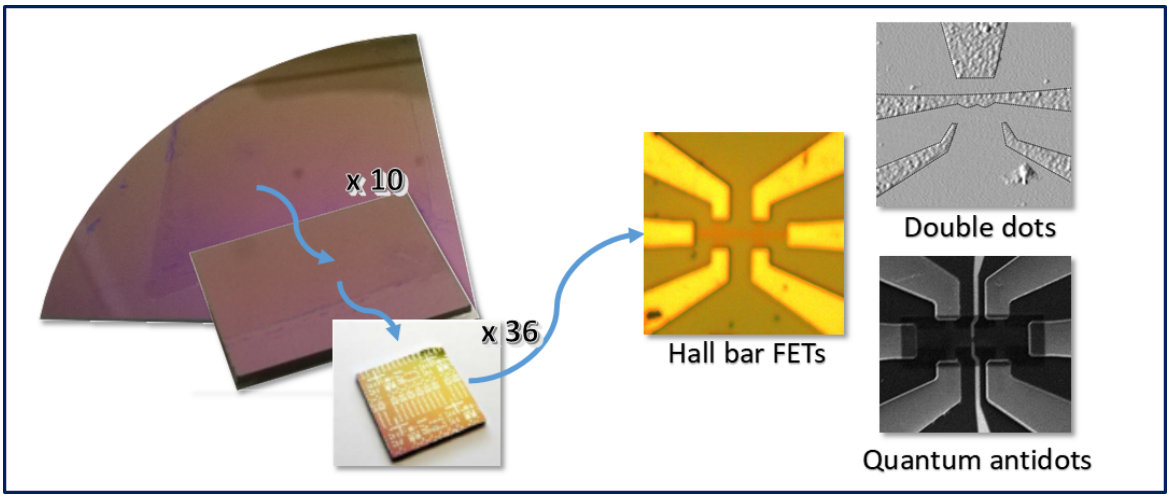

Fig. 1.2 Scale-up of graphene grown by CVD for the purpose of fabricating electronic nanodevices, such as Hall bar, double quantum dots and quantum Hall antidots.

bar field effect transistors (FETs), but also nanoribbons, double quantum dots and antidots measured in the quantum Hall regime, shown in figure 1.2. This thesis lays the foundation towards understanding the quantum physics in CVD graphene and scaling up CVD graphene nanodevices for potential electronic applications.

1.2 Thesis Outline

This thesis consists of 8 chapters. This first chapter gives a brief introduction of the development of graphene and the outline of the thesis. The next chapter will provide a theoretical background on the electronic properties of graphene and graphene nanostructured devices, particularly focusing on the aspects related to the experiments discussed in later chapters.

Chapter 3 describes the details of the processes and techniques that are used to fabricate and measure graphene nanodevices. In particular, the first section outlines the design and fabrication process for making CVD graphene nanodevices. The second section introduces different kinds of cryogenic systems in which low temperature measurements are performed. Two types of measurement circuits setup are presented in the third section. And the last section describes the radio-frequency (RF) reflectometry techniques used to detect the charge and spin of the graphene nanodevices with high sensitivity and accuracy.

Chapter 4 is the first experimental data chapter, probing electron scattering in scalable CVD graphene. First, to improve reproducibility of CVD graphene devices, atomic layer deposition of aluminium oxide is used with in situ gaseous water pretreatments to achieve negligible gate hysteresis, low doping levels, and lower disorder compared to as-fabricated

devices. Second, by electrical characterisation and magnetotransport measurements on encapsulated CVD grown Bernal stacked and large twist angle (30°) bilayer graphene FETs, as well as monolayer graphene FETs for reference, we show that the electron scattering processes and the hot electron effects can be tuned.

In the next data chapter - chapter 5, a study of graphene/WS_2 heterostructure is presented to explore induced spin-orbit coupling in a graphene - TMD heterostructure. A long Hall bar is fabricated with half the Hall bar (one half along its length) being only graphene and the other half a graphene/WS_2 heterostructure, for comparisons in order to better investigate how WS_2 influence graphene performance. Magnetotransport measurements are performed on such a device against temperature and electric field. Information about electron scattering is subtracted from weak localization analysis, which enables us to better characterize the material and understand the physics in CVD produced graphene.

Chapter 6, the third data chapter discusses investigation of two different kinds of quantum dots in graphene. First, multiple quantum dots formation is observed in a nanoribbon device patterned in bilayer SiC graphene. Electron transport in this device is studied as a function of doping, magnetic field, and temperature. Close to charge neutrality, electron transport resembles that in exfoliated graphene nanoribbons and is well described by tunnelling of single electrons through a network of Coulomb-blockaded islands. Second, a CVD graphene antidot defined between a pair of split gates in the quantum Hall regime is investigated by electron transport measurements. This type of antidots can avoid edge disorder induced from etched quantum dots, take advantage of Landau gaps, and thus enhance graphene performance.

Chapter 7 develops a low temperature radio-frequency reflectometry setup to study GaAs quantum antidots and CVD graphene double quantum dots. Using radio-frequency reflectometry we non-invasively probe quantum capacitance change and single-electron tunnelling behaviours in GaAs ADs and graphene DQDs with high sensitivity and at millikelvin temperatures.

Chapter 8 summarizes all the works done in this thesis and proposes the future plan for research in this area based on my results.

Chapter 2

Theoretical Background

This chapter provides a theoretical background on the electronic properties of graphene and graphene nanostructured devices, particularly focusing on the aspects related to the experiments discussed in later chapters. Given that graphene is the prime material used in this thesis, corresponding theories regarding electronic properties of graphene are reviewed. The weak localization and quantum Hall effect are discussed because they both are landmark magnetotransport experiments exhibiting two-dimensional character of graphene, and are also related to the topic in chapter 4 and chapter 5. A background on the physics of graphene nanoribbons and quantum dots is discussed as supporting theory for the first half of chapter 6 and the second half of chapter 7. Lastly, a section is dedicated to quantum Hall antidots to aid in understanding of graphene antidots in the second half of chapter 6 and GaAs antidots in the first half of chapter 7.

2.1 Graphene Theory

In this review of graphene theory, I will first review the electronic properties of graphene. Then I will move on to the weak localization (WL) and quantam Hall effect (QHE) in graphene. Given that some interesting experiments have been performed on bilayer graphene (BLG), I will also describe the basic properties of BLG in the final section.

2.1.1 Electronic Properties of Graphene

Graphene is a two-dimensional allotrope of carbon with a unique conical band structure. The extraordinary promising applications of graphene led to the 2010 Nobel Prize award in Physics for its discovery [141]. Mechanically exfoliated graphene on a Si/SiO_2 substrate can have a mobility as high as 70,000 $cm^2V^{-1}s^{-1}$ at room temperature [35], while that for

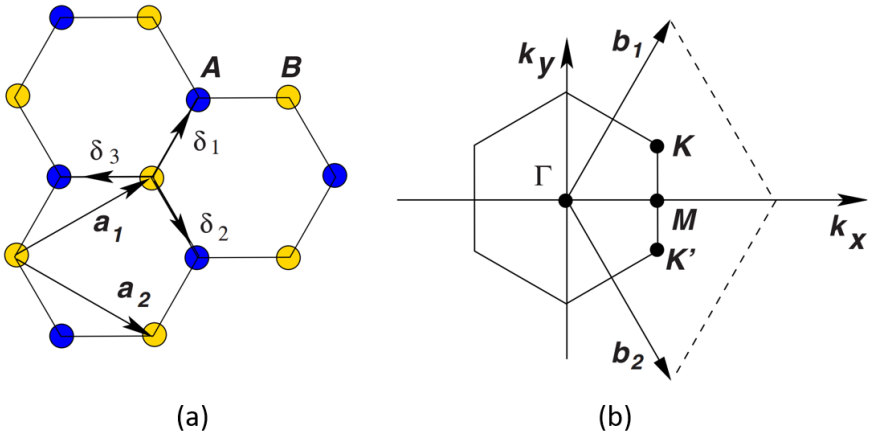

Fig. 2.1 Honeycomb lattice and its Brillouin zone. (a) Lattice structure of graphene, made out of two interpenetrating triangular lattices ($\mathbf{a}_1$ and $\mathbf{a}_2$ are the lattice unit vectors, and δ_i, $i = 1,2,3$ are the nearest neighbour vectors). (b) Corresponding Brillouin zone. The Dirac cones are located at the K and K' points. Adapted from [34].

suspended graphene has been found to approach 200,000 $cm^2V^{-1}s^{-1}$ at low temperatures [22, 51]. Graphene's high mobility, coupled with its unique band structure and zero effective carrier mass makes it a prime candidate in the search for materials to replace or supplement silicon in the race for ever faster and more power-efficient electronics. In addition, the fact that graphene can be patterned using standard silicon-compatible processes, especially with the development of high quality, wafer-sized graphene by chemical vapour deposition (CVD) and epitaxial methods gives it an advantage over carbon nanotubes [16]. This section discusses the electronic properties of graphene which are fundamentally different from other two-dimensional electron gas systems (2DEGs), and make it a promising material to realize the fast speed electronic devices.

The Electronic Band Structure

Graphene is a single layer of carbon atoms arranged in hexagonal lattice, see figure 2.1(a). Each carbon atom has three nearest neighbours and the structure can be regarded as a triangular lattice with two atoms in each unit cell. The lattice vector are given by

$$\mathbf{a}_1 = \frac{a}{2}(3,\sqrt{3}), \quad \mathbf{a}_2 = \frac{a}{2}(3,-\sqrt{3}), \tag{2.1}$$

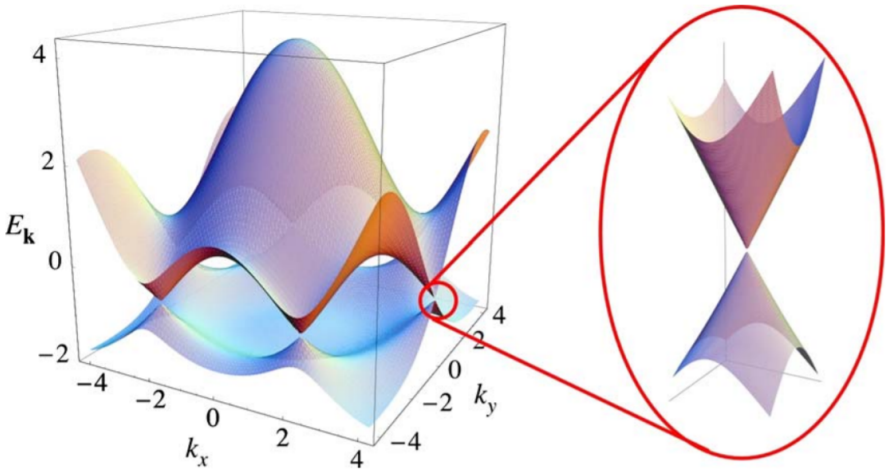

Fig. 2.2 The band structure of graphene, with a close up of the band structure near the Dirac point, adapted from [34].

where $a \approx 0.142$ nm is the shortest carbon-carbon distance. In the reciprocal lattice space, the corresponding vectors are

$$\mathbf{b}_1 = \frac{2\pi}{3a}(1, \sqrt{3}), \quad \mathbf{b}_2 = \frac{2\pi}{3a}(1, -\sqrt{3}). \tag{2.2}$$

The band structure of graphene can be calculated by the tight-binding method and the details of the calculation can be found in Wallace's 1947 paper [187]. When only the nearest three neighbour hopping is considered, the energy bands derived from this paper is as follows:

$$E_{\pm}(\mathbf{k}) = \pm\gamma_0\sqrt{1+4cos(\frac{k_x a}{2})cos(\frac{\sqrt{3}k_y a}{2})+4cos^2(\frac{k_y a}{2})}, \tag{2.3}$$

where + corresponds to the conduction band and – corresponds to the valence band respectively, γ_0 (≈ 0.28 eV) [34] is the nearest neighbour hopping energy between different sublattices. The conduction band and valence band meet at the corners of the Brillouin zone (**K** and **K'**, see figure 2.1(b)), called Dirac points. Their positions in momentum space are given by

$$K = (\frac{2\pi}{3a}, \frac{2\pi}{3\sqrt{3}a}), \quad K' = (\frac{2\pi}{3a}, -\frac{2\pi}{3\sqrt{3}a}). \tag{2.4}$$

Near the Dirac points, the well-know linear dispersion relationship $E(\mathbf{k})$ (see figure 2.2) can be calculated by expanding the band structure close to **K** or **K'**, which satisfies the following equation:

$$E(\mathbf{k}) \approx \pm\hbar\upsilon_F\sqrt{{k_x}^2+{k_y}^2} \tag{2.5}$$

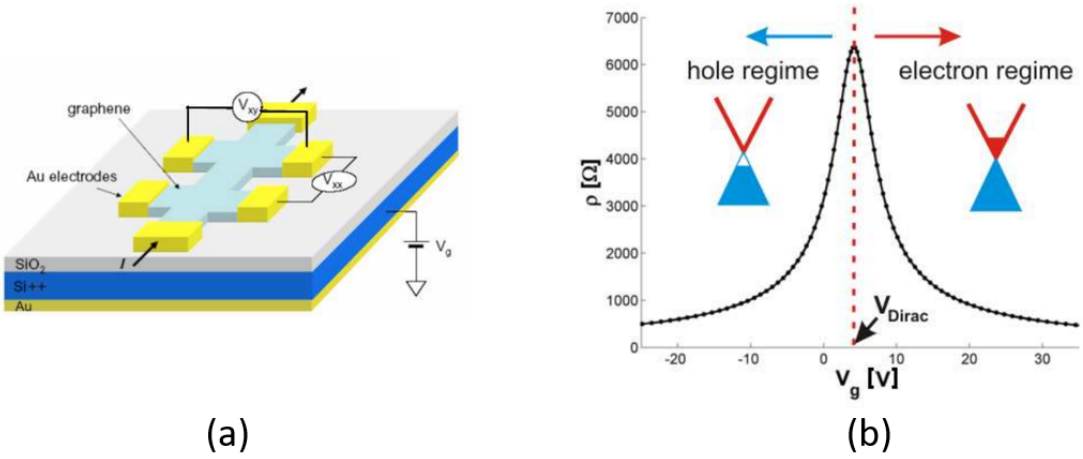

Fig. 2.3 (a) Structure and geometry of basic graphene Hall bar device. (b) A typical graphene resistivity ρ_{xx} dependence as a function of gate voltage V_g. Adapted from[190].

where $\upsilon_F = 10^6$ m/s is the Fermi velocity in graphene [34]. The conical band structure of graphene can be clearly seen in figure 2.2. Graphene has a linear energy-momentum relationship and the conduction band touches the valence band at Dirac points. Thus it is a zero band gap semiconductor, and the dispersion relationship is independent with mass near the Dirac point. All of those are quite different from normal semiconductors, where the energy-momentum ralationship is parabolic given by $E = \hbar^2 k^2 / 2m^*$, where m^* is the effective mass of the charge carrier in the semiconductors and k is the the momentum vector associated with the energy E. Actually, the special dispersion relationship of graphene is similar to those of Dirac particles, and electron dynamics can be treated as 'relativistic', in which the Fermi velocity of graphene υ_F replaces the speed of light [34].

Graphene Electric Field Effect

Figure 2.3(a) shows schematically the basic graphene Hall bar device. By applying an external voltage, one can modify the carrier density in graphene and it resembles a field effect transistor (FET). The thick black arrows mark the current path, while the connections between the contacts V_{xx} and V_{xy} indicate the measuring scheme for longitudinal resistivity ρ_{xx} and transversal resistivity ρ_{xy} (also called Hall resistivity) respectively. In this device, the graphene is patterned on a silicon dioxide (SiO_2) layer, with a doped silicon substrate, which is connected to a back-gate V_g. By applying a voltage on the gate, the SiO_2 insulating layer is like a capacitor and the back-gate induces the opposite charge density in graphene:

$$n = \frac{\varepsilon_0 \varepsilon_r V_g}{te} = \alpha V_g, \tag{2.6}$$

where the coefficient $\alpha = \varepsilon_0 \varepsilon_r / te$,$\varepsilon_0$ is the permittivity of free space, ε_r is the relative permittivity of SiO_2, t is the thickness of SiO_2 layer and e is the electron charge. In addition, Figure 2.3(a) demonstrates two types of resistivity measurements, voltage drop between parallel contacts (V_{xx}) to determine the longitudinal resistivity ρ_{xx}, and that between opposite contacts (V_{xy}) to determine the transversal resistivity ρ_{xy} (also called Hall resistivity) respectively. When changing the back-gate voltage, we can tune the carrier density in graphene and thus modify its Fermi level. In neutral graphene, the Fermi level lies at the Dirac point and there should be no carriers contributing to the electronic transport. Therefore, the graphene shows the maximum resistivity for the Fermi level at the Dirac point. Also, the Dirac point separates the region into two parts, where conduction is governed by holes (p-type) and electrons (n-type) respectively (see figure 2.3(b)).

Normally, the graphene is doped to some extent and the Dirac voltage $V_{Dirac} \neq 0$. Then in doped graphene the charge carrier density as a function of back-gate voltage changes to:

$$n = \alpha(V_g - V_{Dirac}). \tag{2.7}$$

So one can shift the graphene from p-type or n-type to Dirac point or from Dirac point to p-type or n-type, which is fundamentally important in graphene transport measurements.

The mobility is also significant to characterize graphene, reflecting the scattering situation in graphene, which is directly related to the material purity and can be improved by some technological methods, such as annealing. Owing to the symmetrical shape of the energy dispersion relationship (see figure 2.2), the electron mobility μ_e is equal to the hole mobility μ_h. In addition, the mobility can be derived from the following formula:

$$\mu_i = \frac{1}{en_i\rho}, \tag{2.8}$$

where $i = electrons, holes$, ρ is the resistivity. The values of graphene mobility have been introduced at the beginning of this section, which is much higher than normal conducting materials and the value for suspended graphene is even higher than the fastest present inorganic semiconductors (InSb, 78,000 $cm^2V^{-1}s^{-1}$ at room temperature [159]) and semiconducting carbon nanotubes (100,000 $cm^2V^{-1}s^{-1}$ at room temperature [54]).

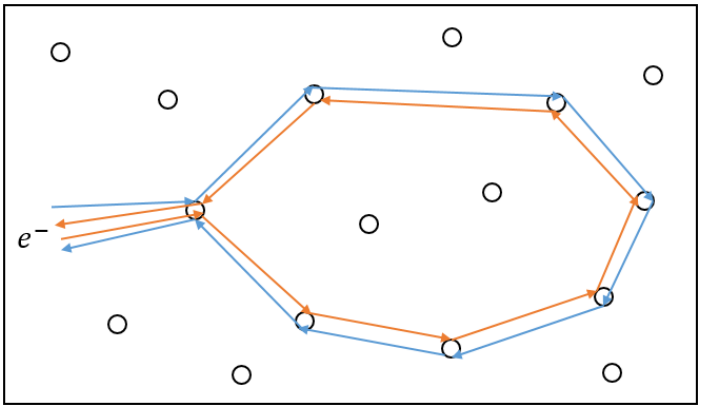

Fig. 2.4 Illustration of the trajectories of an electron scattered by impurities giving rise to a quantum correction to the resistance.

2.1.2 Weak Localization in Graphene

The unique band structure of graphene was illustrated in the previous subsection. Due to the two equivalent but independent triangular sublattices of its honeycomb structure, the charge carriers near the Dirac points in graphene behave like chiral fermions. This introduces an additional quantum number called pseudospin or chirality [102]. The psedospin is parallel to the momentum in one valley but anti-parallel to the momentum in the other. Therefore, the two valleys in graphene host quasiparticles with opposite chirality.

The chiral nature of graphene makes it very different from traditional two-dimensional (2D) systems in many aspects. In particular, the carriers in graphene possess a Berry phase of π [192], which is the additional phase acquired by the electron wave function when an electron transports a closed loop. This, in theory, should result in weak anti-localization (WAL) of charge carriers in graphene compared with the conventional weak localization (WL). The effects of WL and WAL is a useful tool to study electron dephasing process due to inelastic electron scattering or scattering by magnetic impurities.

Figure 2.4 demonstrates how an electron scattered by impurities can interfere on a closed trajectory when treated as a wave. Two electron waves propagate in opposite directions around the trajectory and interfere at the point of intercept. Because the two paths are identical, the phase of the two electron waves is the same. Therefore, the interference is constructive, which increases the probability of back scattering of electrons, as well as the electrical resistance. In experiment, the quantum correction to the resistance can be detected by applying a perpendicular magnetic field to the samples. The magnetic field adds a phase difference to the two waves and destroys the interference, resulting in a decrease of the resistance, which is also called negative magnetoresistance (MR), $\Delta\rho(B) = \rho(B) - \rho(B = 0) < 0$. In graphene, however, there is Berry phase π adding to the two interfering paths, so that they meet with

antiphase and destructive interference happens. This, on the contrary, should result in a reduction of the resistance due to quantum interference and a positive magnetoresistance, $\Delta\rho(B) = \rho(B) - \rho(B=0) > 0$ [127]. The principle of this weak anti-localization (WAL) effect is totally different from what has been observed in other 2D systems with strong spin-orbit scattering [18, 130]. Here, the two waves meet with antiphase because of spin flips in the process of scattering by impurities, while spin-orbit coupling in graphene is known to be weak due to the light carbon atoms [86].

In fact, due to the chiral nature of the charge carriers in graphene, its weak localization effect should be sensitive not only to inelastic, phase coherence breaking process represented by the characteristic scattering rate τ_φ^{-1}, but also to different elastic scattering mechanisms [127, 175]. Elastic scattering that breaks the chirality will destroy the interference within each of the two graphene valleys in k space. Weak anti-localization is expected to be observed only in clean samples and suppressed by defects leading to chiral symmetry breaking, characterized by elastic intravalley scattering rate τ_z^{-1}. And these defects include surface ripples, dislocations and atomically sharp defects [134, 135]. Intravalley weak localization can also be destroyed by anisotropy of the Fermi surface in k space, so called trigonal warping [127], characterized by the rate τ_w^{-1}. The combined effect of the intravalley scattering is characterized by the rate $\tau_*^{-1} = \tau_z^{-1} + \tau_w^{-1}$. There is one elastic process, however, which acts to restore the suppressed interference. This is intervalley scattering, which occurs at a rate τ_i^{-1} on defects with size of the order of the lattice spacing. As the two valleys have opposite chirality and warping, intervalley scattering is expected to negate the chirality breaking and warping effects by allowing interference of carriers from different valleys.

The theory of quantum interference has been demonstrated to be applicable to the description of the magnetoresistance in terms of weak localization in graphene. The resistance correction $\Delta\rho(B) = \rho(B) - \rho(B=0)$ is given by [127]:

$$\begin{aligned} \Delta\rho(B) &= -\frac{e^2\rho^2}{\pi h}[F(\frac{B}{B_\varphi}) - F(\frac{B}{B_\varphi + 2B_i}) - 2F(\frac{B}{B_\varphi + B_*})], \\ F(z) &= ln(z) + \psi(\frac{1}{2} + \frac{1}{z}), \\ B_{\varphi,i,*} &= \frac{\hbar c}{4De}\tau_{\varphi,i,*}^{-1}. \end{aligned} \tag{2.9}$$

Here, ψ is the digamma function and D is the diffusion coefficient. The curvature of $\Delta\rho(B)$ is determined by the dephasing rate τ_φ^{-1} when $B \leq B_\varphi$. The quantum correction can also be expressed in terms of magnetoconductance $\Delta\sigma(B) = \sigma(B) - \sigma(B=0)$ [179]:

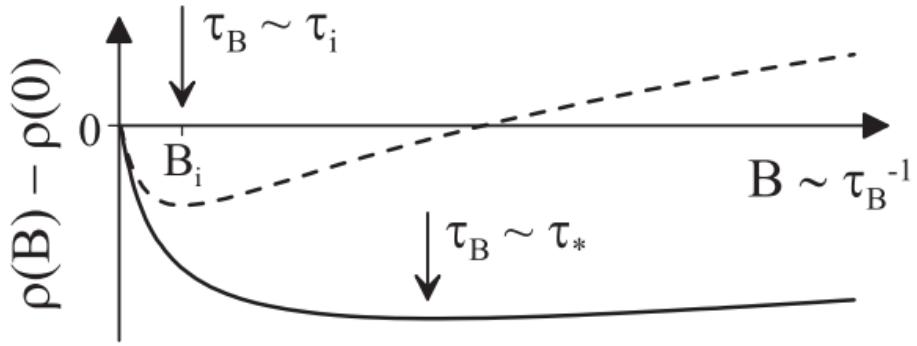

Fig. 2.5 Magnetoresistance expected in a phase-coherence graphene $\tau_\varphi \gg \tau_i$: with $\tau_* \gg \tau_i$ (dashed line) and $\tau_* \ll \tau_i$ (solid line). In the case of $\tau_\varphi < \tau_i$, $\Delta\rho(B) = 0$. Adapted from [127].

$$\Delta\sigma(B) = \frac{e^2}{\pi h}[F(\frac{\tau_B^{-1}}{\tau_\varphi^{-1}}) - F(\frac{\tau_B^{-1}}{\tau_\varphi^{-1} + 2\tau_i^{-1}}) - 2F(\frac{\tau_B^{-1}}{\tau_\varphi^{-1} + \tau_i^{-1} + \tau_*^{-1}})]. \tag{2.10}$$

Here, $\tau_B^{-1} = 4eDB/\hbar$. The first term in this equation is responsible for WL, while the WAL is determined by the second and third terms with negative sign. In the absence of intravalley and intervalley scattering in a ideal defect-free graphene layer, $\tau_{*,i}^{-1} \to 0$, $\Delta\sigma(B)$ is completely controlled by the third term. In the opposite case of strong intravalley and intervalley scattering (small$\tau_{*,i}$), both negative terms are suppressed and the first (positive) term dominates, corresponding to electron localization. The above equations show that the quantum correction to the resistance or conductance has the weak localization sign in real graphene with the intervalley time shorter than the dephasing time $\tau_\varphi > \tau_i$ owing to tight coupling between graphene and the substrate, which generates atomically sharp scatterers.

Figure 2.5 illustrates the corresponding MR in two regimes: $\tau_* \gg \tau_i$ and $\tau_* \ll \tau_i$. Both cases display negative MR when $B < B_i$ (for $\tau_* \gg \tau_i$, the MR changes sign at $B \sim B_i$). A dashed line shows what one would get when neglecting the effect of warping, while the solid curve shows the MR behavior in graphene with a high carrier density, where the effect of warping is strong and leads to a fast intravalley scattering. In the case when the graphene sheet is loosely attached to a substrate (or suspended), the intervalley scattering time may be longer than the decoherence time, $\tau_i > \tau_\varphi$, $\Delta\rho(B) = 0$, so that MR displays neither WL nor WAL behavior.

Equation (2.9) explains why the low field MR observed in the quantum transport experiments in graphene [134], displayed a suppressed WL behavior rather than WAL. For all electron densities in the samples studied in [134] the estimated warping-induced relaxation time is rather short, $\tau_w < \tau_\varphi$, which excluded any WAL. In addition, the observation [134]

of a suppressed WL MR in devices with a tighter coupling to the substrate agrees with the behavior expected in the case of sufficient intervalley scattering, $\tau_i < \tau_\varphi$, whereas the absence of any WL MR, $\Delta\rho(B) = 0$, for a loosely coupled graphene sheet is what the theory predicts for samples with a long intervalley scattering time, $\tau_i > \tau_\varphi$.

2.1.3 Quantum Hall Effect in Graphene

The weak localization effect discussed in the previous subsection happens at low magnetic field ($B < 1$ T). When a larger magnetic field is applied perpendicular to a 2DEG, the quantum Hall effect will happen. The quantum Hall effect, which extends from the classical Hall effect, occurs for high mobility, two-dimensional (2D) electron systems, because the strong magnetic field prompts the density of states into discrete Landau levels, given by the following equation for a 2D system with a parabolic band:

$$E_n = \hbar\omega_c(n + \frac{1}{2}). \tag{2.11}$$

Here, $\omega_c = eB/m^*$ is the cyclotron frequency, m^* is the effective cyclotron mass. Quantization is observed whenever the Fermi energy is located in a gap between these Landau levels and the temperature is low enough that thermal excitation across the gap is impossible (see figure 2.6). The Hall resistance then undergoes quantum Hall transitions to take on quantized values given by:

$$\rho_{xy} = \frac{1}{\nu}\frac{h}{e^2} \tag{2.12}$$

where ν is the filling factor, e is the elementary charge and h is Planck's constant for magnetic field values $B_i = (nh/e)/i$, where n is the carrier density and i is an integer value. The corresponding longitudinal resistance ρ_{xx} drops to zero, which is illustrated in figure 2.7. This can be understood by considering that when quantization occurs, the Landau levels are fully occupied and there are no empty states to host a free electron in the bulk, but there are states at the edge which are topologically protected with forward going states on one side and reverse going ones on the other. They are held by the Lorentz force and can not back scatter through the bulk as there are no states for transport there. Therefore, without electron scattering, the longitudinal resistance naturally drops to a negligible value [186, 107, 15].

As a 2D material with high mobility, graphene also exhibits the quantum Hall effect. Figure 2.8(a) demonstrates experimental observation of quantum Hall effect for both electrons and holes (inset) in graphene [198]. Owing to its unique band structure near the Dirac points, graphene displays some key differeces from other 2D materials in terms of the quantum Hall effect. First, the linear dispersion relation leads to a cyclotron mass dependent on the square

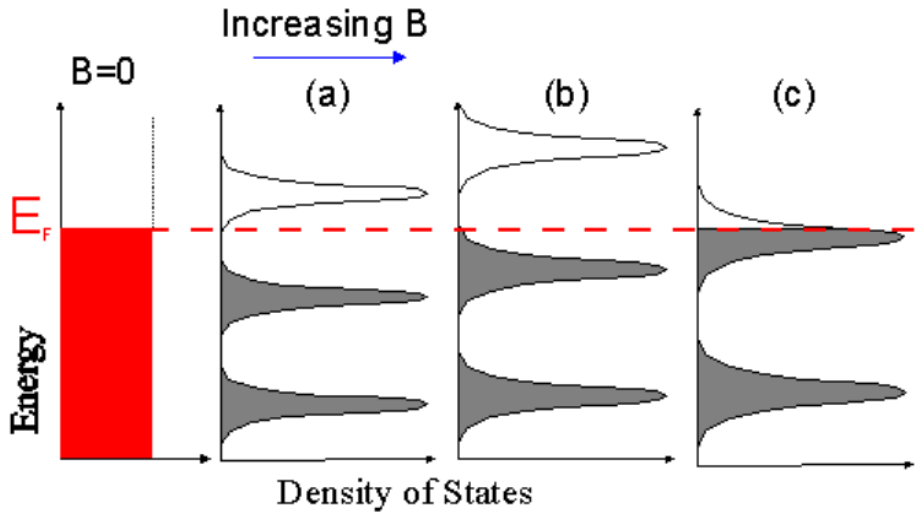

Fig. 2.6 Evolution of the density of states in a 2DEG against a increasing magnetic field. The Fermi level is dotted in red. Adapted from [122].

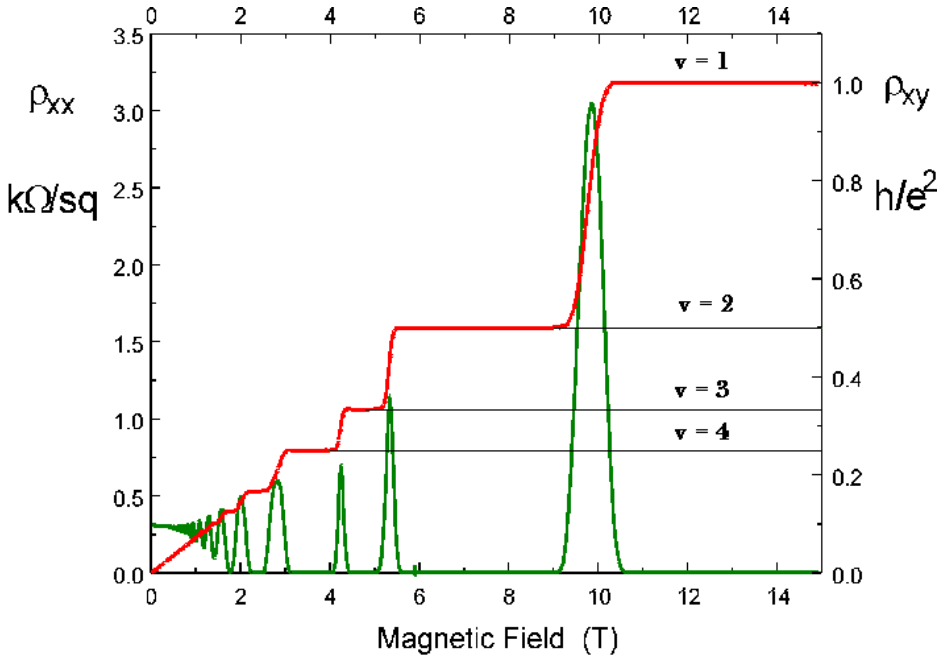

Fig. 2.7 Typical quantum Hall measurement for a 2DEG (GaAs/AlGaAs), showing Hall quantization and longitudinal Shubniknov-de Hass oscillations. Red trace is Hall resisitivity ρ_{xy} and green longitudinal resistivity ρ_{xx}. Figure created by D.R.Leadley, Warwick University (1997) [46].

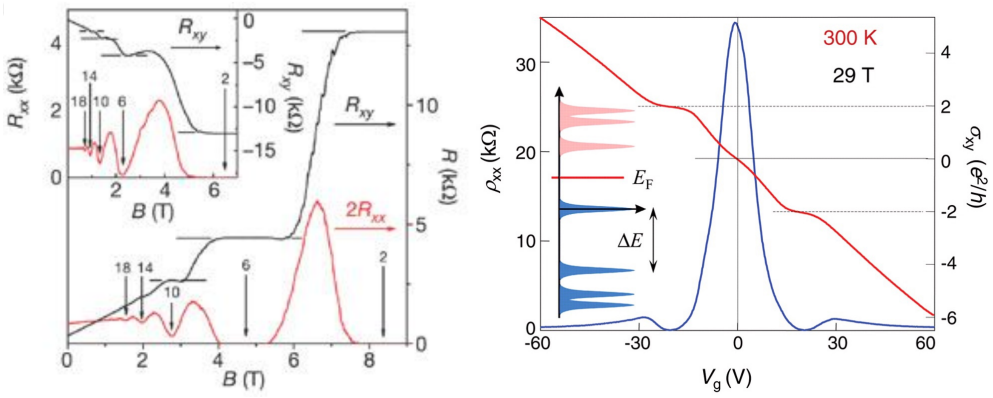

(a) (b)

Fig. 2.8 (a) Hall resistance (black) and magnetoresistance (red) measurements for electrons in graphene, labelled with corresponding filling factors. Inset: quantum Hall effect for holes in graphene [198]. (b) Room-temperature quantum Hall effect in graphene. Inset: illustration of graphene Landau levels quantization with emphasis on large spacing between $n = 0$ and $n = 1$[142].

root of the carrier density given by $m^* = \frac{\sqrt{\pi}}{\upsilon_F}\sqrt{n}$ [34], while the cyclotron mass is constant in semiconductors with a parabolic dispersion relation.

Similarly, under a strong magnetic field, the density of states in graphene is quantized into several Landau levels, though they are not equally spaced. Instead, the Landau levels energy in graphene is described as below [198]:

$$E_n = sgn(n)\upsilon_F\sqrt{2e\hbar B|n|}, \tag{2.13}$$

where the integer n represents an electron-like $n > 0$ or a hole-like $n < 0$ Landau level index. This equation shows that for small n, the Landau level spacing is relatively large in graphene (see the inst of figure 2.8b), which means that the quantum Hall effect might happen with lower magnetic fields or at higher temperatures. In fact, this has been demonstrated by the observation of the quantum Hall effect in graphene at room temperature [142] (see figure 2.8b). In addition, when only low-lying Landau levels are occupied, the separation of E_n is much larger than the Zeeman spin splitting, so each LL has a degeneracy $g_s = 4$, accounting for spin degeneracy and valley degeneracy.

Equation (2.13) demonstrates another interesting point, which is the existence of the $n = 0$ Landau level. This special Landau level straddles the Dirac point and is filled half by the electrons and half by the holes (see figure 2.9(b)). Besides, the Hall conductivity quantization shows a half integer shift, which is given by:

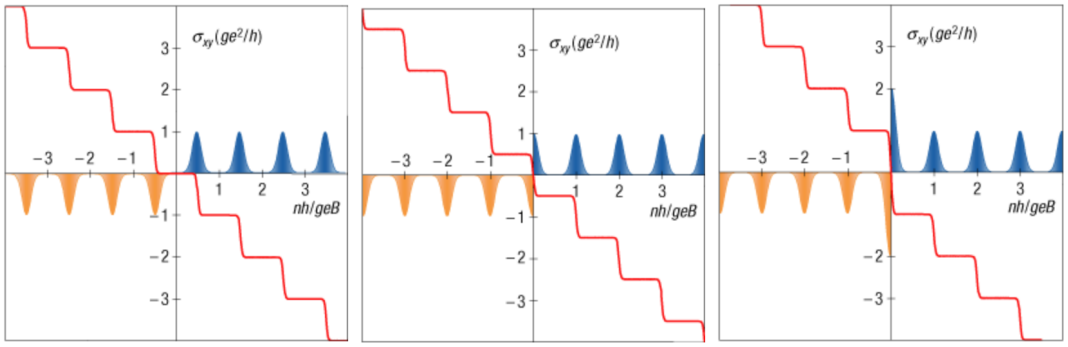

Fig. 2.9 Schematic illustration of Landau levels and Hall conductivity quantization for (a) 2D semiconductor systems, (b) monolayer graphene, and (c) bilayer graphene [143]. The bilayer graphene will be discussed in the next subsection 2.1.4.

$$\sigma_{xy} = \pm g_s(n+\frac{1}{2})\frac{e^2}{h}, \tag{2.14}$$

where n is a non-negative integer and $\pm$ represents electrons and holes, respectively. This quantization condition can also be translated to the quantized filling factor $\nu = g_s(n+1/2)$. The Hall conductivity quantization is also illustrated in figure 2.9(b). Experimental observation of this anomolous half-interger quantum Hall effect is evidence of the massless Dirac fermions in graphene [140, 198].

2.1.4 Bilayer Graphene

The graphene described above is monolayer graphene (MLG). In addition to monolayer graphene, few-layer graphene can also be isolated or grown. Bilayer graphene (BLG) has attracted significant interest due to the ability to tune the electronic properties by changing the relative orientation or twist angle between the two layers. BLG can exist in the usual AB, or Bernal-stacked form, where half of the atoms lie directly over the center of a hexagon in the lower graphene sheet (see figure 2.10(a) and 2.10(b)), and half of the atoms lie over an atom, or, less commonly, in the AA form, in which the layers are exactly aligned. Bernal stacked bilayer graphene offers an electric field tunable band gap [199] and valley transport [97, 167]. Moveover, BLG in twisted style, where one layer is rotated relative to the other, have also been observed. Small twist angle bilayer graphene ($\sim 1^\circ$) has been shown to exhibit exotic electronic phenomena such as superconductivity [28, 27] and topological transport channels [157]. At larger twist angles (5° – 30°) the low energy Dirac points of each are well separated in k-space, and higher energy interlayer interactions dominate [196, 3, 197, 148, 83, 157].

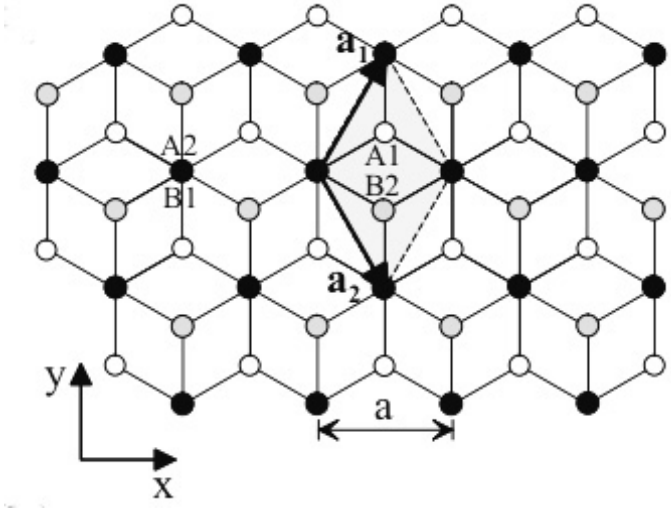

(a)

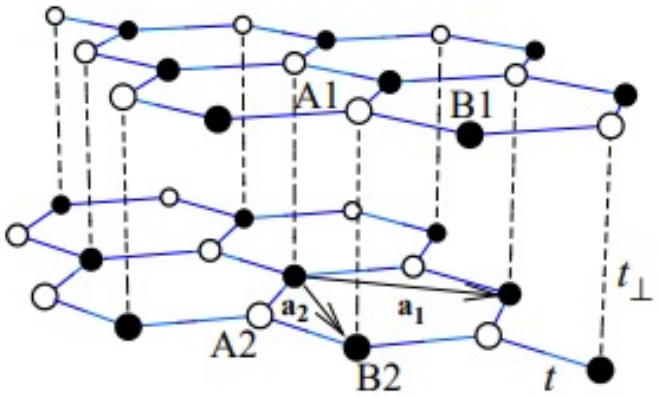

(b)

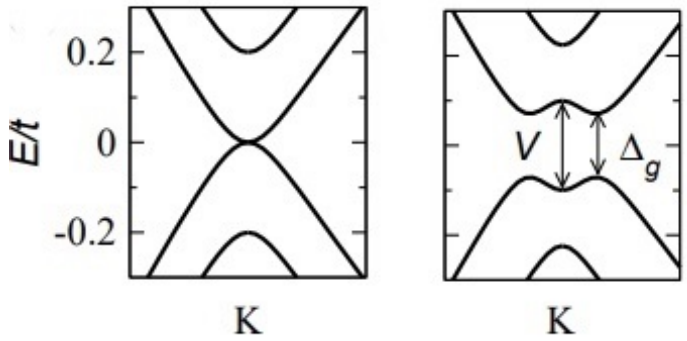

(c)

Fig. 2.10 (a) Top and (b) side view of the lattice structure of Bernal-stack bilayer graphene, labelled with t as the intra-layer hopping energy, and $t_\perp$ as the inter-layer hopping energy. (c) Left: Band structure of Bernal-stacked bilayer graphene near K (or K'). Right: Bernal-stacked bilayer graphene band structure with a gap Δ_g opened due to a potential V applied perpendicular to the graphene surface. Figures (a) adapted from [129, 33].

The most common type of BLG among all these types is AB (Bernal) stacking, which will be discussed in details in this subsection. The low-energy properties of this BLG are described by massive Dirac fermions with a quadratic dispersion close to the neutrality point. In the absence of applied perpendicular electric field, its band structure consisting of four bands is given by [33]:

$$E_{\mathbf{k}}^{\pm\pm} = \pm\sqrt{\varepsilon_{\mathbf{k}}^2 + t_\perp^2/4} \pm t_\perp/2, \tag{2.15}$$

where $\varepsilon_{\mathbf{k}}^2 = t[3 + 2cos(ak_x) + 4cos(ak_x/2)cos(ak_y\sqrt{3}/2)]$ is the dispersion of MLG and t, $t_\perp$ are the intra-layer and inter-layer hopping energies respectively. The band structure defined by equation (2.15) is shown in the left of figure 2.10(c). Near the Dirac points **K** and **K'**, the dispersion relation is given by $E(p) \approx \pm\upsilon_F^2 p^2/t_\perp$, with $p = \hbar q$, where q is the wave vector in momentum space relative to the Dirac points, and υ_F is the Fermi velocity for MLG. Therefore, the low-energy charge carriers in BLG are massive and given by $m^* = t_\perp/(2\upsilon_F^2) \approx 0.03m_e$, where m_e is the bare electron mass [129]. Thus, the Dirac fermion mass in BLG originates from the inter-layer hopping energy $t_\perp$.

Although the band structure is very different from the massless Dirac fermions found in MLG, which has a linear dispersion relation, it has been demonstrated that the charge carriers are still showing the property of chirality or pseudospin but with a Berry phase of 2π instead of π in MLG, which means that the pseudospin turns twice as quickly in the plane than the momentum, while in MLG it is aligned with the momentum. As a consequence, there will be no suppression of backscattering, and the quantum correction in BLG will have the sign of conventional weak localisation [76]. However, its magnitude is still very sensitive to different elastic processes. Weal localization in each of the two graphene valleys can be completely suppressed by defects and trigonal warping of the energy spectrum which is expected to be stronger in BLG than MLG [103]. In the meanwhile, intervalley scattering can partially restore weak localization. The theoretical model for calculating the BLG magnetoresistance can refer to that in MLG (equation (2.9)).

One of the most remarkable properties of BLG is the ability to open up a gap in the spectrum by a perpendicular electric field in contrast with MLG, as the equivalence between the two layers is broken [127]. This has been experimentally realized as a semiconductor whose band gap can be externally tuned [144]. The gap between conduction band and valence band is given by [33]:

$$\Delta_g = \sqrt{t_\perp^2 V^2/(t_\perp^2 + V^2)}, \tag{2.16}$$

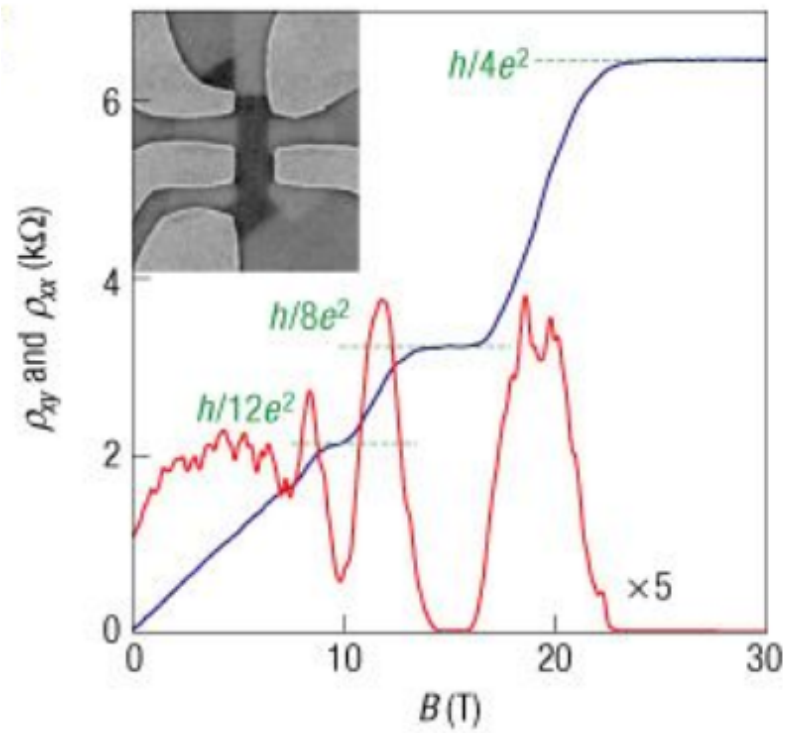

Fig. 2.11 Magnetoresistance measurements exhibiting quantum Hall effect in bilayer graphene. Inset: scanning gate micrography of one graphene Hall bar device. (T = 4 K) Adapted from [143].

where V is the potential of a perpendicular electric field, and therefore the gap can be externally controlled. The resulting gap opening is illustrated in the right of figure 2.10(c). The presence of the gap has been confirmed optically [199], and electrically on both suspended graphene [6] and graphene on hexagonal boron nitride (hBN) [75]. Moreover, gate-defined single quantum dot and double quantum dots have been realized by tuning graphite back-gate and top gates leading to a band gap opening [56, 13, 57]. The fact that a simple perpendicular electric field can create a tunable band gap, clearly exhibits the potential of the BLG system for electronics applications.

The quantum Hall effect in BLG is also distinctive from MLG and other conventional 2DEGs, which can be clearly seen from figure 2.9. Figure 2.11 exhibits both Hall and longitudinal resistance as a function of magnetic field at a fixed carrier density for a BLG Hall bar device describe in reference [143]. At low energy (i.e. small n), the Landau levels are given by $E_n^{\pm} = \pm\hbar\omega_c\sqrt{n(n-1)}$, for $n \geq 2$. The quantization of Hall conductance is shown in figure 2.9(c), which is given by $\sigma_{xy} = \pm n(4e^2/h)$, for $n \geq 1$. Therefore, there is no $n = 0$ plateau leading to an $8e^2/h$ jump across zero carrier density with a corresponding maximum in the longitudinal resistance. It is also noted that this Hall quantization has a degeneracy of four due to spin and valley degeneracies, which is similar to conventional semiconductors, while the eightfold degeneracy across zero carrier density takes into consideration the spin and A and B lattice degeneracies [128, 143].

2.2 Quantum Dots Theory

A quantum dot is an artificially structured zero-dimensional system, also called an 'artificial atom', where the charge carriers are generally confined in a submicron area [82]. The confinement potential in all directions is very strong, giving rise to quantized energy levels, lika an atom. Quantum dots in GaAs/AlGaAs heterostructure have been widely studied over the last few decades due to their potential applications for quantum computation. Quantum dots made from graphene are attractive as the electron spin-decoherence time in carbon-based material is expected to be long, which is advantageous to spin qubit applications. This section serves as an introduction to the general theory concerning single quantum dot, double quantum dots, as well as quantum dots in a nanoribbon, whereas the relevant experiments will be presented in chapter 6 and 7.

2.2.1 Single Quantum Dot

When a quantum dot is isolated from its environment, the number of charges in the dot becomes well defined. The electrostatic energy associated with these electrons makes it necessary for an electron to overcome this energy in order to tunnel on to the dot [78]. This phenomenon preventing current flow through an quantum dot is called Coulomb blockade. There are two necessary conditions for the observation of Coulomb blockade [82]. First, the charging energy of the dot E_C must be significantly larger than the energy caused by thermal fluctuations:

$$E_C = \frac{e^2}{C} \gg k_B T, \tag{2.17}$$

where C is the total capacitance of the dot and k_B is the Boltzmann constant. This happens when confinement in all three directions is strong enough to lead to quantum effects that influence the electron dynamics. Due to the resulting discrete energy spectrum, quantum dots behave in many ways as artificial atoms. The second condition has something to do with the quantum mechanical nature of electrons. In order to form a well-defined number of electrons in the dot, the tunnel barrier describing the coupling between the dot and the source and drain reservoirs has to be high enough so that the electron wavefunction can be localised in the dot. The minimal tunnel barrier resistance R_T to resolve the charging energy e^2/C can be estimated with the uncertainty principle $\Delta E \Delta t > h$. With $\Delta E = e^2/C$ and $\Delta t = R_T C$, the condition for R_T can be found:

$$R_T \gg R_K, \tag{2.18}$$

where $R_K = h/e^2 \approx 25.8 k\Omega$ is the resistance quantum [78].

As long as the above two conditions are satisfied, the number of charges on the quantum dot is quantized. When a electric field is applied to the gate electrode V_G (see figure 2.12(a)), the energy in the dot and hence the number of electrons in the dot can be varied.

To understand the dynamics of a single quantum dot in such a system, a constant interaction model has been proposed [82] and is illustrated in figure 2.12(a). This model is based on two assumptions. First, the Coulomb interactions among electrons in the dot, and between electrons in the dot and those in the environment, can be described by a single parameter C. This capacitance is the sum of the capacitance between the dot and the source C_S, the drain C_D and the gate C_G: $C = C_S + C_D + C_G$. The second assumption is that the single-particle energy-level spectrum E_n is independent of these Coulomb interactions and therefore of the number of electrons. Using this model, the total energy $U(N)$ of a single dot with N electrons in the ground state is given by [82]:

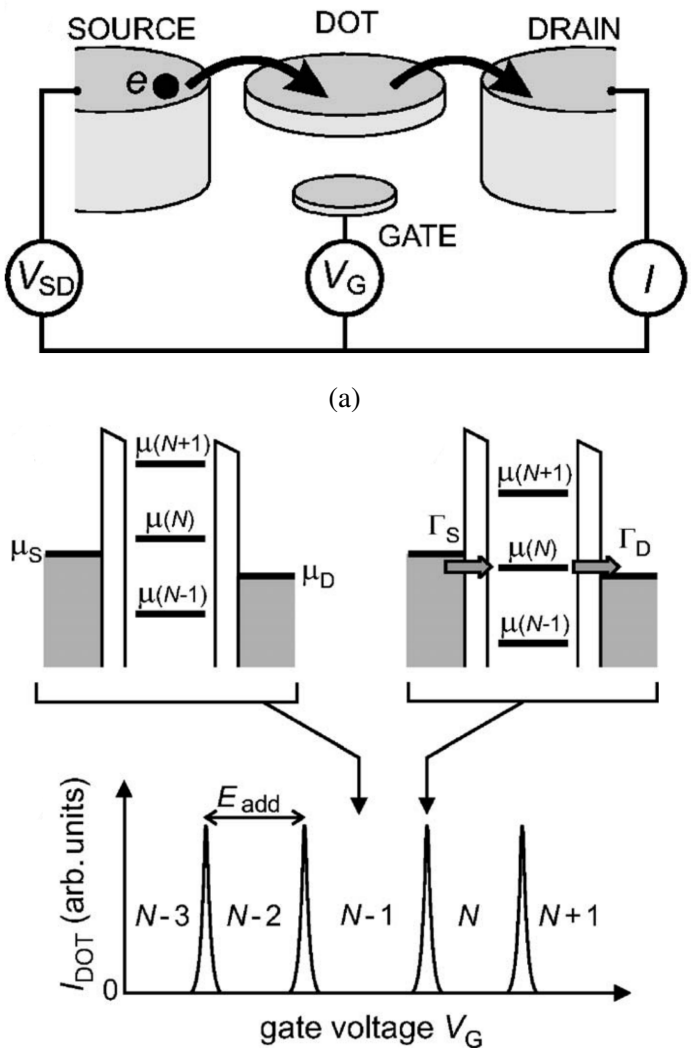

Fig. 2.12 (a) Illustration of a quantum dot in a lateral geometry. The quantum dot represented by a disk is connected to source and drain reservoirs via tunnel barriers, allowing the current through the device I to be measured in response to a bias voltage V_{SD} and a gate voltage V_G. (b) Schematic diagrams of energy levels of a single quantum dot during Coulomb blockade (top left) and when current is not blocked (top right). Bottom: corresponding current in each situation. Figures adapted from [82].

$$U(N) = \frac{[-|e|(N-N_0)+C_SV_S+C_DV_D+C_GV_G]^2}{2C} + \sum_{n=1}^{N} E_n(B), \tag{2.19}$$

where $-|e|$ is the electron charge, $N_0|e|$ is the charge in the dot compensating for the positive background charge and The terms C_SV_S, C_DV_D and C_GV_G can be varied continuously and represent an effective induced charge in the dot due to its surroundings. The last term is a sum over the occupied single-particle energy levels $E_n(B)$ which depend on the characteristics of the confinement potential, and B is the applied magnetic field, if any. The electrochemical potential $\mu(N)$ of a dot is defined as the energy needed to add the Nth electron to a dot with $N-1$ electrons:

$$\begin{aligned} \mu(N) &\equiv U(N) - U(N-1) \\ &= (N - N_0 - \frac{1}{2})E_C - \frac{E_C}{|E|}(C_SV_S + C_DV_D + C_GV_G) + E_N, \end{aligned} \tag{2.20}$$

where $E_C = e^2/C$ is the charging energy. The addition energy E_{add} of single quantum dot is defined as the electrochemical potential of the transitions between two successive ground states:

$$E_{add}(N) = \mu(N+1) - \mu(N) = E_C + \Delta E, \tag{2.21}$$

The addition energy consists of a purely electrostatic part, the charging energy E_C, plus the energy spacing between two discrete quantum levels $\Delta E = E(N+1) - E(N)$, which is independent of the electron number in the dot.

The transport through the quantum dot depends on whether $\mu(N)$ align with the bias window, which is defined as the spacing between the electrochemical potentials of the source μ_S and drain μ_D. Electron tunnelling through the dot happnens only when $\mu(N)$ lies in the bias window set by the two leads, i.e. $\mu_S \geq \mu(N) \geq \mu_D$, which is illustated in the top right of figure 2.12(b). When the electrochemical potential is outside the bias window, the transport is blocked and no current flows through the dot, which is the Coulomb blockade regime and is shown in the top left of figure 2.12(b). When a gate V_G constantly tunes the electrochemical potential of the quantum dot, an on-off current can be observed as peaks with constant spacing E_{add} (see the bottom of figure 2.12(b)). Each current blocked state corresponds to a certain electron number in the dot; thus in this way, the number of electrons in the dot can be varied.

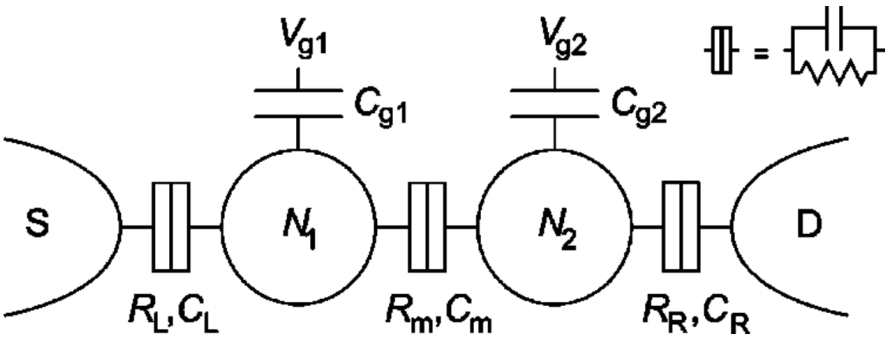

Fig. 2.13 Schematic diagram of a double quantum dot network. Note that tunnel barriers are characterized by a tunnel resistor and a capacitor, as indicated in the inset. Adapted from [184].

2.2.2 Double Quantum Dots

When two single quantum dots are placed in series and connected to source and drain reservoirs, a double quantum dot with a network of source-dot-dot-drain is formed, which is illustrated in figure 2.13. Electron transport through a double quantum dot can first be studied by a purely classical description in which the influence of discrete quantum energy levels is not taken into consideration. According to the reference [184], the double dot can be modeled as a network of tunnel resistors and capacitors (see figure 2.13). The energy of the double dot system is determined by considering the interaction of each dot with each of the gates, source, drain and each other:

$$\begin{aligned} U(N_1,N_2) =& \frac{1}{2}N_1^2E_{C1} + \frac{1}{2}N_2^2E_{C2} + N_1N_2E_{Cm} \\ & - \frac{1}{|e|}[C_{g1}V_{g1}(N_1E_{C1} + N_2E_{Cm}) + C_{g2}V_{g2}(N_1E_{Cm} + N_2E_{C2})] \\ & + \frac{1}{e^2}(\frac{1}{2}C_{g1}^2V_{g1}^2E_{C1} + \frac{1}{2}C_{g2}^2V_{g2}^2E_{C2} + C_{g1}V_{g1}C_{g2}V_{g2}E_{Cm}), \end{aligned} \tag{2.22}$$

where E_{C1}, E_{C2} and E_{Cm} are the charging energies of dot 1, dot 2 and the electrostatic coupling energy, respectively. These energies can be expressed in terms of the capacitances as follows:

$$E_{C1} = \frac{e^2}{C_1}(\frac{1}{1-\frac{C_m^2}{C_1C_2}}), \tag{2.23}$$

$$E_{C2} = \frac{e^2}{C_2}(\frac{1}{1-\frac{C_m^2}{C_1C_2}}), \tag{2.24}$$

$$E_{Cm} = \frac{e^2}{C_m}(\frac{1}{\frac{C_1C_2}{C_m^2}-1}). \tag{2.25}$$

The electrochemical potential of dot 1 is then defined as the energy needed to add the N_1th electron to dot 1 with N_1-1 electrons, while dot 2 has N_2 electrons in it [184]:

$$\begin{aligned}\mu_1(N_1,N_2) \equiv& U(N_1,N_2)-U(N_1-1,N_2)\\ =&(N_1-\frac{1}{2})E_{C1}+N_2E_{Cm}\\ &-\frac{1}{e^2}(C_{g1}^2V_{g1}^2E_{C1}+C_{g2}V_{g2}E_{Cm}).\end{aligned} \tag{2.26}$$

Similarly, the electrochemical potential of dot 2 is defined and given by:

$$\begin{aligned}\mu_2(N_1,N_2) \equiv& U(N_1,N_2)-U(N_1,N_2-1)\\ =&(N_2-\frac{1}{2})E_{C2}+N_1E_{Cm}\\ &-\frac{1}{e^2}(C_{g1}^2V_{g1}^2E_{Cm}+C_{g2}V_{g2}E_{C2}).\end{aligned} \tag{2.27}$$

Therefore one can find that the addition energy or the change in chemical potential in dot 1 equals the charging energy of dot 1 in this classical regime, $\mu_1(N_1+1,N_2)-\mu_1(N_1,N_2)=E_{C1}$, and is caused by simply increasing one electron in dot 1. Similarly, the addition energy of dot 2 equals $E_{C2}=\mu_2(N_1,N_2+1)-\mu_2(N_1,N_2)$. The electrostatic coupling energy is given by the change in chemical potential of dot 1 when one electron is added to dot 2 and vice versa, $E_{Cm}=\mu_1(N_1,N_2+1)-\mu_1(N_1,N_2)=\mu_2(N_1+1,N_2)-\mu_2(N_1,N_2)$.

From the electrochemical potentials in equations 2.26 and 2.27, a stability diagram consisting of information of the V_{g1} and V_{g2} dependent of N_1 and N_2 can be constructed. Figure 2.14 illustrates several cases of the stability diagram of double quantum dots. When the inter-dot coupling is so weak, C_m is close to zero, then the stability diagram resembles that of two uncoupled dots (see 2.14(a)). The gate voltage changes the charge on one dot, without affecting the charge on the other. For the case of strong inter-dot coupling, C_m becomes the dominant capacitance giving rise to a stability diagram of a single combined dot with charge N_1+N_2, as shown in 2.14(c). In terms of the case of intermediate coupling, hexagonal honeycomb domains form (see 2.14(b)). The dimensions of the hexagonal cell

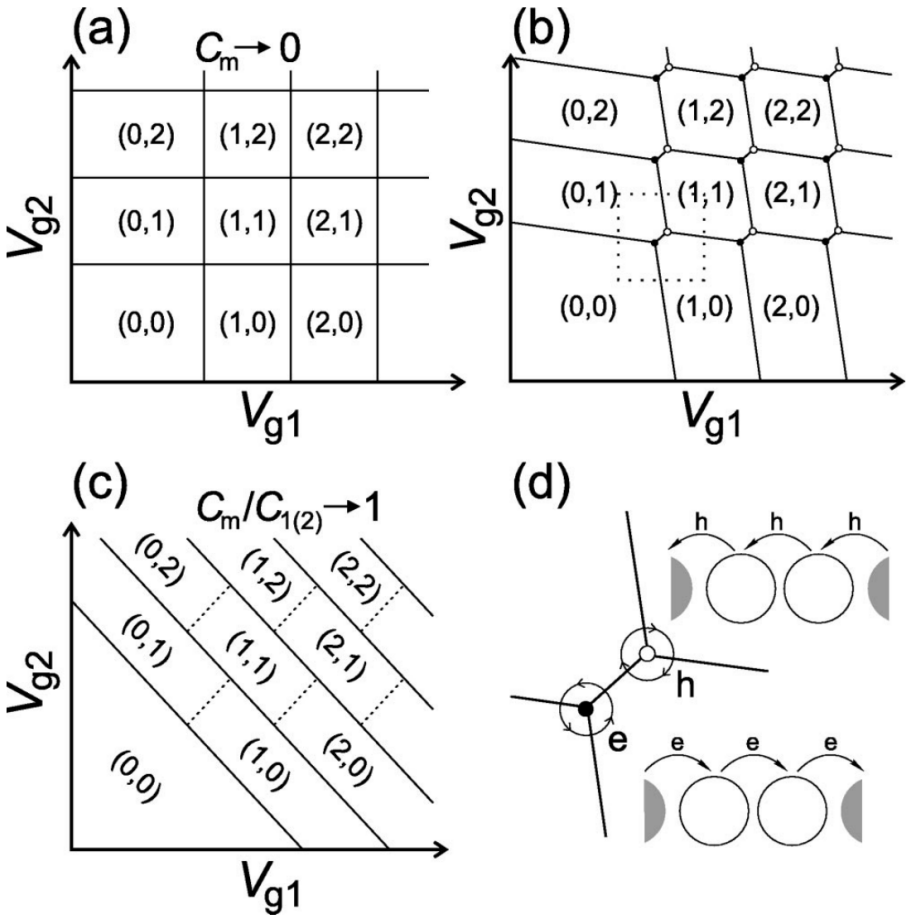

Fig. 2.14 Schematic stability diagram of the double dot system for (a) small, (b) intermediate, and (c) large inter-dot coupling. (d) Triple points of the stability diagram where energy levels in both dots are aligned and transport is not blockaded. Paths around the triple points stand for sequential transfer of electrons (filled circles) or holes (empty circles) through a double quantum dot. Adapted from [184].

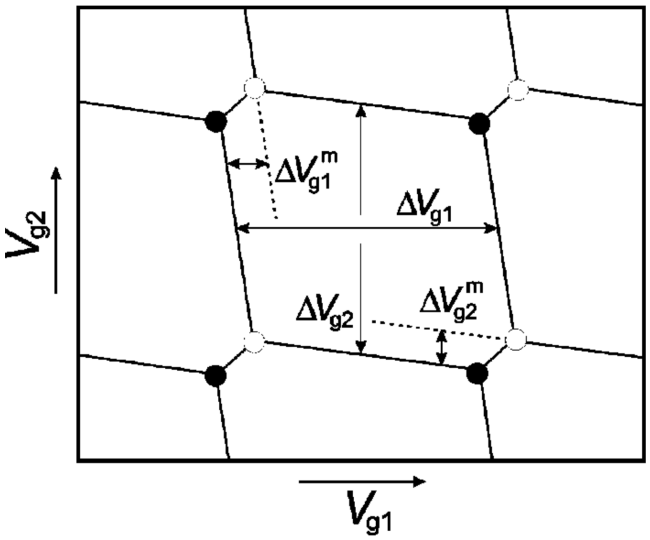

Fig. 2.15 Schematic stability diagram showing the Coulomb peak spacings, which is a zoom-in of the region enclosed by dashed line from figure 2.14(b). Adapted from [184].

(see figure 2.15) in the stability diagram are related to the capacitances of the double dots and are given by:

$$\Delta V_{g1} = \frac{|e|}{C_{g1}}, \tag{2.28}$$

$$\Delta V_{g2} = \frac{|e|}{C_{g2}}, \tag{2.29}$$

$$\Delta V_{g1}^{m} = \frac{|e|C_m}{C_{g1}C_2} = \Delta V_{g1}\frac{C_m}{C_2}, \tag{2.30}$$

$$\Delta V_{g2}^{m} = \frac{|e|C_m}{C_{g2}C_1} = \Delta V_{g2}\frac{C_m}{C_1}. \tag{2.31}$$

The above equations derived are under the assumption that V_{g1} and V_{g2} only couple directly to the respective dots. In practice, however, there is a finite cross capacitance from one gate to the other, resulting in a change of the slope of the charge domain boundaries in the honeycomb diagram.

The discussion of double quantum dots so far has been completely classical. However, the strong confinement of electrons in the dots can cause a discrete energy spectrum. To account for the quantized energy states in the dot, the single-particle energy needs to be incorporated in the electrochemical potential. $\mu_{i,n}$ denotes the electrochemical potential for adding an electron into energy level n of dot i. For the constant interaction model, $\mu_{i,n}$ is the sum of the classical electrochemical potential μ_i^{class} and the single-particle energy E_n:

$\mu_{i,n} = \mu_i^{class} + E_n$. Therefore, in the quantum regime, the addition energy is no longer equal to the charging energy alone, but instead given by [184]:

$$\begin{aligned} \mu_{1,m}(N_1+1,N_2) - \mu_{1,n}(N_1,N_2) &= E_{C1} + (E_m - E_n) \\ &= E_{C1} + \Delta E, \end{aligned} \tag{2.32}$$

and similarly the addition energy of dot 2 is $E_{C2} + \Delta E$. The dimensions of the honeycomb cell depicted in figure 2.15 for the classical regime, are modified accordingly as follows:

$$\Delta V_{g1(2)} = \frac{|e|}{C_{g1(2)}}(1 + \frac{\Delta E}{E_{C1(2)}}), \tag{2.33}$$

$$\Delta V^m_{g1(2)} = \frac{|e|C_m}{C_{g1(2)}C_{2(1)}}(1 + \frac{\Delta E}{E_{Cm}}). \tag{2.34}$$

For double quantum dots coupled in series, a conductance resonance can be found when electrons tunnel through both dots. This condition is satistied whenever three boundaries in the honeycomb diagram meet in one point. Figure 2.14d illustrates two kinds of such triple points, corresponding to different charge transfer processes. At the triple point denoted with filled circles, the dots cycle through the sequence

$$(N_1,N_2) \rightarrow (N_1+1,N_2) \rightarrow (N_1,N_2+1) \rightarrow (N_1,N_2)$$

which shuttles one electron through the system. At the other triple point denoted with empty circles, the sequence is

$$(N_1+1,N_2+1) \rightarrow (N_1+1,N_2) \rightarrow (N_1,N_2+1) \rightarrow (N_1+1,N_2+1)$$

corresponding to the sequential tunneling of a hole in the direction opposite to the electron. Thus in this way, charge pumping can be realized with a double quantum dot device [45].

2.2.3 Nanoribbon Quantum Dots

This section will review the quantum dots related literature in graphene nanoribbons. Graphene nanoribbons have attracted considerable attention due to their scalable band-gap engineering. Graphene nanoribbons are divided into two types, zigzag and armchair, depending on the edge shapes. Tight-binding calculations of graphene nanoribbons demonstrates that zigzag-edged graphene nanoribbons should behave like metal, while armchair-edged nanoribbons are expected to be semiconductors, with the gap increasing when decreasing the width of

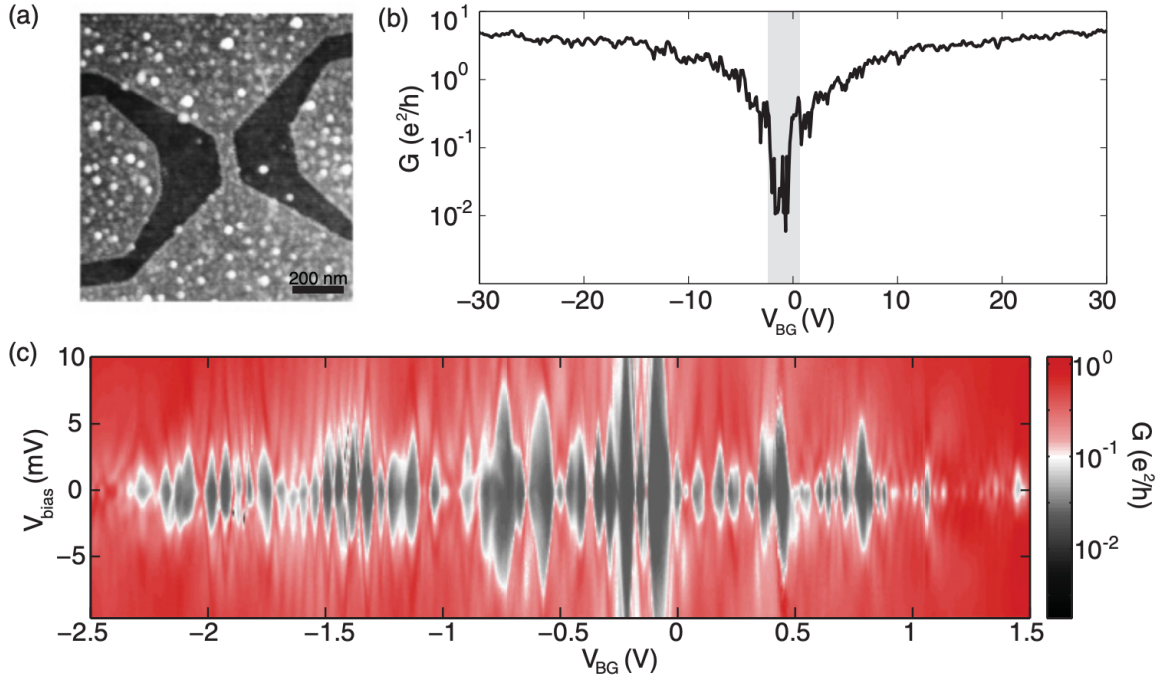

Fig. 2.16 (a) Scanning force micrograph of an etched graphene nanoribbon device. (b) Back gate sweep of the nanoribbon in a large density range showing a transport gap. (c) Coulomb blockade diamond measured inside the transport gap. Figures adapted from [50].

the nanoribbons [24, 59, 174]. Experimental studies on graphene nanoribbon defined by lithography do prove that the width of a ribbon depends on the gap size near the Dirac point. However, the gap size is much larger than the predicted value in theory [38, 80]. In addition, experimental results show that the gap is larger for longer nanoribbons, and Coulomb diamond shaped feature which is a signature of quantum dot formation can also be observed inside the transport gap, which is shown in figure 2.16(c) adapted from reference [50]. However, due to the disordered nature of etched graphene edges [108], there is a mixed edge of both zigzag and armchair in real devices. Moreover, the width of a real graphene nanoribbon is not strictly uniform along the whole length of the ribbon. Therefore, one can expect that there must be some other contributions to the gap size other than the theoretically calculated band gap value. The most acceptable idea is that a combination of the edge-roughness-induced Anderson localisation [136, 58, 172], and the disorder potential due to charge inhomogeneous distribution i.e. electron-hole puddles [1], results in the formation of multiple quantum dots along the nanoribbon. The presence of a gap is necessary for the quantum dots formation in a graphene nanoribbon, otherwise Klein tunnelling will allow charge tunnelling between these localized regions and thus prevent the formation of quantum dots. The detection of charge transfer between these localized states in a nanaribbon using a

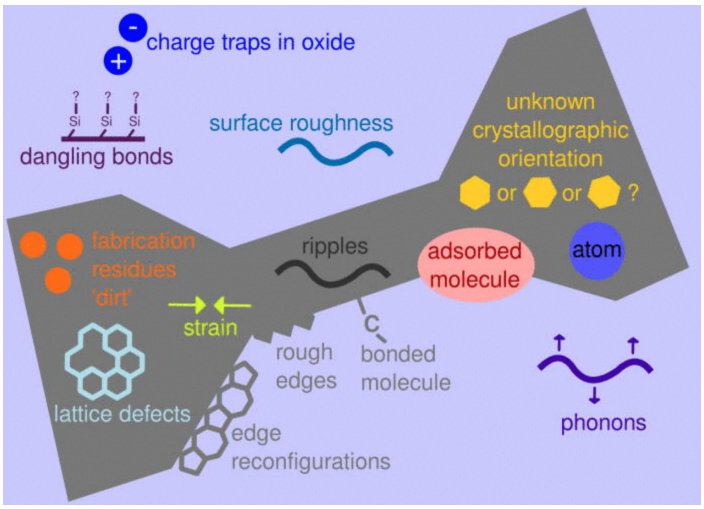

Fig. 2.17 Cartoon of a graphene nanoribbon along with possible sources of disorder. Adapted from [21].

single electron transistor (SET) further confirms the formation of multiple quantum dos in etched graphene nanoribbons [174].

Figure 2.16(c) exhibits the overlapping Coulomb diamonds, which are reminiscent of stochastic Coulomb blockade. It happens when electron transports through multiple quantum dots. Figure 2.17 illustrates different sources of disorder, leading to potential inhomogeneities, which create a serial arrangement of quantum dots. There are two distinct gaps. First, from back gate sweep shown in 2.16(b), the quantum dot behavior is only apparent when the Fermi level is close to the charge neutrality point where the carrier density varies spatially from electron-like to hole-like region (see figure 2.18(a)). Otherwise there will be no tunnel barriers between these electron-hole puddles to form quantum dots. Therefore, the transport gap, the region of suppressed conductance at zero source-drain bias shown in figure 2.16(b), is an indication of the strength of the disorder potential plus the confinement gap, which is influenced by the width of the nanoribbon. The second gap is the source-drain bias gap, which is roughly the largest value of source-drain voltage when conductance is suppressed at certain Fermi level. In the simplest case of a single quantum dot introduced previously, the source-drain gap is the charging energy of the dot, which does not show a clear dependence on the disorder potential. However, for multiple quantum dots, determining the source-drain gap is more complicated, experimental observation has demonstrated that deceasing the width of the ribbon can increase both the transport gap and the source-drain bias gap, whereas increasing the length can only increase the source-drain bias gap. This suggests that the source-drain bias is influenced by how many quantum dots are in series. It is also expected

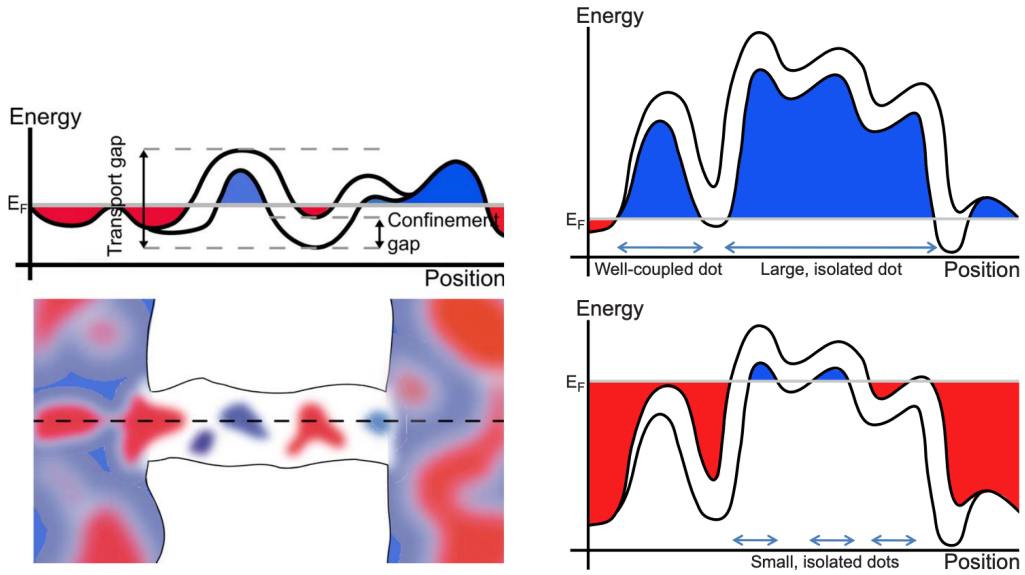

(a) (b)

Fig. 2.18 (a) Top: cartoon of quantum dots forming along the ribbon due to potential inhomogeneities and a confinement gap. Bottom: Top view illustration of a nanoribbon with the potential disorder shown above. (b) Cartoon of a potential profile at different Fermi levels (top and bottom), illustrating the location and the size of the quantum dots depend on the Fermi level. Figures adapted from [64].

to depend on the particular shape of the disorder potential, and the shape of the disorder potential is not strongly constrained by its amplitude [64].

The presence of multiple quantum dots in graphene nanoribbons has been confirmed by scanning gate measurements, which also demonstrate that the location and the size of these quantum dots depend on the Fermi level. This effect can be understood with the help of figure 2.18(b). Moreover, experimental study suggests that the quantum dots are located along the edges other than the bulk, especially for the cases where the edge disorder is stronger than that in the bulk [20]. The finding that reactive ion-etched graphene nanoribbons have different electrical characteristics compared with those etched by plasma, further supports the importance of edge disorder [19].

Although it is difficult to achieve atomic control of the nanoribbon edges using lithographic etching, the fabrication method of standard cleanroom processes, which will be described in chapter 3, is still attractive due to its simplicity and compatibility. The next section will introduce an antidot in the quantum Hall regime, which can avoid the edge disorder in etched graphene quantum dots while keeping the electron transport properties of graphene.

2.3 Quantum Hall Antidots

An antidot is a potential hill in a two-dimensional electron gas (2DEG), which was first studied in a GaAs/AlGaAs heterostructure [169]. It can be fabricated by applying a negative voltage on a top gate [63] or by an etched pit [74] in the chip surface. The former method is more suitable for graphene, due to its adjustable potential level and at the same time avoiding the disorders of the etched edges. An antidot is considered to be the counter part of a quantum dot, as it can be regarded as an artificial repulsive impurity. The idea of an antidot in the quantum Hall system was first presented in 1988 [88] in order to explain resistance peaks observed in a narrow Hall bar device [180]. The first experimental observation of Aharonov–Bohm oscillations in a gate-defined antidot was performed in 1989 [171].

When a strong magnetic field of the order of one Tesla is applied perpendicular to the 2DEG, an antidot provides a local depletion region inside a quantum Hall system. In this case, localized states are formed around the antidot, coupled with the quantum Hall edge states (see figure 2.19). The localized states have been investigated in the quantum Hall regime by observation of Aharonov–Bohm oscillations of conductance, which occur when the charge carriers tunnel between localized orbits and extended edge channels along the boundary of the 2DEG.

This section will introduce a single-particle model of an integer quantum Hall antidot. In Section 2.3.1, it describes single-particle localized states around an isolated antidot. The properties of the single-particle states are governed by the Aharonov–Bohm flux enclosed by them. In Section 2.3.2, Aharonov–Bohm oscillations of conductance will be discussed when electrons can tunnel between the extended edges of the 2DEG and the antidot via resonant scattering.

2.3.1 Single-particle energy levels

In a simple description of an isolated antidot, the antidot states are decoupled from the extended edge channels of the 2DEG. When the magnetic field is applied perpendicular to the 2DEG, electrons can form single-particle discrete energies around the antidot. The localized orbits are quantized so that their enclosing area S_m can satisfy the Aharonov–Bohm condition:

$$BS_m \sim m\phi_0, \tag{2.35}$$

where m is the orbital quantized number $\phi_0 = h/e$ is the magnetic flux quantum, h is Planck constant, and e is the electron charge. Due to the sloping shape of the antidot potential,

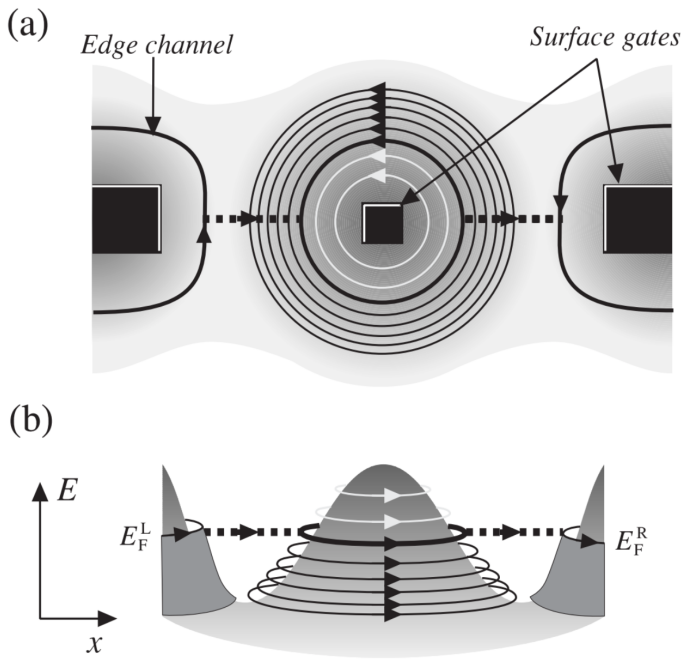

Fig. 2.19 Illustration of single-particle states formed around an antidot in the quantum Hall regime. (a) Top view of the antidot potential and the extended quantum Hall edge channels. The dotted lines represent the tunneling between the antidot state and the extended edge channels along the left and right edges. (b) Side view of the potential profile created by the voltages on the antidot and side gates, describing the continuous states along the extended edges, and the discrete states around the antidot. Adapted from [169].

the quantized states form a ladder in energy around the antidot (see figure 2.19b). If the antidot potential $V_{AD}(r)$ varies slowly enough, the single-particle energy of the mth orbital single-particle state of the isolated antidot is given by [169]:

$$\varepsilon_m \approx \frac{1}{2}\hbar\omega_c + \overline{V}_{AD}(m) + \varepsilon_m^Z, \tag{2.36}$$

where $\omega_c = eB/m^*$ is the cyclotron frequency, m^* is the electron effective mass, $\overline{V}_{AD}(m)$ is the mean antidot potential energy, ε_m^Z is the Zeeman energy of a spin electron. For simplicity, only the antidot states from the lowest Landau level are considered. The spatial separation $\Delta r_m \equiv r_{m+1} - r_m$ between two adjacent states depends on magnetic field and is given by:

$$\Delta r_m \simeq \frac{\phi_0}{2\pi r_m B}, \tag{2.37}$$

for large $m \gg 1$. In this case, the single-particle energy gap (see figure 2.20) between two neighboring states is given by [169]:

$$\delta\varepsilon_m \equiv \varepsilon_{m-1} - \varepsilon_m \simeq -\Delta r_m \frac{dV_{AD}(r)}{dr}|_{r=r_m} = \frac{\phi_0}{2\pi r_m B}\frac{dV_{AD}(r)}{dr}|_{r=r_m}. \tag{2.38}$$

The single-particle localized states around an antidot can be experimentally controlled by tuning either the antidot-gate voltage or the magnetic field B. The properties of the single-particle states are determined by the quantization of enclosed magnetic flux. To be specific, when B increases, the antidot states move towards the center of the antidot to keep the magnetic flux enclosed constant. Therefore, the states rise up in energy, and the highest occupied states pass through the Fermi level and become empty one by one. The period of this periodic depopulation process in magnetic field is:

$$\Delta B \simeq \frac{\phi_0}{S}, \tag{2.39}$$

where $S = \pi r^2$ is the effective antidot area enclosed by the state at the Fermi level. The same processes happen when tuning the antidot-gate voltage, which changes the potential at each radius relative to the Fermi level.

2.3.2 Aharonov–Bohm oscillations

Due to the depopulation of single-particle states near the Fermi level, the localized antidot states can be observed in Aharonov–Bohm resonance oscillations in conductance measurements when electron tunnels between the antidot states and the extended edge channels of the 2DEG, which is illustrated in figure 2.19 [169]. The size or the energy levels of the antidot

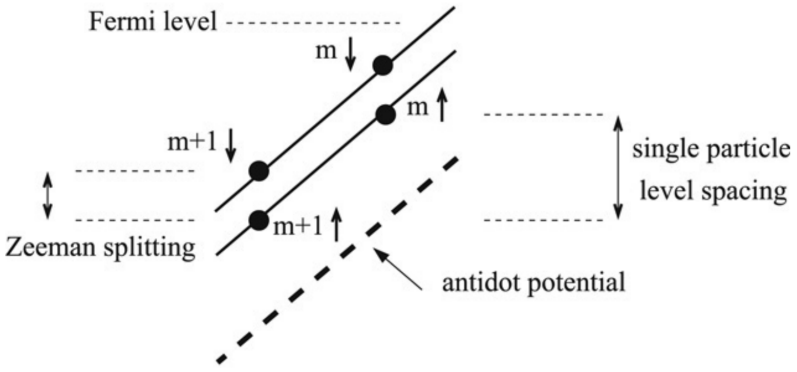

Fig. 2.20 Illustration of single-particle antidot energy states. For simplicity, only the spin-split branches of the lowest Landau level are drawn. The single-particle energy spacing between the mth and $(m+1)th$ localized states and Zeeman energy splitting of spin-up and spin-down states are shown. The dashed line indicates the antidot potential. Adapted from [169].

and the electrical widths of the constrictions can be tuned by applying negative voltages to the gates. The antidot conductance can be measured with a four-terminal setup, which can get rid of quantization of the background conductance as well as contact resistance compared with a two-terminal method (see details in the next chapter). Following the Landauer–Buttiker formula [26], four-terminal longitudinal conductance is derived as follows:

$$G_{AD-4T} = \frac{I}{V_L} = (\frac{1}{\nu_c} - \frac{1}{\nu_{bulk}})^{-1}\frac{e^2}{h}, \tag{2.40}$$

where V_L is the longitudinal voltage drop, ν_c and ν_{bulk} are the filling factors of the antidot and the bulk, respectively. Figure 2.21(a) demonstrates a typical experimental setup for measuring Aharonov–Bohm oscillations in antidot conductance. The diagonal voltage drop V_{dg} is introduced to remove the effect of the bulk filling factor:

$$G_{AD-dg} = \frac{I}{V_{dg}} = \nu_c\frac{e^2}{h}. \tag{2.41}$$

A typical Aharonov–Bohm oscillation of conductance in an antidot as a function of magnetic field is shown in Figure 2.21(b). The effective antidot radius can be estimated from the oscillation period using equation (2.38).

The discussion about quantum Hall antidots above is based on single-particle models [26], where electron–electron interactions are often neglected. However, there have been many interesting experimental observations including $h/2e$ Aharonov–Bohm conductance oscillations [162, 99, 63], the signature of electron interactions shown in the line shape of conductance peaks [124], the detection of antidot charging effect [98], Kondo effect [100],

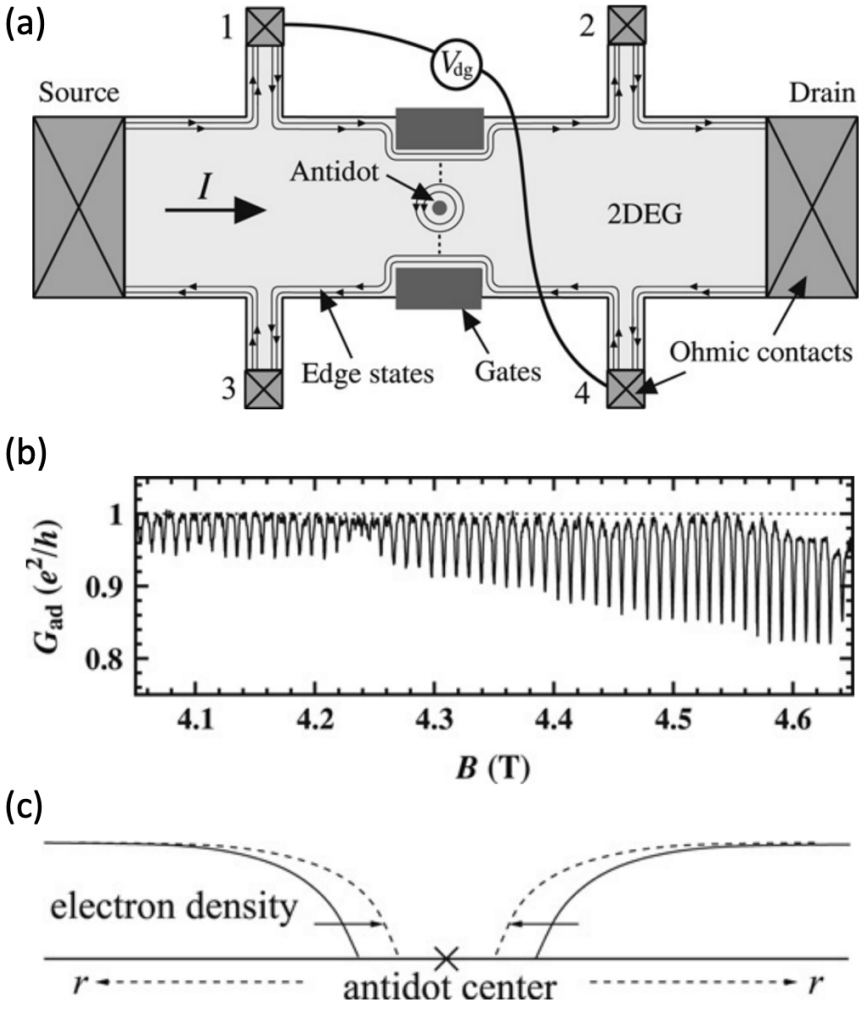

Fig. 2.21 (a) A typical experimental setup for antidot conductance measurements. Adapted from [169]. (b) Typical Aharonov–Bohm oscillations of conductance in an antidot as a function of magnetic field (T = 100 mK). Adapted from [169]. (c) Illustration of the accumulation of excess charge Δq around an antidot as the magnetic field increases. The electron density shift results from the enclosed magnetic flux movement of the discrete single-particle states to keep the enclosed magnetic flux constant. Adapted from [170].

and spectator modes in an antidot molecule [77], and none of them can be understood within single-particle models. The concept of excess charge [63] was introduced to explain these observations when electron-electron interactions get involved. The excess charge can be formed around an antidot due to the magnetic flux quantization. As magnetic field increases, all the states encircling the antidot move inwards to keep the enclosed magnetic flux constant, while the density of the positive background charges is fixed (see figure 2.21(c)). If the occupation of the antidot states does not vary during their movement, excess (negative) charge Δq accumulates around the antidot. Excess charges can provide a source of electron–electron interactions in the antidot. Therefore, the antidot is reminiscent of a quantum dot discussed in the previous sections, with a capacitive energy of $\Delta q^2/(2C)$, where C is the effective capacitance of the antidot. The excess charge accumulated at the perimeter of the antidot is approximated as:

$$\delta q = (2\pi r \delta r) e n_e, \tag{2.42}$$

where n_e is the electron density and given by

$$n_e = \frac{eB}{h} \nu_{AD}, \tag{2.43}$$

here, ν_{AD} is antidot filling factor. From the equation (2.35) we can derive the following equation for the single-particle orbits:

$$\delta r = -\frac{r}{2B} \delta B. \tag{2.44}$$

Therefore, combined with the charging condition $\Delta q = \pm e$ we can obtain the resonance period of the Aharonov–Bohm oscillations:

$$\Delta B = \frac{1}{\nu_{AD}} \frac{h}{e\pi r^2}. \tag{2.45}$$

The period in B only depends on the radius and filling factor of the antidot.

Chapter 3

Experimental Techniques

This chapter describes the details of the processes and techniques that are used to fabricate and measure graphene nanostructures, such as Hall bar, quantum Hall antidots and double quantum dots discussed in the following experimental chapters. In particular, section 3.1 outlines the design and fabrication process for making Chemical Vapor Deposition (CVD) graphene nanodevices. Section 3.2 will introduce different kinds of cryogenic systems in which low temperature measurements are performed. Two types of measurement circuits setup will be presented in section 3.3. The last section 3.4 describes the radio-frequency (RF) reflectometry techniques used to detect the charge and spin of the graphene nanodevices with high sensitivity and accuracy.

3.1 Device Fabrication

This section shows the detail of the techniques to fabricate graphene nanodevices. The graphene material used in this thesis was grown by our collaborator, Centre for Advanced Photonics and Electronics (CAPE) of the University of Cambridge by using CVD method due to its high productivity, and all the fabrication described in this section was done in the Semiconductor Physics (SP) group cleanroom in the Cavendish Laboratory unless otherwise specified. The substrate used for these devices is doped or undoped silicon wafer which has a native silicon dioxide layer of 300 nm thickness.

The basic procedure to transfer and pattern CVD graphene devices is as follows. The first step is to transfer graphene on a precleaned silicon substrate. In order to align well in the following processes, alignment markers are metallized onto the chip. Then a layer of photoresist, which is for later optical lithography, or Poly(methyl methacrylate), also known as PMMA, which is for later electron beam lithography (EBL) is spin-coated on the chip. The spin-coating step is the basis for the next both etching and metal contacts deposition

processes. Depending on the features of the desired device, a specific area of graphene is exposed under the UV light (if the feature is about several microns) or under an electron beam (if the feature is under 1 micron). After patterning and developing the resist, the exposed graphene area is etched away by oxygen plasma and the desired device pattern is left on the chip. For the contacts deposition step, the exposed contact area has metal deposited (usually Ti/Au in SP group) by thermal evaporation followed by lift-off processing. Finally, the leadless device is mounted onto a leaded chip carrier (LCC) or some specific sample carrier and bonded with gold wires in order to enable measurements in low-temperature systems. The processes described above are for the fabrication of basic graphene field effect transistors (FETs), i.e Hall bar, and for the antidots device, the top-gate will be coated with a layer of dielectric between the top-gate and graphene Hall bar, which can be completed using self-alignment methods i.e. cross-linked PMMA coating [177] or global methods i.e. atomic layer deposition (ALD) [68]. The details of each step are as follows:

Wafer preparation

The silicon substrate is first cleaned by rinsing in acetone and subsequently in isopropanol (IPA) followed by being dried with nitrogen gas. The graphene is grown on copper using CVD method by CAPE and then transferred onto the cleaned silicon substrate by using PMMA (the details about graphene growth and tranfer will be introduced in the chapter 4). Before further processing, the wafer is cleaved by using a scriber into several 10 cm $\times$ 10 cm chips, which makes the following fabrication processes much easier. In addition, in order to align well in the following fabrication steps, alignment markers are metallized onto the cleaved chip by optical lithography, which will be discussed in detail in the next part. Those metal markers, with size ranging from 5 μm (for EBL alignment) to 50 μm (for optical lithography alignment), are located at the four corners of each device. Depending on the feature requirements, both optical lithography and EBL may have been used in the fabrication processes.

Optical lithography

Spin-coating is used to deposit a photosensitive or electron beam-sensitive fluid resist on a wafer surface at high spin speed. It is a standard microelectronic procedure to form a relatively uniform and desired thickness of a coating layer by controlling the spin speed and the resist viscosity. For optical lithography, the standard photoresist is s1813 in the cleanroom of SP group. The spin-coating process is completed in a spinner for 30 seconds at spin speed 5500 rpm. Then the chip is placed on a hot plate for 1 minute at a temperature of 115°C. After

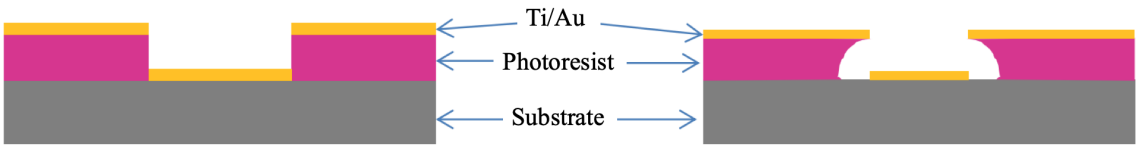

Fig. 3.1 Schematic profiles of the sample without Chlorobenzene (left) and with Chlorobenzene (right).

baking, the chip is moved onto a mask aligner and exposed for 6.5 seconds under ultra-violet light, along with an optical mask with the desired patterns. Finally, a corresponding developer is used to develop the patterns on the chip and for s1813, the developer is MF319. If the next process is metal deposition, chlorobenzene is needed before development, because chlorobenzene can make photoresist less sensitive to developer solution at the surface. This allows for a more well-defined undercut (see figure 3.1), which makes the following lift-off easier. The whole procedure of standard optical lithography is described above. In addition, sometimes negative photoresist i.e. AZ 5214E will be needed according the designed optical mask, in which case the unexposed areas will be developed, opposite to standard optical lithography. The corresponding developer for AZ 5214E photoresist is AZ 726MIF.

Electron beam lithography

In order to get finer features, EBL provides a good tool for fabrication. The EBL PMMA spin-coating recipe used for metal deposition is shown in table 3.1. The wafer is baked on a hotplate at 125°C for 5 – 10 minutes after each layer is spin coated to get rid of any solvents. This double layer structure is used because the low molecular weight short chain PMMA in the bottom layer is more sensitive to the developer after exposure. The function of the double layer structure is similar to chlorobenzene processing in optical lithography, to make the following lift-off process easier. The recipe in table 3.1 can lead to two PMMA layers with total thickness over 160 nm (the thickness can be calculated by Ellipsometre), which is enough to lift off around 100 nm of deposited metal during thermal evaporation described in the next part, and thin enough so that the PMMA layer hanging over the undercut does not collapse readily.

Apart from defining metal contacts and gates, EBL is also used for defining the etch mask for small the graphene features. In this case, only single layer PMMA needs to be spin-coated, and the recipe is shown in table 3.2. The spun layer also needs to be baked on a hotplate at 125°C for 5 – 10 minutes to remove any solvents left.

Table 3.1 EBL PMMA recipe used for metal deposition

	Molecular weight	Dilution/Solvent	Spin speed (rpm)	Spin time (s)
Bottom layer	100K	A6 1:1 Anisole	3500	60
Top layer	950K	A11 1:5 MIBK	3500	60

Table 3.2 EBL PMMA recipe used for definition of etch mask

	Molecular weight	Dilution/Solvent	Spin speed (rpm)	Spin time (s)
Etch layer	950K	A4 1:1 Anisole	6000	60

Because PMMA is a positive resist, regions exposed to the electron beam become soluble and can be removed when submerged in the developer (MEK:MIBK:IPA = 1:5:15) for seven seconds. This works for both double layer and single layer PMMA.

In the fabrication process of quantum antidot devices, PMMA is crosslinked by electron beam [177] to work as a dielectric layer for further top gates. In this case, the cross-linked PMMA is a negative resist and the areas exposed to the electron beam will be left on the chip after being submerged into acetone. This process requires a much higher dose than for exposing PMMA as a positive resist.

Thermal evaporation

Metal is deposited on the whole chip by using a thermal evaporator, which can heat the source metal to high temperature in a vacuum condition so that the desired metal vapour travels to the sample directly above the source metal, and then a uniform layer of metal is formed on the surface of the chip.

Before the evaporation, the sample is loaded into a sample holder in the evaporator chamber and then the chamber is pumped until the pressure is under 2×10^{-6} mbar (this pumping process may take around one hour). The rate of metal evaporation can be controlled by tuning the current through the boat, which holds the source metal, so that a known amount of metal is deposited onto the chip. For the devices discussed in this thesis, a thin layer of titanium ($\sim$ 10 nm) is deposited before a thicker gold layer ($\sim$ 90 nm) to improve the adhesion of the gold to the chip. After the evaporation process, the sample is cooled down and then put into a beaker with enough acetone in it for the lift-off processing. The previously patterned photoresist or PMMA layer works as a mask for the deposition step. During the lift-off step, the metal deposited on the resist is removed together with the resist while the metal in other areas will be left on the sample.

The success of the lift-off step depends on whether there is a path for acetone to touch and dissolve all the resist covered by the metal layer. This condition requires a minimum thickness of resist for a given thickness of deposited metal layer. The thickness of resist should be much larger than that of metal layer and it turns out that 100 nm deposited metal can be successfully lifted off with the double layer PMMA thickness $\sim$ 160 nm.

Oxygen plasma etch

The function of etching is to etch sample into the desired patterns during the device fabrication process. After the development processing for the lithography, the desired patterns are covered by resist as an etch mask, whereas the rest of the area is unprotected and can be etched away under some conditions. For graphene, the devices are usually dry-etched by oxygen plasma. The plasma is generated by applying a high frequency voltage on a low pressure of oxygen gas ($\sim$ 150 mTorr). In this process, a cascade of ionization happens until a certain density of ions is reached and a plasma is formed. The created plasma consists of ions and atoms in the excited state. The excited ions and atoms release energy in the vacuum UV range, which can break the molecular bonds. In addition, the oxygen species created in the plasma are also highly reactive to carbon-based molecules, like graphene, and readily form low molecular weight hydrocarbons that can be removed away from the surface of the chip through evacuation of the chamber. The pressure can be controlled by balancing the oxygen gas flow rate and evacuation through a adjustable valve.

It is important to adjust the etch parameters to make sure the unprotected graphene can be fully etched away, but the etch mask (PMMA is usually used for graphene) should still cover the protected areas to avoid damage to the graphene patterns. There are many factors that may affect the etching process, such as the size and shape of the graphene features, as well as the gas flow rate, pressure and the species of neutral gas inside the chamber [49]. Among these factors, we can freely change the RF power, etching time and gas pressure during the experiments. RF power determines the amplitude of the voltage applied to the plasma and the higher the RF power is, the more aggressively it will etch. A longer etching time leads to more material being etched, but the etching rate is not linear against time. It was found that less graphene is etched during the first few seconds due to the plasma not striking immediately or some resist residual left on the surface of exposed areas. The gas pressure determines the energy of the ions hitting the graphene during the etch. The physical etch is more likely to happen at low gas pressures, where the ions energy is high.

The etching process is determined by the factors mentioned above, as well as the thickness of the etch mask, which in turn is determined by the minimum feature size of the graphene devices. For instance, in terms of the Hall bar devices, the minimum feature size is 2 μm, so

that a 1.4 μm photoresist mask is enough to make sure all the features are precisely defined. But for double quantum dot devices, whose minimum feature size is about 50 nm, a 50 nm PMMA etch mask needs to be used to ensure that all the features can be accurately transferred to the graphene. The recipe used for etching fine graphene features in this thesis is an RF power of 30 W with an oxygen gas pressure of $\sim$ 40 mTorr in a chamber pressure of $\sim$ 150 mTorr for 8s to remove graphene and around 40 nm of PMMA.

During the fabrication processes in this thesis, 3 s light plasma etch with an RF power of 3 0W is usually applied just before the metal deposition to get rid of the residual photo resist or PMMA to reduce the contact resistance, as well as improve the contact adhesion to the substrate for better wire bonding afterwards.

Packaging and bonding

Before the fabricated devices are ready for measurements, they are mounted with some kind of glue and then bonded via gold wire onto LCC package or other specific sample carriers. There are two different kinds of glue in the SP group that can be used to stick the sample chip onto the LCC package: GE varnish and silver dag. Silver dag is conducting while the GE varnish is insulating, so in some cases silver dag can be used to add a back-gate to the sample when mounting.

In terms of bonding, there are two types of bonding machines in the SP cleanroom: a ball bonder and a wedge bonder. For any bonder, there is a needle-like tool called a capillary where a gold wire can be passed through. There are two steps for each bonding process, bonding the pads on the sample and on the chip carrier respectively. When the tip of the capillary is pressed down against the surface of a previously patterned bond pad, a combination of heat, pressure and ultrasonic energy causes the tip of the wire to weld with the bond pad. That is how the bonding works.

The big difference between the two kinds of bonder lies in the first step bonding. For the ball bonder the tip of the gold wire is a ball, which makes it easier to bond than wedge bonder. The second step for both is wedge bonding. In addition, due to the special structure of the wedge bonder capillary, the bonding direction for the two steps can only be from package to sample while there is no such requirements for ball bonder in the bonding direction. Moreover, the wedge bonder is suitable for sensitive devices with small bond pads, as no ball forms during bonding, which reduce the risk of damage from electrostatic discharge (ESD) used to form the ball.

Force, power and time settings are important in bonding devices. For different materials, the bonder needs different setting parameters. Additional precautions include grounding all the conducting surfaces surrounding the bonding pads, as well as providing a constant

spray of charges to the bonding pads through an antistatic fan in order to minimize charge accumulation in the devices. It is also important to make sure that one needs to be grounded before touching the devices and store the packaged samples in a conducting sample holder.

3.2 Cryogenic Systems

Cryogenic systems, also called cryostats or refrigerators, are apparatus used to maintain low cryogenic temperature of samples mounted within the system. All the low temperature measurement experiments are carried out in cryogenic systems. Most of the data presented in this thesis were taken at low temperatures varying from 40 mK to 4.2 K. Various cryogenic systems have been used depending on the temperature required. There are different levels of cryogenic systems due to the temperature limitation it can reach. Here different types of cryogenic systems are introduced.

3.2.1 4.2 K dipping station

The simplest cryogenic system is 4.2 K dipping station. From the name one can tell that the temperature it can reach is 4.2 Kelvin, which is the boiling temperature of He-4 at 1 atm. It works by just dipping the probe, which holds the device, into a liquid He-4 storage dewar which keeps the temperature of the device constantly at 4.2 Kelvin. Simple transport measurements can be carried out in a 4.2 K dipping station even though in most cases the temperature is too high to study quantum transport, and magnetic field cannot be applied in such a system. But it allows us to change the sample quickly and easily, thus making it useful for testing the conductivity and gate-effect of graphene nanodevices at low temperature to prepare for further lower temperature measurements with more complicated cryostats.

3.2.2 1.2 K pumped He-4 cryostat

In order to achieve temperatures lower than that of 4.2K, a more complicated cryostat is used which separates the sample space from the liquid helium bath using a vacuum can, which is in thermal contact with the liquid helium bath. Temperatures around 1.2K can be reached by using a 1-K pot, which is a helium container connected to a rotary pump. When the surface of the 1-K pot is pumped, the liquid helium evaporates and carries heat energy away to cool down the temperature of the device to around 1.2-1.6 Kelvin. The exact temperature it can reach depends on the vapor pressure. In this kind of cryostat, a magnetic field could be applied to the sample space, so it allows magneto-transport measurements to be performed.

3.2.3 He-3 refrigerator

The helium mentioned above is He-4, the main isotope of helium. Temperatures below 1 K down to 300 mK can be achieved by pumping on liquid He-3 (a rare isotope of helium) instead of He-4.

Different from a He-4 cryostat, the He-3 is adsorbed in a sorption pump (sorb), which is placed at the top of the sample space. To achieve the base temperature, firstly liquid He-4 is introduced into the 1K pot from the main bath, which is then pumped to cool it down to 1.2 K, which is cold enough to condense the He-3. This step is the same as a He-4 cryostat system. Secondly, the sorption pump is heated to around 50 K by an electric heater, releasing He-3 atoms into the sample space. Then the He-3 gas is cooled down by the 1K pot and starts to condense. After a sufficient amount of the liquid He-3 has been collected at the bottom of the sample space, the sorption pump is cooled down by pumping cold He-4 gas through the pipe that is in thermal contact with the sorb. Then the sorb starts to adsorb the residual He-3 gas, reducing the pressure, and hence cooling the sample space. Therefore the base temperature of 300 mK can be reached. It can keep at base temperature for as long as ten hours or more depending on the cryostat or the sorb pumping rate. After that, the sample space starts to warm up, therefore the same process of condensation and cooling-down will be repeated.

3.2.4 Dilution refrigerator

When the mixture of He-3 and He-4 is cooled down below a critical temperature (approximately 870 millikelvins), it undergoes spontaneous phase separation to form a He-3 rich phase (the concentrated phase) and a He-3 poor phase (the dilute phase). At very low temperature the concentrated phase is essentially pure He-3, while the dilute phase contains about 6.6% He-3 and 93.4% He-4. In the mixing chamber, the two phases are in equilibrium and separated by a phase boundary. He-3 is the working fluid and it is diluted as it flows from the concentrated phase through the phase boundary into the dilute phase to supply a useful cooling power for the refrigerator, as the process of moving the He-3 through the phase boundary is endothermic and removes heat from the mixing chamber environment. One dilution refrigerator called the MX400 in the SP group of the Cavendish Laboratory was used in the work presented in this thesis. The MX400 is also equipped with an RF reflectometry setup, allowing for realizing high sensitive and accurate measurements, which will be described in section 3.4.

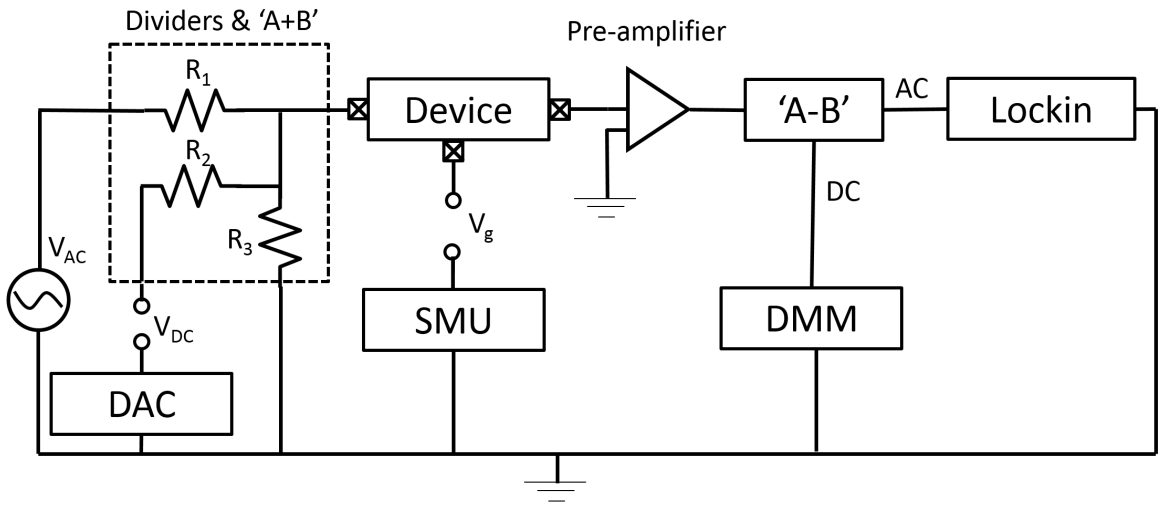

Fig. 3.2 Two terminal measurement circuit.

3.3 Measurement Circuits

The cryogenic system, along with a sample probe, has a computer work station which controls the instrumentation that includes a lock-in (LI), a digital to analogue converter (DAC), a source measure unit (SMU), a digital multimeter (DMM), a pre-amplifier, a thermometer, a magnetic field controller and so on. Two-terminal measurement and four-terminal measurement are two typical methods for performing electronic transport measurements. In the process of performing measurements, all the instruments are communicated with a computer. The signal control and data collection are realised by software such as Cryomeas, Labview or Matlab.

Figure 3.2 and figure 3.3 exhibit the circuits of two-terminal and four-terminal measurements respectively for the CVD graphene nanodevices discussed in this thesis. A DAC is used to supply a DC signal while a LI is used to supply an detect an AC signal. Dividers are employed to reduce the voltage before mixing the signals using an 'A+B box', to make sure the current through the device is not too high. An SMU is used to add a gate voltage to the device. Then the current is amplified before being separated by an 'A-B box' to a DC signal (received by a DMM) and AC signal (received by the LI). The big difference for four-terminal measurement is that a resistor, whose resistance is much higher than the device, is added before the current goes through the device, to keep the current constant, while it is constant voltage for two-terminal measurement. As it uses separate pairs of voltage-sensing electrodes, the four-terminal measurement circuit can measure the device conductance more accurately. Compared to the simpler two-terminal method, the four-terminal technique can

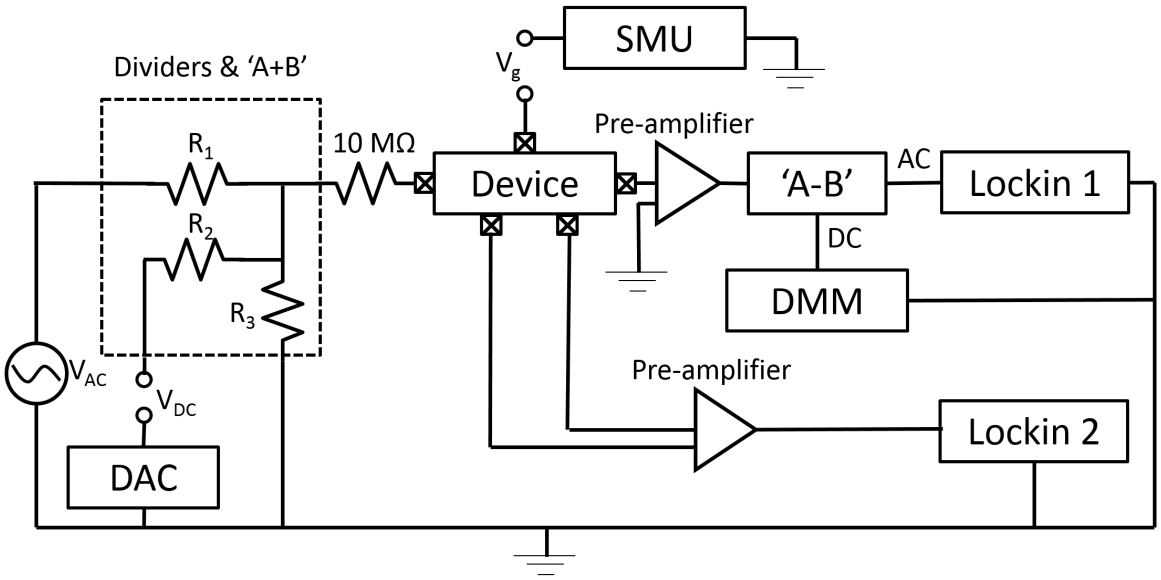

Fig. 3.3 Four terminal measurement circuit.

eliminate the contact and lead resistance contribution onto the measurement result. Therefore, it is preferably applied to low resistive measurements.

3.4 Radio-frequency Reflectometry Technique

The measurement circuits described above are the conventional low frequency cryogenic measurement methods. There are two main issues with these methods. One is the need for long wiring resistance connecting the sample at low temperature to the room temperature amplifiers. The high capacitance of the wiring ($\sim$ 1 nF), together with the large resistance of typical samples ($\sim$ 50 kΩ) leads to a large RC time constant and limits the measurement bandwidth to $\sim$ 1 kHz. Furthermore, the charge sensitivity at these low frequencies, typically tens or hundreds of Hertz, is limited by 1/f noise [202] due to the motion of background charges.

A well known solution to overcome these problems is to embed the sample into an impedance matching LC circuit. Impedance matching is an important microwave engineering technique which ensures that maximum power is delivered to the sample and that power loss in the transmission line is minimized. The impedance matching of the LC circuit terminates a transmission line connected to the room temperature measurement setup and use radio-frequency (RF) reflectometry techniques to measure instantaneous changes in the impedance of the devices. By matching the device to the characteristic impedance of the transmission line Z_0 (50 Ω) its capacitance is no longer relevant. Therefore, this method can achieve a

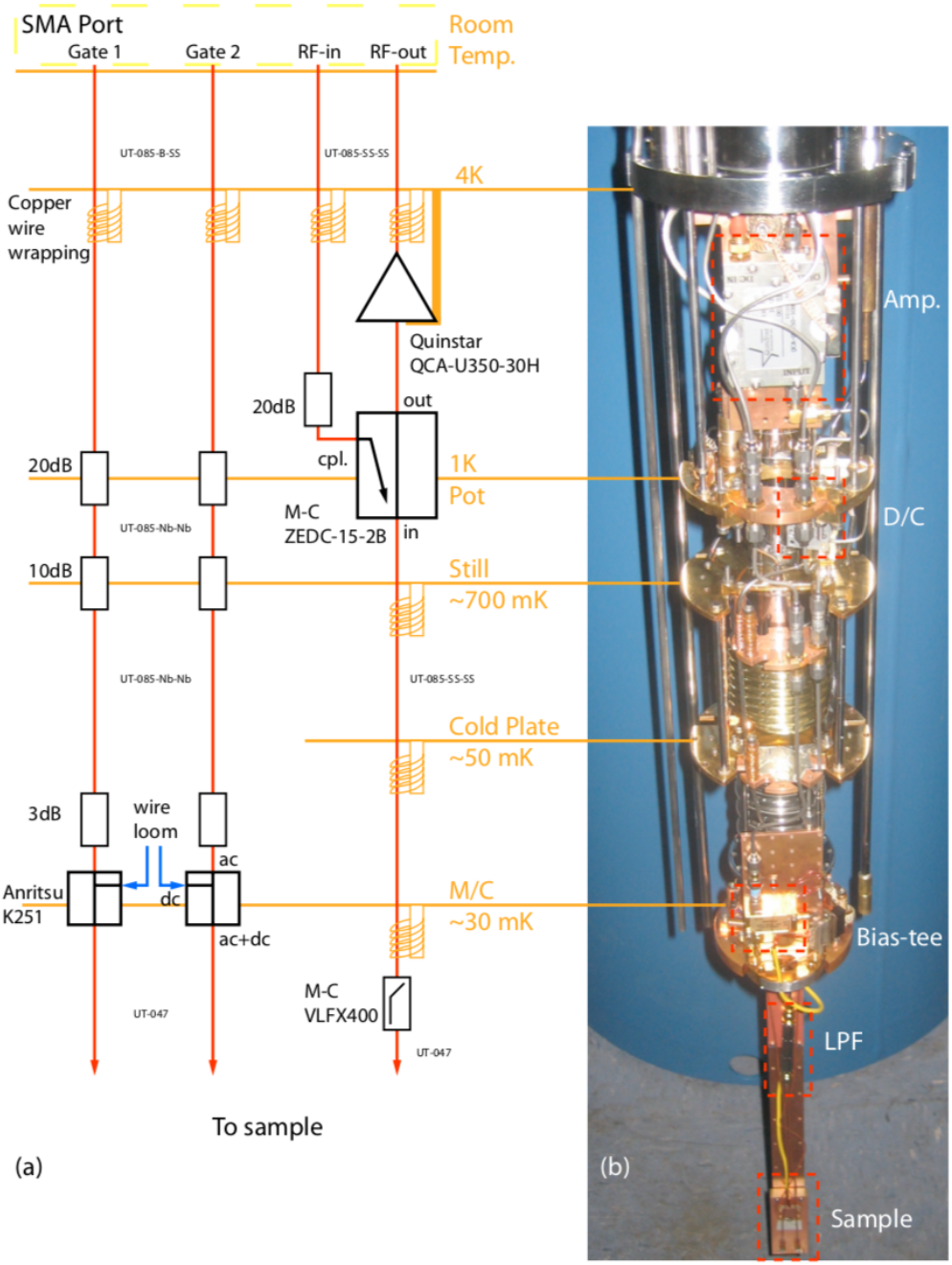

Fig. 3.4 (a) Schematic of the high frequency wiring for the fridge. (b) Photograph of the lower section of the dilution fridge with the high frequency wiring installed. Adapted from Karl Petersson's PhD thesis.

much higher bandwidth and it can operate even at frequencies in excess of 100 MHz, where the 1/f noise due to background charge motion is completely negligible.

Previously the RF reflectometry technique has been used to increase the measurement bandwidth of a single electron transistor (SET) [166] and quantum point contact (QPC) [32] electrometers, as well as large area gated 2D systems [176]. It was initially expected that it would not be possible to be used by the RF reflectometry technique on these large samples due to the large capacitance, which results in low resonance frequency and a negligible sensitivity at high resistances.

As mentioned previously in the dilution fridge subsection, the MX400 dilution fridge in the SP group was used to perform the RF reflectometry measurements described in this thesis. The probe wiring was done by a previous PhD student Karl Petersson in the SP group. The wiring of the RF reflectometry circuit of the MX400 dilution fridge is shown in figure 3.4 adapted from Karl Petersson's PhD thesis. I modified the radio-frequency reflectometry setup by replacing the RF sample holder with a smaller one, which can fit into the probe and work in a perpendicular magnetic field (see figure 3.5(b) and 3.5(c)). The RF tank circuit and two RF ground lines (each with a capacitor) are soldered on a printed circuit board (PCB). This RF sample holder also consists of ten normal contacts for transport measurement, which are connected to the probe via a 21-way Conan connector, and two fast gates connected to the probe via an SMA connector (the bottom two shown in figure 3.5(c) and the top one is for the RF reflectometry circuit) and coaxial line. During my PhD, I also designed and wired another RF probe (see figure 3.5(a)) used as a dip probe for quick testing at 1.2 K before further experiments are performed. This RF probe is equipped with a breakout box with ground switches, as well as four fast gate lines. The bottom sample space of the probe is for placing the sample holder as well as the components (i.e. direct coupler and amplifier) of the RF reflectometry circuit.

The core part of RF reflectometry technique is the impedance matching LC tank circuit, by which the impedance of the device is matched to the characteristic impedance of the transmission line Z_0 (50Ω). The matching circuit consists of an inductor L, typically a surface mounted component placed close to the sample, and the capacitance C_s which includes the stray capacitance from the inductor and the sample holders to ground. The inductance L and capacitance C_s form an LC resonator with resonance frequency $f_0 = 1/2\pi\sqrt{LC_s}$. At the resonance frequency the impedance of the matching circuit is real and is given by $Z_t = L/RC_s$, where R is the device resistance. Perfect matching occurs when $Z_t = L/Z_m C_s = Z_0$, where Z_m denotes the matching impedance. Variations in the device impedance change the transformed impedance Z_t and hence the reflection coefficient $\Gamma = (Z_t - Z_0)/(Z_t + Z_0)$. Then, instead of measuring the device resistance directly, one launches a RF carrier wave down the

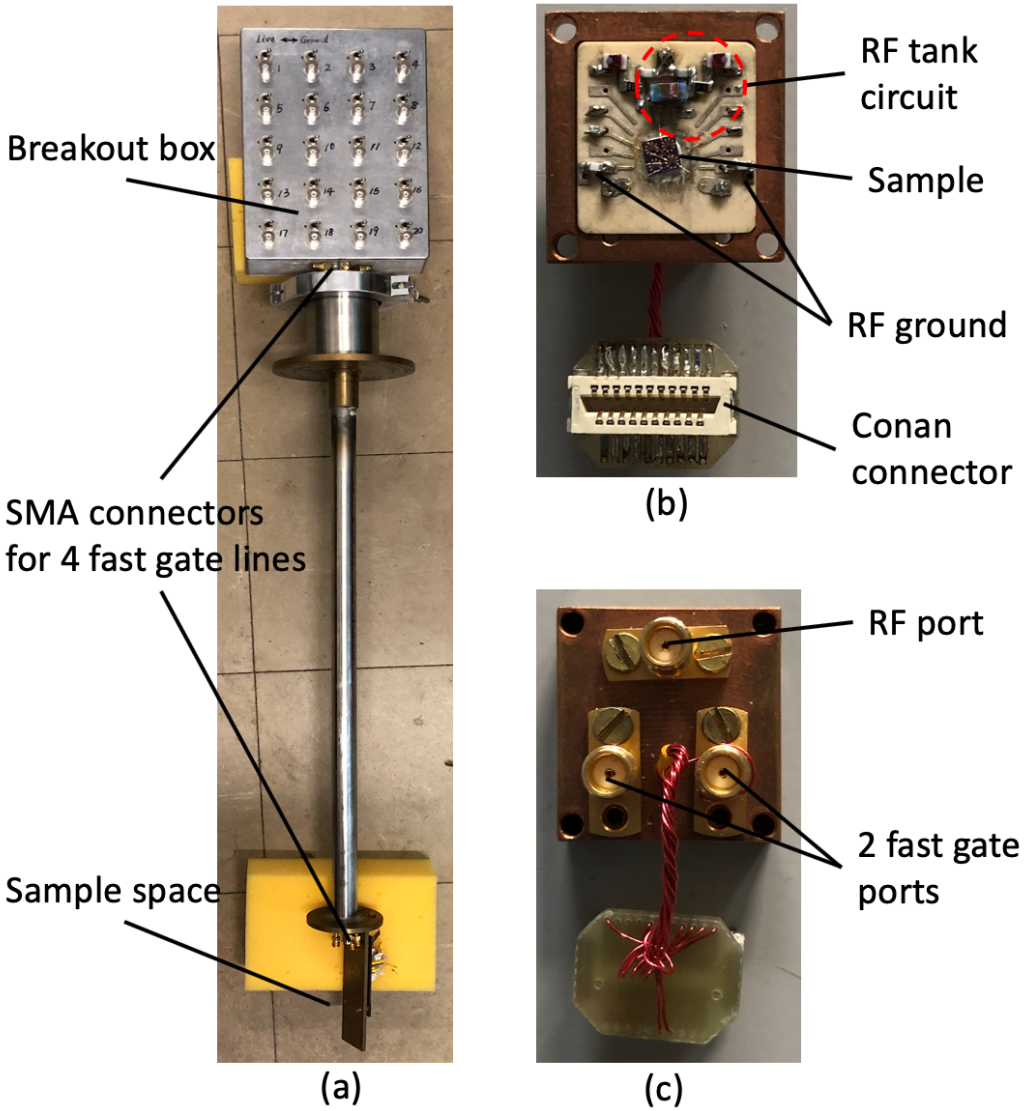

Fig. 3.5 (a) Photograph of a RF probe designed and wired by me during my PhD used as a dip probe for quick test at 1.2 K. (b)(c) Photographs of the front and back of a perpendicular RF sample holder with tank circuit soldered on the PCB manufactured by me used in this thesis.

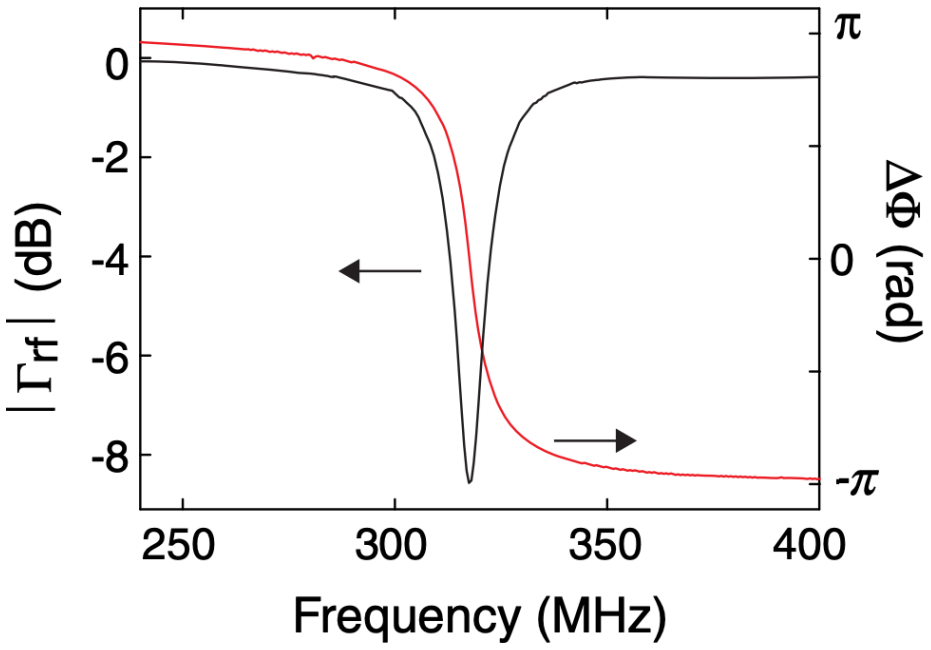

Fig. 3.6 Measured amplitude and phase response of a resonant circuit adapted from [150]

transmission line at a frequency close to f_0, where the sensitivity to the changes in impedance is largest, and monitors the amplitude of the reflected carrier wave. Figure 3.6 adapted from [150] shows the measured amplitude and phase response of a resonant circuit. When resonance happens, there will be a dip in the reflected signal, suggesting most of the signal energy is absorbed in the matching circuit and in the meantime, the phase is shifted from π to $-\pi$. The precise resonant frequency depends on the quantum impedance of the measured system, which can, therefore, be read out using this RF reflectometry technique.

The total quality factor Q that sets the bandwidth is given by $1/Q = 1/Q_1 + 1/Q_2$, where $Q_1 = R/\sqrt{L/C_s}$ is define as the unloaded quality factor, and $Q_2 = \sqrt{L/C_s}/Z_0$ is the external quality factor. For details of the RF reflectometry technique see [166, 160]. The key point to the readout scheme is that the phase of a reflected RF signal depends on the quantum impedance of the device, and phase measurements thus provide a sensitive and noninvasive probe of the system.

Chapter 4

Probing Electron Scattering in Scalable CVD Graphene

4.1 Introduction

As many graphene-based electronic and optoelectronic device concepts start to make the transition from the laboratory research into industrial applications [139], it is imperative that factors such as long term stability, large area reproducibility and low-cost need to be addressed. As described in the introduction chapter, the lack of scalability and reproducibility of graphene devices fabricated from small exfoliated flakes and the high cost of epitaxial graphene on silicon carbide, remain the major obstacles for further commercialization of graphene electronics and optoelectronics. Thus, graphene grown by chemical vapor deposition (CVD) [84] stands out as a useful alternative to mechanically exfoliated graphene and epitaxial graphene, because its wafer-scale growth enables large scale production with a low cost [156]. However, environmental factors such as ambient air [164, 161], lithography resists and polymers used in the transfer process [154], cause unintentional, generally p-type, doping and hysteretic [188, 31, 96] behaviour in graphene field effect transistor (FET) devices, especially for CVD graphene.

First, this chapter will discuss the fabrication progress towards scalable CVD graphene FET devices, by introducing an encapsulation and passivation approach to overcome those issues existing in the conventional fabrication process. This section is partly adapted from a published article in the journal 2D Materials, entitled "Encapsulation of graphene transistors and vertical device integration by interface engineering with atomic layer deposited oxide" [4]. Second, by studying electrical characterisation and magnetotransport phenomena in encapsulated CVD grown Bernal stacked and large twist angle (30°) bilayer graphene FETs,

as well as monolayer graphene FETs for reference, we show that electron scattering processes and hot electron effects can be tuned. The results of the second part of this chapter is expected to be published in another article "Twist angle dependent electron scattering in as-grown CVD bilayer graphene", which is in preparation for journal Physical Review B.

The works in this chapter are completed in collaboration with Dr. Jack Alexander-Webber (who supplied the graphene material and the Atomic Layer Deposition (ALD) techniques) and Dr. Ye Fan (who helped with fitting the data) from the Centre for Advanced Photonics and Electronics (CAPE) of the University of Cambridge.

4.2 ALD Encapsulated Scalable Graphene FETs

Encapsulating graphene field effect transistors (FETs) with Al_2O_3 barrier layers deposited by ALD can significantly reduce gate hysteresis and provide reproducible performance over several months [163]. For graphene electronics, the potential advantages of such an encapsulation are twofold. First, Al_2O_3 is increasingly used as a moisture barrier in applications due to its exceptionally low water vapour transmission rate [30]. This leads to long term stability and protection of devices from humidity and other atmospheric effects. Second, the ALD process has been shown to effectively passivate charge trap sites such as silanol ($SiOH^-$) groups at the SiO_2 — graphene interface which are responsible for much of the observed unintentional doping and hysteretic device behaviour [163, 118]. Growth of ALD dielectric films on graphene is commonly achieved through an additional *ex situ* process step to promote nucleation, typically including deposition of an additional seed layer such as a thin polymer [39, 61], metal/oxide films [158, 105], or other surface functionalisation pretreatments [189, 29, 106, 65]. Such *ex situ* treatments may include time-consuming additional process steps, can degrade the quality of the graphene [158] and crucially may compromise the quality of the interface by introducing additional surface states. Recently, *in situ* pretreatments, such as exposing graphene to pulses of H_2O [9, 200], O_3 [126, 89, 116, 117] or trimethylaluminum (TMA) [93], have shown promise in promoting uniform ALD of thin dielectric films. Most of these nucleation engineering studies have focused on process optimisation towards factors such as film coverage and density, however the impact and suitability of these in situ pretreatments for real device encapsulation has not yet been studied in detail. By using H_2O or O_3 exposure in situ to act as a gaseous pretreatment to promote nucleation of Al_2O_3 directly on graphene during early ALD growth, followed by dense film growth after nucleation, we show near complete surface passivation of graphene FETs with enhanced mobility, reproducibility and long term stability.

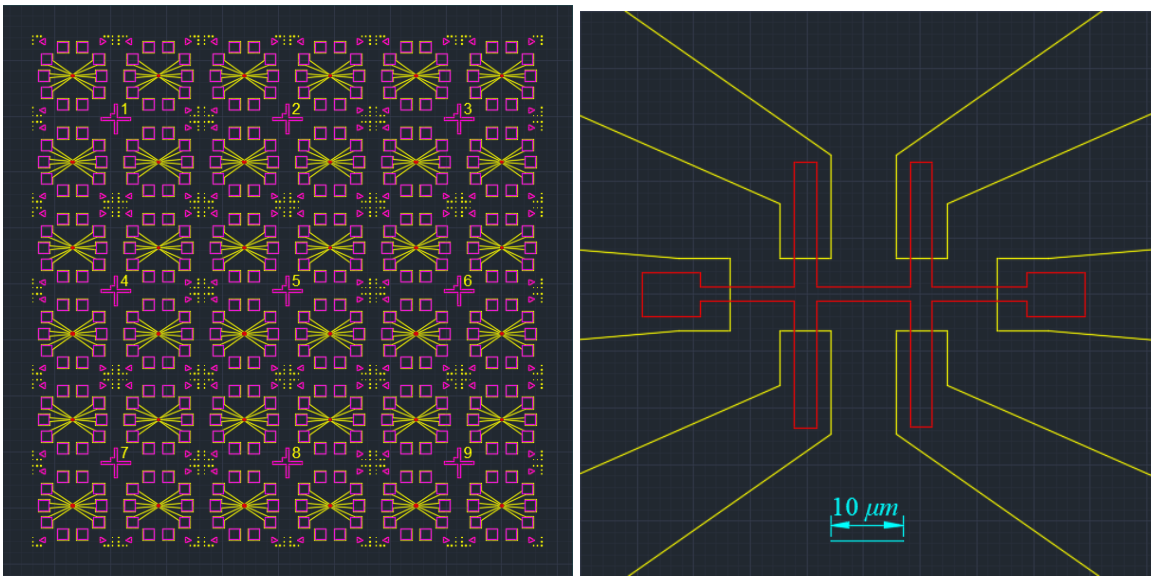

(a) (b)

Fig. 4.1 (a) AutoCAD design of the optical lithography mask with 36 (6 by 6) devices on one 10 mm by 10 mm chip. Red colour layer represents graphene mesa pattern, yellow layer represents metal contacts and purple layer stands for the probing/bonding pads. (b) Zoom-in of one of the 36 devices.

4.2.1 Graphene Growth and Device Fabrication

The graphene material used in this chapter is synthesized by the chemical vapor deposition (CVD) method [156], where the substrate is exposed to one or more volatile precursors, which react or decompose on the substrate surface to produce the desired deposit. Methane gas is used as the carbon source, copper is used as the substrate, and mixed hydrogen/argon is used as the gas environment in this thesis to grow graphene.

The details of CVD growing graphene is given as below: Cu foil was initially slowly heated to 1065 °C in a mixed H_2/Ar environment (50/200 sccm) at 100 °C min^{-1}. Once the growth temperature was reached, the Cu foil was kept in H_2/Ar (50/200 sccm) for 30 minutes. Graphene was subsequently grown in an H_2/Ar gas environment (26/250 sccm) using 9 sccm of CH_4 (0.1% diluted in Ar), for 45 min. Samples were cooled in 250 sccm Ar to room temperature. The total pressure at all process stages was 50 mbar. The graphene films were then transferred to Si/SiO_2 wafer (dielectric thickness $t_{ox} = 300$ nm) support using a wet transfer method with PMMA as sacrificial transfer layer and ammonium persulfate as Cu etchant. Then graphene was grown and ready for the next fabrication processing.

As the smallest feature of the designed graphene FET devices in this chapter is larger than 1 μm, in order to increase the efficiency of the fabrication procedure, all the FET devices

are made by optical lithography, using S1813 or AZ5214E as positive and negative resist, respectively. Therefore an optical mask (see figure 4.1(a)) had been designed with 36 (6 by 6) devices on one 10 mm by 10 mm chip, with each device 1.5 mm by 1.5 mm size and 0.5 mm width edge bean. The graphene is patterned into Hall bar as shown in figure 4.1(b). The graphene patterns are etched by oxygen plasma and contacts are deposited by thermal evaporation. All of these relevant fabrication techniques have been described in section 3.1. Then a 90 nm aluminium oxide layer is encapsulated onto the Hall bar devices by atomic layer deposition (ALD), which will be discussed in detail in the following section. After encapsulation a further lithography step is required to expose probing/bonding pads located away from the graphene channels which will be subsequently etched using phosphoric acid (64%) at 80 °C for $\sim$ 3 minutes.

4.2.2 Process of ALD encapsulation

Figure 4.2(a) schematically shows the process of our ALD device encapsulation. Initially a wafer containing an array of globally back-gated CVD graphene FET devices on doped Si/SiO_2 was prepared as described in the previous section. 90 nm Al_2O_3 was deposited by ALD (Cambridge Nanotech Savannah S100 G1) afterwards using TMA (purity $> 98\%$, Strem Chemicals 93-1360) and deionized water (H_2O) or ozone (O_3, DELOzone LG-7, $\sim 90\%$ power) that were delivered alternatingly into the reaction chamber by 20 sccm of N_2 flow. The dose for TMA and H_2O is $\sim$ 0.5 Torr·s, while the dose for O_3 is $\sim$ 5 Torr·s, which is approximated by the product of the peak delivery pressure with the residence time (full width at half maximum) determined by the pressure profile. The purging time between pulses was 20 s. Schematic of ALD pulse sequences for the pretreatment and subsequent growth processes showing the chamber pressure P as a function of time t is presented in figure 4.2(c).

For a number of device applications ambipolar transport in graphene devices is desirable. As such, the unipolar (p-type) behaviour observed in as-fabricated/unencapsulated devices needs to be converted to ambipolarity and, importantly, this must be stable during device operation and storage in ambient conditions. Hence, we tune the ALD encapsulation layers using three different growth conditions to determine the interface quality required for stable ambipolar device performance. The three growth conditions were as follows: (1) direct deposition of 90 nm Al_2O_3 at 120 °C using H_2O/TMA precursors; (2) a pretreatment of ten pulses of O_3 followed by 10 nm growth of Al_2O_3 interface layer using O_3/TMA at 80 °C followed by an additional layer of 80 nm using H_2O/TMA growth at 120 °C; (3) a pretreatment of ten pulses of H_2O at 120 °C followed by 90 nm of growth using H_2O/TMA precursors at 120 °C, as shown schematically in figure 4.2(c). For long term

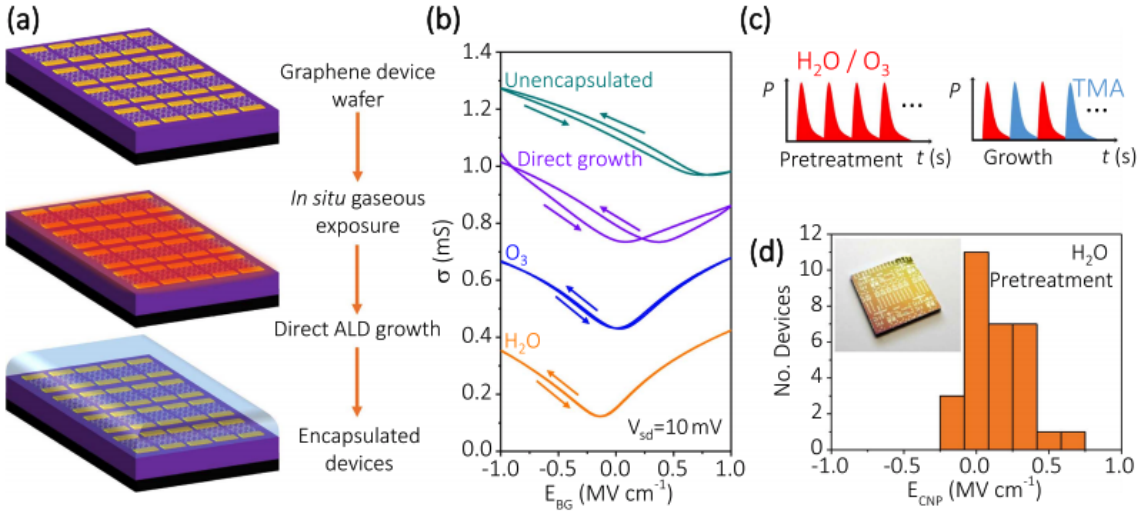

Fig. 4.2 (a) Schematic of process flow for ALD encapsulation of graphene devices. (b) Comparison of unencapsulated (green) graphene FET characteristics with those encapsulated with 90 nm of Al_2O_3 using direct growth (purple), O_3 (blue) and H_2O (orange) pretreatments, respectively. Blue, purple and green curves are offset vertically by 0.3, 0.6 and 0.9 mS, respectively. (c) Schematic of ALD pulse sequences for the pretreatment and subsequent growth processes showing the chamber pressure P as a function of time t. (d) Distribution of Dirac point (E_{CNP}) for 30 devices after encapsulating with an H_2O pretreatment. Inset: an optical micrograph of the 10 mm^2 encapsulated chip. Adapted from [4]

stability the barrier properties of the encapsulating ALD layer is crucial to obtain low gas transmission rates which would begin to affect the graphene over time [30]. Hence, devices were encapsulated with 90 nm of Al_2O_3 which has been demonstrated to be sufficient to enable long term stability [163].

4.2.3 Electric Field Effect Characterization

The field effect characteristics of a test device are shown in figure 4.2(b), which summarises the comparison of electronic performance of unencapsulated (green) graphene FET characteristics with those encapsulated with 90 *nm* of Al_2O_3 using direct growth (purple), O_3 (blue) and H_2O (orange) pretreatments, respectively. Three encapsulation techniques which are found to have a significant effect on the graphene - oxide (2D - 3D) interface. Electrical transport measurements are acquired on Keithley 4200-SCS connected to a probe station. The device conductivity σ is related to the current I_d by $\sigma = (L/W)(I_d/V_{sd})$ (L and W are the length and width of channel), with applied source-drain voltage V_{sd} = 10 mV, which is plotted as a function of gate electric field $E_{BG} = V_{BG}/t_{ox}$. The gate voltage is swept from negative to positive values (up sweep) and then back to negative values (down sweep) with a rate of

$dE_{BG}/dt = 0.37 MV cm^{-1} s^{-1}$ ($dV_{BG}/dt = 11 V s^{-1}$). In line with previous literature at room temperature and under ambient conditions significant unintentional p-type doping is observed in the as-fabricated/unencapsulted device where the conductivity minimum associated with the charge neutrality point E_{CNP} is observed at high positive gate voltages [195].

For the unencapsulated device shown in figure 4.2(b) we measure a peak field effect hole mobility μ_h, for the up sweep, to be 620 $cm^2 V^{-1} s^{-1}$, calculated using $\mu = (|d\sigma/dV_G|_{max})/C_G$, where the gate capacitance is taken to be C_G = 11.6 $nF cm^{-2}$ for 300 nm SiO_2. Such a value is typical for polycrystalline CVD films [92], and it is important to note that this two-terminal mobility value is reduced by including contact resistances [105]. For direct ALD encapsulation without pretreatment we observe some reduction in residual doping levels and an increase in mobility to μ_h = 830 $cm^2 V^{-1} s^{-1}$. However, significant hysteresis of ΔE_{CNP} = 0.3 $\pm$ 0.085 $MV cm^{-2}$ is still observed, where we define $\Delta E_{CNP} = E_{CNP}(down) - E_{CNP}(up)$. Using a simple capacitor model, with the gate capacitance per unit area C_G, we can estimate the corresponding change in carrier density due to trapped charges to be $\Delta n = C_G t_{ox} \Delta E_{CNP}/e = 6.5 \times 10^{11} cm^{-2}$. This suggests that a large density of trap states remain at the interface after the encapsulation. In contrast, the device characteristics for the two encapsulated samples using gaseous pretreatments are dramatically different with minimal hysteresis. Indeed, levels of hysteresis are significantly reduced to 0.033 $\pm$ 0.085 $MV cm^{-1}$ and 0.017 $\pm$ 0.085 $MV cm^{-1}$ for O_3 and H_2O pretreatments, respectively. For the H_2O pretreated encapsulation this corresponds to a remarkably low hysteresis induced by carrier trap density of $\Delta n \sim 3.6 \times 10^{10} cm^{-2}$. This value is comparable to the best performance devices reported in [163], but achieved while halving the number of encapsulation process steps. In addition, the values of μ_h for the test device shown in figure 4.2(b) increase to 920 $cm^2 V^{-1} s^{-1}$ and 950 $cm^2 V^{-1} s^{-1}$ for O_3 and H_2O pretreatments, respectively. This mobility improvement can be linked to the reduction in charge traps in the vicinity of the graphene as such charged interface states are known to act as scattering centres [109]. By characterization of the electric field effect on the test device, We can therefore conclude that the growth of 90 nm of Al_2O_3 directly on graphene using an H_2O pretreatment can provide thorough passivation of graphene FETs and almost doping-free ambipolar behaviour whilst maintaining, or indeed enhancing, carrier mobility under ambient conditions.

4.2.4 Scalable graphene FETs

Then we focus on our encapsulated scalable graphene FET devices, where a 90 nm Al_2O_3 encapsulation layer was deposied by ALD directly on an array of graphene FETs using an H_2O pretreatment, which has been proved by field effect characterization previously to

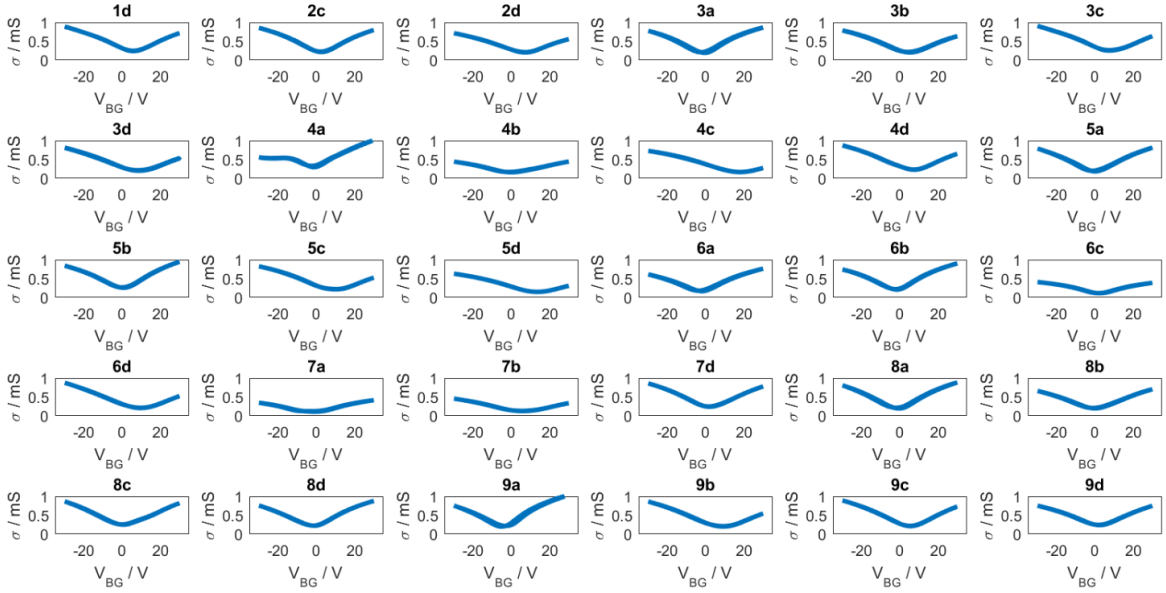

Fig. 4.3 Electric field effect of all the 30 working graphene Hall bar devices encapsulated using an H_2O pretreatment. The measurements are performed with a probe station at room temperature under ambient conditions.

be able to enhance graphene performance significantly. Electrical transport measurements were taken under ambient conditions following a further lithography step to expose and etch through the Al_2O_3 above the probing pads as detailed in the last section for the test device.

We fabricate 36 graphene FET devices on a a 10 mm^2 chip for each batch. Probe station measurement result suggests 30 among the total 36 devices are conducting for one of the batches we fabricated. And the electric field effect measurements of all the 30 working encapsulated graphene Hall bar devices are shown in figure 4.3. The measurements are performed with a probe station at room temperature under ambient conditions. We observe a highly reproducible average residual doping level of $3 \times 10^{11} cm^{-2}$ (p-type), with a standard deviation of $4 \times 10^{11} cm^{-2}$, as shown for the 30 devices in figure 4.2(d). Some devices show low levels of n-type doping due to negative charges in the Al_2O_3 matrix [109]. Statistic analysis is plotted in figure 4.4(d), showing the distribution of hole mobility μ_h and electron mobility μ_e, as well as Dirac point V_{Dirac} of the 30 devices. The average hole mobility μ_h of the 30 devices is 1910 $cm^2V^{-1}s^{-1}$, while the average electron mobility μ_e is a bit higher with value 2050 $cm^2V^{-1}s^{-1}$. Compared with the test device, whose mobility has been improved to $950 cm^2V^{-1}s^{-1}$ after ALD encapsulation using an H_2O pretreatment, the mobility exhibits a significant increase in our graphene Hall bar devices. The possible reason is that we optimize the fabrication process by doing a 3 s light etch using oxygen plasma just before depositing metal contacts, which can effectively remove resist residual and reduce the contact resistance.

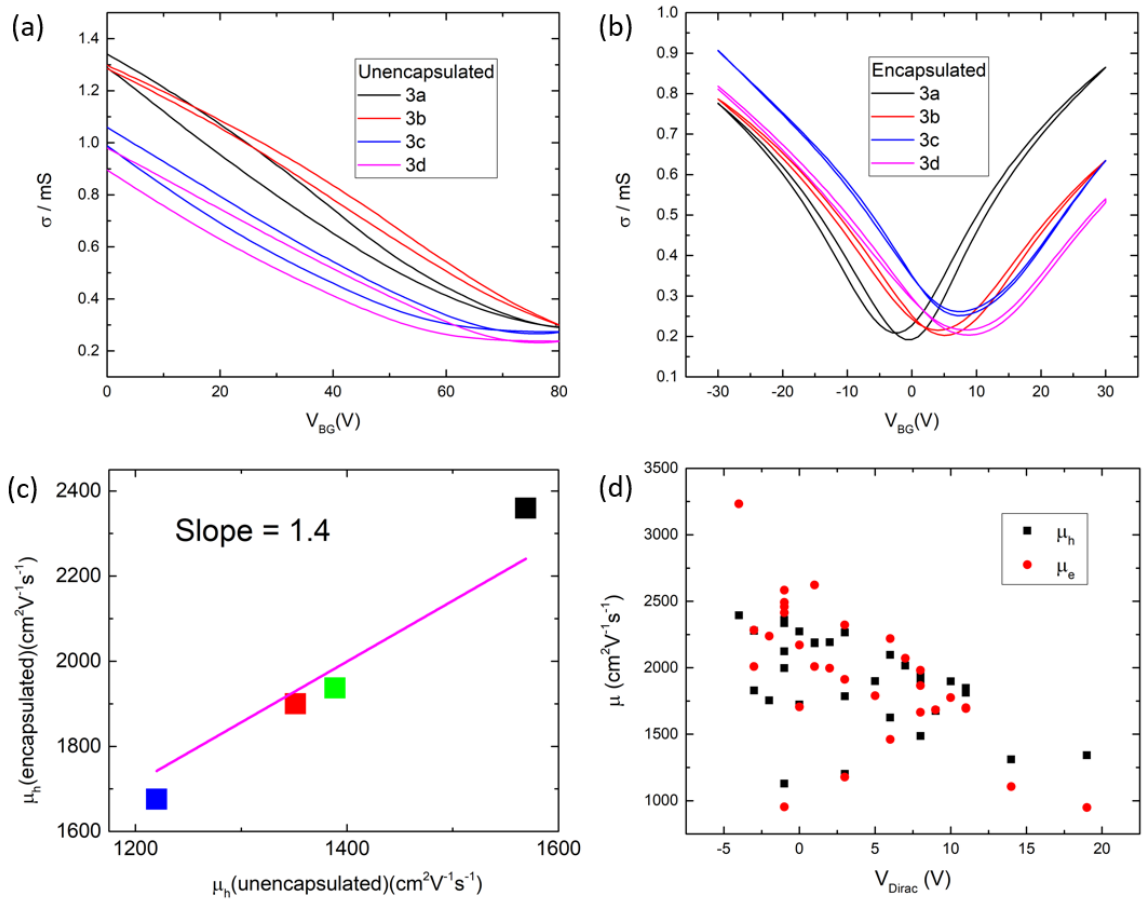

Fig. 4.4 Electric field effect comparisons of 4 devices among the 30 working graphene Hall bar devices before (a) and after (b) ALD encapsulation process. (c) Plot of the hole mobility μ_h of the 4 devices after the ALD encapsulation against that before encapsulation, showing an enhanced mobility with a ratio 1.4. (d) Distribution of hole mobility μ_h and electron mobility μ_e, as well as Dirac point V_{Dirac} of the 30 working encapsulated graphene Hall bar devices.

To get a better understanding of how ALD encapsulation process enhance our graphene performance, we compare 4 among the 30 devices before and after the encapsulation processing. The electric field effect comparisons of the four devices before and after the ALD encapsulation process are shown in figure 4.4(a) and figure 4.4(b), respectively. We can clearly observe a doping drop from a highly p-type doping with $V_{Dirac} > 80V$ to $V_{Dirac} \sim 0V$. In terms of the mobility, figure 4.4(c) exhibits the plot of the hole mobility μ_h of the 4 devices after the ALD encapsulation against that before encapsulation, showing an enhanced mobility with a ratio 1.4. This mobility improvement is also related to the reduction in charge traps in the vicinity of the graphene.

In order to obtain insights into the potential of our scalable graphene FET devices for further nanostructure experiments, we cooled one Hall bar device down to 1.4 K with a cryostat called the Assessment Lab in the SP group to carry out magnetotransport measurements. We observed the quantum Hall effect (QHE) in this device. The Hall resistivity measurements of this Hall bar device as a function of back-gate V_{BG} is shown in 4.5 with a magnetic field of 0 T (purple), 3 T (green), 5 T (blue), 8 T (black), respectively, exhibiting QHE with a Hall resistivity plateau at $\sim 0.5h/e^2$. This result is in agreement with the theoretical equation $\sigma_{xy} = 4(n+1/2)e^2/h$, showing the half-integer QHE in graphene [94].

In conclusion, we have demonstrated a scalable and simple approach towards encapsulating and passivating high quality CVD graphene electronic devices by using a gaseous H_2O pretreatment to allow direct ALD of dense Al_2O_3 films on graphene. Using this technique, contained within a single piece of equipment, we eliminate the additonal time consuming processing steps and tools required to deposit the metal or metal oxide seed layers most commonly used to promote ALD growth. We obtained thorough passivation of graphene FETs and almost doping-free ambipolar behaviour whilst maintaining, or indeed enhancing, carrier mobility under ambient conditions. The quantum Hall measurement suggests that the Hall bar device processed by this technique is promising for further electronic applications. This approach is also used in the devices which will be discussed in the next section of this chapter and later chapters. We hope that this work will motivate further device performance enhancements for new generations of low dimensional materials by using *in situ* gaseous pretreatments within the large parameter space offered by ALD.

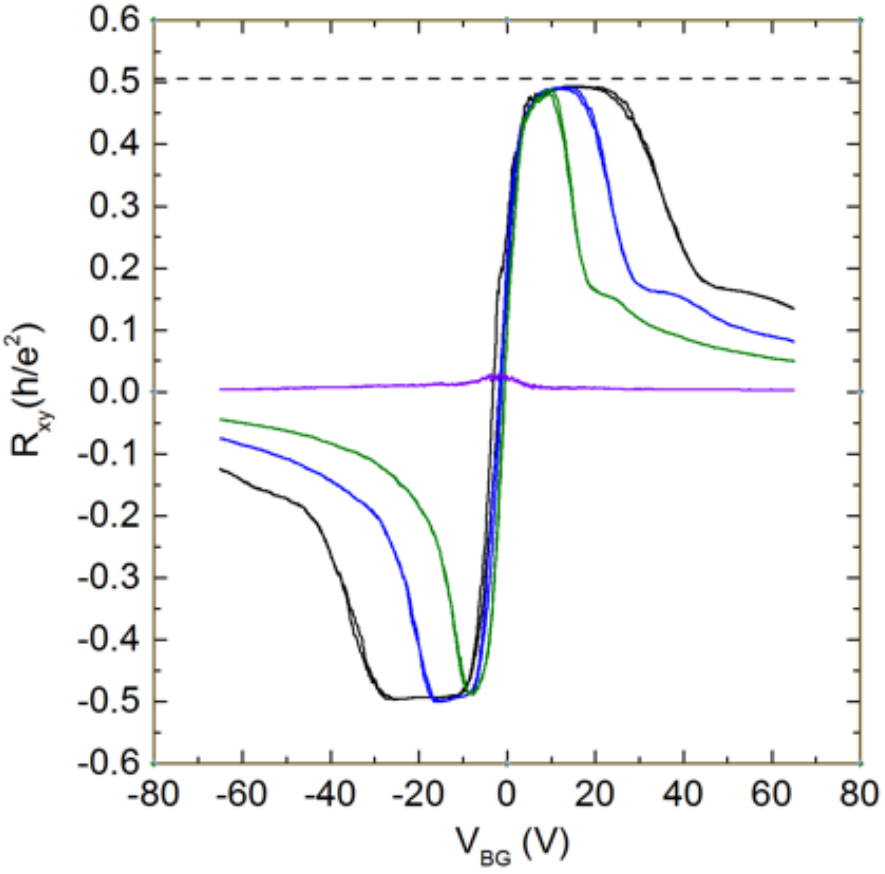

Fig. 4.5 Hall resistivity measurements of one of the 30 working encapsulted graphene Hall bar devices as a function of back-gate V_{BG} with temperature down to 1.4 K and magnetic fields of 0 T (purple), 3 T (green), 5 T (blue), 8 T (black), respectively, exhibiting the quantum Hall effect with a Hall plateau at $\sim 0.5h/e^2$.

4.3 Twist angle dependent electron scattering in as-grown CVD bilayer graphene

Bilayer graphene has attracted significant interest due to the ability to tune the electronic properties by changing the relative orientation or twist angle between the two layers. Bernal or AB stacked bilayer graphene offers an electric field tunable band gap [199] and valley transport [97, 167]. Small twist angle bilayer graphene ($\theta_{tw} \sim 1^\circ$) has been shown to exhibit exotic electronic phenomena such as superconductivity [28, 27] and topological transport channels [157]. At larger twist angles ($\theta_{tw} \sim 5^\circ$ - 30°) the low energy Dirac points of each are well separated in k-space, and higher energy interlayer interactions dominate[196, 3, 197, 148, 83, 157]. Chemical vapour deposition (CVD) [84] has been shown to provide a scalable route towards high electronic quality graphene [47], and significant effort has been made to tailor the growth parameters to selectively obtain bilayer graphene [60]. The angle between two monolayers of artificially stacked graphene can be accurately controlled over small areas [37, 28], but any contamination between layers during processing can reduce the interlayer coupling, destroying any angular dependent phenomena [83]. By comparison, atomically clean interlayer interfaces can be found in as-grown CVD bilayer graphene [123]. Under appropriate growth conditions CVD bilayer graphene can preferentially align in one of two energetically stable stacking orientations [123], either AB stacked or 30° rotated (turbostratic), with only a small proportion of misaligned bilayers. These two stacking orientations therefore represent two technologically relevant material systems with distinctly different electronic properties. By studying magnetotransport phenomena in CVD grown AB and 30° bilayer graphene, as well as monolayer graphene for reference, we show that the electron scattering processes and hot electron effects can be tuned.

4.3.1 Device Preparation and Characterization

The graphene was grown in an Aixtron BM Pro 4" reactor using 25 μm thick Cu foil (Alfar Aesar, 99.8%), methane, hydrogen and argon at a temperature of approximately 1070 °C. Graphene grown on copper typically includes a small number of multilayers that form during growth. We found that the introduction of oxygen into the system [23] and growing at a higher methane to hydrogen ratio allowed for larger (> 50 μm diameter), more frequent multilayers in the graphene film. Figure 4.6(a) shows an example with a particularly high density of as-grown bilayer graphene regions after transfer onto a Si/SiO_2 substrate. The imaged area is fully covered with graphene and areas of higher contrast represent bilayer and multilayer regions as shown schematically in figure 4.6(b). The results of a scanning Raman

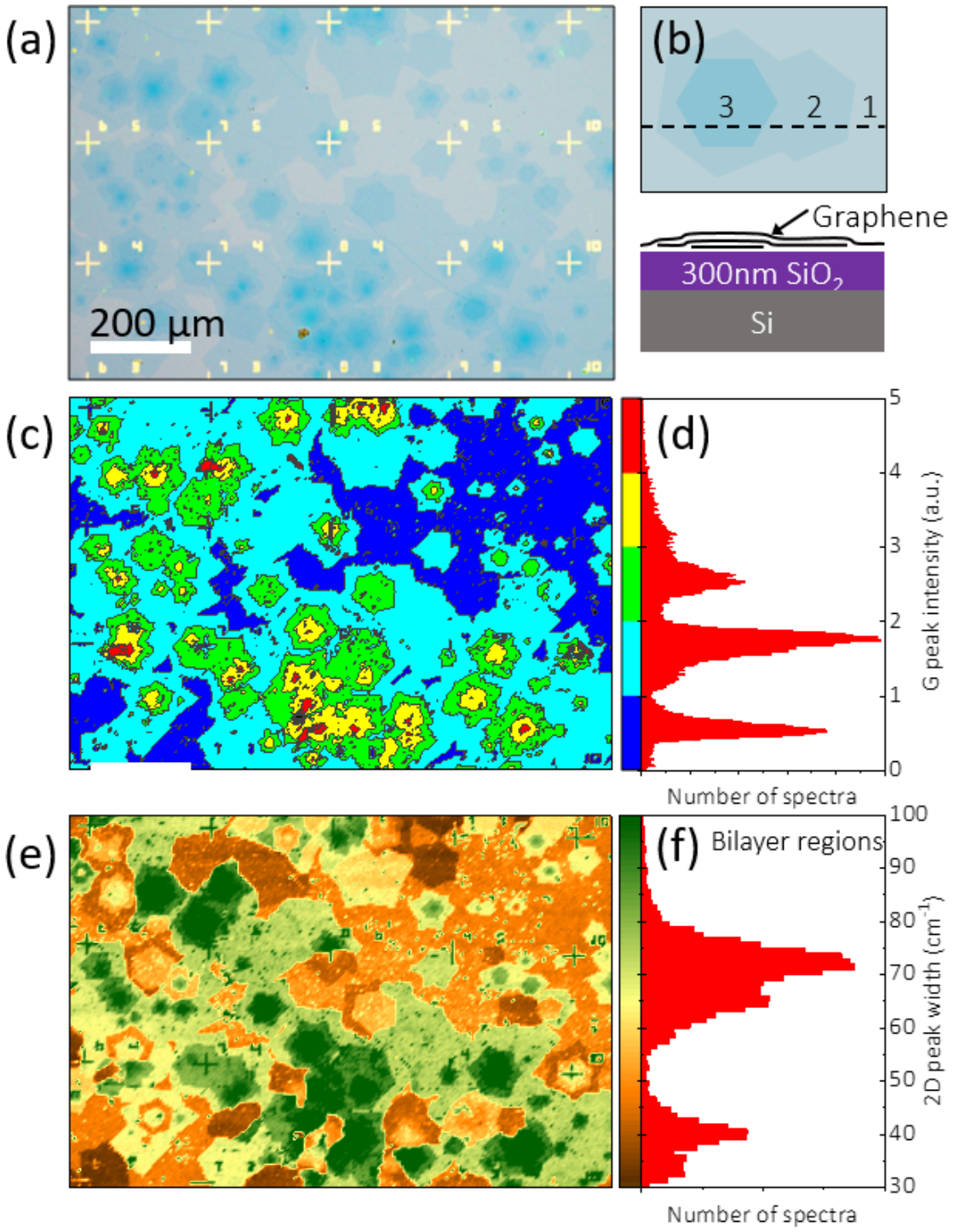

Fig. 4.6 (a) Optical micrograph of CVD graphene transferred onto a Si substrate with 300 nm SiO_2. The scale bars are 200 μm. The area is completely covered in graphene, darker regions represent bilayers and trilayers as shown schematically in (b). Scanning Raman map of the same region showing (c) the intensity of the G peak and (e) FWHM of the 2D peak. (d) A histogram of the intensity of the G peak of the mapped region showing peaks corresponding to layer thickness. (f) A histogram of the FWHM of the 2D peak for spectra selected only from bilayer regions of the map, as determined by the G peak intensity.

map of the region are shown in figure 4.6(c) - (f). The intensity of the graphene G peak (where $P_{os}(G) \sim 1587cm^{-1}$) is found to be a useful measure of layer number and is strongly correlated with the areas of increased optical contrast found in figure 4.6(b). A histogram of G peak intensity across the mapped region shows three clear peaks which we attribute to monolayer, bilayer and trilayer graphene, respectively (see figure 4.6(d)). We note that when the θ_{tw} dependent energy separation between the Van Hove singularities in bilayer graphene is resonant with the laser excitation energy, typically for $\theta_{tw} \sim 5^\circ$ - 15°, the intensity of the G peak is enhanced [104]. However, the majority of our as-grown bilayer graphene is non resonant as observed previously [123] and described further below. Indeed, we find that areas which do display optical resonances are often associated with strain or wrinkles indicating that the misalignment between layers occurred after growth. Figure 4.6(e) shows the full width at half maximum (FWHM) of the 2D peak ($P_{os}(2D) \sim 2680cm^{-1}$). Depending on the stacking angle, the 2D peak in bilayer and multilayer graphene can be composed of four or more components [23], but here for simplicity we perform a global fit with a single Lorentzian peak. After fitting, we use the intensity of the G peak to extract just the regions which we associate with bilayer graphene. A histogram of FWHM (2D) shows two distinct peaks around 35 cm^{-1} and 70 cm^{-1} which we attribute to large angle ($\theta_{tw} \sim 30^\circ$) rotated and AB stacked bilayer graphene respectively [104]. From this we estimate that the as-grown bilayer graphene is composed of approximately 1/3 large angle rotated bilayer and 2/3 AB stacked bilayer. A similar distribution of stacking was shown previously for as-grown CVD bilayer graphene [123] where the large angle rotated bilayer was confirmed by transmission electron microscopy to be predominantly $\theta_{tw} = 30^\circ$.

After transfer onto Si coated with 90 nm of thermally grown SiO_2 individual isolated bilayer regions were selected and identified based on optical microscopy. Electron beam lithography followed by oxygen reactive ion etching was used to define 4 μm wide Hall bars. Contacts were made by thermally evaporated Ti/Au (10/100 nm). Monolayer graphene devices were also fabricated, and all the devices studied are from the same growth. After fabrication, 90 nm of Al_2O_3 was deposited on the devices by atomic layer deposition which provides long term stability, passivation of charge traps and a reduction in hole doping [4], which has been discussed in the first half of this chapter. Figure 4.7(a) shows the Raman spectra of three graphene devices using 532 nm laser excitation wavelength. Based on the discussion above we conclude that the three devices represent monolayer graphene, AB stacked and 30° rotated bilayer graphene respectively. The same devices are studied throughout the rest of the chapter. Spatial mapping confirms the uniformity of the layer number and stacking throughout each of the devices (see figure 4.7(a) - (e)). Figure 4.7(e) shows room temperature field effect transistor measurements were under a fixed source drain

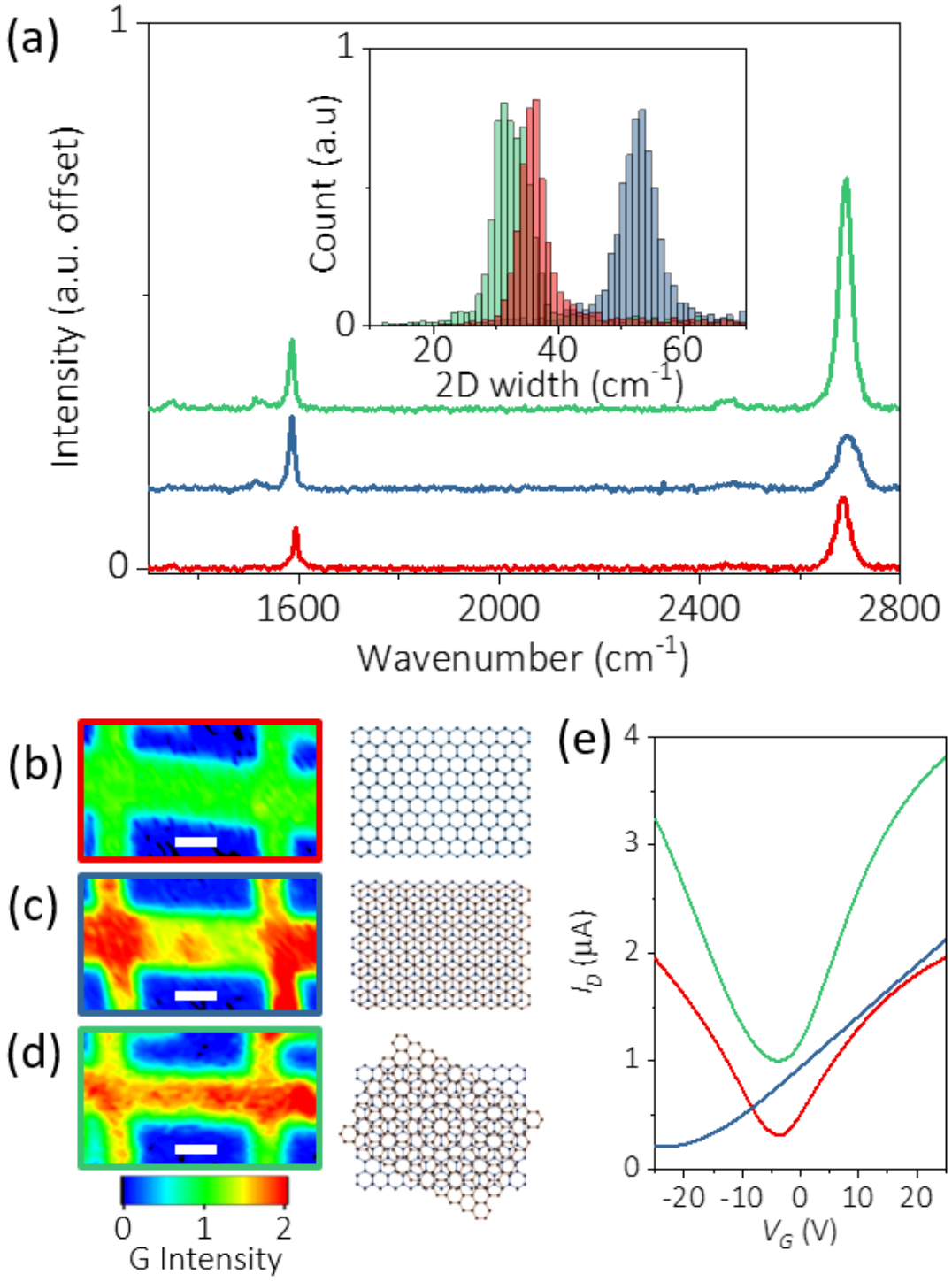

Fig. 4.7 (a) Raman spectra, (b)-(d) G peak intensity maps and (e) room temperature transfer characteristics (V_{SD} = 10 mV) of the monolayer (red, b), AB stacked bilayer (blue, c) and turbostratic bilayer (green, d) devices. (a) Inset: Histograms of the FWHM of the 2D peak for the three Raman maps. Scale bars are 4 μm.

voltage of 10 mV. The monolayer graphene device shows the characteristic symmetric transfer curve with a Dirac point of -4 V and a field effect mobility of μ_{MLG} = 2926 $cm^2V^{-1}s^{-1}$, measured on the n-type side of the curve. The transfer characteristics of the 30° rotated bilayer graphene are very similar to monolayer with a Dirac point at $-4V$ but with a noticeably higher conductivity and a field effect mobility of μ_{30} = 4995 $cm^2V^{-1}s^{-1}$. This is consistent with the presence of two layers of graphene maintaining their linear band structure at low energies. For the AB stacked bilayer graphene we observe a lower mobility of μ_{AB} = 1526 $cm^2V^{-1}s^{-1}$, consistent with the expected quadratic band structure [199].

4.3.2 Magnetotransport Measurement

The magnetotransport measurements are carried out with a four-terminal low frequency circuit setup in the cryostat called the Assessment Lab in the SP group, which can supply a perpendicular magnetic field up to 8 T and a controllable temperature from a base temperature of 1.4 K up to room temperature if needed. 1 V excitation is supplied by a lock-in amplifier at a frequency of 77 Hz. This AC voltage is mixed with a DC bias supplied by a SMU before going through a 10 MΩ resistor to form a constant AC current I = 100 nA through the device. Another two lock-ins are used to record longitudinal voltage V_{xx} and Hall voltage V_{xy} respectively.

Figure 4.8(a) shows the measured longitudinal resistivity ρ_{xx} as a function of magnetic field (between -6 T and 6 T) of the monolayer (red), AB stacked bilayer (blue) and turbostratic bilayer (green) devices, exhibiting Shubnikov-de Haas (SdH) oscillations. All the three devices show a WL peak at low magnetic field, but AB stacked BLG shows very small magnetoresistance at higher magnetic fields, while both MLG and turbostratic BLG exhibit pronounced SdH oscillations with resistance plateaus. This can be understood by the higher mobility in monolayer and turbostratic bilayer graphene than that in AB stacked bilayer. Then we move on to the low field (between -0.3 T and 0.3 T) measurements to explore the WL effect in these devices. Figure 4.8(b) - (d) show the WL measurement results of these three devices as a function of temperature from base temperature of 1.4 K to around 80 K, where the WL effect seems not observable. Our experiments are performed at much higher temperatures than the previous studies of WL in exfoliated graphene [179] where T < 20 K. Moreover, the quantum correction in conventional 2D systems usually disappears at much lower temperatures, due to intensive electron-phonon scattering [70]. The weak electron-phonon scattering in graphene [87] makes it possible to analyse WL in a large temperature range. We can see that MLG, AB BLG show similar WL results, while WL in large twist angle (30°) BLG is quite different. In order to examine the difference, we plot the conductance correction $\Delta\sigma(B) = \sigma(B) - \sigma(B = 0)$ of these three devices at T =

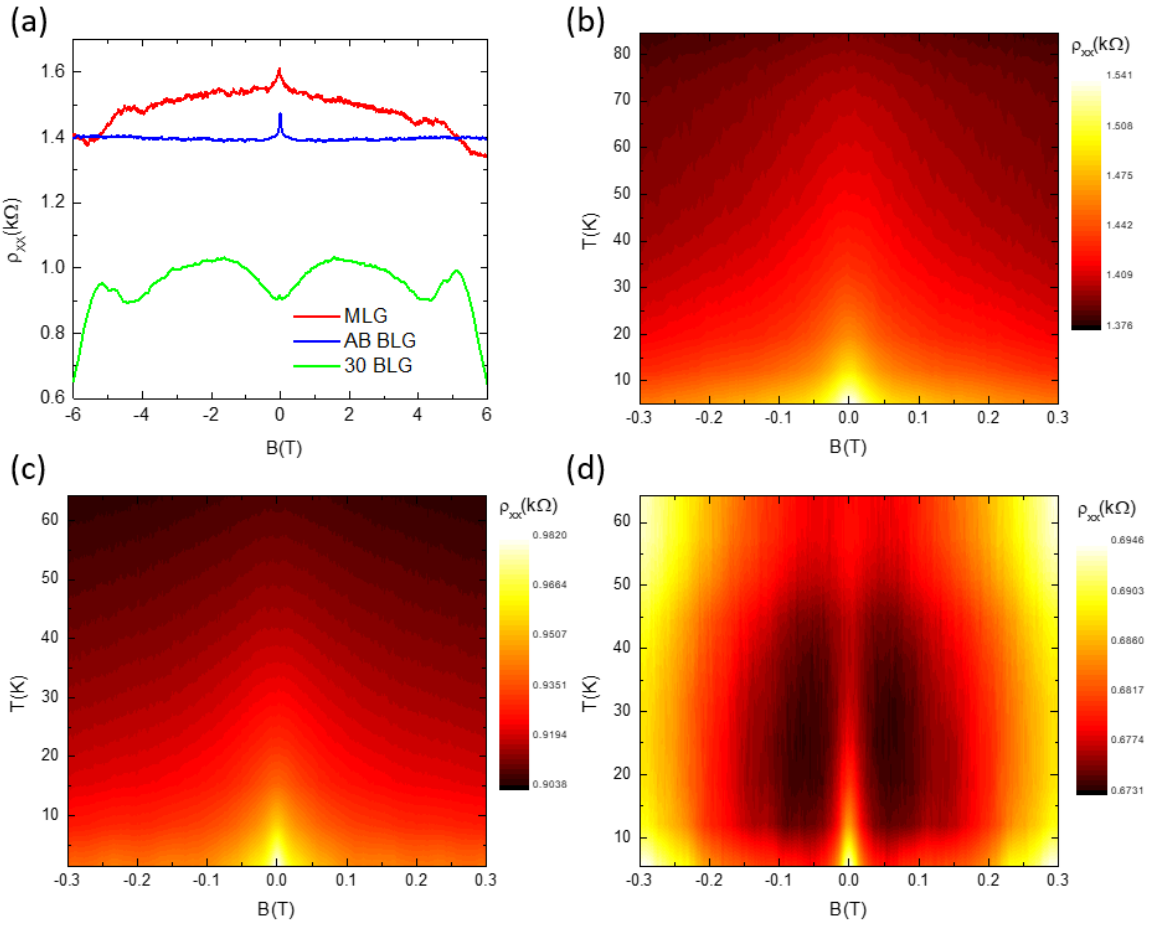

Fig. 4.8 (a) Longitudinal resistivity ρ_{xx} as a function of magnetic field (between -6 T and 6 T) of the monolayer (red), AB stacked bilayer (blue) and turbostratic bilayer (green) devices, exhibiting Shubnikov-de Haas (SdH) oscillations (T = 1.4 K). Low magnetic field (between -0.3 T and 0.3 T) transport measurement results of (b) monolayer, (c) AB stacked bilayer and (d) turbostratic bilayer graphene devices, showing WL effect against temperature.

1.4 K in figure 4.9(a). Both MLG and AB BLG show positive magnetoconductance, while negative magnetoconductance occurs at higher B field in turbostratic BLG. The quantum correction depends not only on the dephasing time τ_φ, but on elastic scattering times τ_i and τ_*, indicating intervalley scattering time and intravalley scattering time. The shape of the magnetoconductance curves is controlled by the interplay between all scattering times involved. According to the figure 2.5 described in chapter 2, this difference in the shape of WL curves suggests enhanced intervalley scattering in twisted BLG with $\tau_* \ll \tau_i$. The quantum correction in conductance $\Delta\sigma(B)$ can be fitted with the following equation [179] by using the theory in [127]:

$$\Delta\sigma(B) = \frac{e^2}{\pi h}[F(\frac{\tau_B^{-1}}{\tau_\varphi^{-1}}) - F(\frac{\tau_B^{-1}}{\tau_\varphi^{-1}+2\tau_i^{-1}}) - 2F(\frac{\tau_B^{-1}}{\tau_\varphi^{-1}+\tau_i^{-1}+\tau_*^{-1}})]. \tag{4.1}$$

Here, $F(z) = ln(z) + \psi(0.5+z^{-1})$, $\psi(x)$ is the digamma function, $\tau_B^{-1} = 4eDB/\hbar$ and D is the diffusion coefficient. The first term in this equation is responsible for WL, while the WAL is determined by the second and third terms with negative sign. All the three devices show WL with turbostratic BLG exhibiting the sharpest conductance correction dip and the dip in AB stacked BLG is a bit sharper than MLG at base temperature, as shown in figure 4.9(a). The sharpness of the dip is determined by the phase coherence length L_φ. The temperature dependence of L_φ contains information about the inelastic mechanism responsible for the dephasing of charge carriers [178]. By fitting the WL with equation (4.1) combined with the equation $L_\varphi = \sqrt{D\tau_\varphi}$, we can subtract L_φ as a function of temperature of the three devices (see figure 4.9(b)). We can see that turbostratic BLG has the longest L_φ over the measured temperature range (from 1.4 K to $\sim$ 70 K) with $L_\varphi \approx 220$ nm at base temperature and decays to 100 nm at 65 K, while L_φ in AB stacked BLG is longer than that in MLG at base temperature but decays faster with temperature. At T $\approx$ 15 K, L_φ in AB BLG starts to be shorter than that in MLG.

We then move on to the temperature dependent measurements at a series of fixed carrier concentrations. We performed the WL measurements of the three devices at 5 or 6 different back-gate voltages leading to different carrier concentrations, and extracted the corresponding phase coherence length L_φ from the conductance correction results using equation (4.1), as shown in figure 4.10 with (a) - (c) corresponding to MLG, AB stacked BLG and turbostratic BLG respectively. The data have been converted into log_{10} format for further discussion. One obvious conclusion we can draw is that both MLG and turbostratic BLG have strong carrier density dependence while AB stacked BLG not so much. In order to quantitatively analyze how L_φ decays against temperture, we processed the data by linear fitting $log_{10}L_\varphi$ versus $log_{10}T$ at V_g = 0 V of these three devices. The fitting information is shown in

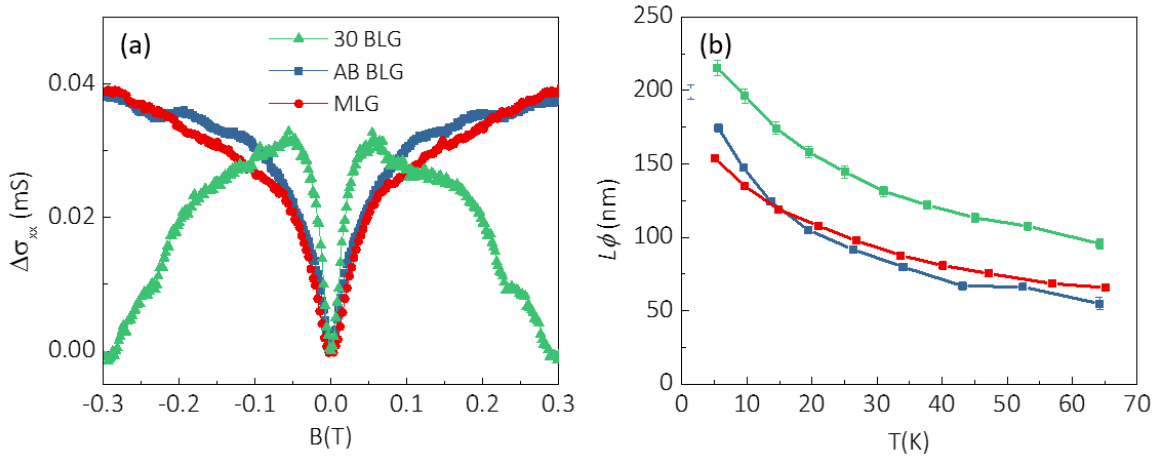

Fig. 4.9 (a) Quantum correction in longitudinal conductivity σ_{xx} as a function of low magnetic field (between -0.3 T and 0.3 T) of the monolayer (red), AB stacked bilayer (blue) and turbostratic bilayer (green) devices, showing different WL curves (T = 1.4 K). (b) Phase coherence length L_φ of the three devices as a function of temperature.

the inset of figure 4.10. For both MLG and turbostratic BLG, the fitting slope is around -1/3, and there is not much difference at different carrier concentrations. Thus we can obtain $log_{10}(L_\varphi) \propto -1/3 log_{10}(T)$, then $L_\varphi \propto T^{-1/3}$. And for AB stacked BLG, we can get $L_\varphi \propto T^{-1/2}$. The exponent n in the relation $L_\varphi \propto T^n$ determines the electron scattering types and can be a useful tool to examine the dephasing source at high temperature. Noted that $L_\varphi = \sqrt{D\tau_\varphi}$, then we can find the dephasing rate $\tau_\varphi^{-1} \propto L_\varphi^{-2}$. Therefore, we can conclude that, for MLG and turbostratic BLG, the electron dephasing rate $\tau_\varphi^{-1} \propto T^{2/3}$, while for AB stacked BLG, $\tau_\varphi^{-1} \propto T$. Our results show that the electron dephasing rate for AB stacked BLG obeys the linear temperature dependence caused by electron-electron scattering in the diffusive regime [7]:

$$\tau_\varphi^{-1} = \alpha \frac{k_B T}{2E_F \tau_p} ln(\frac{2E_F \tau_p}{\hbar}) \tag{4.2}$$

where α is a coefficient of the order of unity, τ_p is the momentum relaxation rate and is the highest in the system and comes from charged impurities, and does not affect the electron interference according to the assumption of the theory used in equation (4.1) [179]. This diffusive regime happens when the condition $k_B T \tau_p / \hbar < 1$ is satisfied, which means that during the interaction time $\hbar / k_B T$ two interacting electrons experience many collisions with impurities. And for MLG and turbostratic BLG, electron dephasing rate τ_φ^{-1} is proportional to $T^{2/3}$. In these two cases the exponent $2/3$ is smaller than 1, which cannot be explained by the electron-electron scattering in the diffusive regime. Unfortunately, we did not find

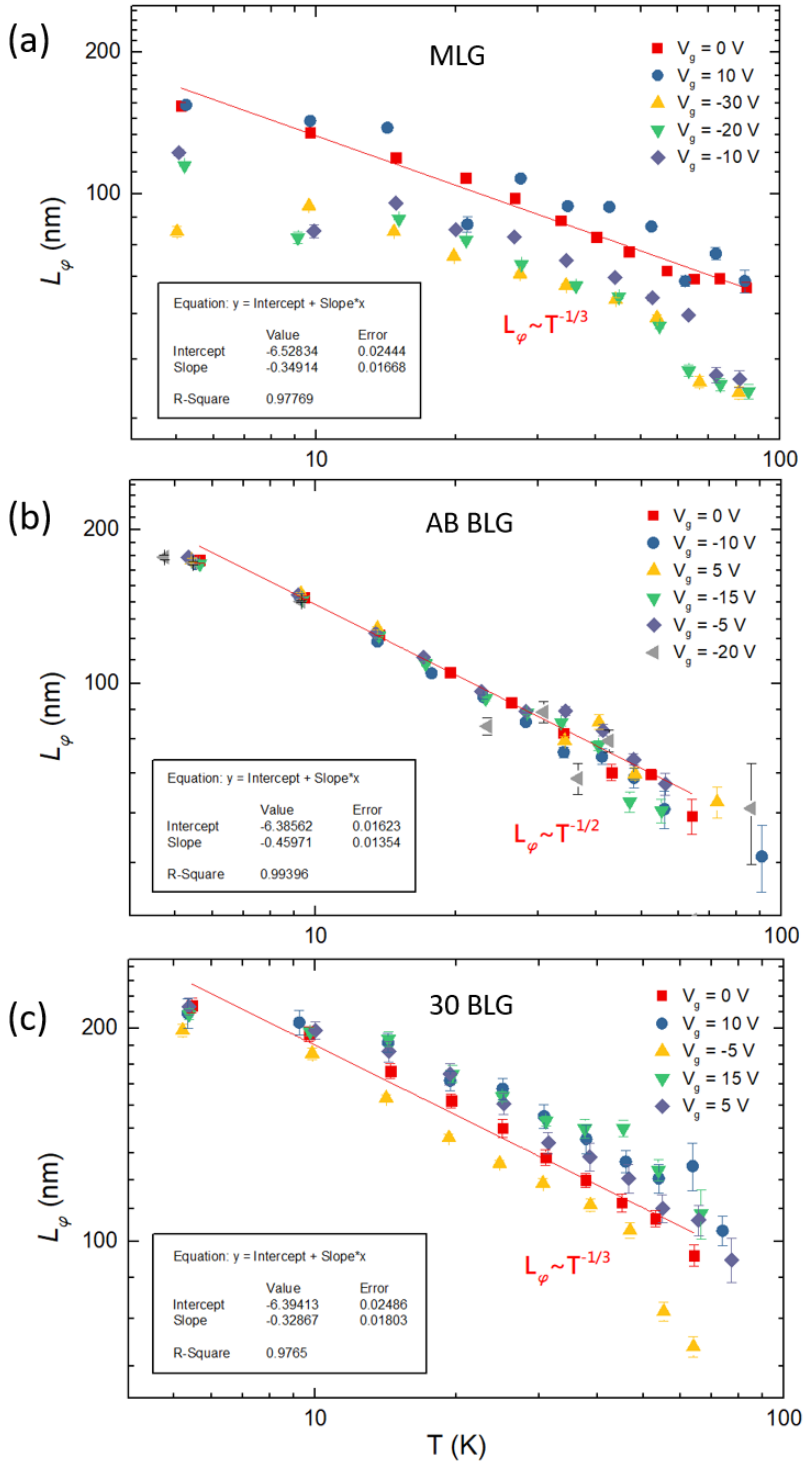

Fig. 4.10 Subtracted phase coherence length L_φ from WL measurements of (a) MLG, (b) AB stacked BLG and (c) turbostratic BLG devices as a function of temperature at different carrier concentrations. The presented data is processed by log_{10}. Inset: Information about the linear fitting of the data at $V_g = 0$ V.

a theory in 2D systems which the electron scattering in MLG and turbostratic BLG is in agreement with, but according to Nyquist scattering, the dephasing rate τ_φ^{-1} in 1D systems is predicted to follow a law on temperature $\tau_\varphi^{-1} \propto T^{2/3}$ [131, 8, 2]. Nyquist scattering describes the scattering of an electron by the field fluctuations of the other surrounding electrons. The statistical nature of these fluctuations makes this scattering different for each electron, thus the electronic ensemble loses its coherence. We argue that due to the electron-hole puddle formation in MLG and turbostratic BLG close to the Dirac point, quasi 1D channels might form in the Hall bar devices. Therefore, Nyquist scattering can account for the scattering mechanism but only close to the Dirac point.

4.3.3 Energy Loss Rates

When a electric current is applied passing through the device at a fixed ambient temperature, the carriers are unable to lose energy at a sufficient rate to reach thermal equilibrium with the lattice and thus the electron temperature goes up [69, 119, 115, 11]. The energy loss rates were determined by comparison of the current and temperature dependence of the WL peak. Both temperature and current through the devices can suppress the WL peak. Here, we take AB stacked BLG device as an example to see how the current through the device works on the WL effect. Figure 4.11(a) shows the comparison between the temperature (full blue circles) and current (open red circles) dependences of the WL peak height ΔR_{xx}. The peak height ΔR_{xx} are calculated as the difference of the longitudinal resistance R_{xx} between 0 T and fixed small magnetic field of 0.3 T, sufficient to entirely suppress the WL behavior. All the current dependence data were taken at a very low lattice temperature of 1.4 K, while all the temperature dependence data were obtained from measurements using a low fixed current of 100 nA. ΔR_{xx} is significantly reduced by increasing current or lattice temperature, and the comparison of the suppressed values between these two dependences generates a measurement method of the carrier temperature T_e as a function of applied current I. Figure 4.11(b) shows the the relationship between the carrier temperature T_e and the corresponding current I by measuring the suppression of the weak localization peak heights ΔR_{xx}. We can see that $log_{10}T_e$ is in linear relationship with $log_{10}I$ with the following fitting equation: $log_{10}T_e = 0.5789 log_{10}I + 4.11935$, and the fitting details are show in the inset of figure 4.11(b). This result suggests that an increase of the lattice temperature and the electron temperature will have an equal effect on the weak localization. This study can be used to explore the hot carrier energy loss rate in CVD graphene [11].

When the system is in a steady state, energy balance requires that the energy loss rate should equal the power input to the system. The energy loss rate per carrier for a given

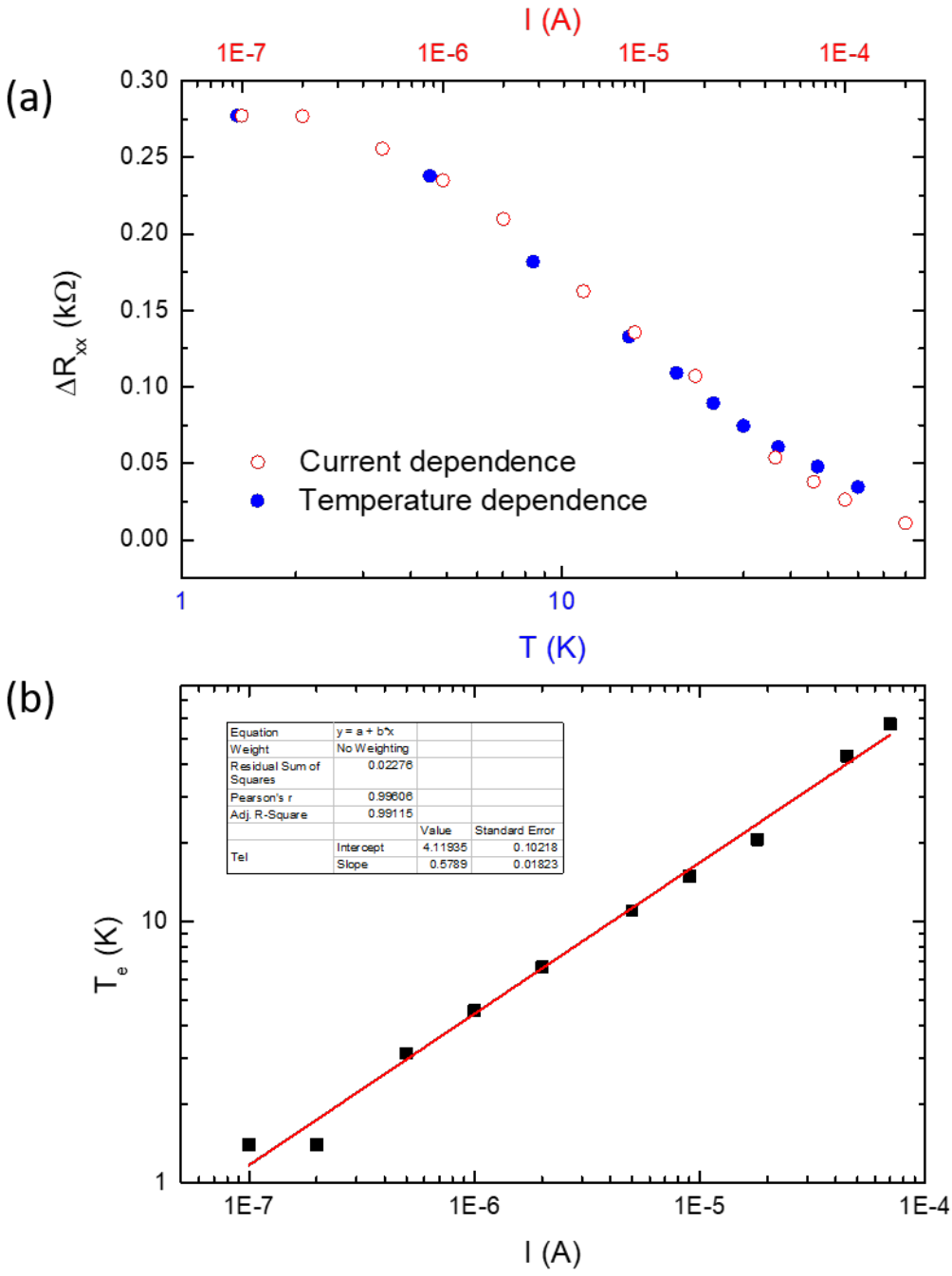

Fig. 4.11 (a) Comparison between the temperature (full blue circles) and current (open red circles) dependences of the weak localization peak height ΔR_{xx}. (b) The relationship between electron temperature T_e and current I obtained using this WL method. Inset: Linear fitting information about the $T_e - I$ relationship.

electron temperature can be therefore evaluated using the following equation from the $T_e - I$ relationships:

$$P(T_e) = \frac{I^2 R_{xx}}{nA}, \tag{4.3}$$

where I is the applied current, R_{xx} is the longitudinal resistance, n is the carrier density, and A is the area within the device over which R_{xx} is measured. The carrier density n for the AB stacked BLG device is $6.59 \times 10^{12} cm^{-2}$ given by the equation $n = \varepsilon_0 \varepsilon_r V_(Dirac)/te$ introduced in chapter 2 and device area as $A = 6.4 \times 10^{-11} m^2$. The temperature dependence of the energy loss rates $P(T_e)$ by measuring the WL peak height over a carrier temperature range of 1.4 K to 70 K is shown in figure 4.12. We first fitted the temperature-dependent energy loss rates $P(T_e)$ to the Bloch-Grüneisen power-law [182, 112] (see the red dash curve in figure 4.12):

$$P(T_e) = \alpha(n)(T_e^4 - T_l^4), \tag{4.4}$$

where $\alpha(n)$ is a carrier density dependent scaling factor and the lattice temperature T_l is 1.4 K. The scaling factor α in our fitting equals $8 \times 10^{-18} WK^{-4}/carrier$. Previous studies on monolayer graphene produced by epitaxial growth on SiC, exfoliation, and CVD [11], as well as bilayer epitaxial graphene [85] suggest that the energy loss rates of hot carrier in graphene follow the predicted Bloch-Grüneisen power-law behaviour of T_e^4 at carrier temperatures from 1.4 K up to 100 K, due to electron-acoustic phonon interactions. Our result shows that the energy loss rates in AB stacked CVD graphene are closer to a T_e^3 power-law (see the blue solid curve in figure 4.12), especially for high temperatures, where we can see a decrease in the energy loss rate. This finding is in agreement with that reported for exfoliated graphene [12] at high carrier temperatures. It is likely that at higher temperatures, some additional contribution may happen due to optical phonons in both graphene and the silicon substrate [182, 36]. Moveover, theoretical work from [173] proposed that disorder-assisted scattering (supercollisions) dominates electron-lattice cooling and plays a disproportionately large role in the energy loss processes for higher-energy carriers. This theory predicts that for strongly disordered samples, energy loss rates should exhibit a T_e^3 dependence at high temperatures. Our CVD BLG contains significant amounts of disorder and hence the disorder-assisted scattering process could potentially account for the energy loss rates of our device relative to the theoretical predictions [112]. This can be suggested from the comparison of T_e^3 and T_e^4 fittings in figure 4.12.

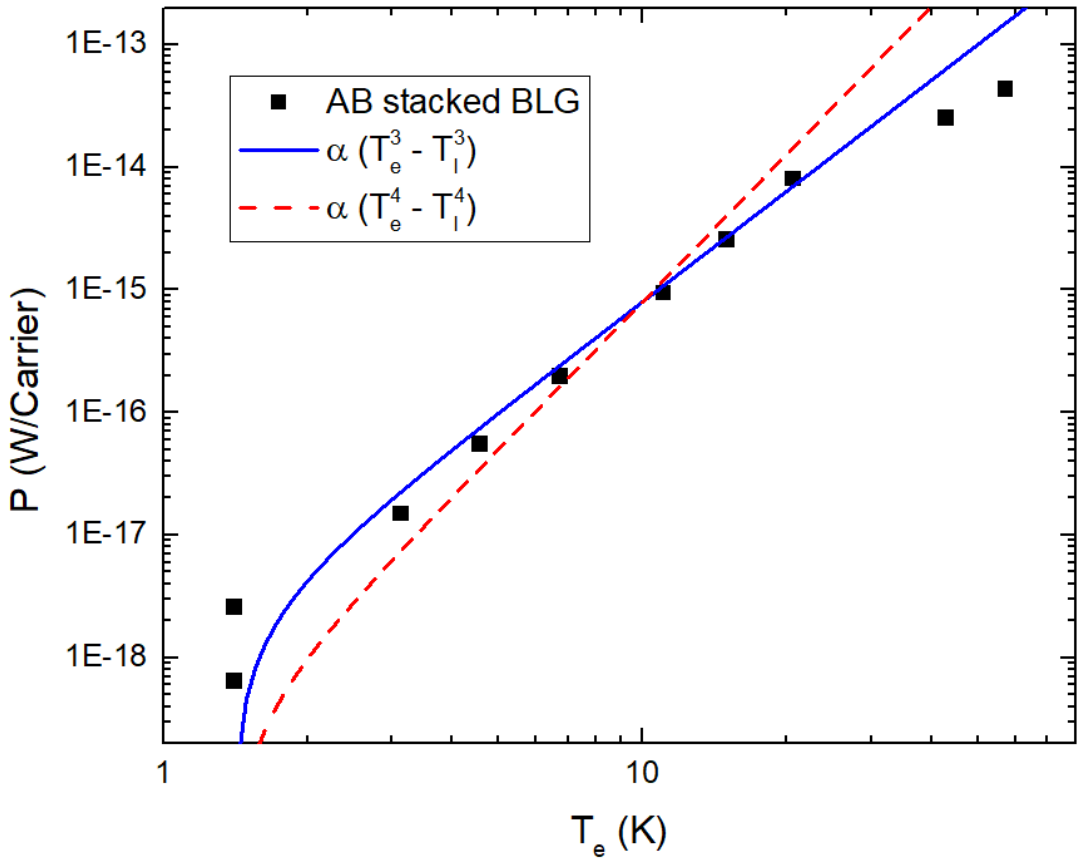

Fig. 4.12 Energy loss rate per carrier as a function of carrier temperature for AB stacked bilayer CVD graphene. The energy loss rates are fitted by the T^4 and T^3 power laws shown as the red dash curve and blue solid curve respectively.

4.4 Conclusions

We investigated electron scattering in scalable CVD graphene FETs in this chapter. First, We have demonstrated a scalable and simple approach towards encapsulating and passivating high quality CVD graphene electronic devices by using a gaseous H_2O pretreatment to allow direct ALD of dense Al_2O_3 films on graphene. We obtained thorough passivation of graphene FETs and almost doping-free ambipolar behaviour whilst enhancing carrier mobility under ambient conditions. The result of quantum Hall measurement suggests that the Hall bar device processed by this technique is promising for further electronic applications. This fabrication progress lays a foundation for scalable graphene research and operation of graphene-related electronic devices.

Second, by studying electrical characterisation and magnetotransport phenomena in encapsulated CVD grown AB stacked and large twist angle (30°) bilayer graphene FETs, as well as monolayer graphene FETs for reference, we show that electron scattering processes and hot electron effects can be tuned. It was found that phase coherence length in AB stacked graphene is longer than that in monolayer but decays faster with temperature, while large twist angle bilayer graphene has the longest phase coherence length among them with enhanced inter-valley scattering. The result for the temperature dependent dephasing rate in AB stacked bilayer graphene is in agreement with electron-electron scattering in the diffusive regime, while Nyquist scattering might account for the scattering mechanism in monolayer graphene and twist angle graphene due to quasi 1D channels formation caused by electron-hole puddles. The result suggests that an increase of the lattice temperature and the electron temperature will have an equal effect on the weak localization. This study can be used to explore the hot carrier energy loss rate in CVD graphene. We have also explored the hot carrier effects by comparing the WL suppressions using lattice temperature and current through the device. It was found that the carrier temperature dependent energy loss rates of hot carriers in AB stacked CVD bilayer graphene follow closer to a T_e^3 power-law than a T_e^4 power-law, predicted in most previous graphene studies. This result enables us better understand the hot carrier behaviours in CVD graphene.

The study of twist angle dependent of electron scattering in CVD graphene can be further performed on a doped silicon substrate, so that the carrier density can be tuned continuously and effectively at low tempertures. Overall, the findings in this chapter have a significant impact on the study of CVD graphene and its further scalable device applications.

Chapter 5

Induced Spin-orbit Coupling in Graphene/TMD Heterostructures

5.1 Introduction

The significant success of graphene has been followed by the development of other impressive 2D materials that can form atomic sheets with exotic properties [91, 52, 41, 25]. Transition metal dichalcogenide (TMD) monolayers represent a large family of 2D materials, which are atomically thin semiconductors of the type MX_2, with M a transition metal atom and X a chalcogen atom. Similar to graphene, 2D TMDs demonstrate unique electrical and optical properties that evolve from the quantum confinement and surface effects that arise during the transition of an indirect bandgap to a direct bandgap when bulk materials are scaled down to monolayers [41]. The tunable bandgap, combined with atomic-scale thickness and strong spin-orbit coupling (SOC) makes them interesting for fundamental studies and for applications in next-generation spintronics, electronics and optoelectronics devices [125].

Since its discovery, graphene has been a promising material for spintronics due to its low spin–orbit coupling [86, 110, 72], negligible hyperfine interaction [191, 81], and high electron mobility [22, 51, 35, 14], which are obvious advantages for transporting spin information over long distances [66]. However, such outstanding transport properties prevent novel quantum states from emerging, such as the quantum anomalous Hall state [125] and also limit the capability to engineer active spintronics, where strong spin–orbit coupling is crucial for creating and manipulating spin currents. Many efforts have been made towards increasing SOC in graphene. Due to their strong SOC and good interface matching with graphene, TMDs provide an ideal platform to enhance spin-dependent features of graphene while maintaining its superior charge transport properties, by proximity effect

if graphene and TMDs are stacked vertically to form a heterostructure. Tungsten disulfide (WS_2) is one member of the TMDs family and bulk WS_2 is an indirect-bandgap (1.4 eV) semiconductor, but is expected to turn into a direct-bandgap (2.1 eV) material when exfoliated into monolayer films [113]. This chapter presents a study of graphene/tungsten disulfide (Gr/WS_2) heterostructure, aiming for achieving enhanced SOC in CVD graphene for further CVD graphene spintronics applications.

The works in this chapter are completed in collaboration with Dr. Ye Fan (who supplied the heterostructure material and helped with analysing the data) from Centre for Advanced Photonics and Electronics (CAPE) of the University of Cambridge. The results in this chapter is expected to be published in another article "Induced spin-orbit coupling in CVD graphene - transition metal dichalcogenide heterostructures", which is in preparation.

5.2 Device Description and Measurement Setup

The WS_2 was exfoliated using Scotch tape onto a Si/SiO_2 substrate with dielectric thickness 300 nm. The graphene was grown by CVD approach in an Aixtron BM Pro 4" reactor using 25 μm thick Cu foil (Alfar Aesar, 99.8%), methane, hydrogen and argon at a temperature of approximately 1070 °C. The grown CVD graphene was then tranferred onto the silicon substrate with WS_2 already prepared using a wet transfer method with PMMA. The cartoon in figure 5.1(a) illustrates graphene stacked on the top of TMD monolayer to form a heterostructure. A long Hall bar was patterned using electron beam lithography followed by thermal evaporation of Ti/Au (20 nm/120 nm) contacts. This device was designed with half the Hall bar (one half along its length) being only graphene and the other half a Gr/WS_2 heterostructure, for comparisons in order to better investigate how WS_2 influence graphene performance. The AutoCAD design and optical microscope photograph of the long graphene/WS_2 Hall bar device measured in this chapter are shown in figure 5.1(b) and 5.1(c) with the left half of the Hall bar being a graphene/WS_2 heterostructure, while the right half only graphene.

The experiments were carried out in a 1.2 K pumped He-4 cryostat in Thin Film Magnetism (TFM) group of Cavendish Laboratory with a four-terminal measurement setup. 1 V excitation is supplied by a Lock-in amplifier at a frequency of 77 Hz. This AC voltage is mixed with a DC bias supplied by an SMU before going through a 10 MΩ resistor to form a constant AC current I = 100 nA through the device. Another two Lock-ins are used to monitor the AC voltage drops (longitudinal voltage V_{xx} and Hall voltage V_{XY}) of the two parts of the long Hall bar simultaneously. Another SMU is used to apply a back-gate voltage

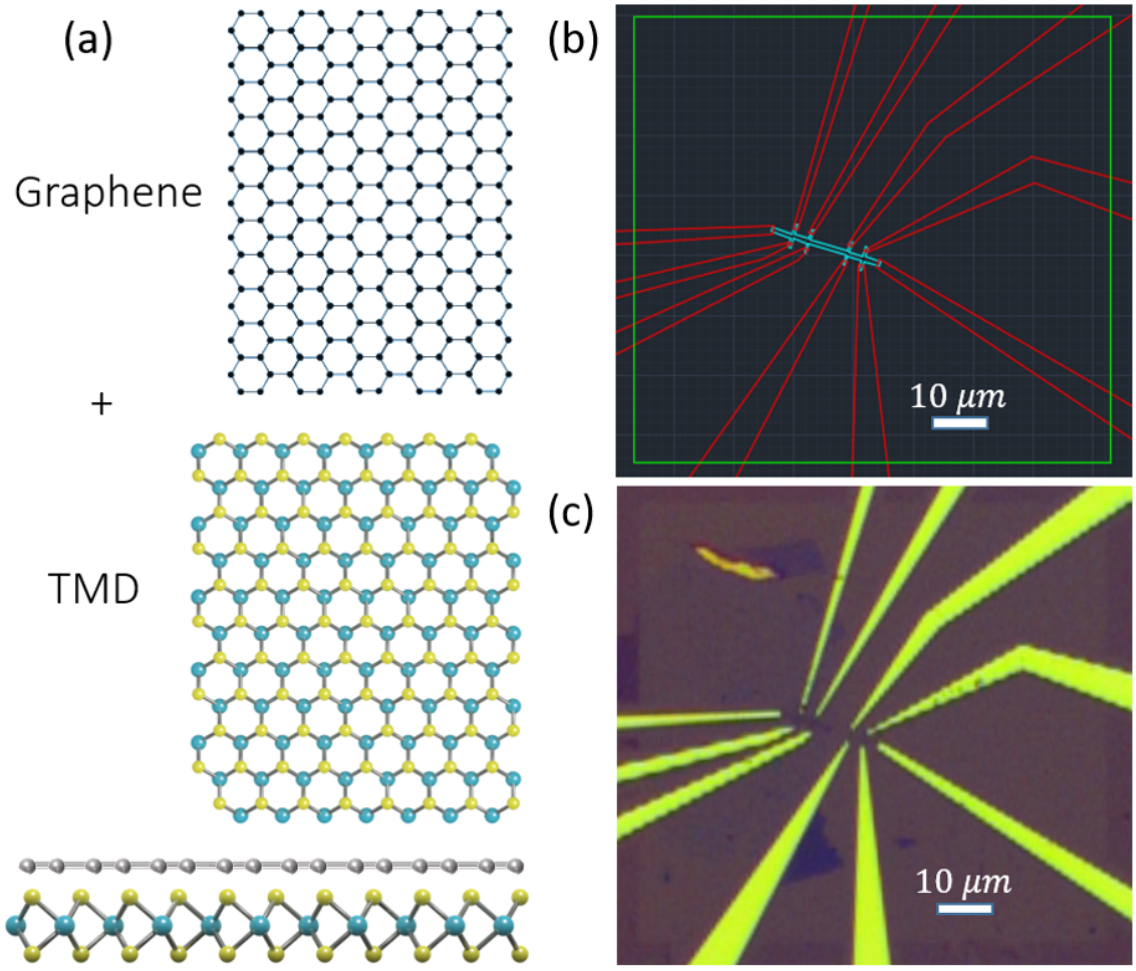

Fig. 5.1 (a) Cartoon illustrating graphene are stacked on top of transition metal dichalcogenide monolayer to form a heterostructure. (b) AutoCAD design and (c) Optical microscope photograph of the long graphene/WS_2 Hall bar device measured in this chapter, with the left half of the Hall bar being a graphene/WS_2 heterostructure, while the right half only graphene. Scale bars are 10 μm.

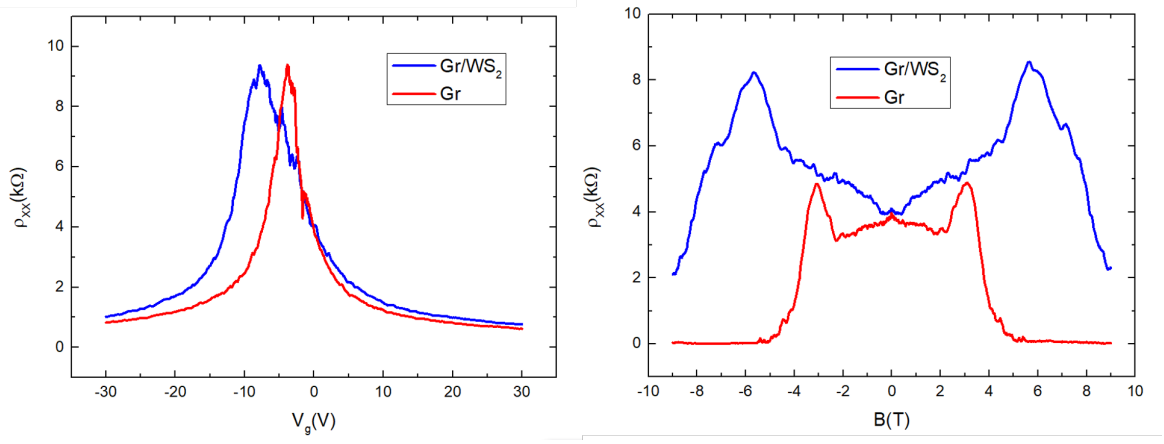

Fig. 5.2 (a) Longitudinal resistivity ρ_{xx} as a function of back-gate voltage V_g, with blue and red lines showing Gr/WS_2 heterostructure half and graphene half of the Hall bar respectively. The aspect ratio of both parts of the Hall bar is 3.5. (b) Longitudinal resistivity ρ_{xx} as a function of magnetic field B at V_g = 0 V, showing Shubnikov–de Haas effect (SdH) in both parts of the device. (T = 1.5 K)

V_g to the Si substrate via a 300 nm SiO_2 dielectric. The magnetic field can be applied up to 10 T and the temperature can vary from a base temperature of 1.5 K up to over 100 K.

5.3 Results and Discussion

We first study the device at base temperature of 1.5 K. Figure 5.2(a) shows longitudinal resistivity ρ_{xx} as a function of back-gate V_g, with blue and red lines showing the Gr/WS_2 heterostructure half and graphene half of the Hall bar respectively. The aspect ratio of both parts of the Hall bar is 3.5, which was taken into account when calculating the longitudinal resistivity. Both parts are n-type doped, whereas it is more doped when WS_2 and graphene form a heterostructure, as the location of the Dirac point of the only graphene part is at $V_{Dirac(Gr)}$ = -3.5 V, while it is $V_{Dirac(Gr/WS_2)}$ = -7 V for the heterostructure part. Another point that can be deduced from figure 5.2(a) is that the electrical quality of graphene is reduced when WS_2 is introduced, because the peak of the Gr/WS_2 field effect is broader than that in graphene. This can also be deduced from a quantitative comparison in mobility. Using $\mu = (|d\sigma/dV_g|_{max})/C_G$, where the gate capacitance is taken to be C_G = 11.6 $nF cm^{-2}$ for 300 nm SiO_2, we calculated the electron mobility of both parts μ_{Gr} = 2471 $cm^2V^{-1}s^{-1}$ and μ_{Gr/WS_2} = 1162 $cm^2V^{-1}s^{-1}$. This suggests WS_2 might induce some disorders into graphene when we stack the two kinds of material. In terms of how the longitudinal resistivity ρ_{xx} varies against magnetic field B, figure 5.2(b) exhibits Shubnikov–de Haas effect (SdH) in both parts of the device, when B changes between -9 T and 9 T and V_g = 0 V. The first Landau

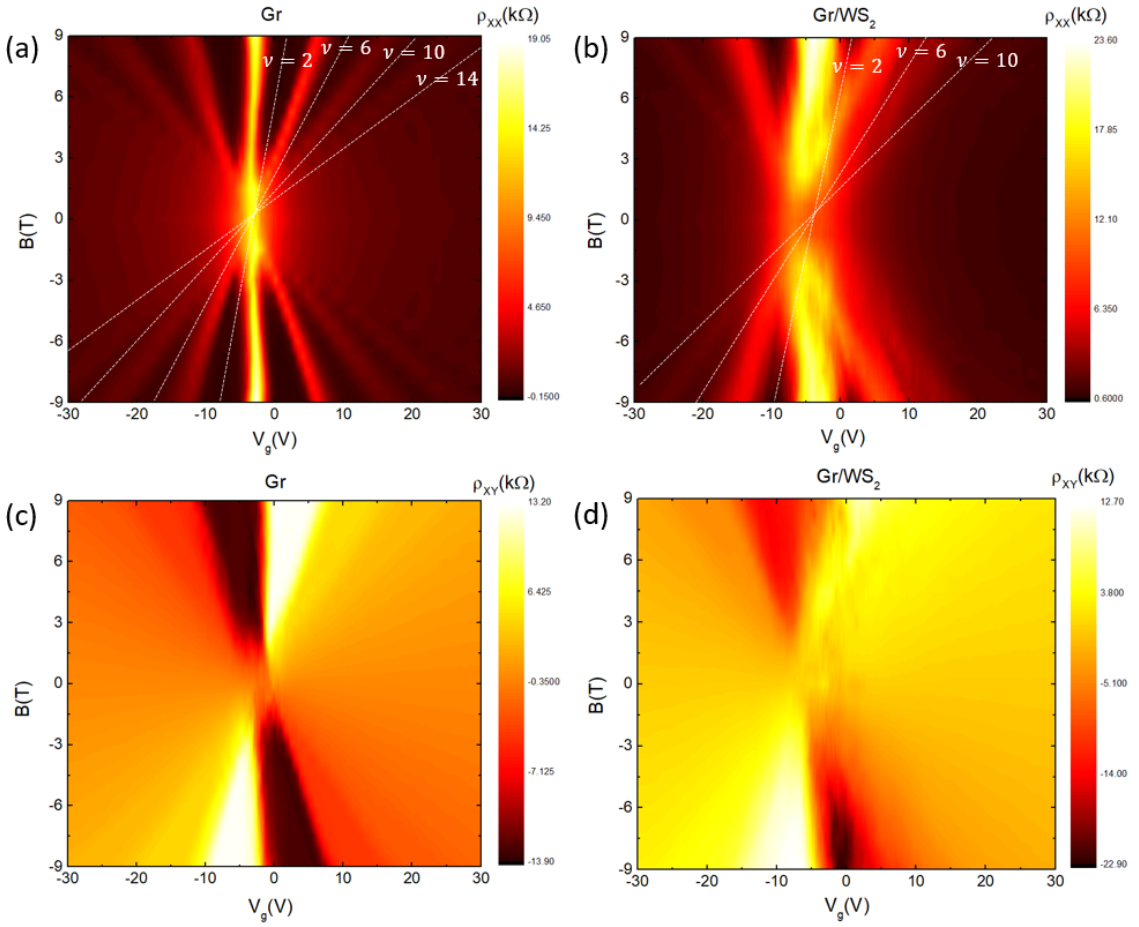

Fig. 5.3 Longitudinal resistivity ρ_{xx} as a function of back-gate voltage V_g and magnetic field B, showing Landau fan diagrams in (a) graphene and (b) Gr/WS_2 heterostructure respectively. Hall resistivity ρ_{XY} as a function of back-gate voltage V_g and magnetic field B for (c) graphene and (d) Gr/WS_2 heterostructure respectively. (T = 1.5 K)

gap in graphene starts to appear at around $|B| \approx 5$ T, while it will be at some point when $|B|$ > 9 T for the heterostructure. This means that WS_2 broadens the Landau levels in graphene.

In order to obtain a big map of the device resistivity as a function of back-gate voltage V_g and magnetic field B, we drew the 2D plots in figure 5.3. Figure 5.3(a) and figure 5.3(b) show the longitudinal resistivity ρ_{xx}, exhibiting the Landau fan diagrams in graphene and Gr/WS_2 heterostructure respectively, while figure 5.3(c) and figure 5.3(d) show the corresponding Hall resistivity. One obvious feature of the figures is that the Landau levels start to separate when $|B| > 2$ T. The Landau energy levels are given by the equation $E_n = sgn(n)\upsilon_F\sqrt{2e\hbar B|n|}$, where n is the Landau level index. For a certain n, the Landau energy levels E_n are proportional to $\sqrt{B}$. When $|B| < 2$ T, no obvious Landau gap formation suggests the disorder in the sample broadens the Landau levels so that adjacent Landau levels

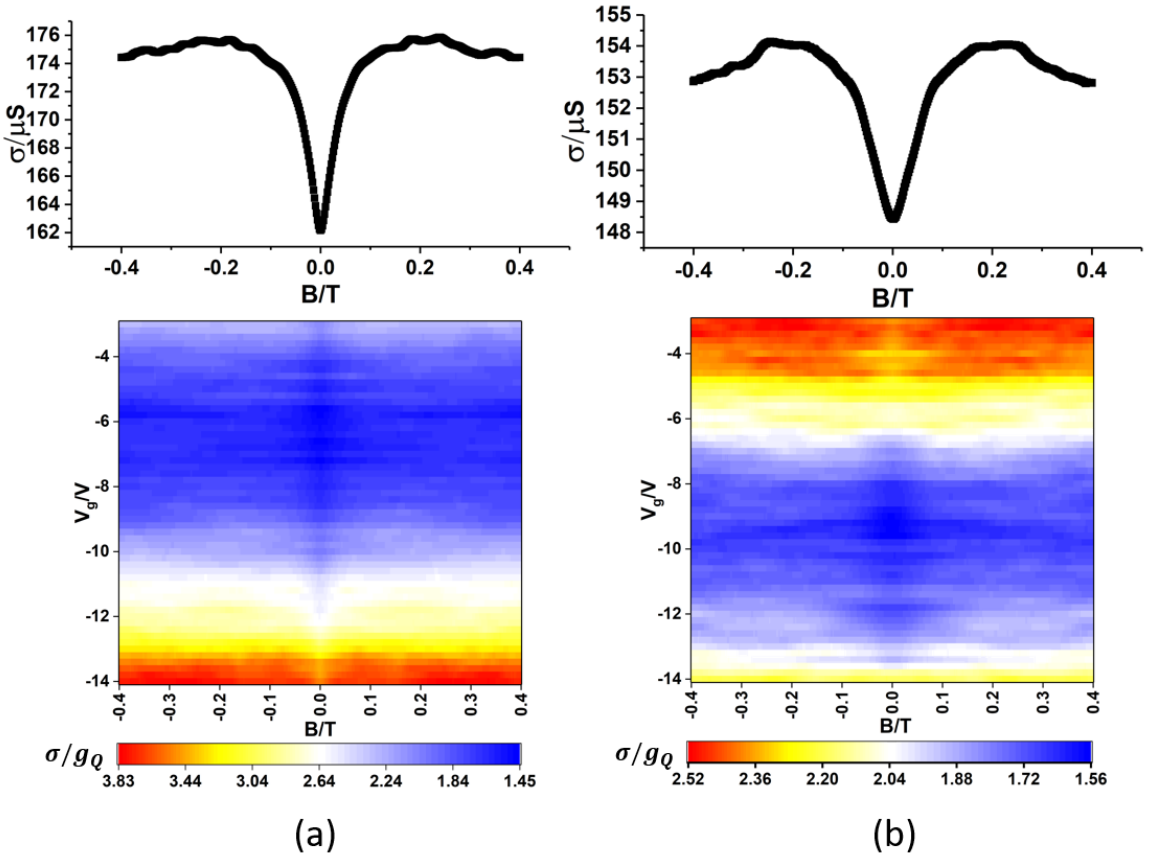

Fig. 5.4 Longitudinal conductivity as a function of back-gate voltage V_g and magnetic field B between -0.4 T and 0.4 T, exhibiting weak localization measurement results against back-gate voltage in (a) graphene and (b) Gr/WS_2 heterostructure respectively. The average processed data over back-gate voltage is shown above the 2D maps. (T = 1.5 K)

merge together and no gaps can be observed until B is strong enough to separate those energy levels. We can also observe some differences between graphene and Gr/WS_2. Landau gaps corresponding to filling factor $\nu = \pm 2, \pm 6, \pm 10, \pm 14$ can be observed in graphene, while only $\nu = \pm 2, \pm 6, \pm 10$ Landau gaps are observable in Gr/WS_2 in the same V_g and B ranges. This phenomenon reveals the fact that WS_2 introduces disorder into graphene leading to Landau energy levels broadening. In addition, from the Hall resistivity maps, we observed that the first plateau corresponding to filling factor $\nu = \pm 2$ with a resistance value $\sim 0.5h/e^2$. This result is in agreement with the theoretical equation $\sigma_{xy} = 4(n + 1/2)e^2/h$, showing half-integer quantum Hall effect in graphene [94].

Then we move on to the low magnetic field measurement to study the weak localization effect in both graphene and Gr/WS_2 heterostructure. The 2D maps of weak localization measurement results plotted against back-gate voltage V_g with a magnetic range between

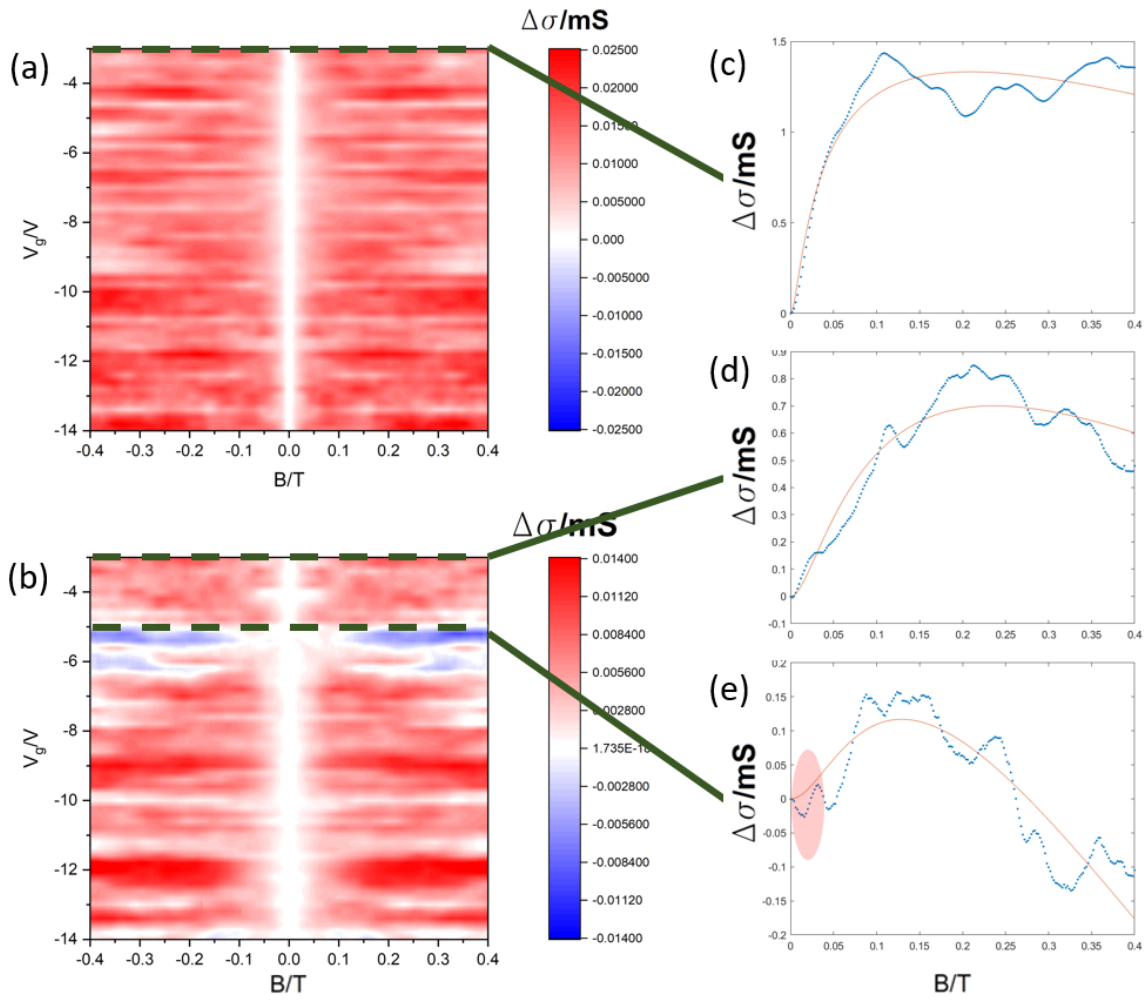

Fig. 5.5 Weak localization measurement results against back-gate voltage V_g in (a) graphene and (b) Gr/WS_2 heterostructure respectively. Line plots of the quantum correction in conductance at $V_g = -3V$ are shown in (c) and (d) of graphene and Gr/WS_2 heterostructure respectively. (e) shows the line plot of the quantum correction in conductance at $V_g = -5V$ of Gr/WS_2 heterostructure. (T = 1.5 K)

-0.4 T and 0.4 T, are shown in figure 5.4(a) and figure 5.4(b) corresponding to graphene and Gr/WS_2 heterostructure respectively. The conductance fluctuations (which can be seen more clearly in figure 5.5(c), 5.5(d) and 5.5(e)) are much stronger than that observed in the Hall bar devices of chapter 4. One possible reason is that the width of the Hall bar device discussed in this chapter is 1 μm, narrower than that in chapter 4, whose width is 4 μm. In this case, edge scattering will play a role [193, 53]. Moreover, the number of channels will be less in the narrow channel so that a fluctuation in one channel will result in large total fluctuation in the narrower channel. Another possibility is that since the device measured in this chapter has not been processed by an ALD encapsulation technique, it was exposed to the environment and might be contaminated to some extent. In order to get rid of the influence of conductance fluctuations and better analyze the weak localization, we averaged the data over the back-gate voltage V_g and obtained the weak localization curves shown above the map figures. The details about the weak localization analysis will be discussed later. Then we subtracted the conductivity value at zero magnetic field and plotted the 2D maps of the conductance correction $\Delta\sigma_{xx}(B) = \sigma_{xx}(B) - \sigma_{xx}(0)$, as shown in figure 5.5(a) and figure 5.5(b) for the graphene and Gr/WS_2 heterostructure respectively. The region with red colour means the conductivity is positive, while blue means negative. We can see a negative change in conductivity in the Gr/WS_2 heterostructure around V_g = -5 V. The conductance correction $\Delta\sigma_{xx}$ is negative at higher magnetic field and when we look close at the region around zero magnetic field at V_g = -5 V (see figure 5.5(e)), we can see a flat plateau with conductance fluctuations. By comparison, we also exhibit the line plots for graphene and the Gr/WS_2 heterostructure at V_g = -3 V in figure 5.5(c) and figure 5.5(d) respectively, with their fitting curves. The fitting is done using the following equation [179] in terms of the quantum correction in conductivity $\Delta\sigma(B) = \sigma(B) - \sigma(B=0)$ by using the theory in [127] described in chapter 2 for monolayer graphene:

$$\Delta\sigma(B) = \frac{e^2}{\pi h}[F(\frac{\tau_B^{-1}}{\tau_\varphi^{-1}}) - F(\frac{\tau_B^{-1}}{\tau_\varphi^{-1}+2\tau_i^{-1}}) - 2F(\frac{\tau_B^{-1}}{\tau_\varphi^{-1}+\tau_i^{-1}+\tau_*^{-1}})]. \tag{5.1}$$

Here, $F(z) = ln(z) + \psi(0.5+z^{-1})$, $\psi(x)$ is the digamma function, $\tau_B^{-1} = 4eDB/\hbar$ and D is the diffusion coefficient. The first term in this equation is responsible for weak localization, while the anti-localization is determined by the second and third terms with negative sign. The quantum correction depends not only on the dephasing time τ_φ, but on the elastic scattering times τ_i and τ_*, indicating intervalley scattering time and intravalley scattering time. As shown in figure 2.5 of chapter 2, the shape of the magnetoconductance curves can be very different as it is controlled by the interplay between all scattering times involved. When the intervalley scattering time is much longer than the intravalley time, $\tau_i \ll \tau_*$, the

conductance correction curve will always be positive (see solid line in figure 2.5), like most regions in figure 5.5(a) and figure 5.5(b). However, for the Gr/WS_2 heterostructure, when V_g is around -5 V, negative magnetoconductance appears at higher magnetic field (blue colour region). This means in this small region, the intervalley scattering is stronger than intravalley (see dashed line in figure 2.5). We explain this as resulting from charged puddles formation in WS_2. The WS_2 might turn on at certain electric fields and the rough surface of WS_2 leads to some charged puddles, which can screen the top layer of graphene. This can also explain why the longitudinal resistivity ρ_{xx} jumps at a gate voltage of around V_g = -5 V from figure 5.2(a). Another interesting point in figure 5.5(e) is that a small flat plateau forms instead of a sharp dip near zero B field when $V_g \approx$ -5 V, denoted by the red colour circle. This is a combined effect of both WL and WAL. Figure 5.6 shows the AFM image of the material used in this chapter. The bottom right corner is the surface of the Gr/WS_2 heterostructure showing some disorder. Therefore, under certain electric fields ($V_g \approx$ -5 V), some regions of the graphene are induced spin-orbit coupling from WS_2 while some are not. This results in some regions exhibiting WL while some WAL. Therefore, the overall result is a flat plateau in figure 5.5(e).

We then move on to the temperature dependent WL measurements. Figure 5.7 presents the WL measurement results of this Hall bar device, showing conductance correction $\Delta\sigma(B)$ as a function of temperature at three different carrier concentrations, with (a) and (b) corresponding to V_g = 0 V, (c) and (d) to V_g = -3.5 V (the Dirac point of graphene), and (e) and (f) to V_g = -7 V (the Dirac point of Gr/WS_2). The left figures (a), (c) and (e) are for graphene, while the right figures (b), (d) and (f) are for Gr/WS_2 heterostructure. Obvious conductance fluctuations can be observed in both parts, but the fluctuations can be removed by averaging the carrier concentration over a certain range as discussed previously shown in figure 5.4. The WL measurements are performed from the base temperature 1.5 K to around 100 K and from figure 5.7 one can see that the temperature dependent magnetoconductance still exists at temperatures T $\sim$ 100 K, while in conventional 2D systems the quantum correction usually disappears at much lower temperatures, due to intensive electron-phonon scattering [70]. The weak electron-phonon scattering in graphene [87] makes it possible to analyse WL in a large temperature range. By fitting the conductance correction $\Delta\sigma(B)$ of WL measurement using equation (5.1), we calculated the phase coherence length L_φ of graphene and Gr/WS_2 in this device at these three different carrier concentrations. The calculated results are shown in figure 5.8. Both phase coherence length and temperature are converted into log_{10} format for further analysis. From the temperature dependent phase coherence length results, we can draw the following conclusions. First, L_φ in graphene is generally longer than that in Gr/WS_2, especially at low temperature T < 15 K, except for V_g = -3.5 V (the Dirac point

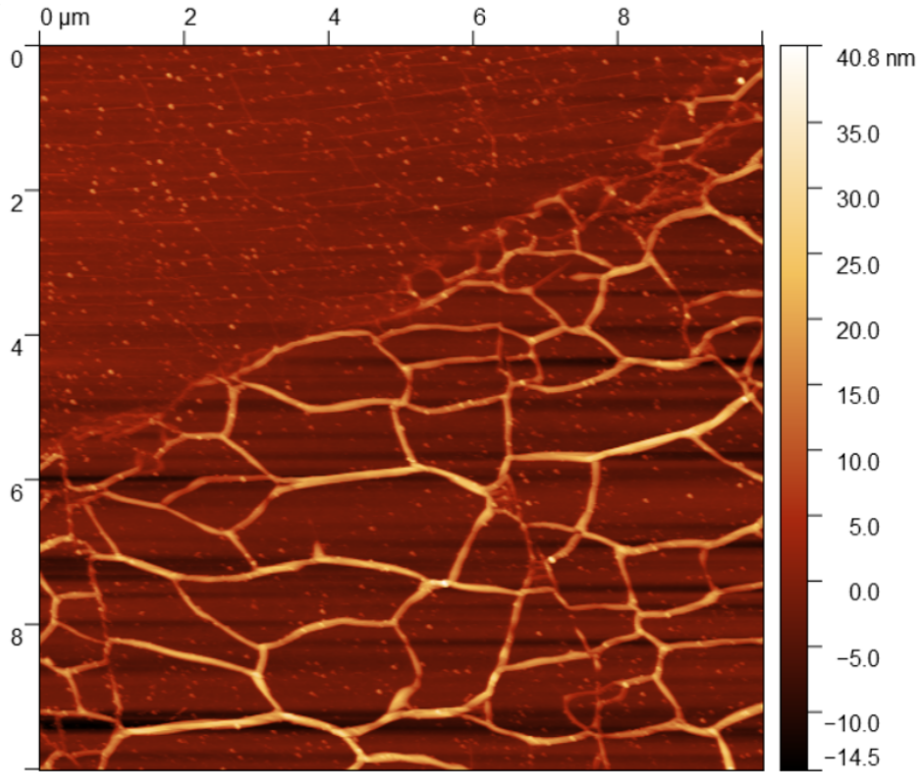

Fig. 5.6 Atomic force microscope image of the material used to fabricate the Gr/WS_2 Hall bar device in this chapter, showing the boundary of graphene (top left corner) and Gr/WS_2 heterostructure (bottom right corner).

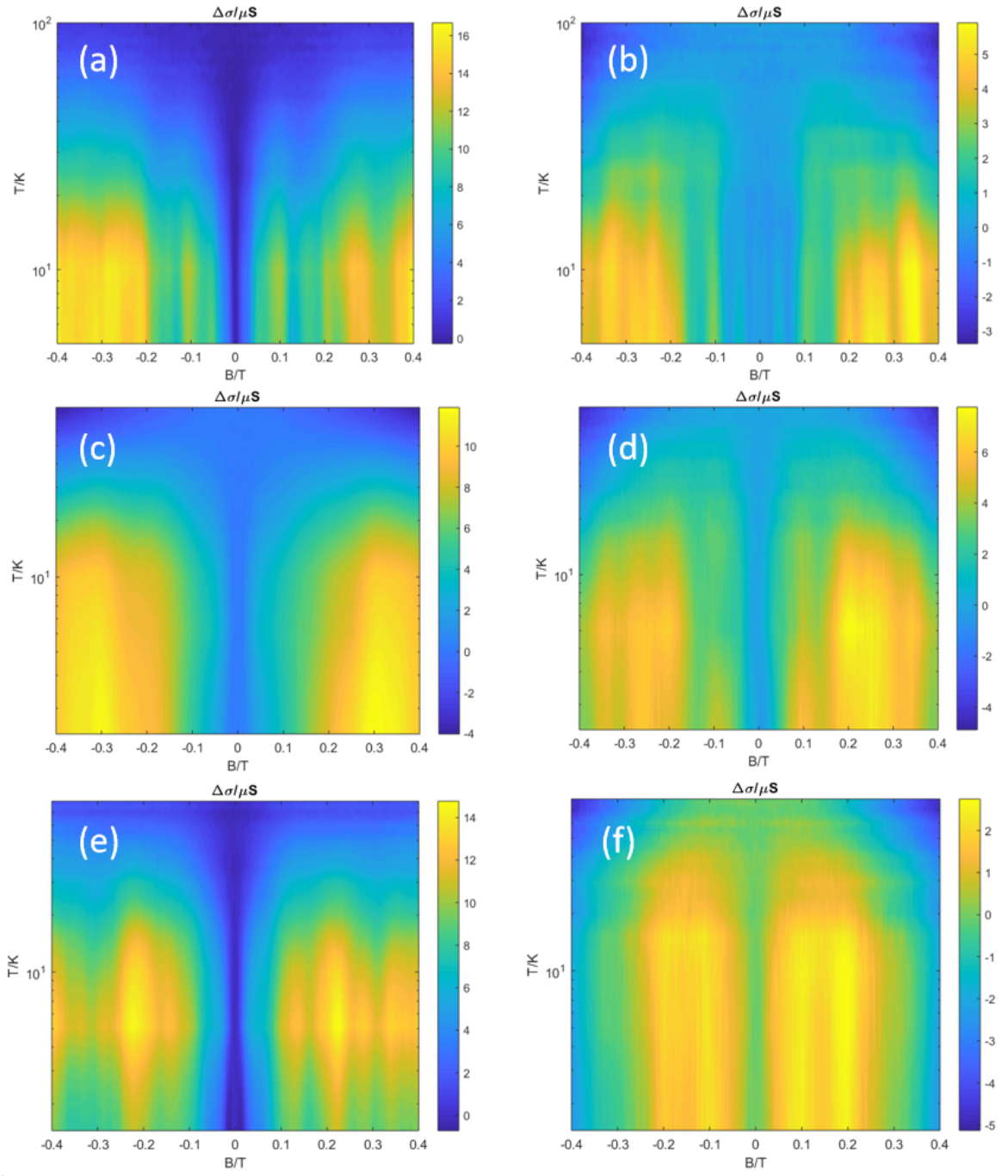

Fig. 5.7 Conductance correction $\Delta\sigma(B)$ of weak localization measurement as a function of temperature at three different carrier concentrations, with (a) and (b) corresponding to V_g = 0 V, (c) and (d) to V_g = -3.5 V (the Dirac point of graphene), and (e) and (f) to V_g = -7 V (the Dirac point of Gr/WS_2). The left figures (a), (c) and (e) are the results of graphene, while the right figures (b), (d) and (f) are for the Gr/WS_2 heterostructure.

of graphene), where L_φ in graphene is reduced from $\sim$ 200 nm down to $\sim$ 120 nm at base temperature, and it decays faster than that in Gr/WS_2 and is shorter than that in Gr/WS_2 when T > 15 K. Second, L_φ in Gr/WS_2 seems weakly dependent on the carrier concentration with values around 100 nm at base temperature. Moreover, it is also weakly dependent on the temperature when T < 20 K probably due to enhanced spin-orbit coupling in graphene induced by WS_2. Finally, we performed linear fitting on $log_{10}(L_\varphi)$ against $log_{10}(T)$ to quantitatively describe how L_φ decays against temperature T and the fitting information are shown by the right of each graph of figure 5.8.

From the linear fitting results in figure 5.8, we can obtain the exponents n_L for phase coherence length L_φ against temperature T in the relation $L_\varphi \propto T^{n_L}$, which are listed in table 5.1. At zero back-gate voltage V_g = 0 V, $L_\varphi \propto T^{-1/2}$ for graphene while $L_\varphi \propto T^{-1/3}$ for Gr/WS_2. And for both V_g = -3.5 V and V_g = -7 V, $L_\varphi \propto T^{-1/3}$ for graphene while $L_\varphi \propto T^{-1/4}$ for Gr/WS_2. Given that $L_\varphi = \sqrt{D\tau_\varphi}$, we can find the dephasing rate $\tau_\varphi^{-1} \propto L_\varphi^{-2}$, thus the exponent for dephasing rate τ_φ^{-1} is $n_{\tau^{-1}} = -2n_L$. The value of $n_{\tau^{-1}}$ of both graphene and Gr/WS_2 at the three different back-gate voltages are also listed in table 5.1. The exponent n_L or $n_{\tau^{-1}}$ determines the electron scattering types and can be a useful tool to examine the dephasing sources at high temperature. Our results show that the $n_{\tau^{-1}}$ values in graphene are higher that that in Gr/WS_2 for all the three cases, which suggests that the dephasing process against temperature is faster in graphene than that in Gr/WS_2. We can argue the graphene part is cleaner than the heterostructure part. To be specific, for the case at zero back-gate voltage, we observed the dephasing rates τ_φ^{-1} are found to have T^1 and $T^{2/3}$ dependence for graphene and Gr/WS_2 respectively, and saturate at extremely low temperatures, where we argue that the exponents 1 and 2/3 represent quasi-2D and quasi-1D transport with electron-electron interaction in the diffusive regime respectively [7, 44]. This explanation has been discussed in chapter 4 for bilayer graphene. For a very clean sample, there is an alternative inelastic electron scattering mechanism, which gives a parabolic temperature dependence, $\tau_\varphi^{-1} \propto T^2$ [138, 179]. In this case, electron-electron interaction is mediated by only a few impurities and the electron-electron scattering is in the ballistic regime. The quasi-1D channel formation in Gr/WS_2 heterostructure can be easily understood from the surface roughness visible in the AFM photograph in figure 5.6. In terms of cases at V_g = -3.5 V and V_g = -7 V, the dephasing rate in graphene obeys the $T^{2/3}$ dependence law probably due to quasi-1D transport happening at these carrier concentrations, but Gr/WS_2 shows a $T^{1/2}$ dependent dephasing rate. So far we did not find a physics model from literature to explain the $T^{1/2}$ dependence behaviour in graphene. The reason might lie in the fact that the electronic properties of graphene are changed by the WS_2, i.e. induced spin-orbit coupling in Gr/WS_2 by the proximity effect. The physics underlying our results is still under discussion.

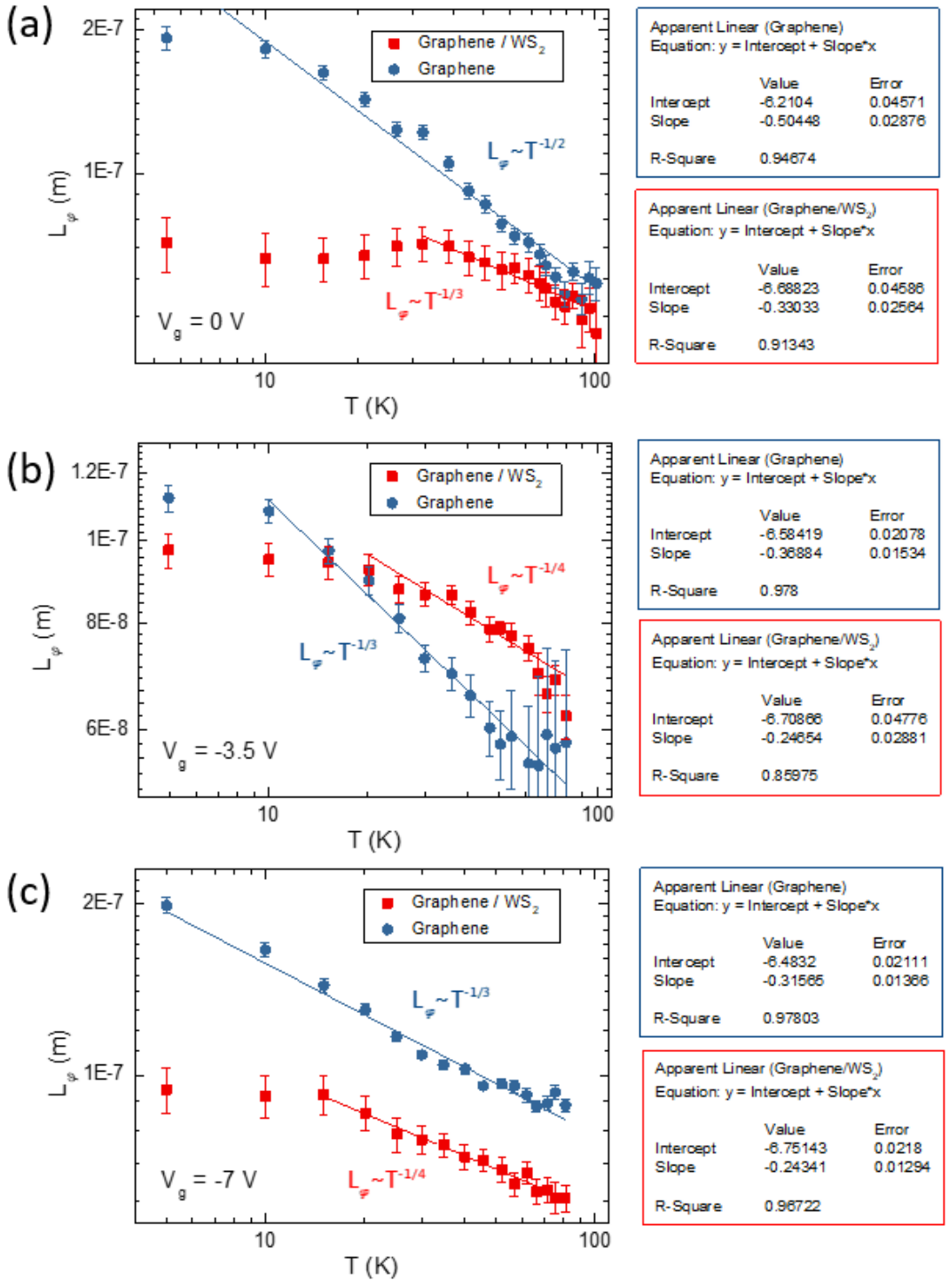

Fig. 5.8 Subtracted phase coherence length as a function of temperature based on the previous weak localization measurement results at three different carrier concentrations, with corresponding to (a) V_g = 0 V, (b) V_g = -3.5 V (the Dirac point of graphene), and (c) V_g = -7 V (the Dirac point of Gr/WS_2). The corresponding linear fitting lines are also shown with fitting information exhibited by the right of each graph. The blue colour stands for graphene and red for Gr/WS_2.

Table 5.1 Phase coherence length L_φ and dephasing rate τ_φ^{-1} exponents against temperature T.

	n_L (Graphene)	$n_{\tau^{-1}}$ (Graphene)	n_L (Gr/WS_2)	$n_{\tau^{-1}}$ (Gr/WS_2)
$V_g = 0V$	-1/2	1	-1/3	2/3
$V_g = -3.5V$	-1/3	2/3	-1/4	1/2
$V_g = 7V$	-1/3	2/3	-1/4	1/2

5.4 Conclusions

This chapter presents a study of a Gr/WS_2 heterostructure, with exfoliated WS_2 stacked on top of CVD graphene, aiming for achieving enhanced SOC in CVD graphene for further CVD graphene spintronics applications. The material was patterned into a long Hall bar with half its length being a Gr/WS_2 heterostructure and the other half being only graphene for reference. Electron transport measurements were performed as a function of magnetic field, electric field and temperature. The phase coherence length was found to be reduced in the heterostructure compared with only graphene at low temperature, and a special transition from weak localization (WL) to weak anti-localization (WAL) occurred around a certain carrier concentration possibly due to surface roughness induced patches. Moreover, the dominant scattering mechanism in the heterostructure only weakly depends on temperature up to 20 K, with phase coherence length value around 100 nm at low temperatures. This weak temperature dependence is probably due to induced spin-orbit coupling in Gr/WS_2 by a proximity effect. Finally, we discussed the dephasing rate against temperature quantitatively to explore the electron scattering types and examine the dephasing sources at high temperature. Some physics in terms of electron scattering in Gr/WS_2 still requires further explanation.

The study of graphene/TMD heterostructures can be further optimized by stacking CVD grown TMD material on top of CVD graphene, in which case we can not only realize a more scalable route, but also expect to observe a strong induced spin-orbit coupling in graphene due to less surface ripples. The results of this chapter provide insight into fabrication and operation of scalable graphene spintronic devices, opening a path for the future applications of graphene-based spintronics.

Chapter 6

Quantum Transport in Graphene Nanoribbons and Quantum Hall Antidots

The previous two experimental chapters discussed the Hall bar devices, the minimum features of which are over one micron. The study of micro-size Hall bar devices is useful for characterizing the properties of the graphene material, whereas if the graphene is patterned into sub-micron nanostructures i.e. quantum dots, quantum transport phenomenon such as coulomb blockade, and Aharonov-Bohm effect, can be probed. This chapter discusses two types of graphene nanostructures: nanoribbons patterned in epitaxial bilayer graphene on silicon carbide and quantum Hall antidots on CVD graphene.

Despite the high growth cost of SiC epitaxial graphene, its wafer-scale growth enables large scale production compared with exfoliated graphene, and its natural insulating substrate makes it suffer less potential contamination caused by graphene transfer from other substrates (i.e. CVD graphene transfer from a Cu substrate) [16, 17]. The first half of this chapter studies electron transport in nanostructures patterned in bilayer graphene patches grown epitaxially on SiC as a function of doping, magnetic field, and temperature, and multiple quantum dots formation is observed in graphene nanoribbons (GNRs). The results have been published in the journal Carbon, entitled 'Observation of Coulomb blockade in nanostructured epitaxial bilayer graphene on SiC' [43]. This work is in collaboration with my colleague Cassandra Chua, who designed and fabricated the devices and we worked together to carry out the low temperature measurements and analyse the data. The material is sourced from Chalmers University of Technology in Sweden.

The second half of this chapter will discuss a quantum antidot between a pair of split gates based on a CVD graphene Hall bar, which was discussed in chapter 4. The quantum Hall

antidots can effectively avoid the disorder caused by etched edges and enable graphene dots to perform better compared to conventional etched quantum dots. The tunnelling between localized antidot states and extended quantum Hall edge states is studied and Aharonov-Bohm oscillations are observed and analysed.

6.1 Silicon Carbide Graphene Nanoribbons

Although SiC provides a naturally insulating substrate and direct growth avoids contamination and sample degradation incurred during transfer or exfoliation, the strong n-type doping of as-grown material [90, 183, 111] must be neutralised in order to tune to the Dirac point [146, 120] where tunnelling and single-electron charging effects can be observed. In this section, a combination of side- and corona-discharge gating [114] is used to tune the doping and single-electron charging effects are observed in nanostructured bilayer graphene patches on the Si-face (0001) of SiC substrates [185]. The development of single-electron tunnelling spectroscopy in SiC graphene would not only provide additional insights about the graphene-SiC interaction but also enable the fabrication of large arrays of single-electron quantum devices such as pumps [45] and spin qubits [165].

6.1.1 Sample Preparation and Measurement

The devices studied in this section are defined by electron-beam lithography and dry-etched using an O_2 plasma. To modify the global carrier density we use corona-discharge gating [114], which involves spraying charges on a dielectric layer spin-coated over the device, and a local graphene side gate for fine tuning the doping over a narrower range. We focus on the behaviour of a bilayer GNR device with width (W) $\approx$ 100 nm and length (L) of $\approx$ 700 nm with a side gate $\approx$ 180 nm from the nanoribbon channel. A Kelvin probe micrograph [147] confirming that the nanoribbon is predominantly composed of bilayer graphene is shown in figure 6.1(a). Figure 6.1(b) presents a plot of the two-terminal conductance as a function of the number of negative discharges from the ion gun. As expected, the conductance drops due to the reduction in electron carrier density. Hall effect measurements from samples fabricated from similar wafers would suggest the doping of as-prepared devices is 10^{13} carriers per cm^2. To examine the low-temperature behaviour at different carrier densities we measured at three stages of discharge doping and cooldowns. In the absence of precise knowledge of the doping we refer to these as high (HD), medium (MD), and low (LD) doping, indicated in figure 6.1(b). Electron transport is investigated by two-terminal measurement with fields up to B = 8 T and temperatures down to T = 1.4 K.

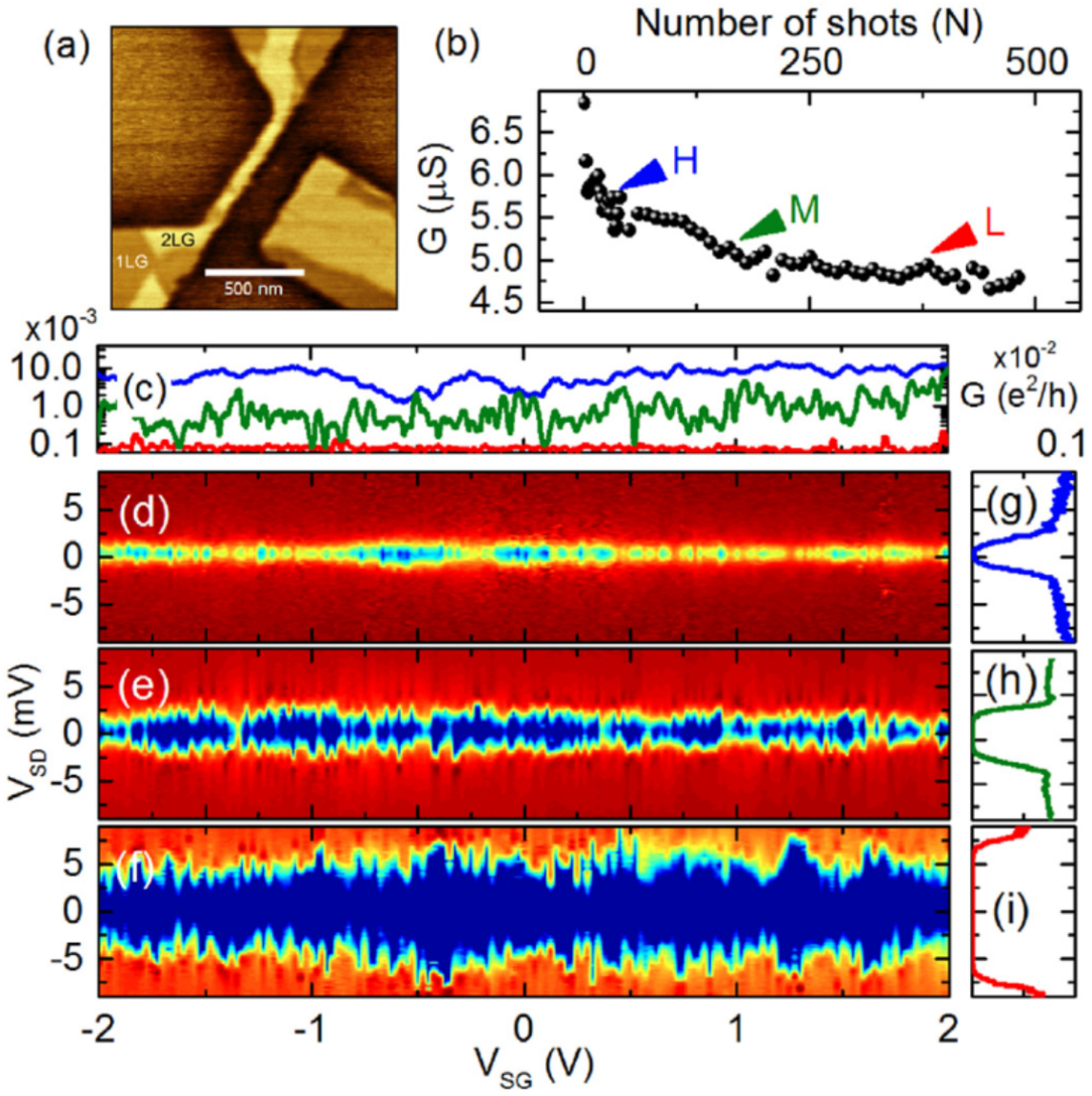

Fig. 6.1 (a) Kelvin probe micrograph of the graphene nanoribbon, where light and dark correspond to bilayer and single layer graphene, respectively. (b) Conductance at room temperature as a function of the number of corona discharge shots, with arrows indicating the three different carrier concentrations studied. (c) Conductance as a function of side-gate voltage at HD (blue), MD (green), and LD (red). Conductance as a function of source drain bias (V_{SD}) and side gate voltage (V_{SG}) for (d) HD, (e) MD, and (f) LD. (g)–(i) Conductance as a function of source-drain bias showing the maximum gap (T = 1.4 K).

6.1.2 Results and Discussion

Figure 6.1(c) demonstrates a comparison of the linear conductance measured at V_{SD} = 1 mV as a function of side-gate voltage (V_{SG}) at 1.4 K for each doping level. At HD and MD the conductance exhibits reproducible fluctuations, but for LD it is mostly within the noise floor. To uncover the origin of this behaviour we performed bias spectroscopy by sweeping V_{SD} and V_{SG} and plot the charge-stability diagrams in figure 6.1(d) - (f). At HD the conductance is suppressed but remains non-zero (soft gap) for $\approx$ 1 mV around V_{SD} = 0 V, while at MD and LD conductance G exhibits a hard gap (where G remains zero for a finite range of V_{SD}) of $\approx$ 2 mV and $\approx$ 5 mV, respectively (see figure 6.1(g) - (i)). Furthermore, the latter exhibit diamond or shard-like features reminiscent of the charge stability in a network of Coulomb-blockaded quantum dots. At LD the shards are less well defined with a periodicity in V_{SG} of about 60 mV, but as they rarely close the total conductance at low bias is strongly suppressed for all V_{SG}.

We first focus on the device at the MD regime. Figure 6.2(a) shows a region of the charge stability diagram in more detail. We observe multiple diamonds with roughly uniform height and width. A typical diamond is shown in figure 6.2(b) and a line-cut across zero bias shows the periodic conductance resonances as a function of V_{SG} (see figure 6.2(c)). The maximum source-drain gap is around 2 mV and consecutive resonances are spaced by $\Delta V_{SG} \approx 15$ mV. The periodicity over this range strongly suggests that transport occurs either via a single or a few similar quantum dots with typical charging energy $E_c \approx 2$ meV. To test this we fit the following equation describing single-electron tunnelling through many nearly degenerate states in the classical Coulomb blockade regime [73]:

$$G_T = G_P \frac{(\mu - E_0)/k_B T}{sinh[(\mu - E_0)/k_B T]}, \tag{6.1}$$

where G is the temperature-dependent conductance, μ is the chemical potential, E_0 is the energy of the resonant bound state where tunnelling occurs, $\Gamma = \Gamma_L + \Gamma_R$ (Γ_L and Γ_R are the tunnelling rates through the left and right barriers, respectively), and $G_P = (e^2/h)(\rho\Gamma_L\Gamma_R/2\Gamma)$ (ρ is the density of bound states at the chemical potential μ). Using $T = 1.4K$, and the relationship $E_0 = \alpha V_{SG}$, we obtain values for G_P and α that can be compared with the lever arm deduced from the slope of their respective Coulomb diamonds. One of the fits is shown in figure 6.2(d) and we find reasonable general agreement between the measured and fitted lever arms, yielding an average $\alpha \approx 0.175$ meV/V.

To explore the quantum dot structure in more detail, figure 6.3(a) shows the effect of a perpendicular magnetic field on the single-particle addition spectrum at MD. As a function of B, the Coulomb blockade resonances fluctuate around an average energy. This behaviour

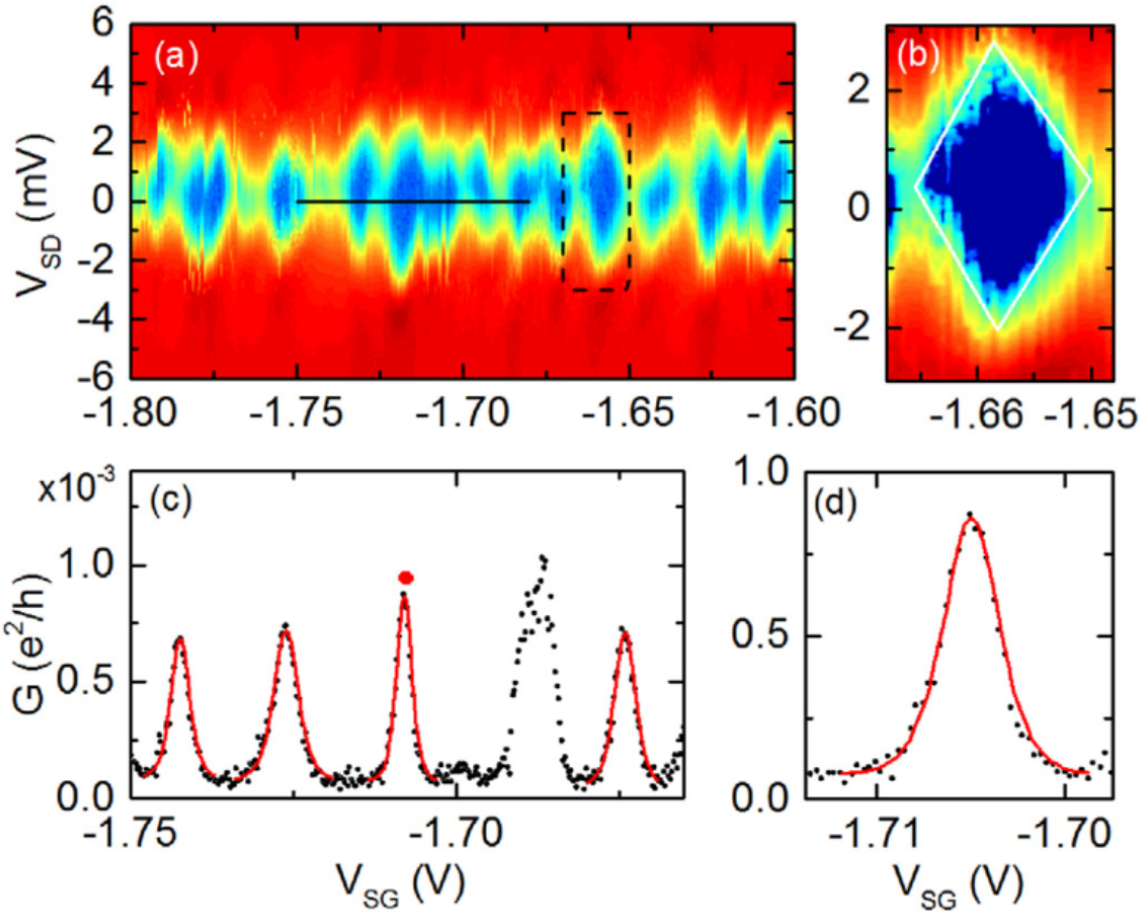

Fig. 6.2 (a) Conductance as a function of V_{SD} and V_{SG} at MD. (b) Representative Coulomb diamond outlined by the dashed box in (a). (c) Conductance as a function of V_{SG} at zero bias along the line in (a), showing conductance resonances (black points) and fits (red lines) based on Coulomb blockade theory. (d) Detailed plot of the fitted peak indicated by a red dot in (c). (T = 1.4 K)

is now well understood and arises from anticrossings between the single-particle levels [121, 79]. At a large particle number there are a large number of such anticrossings, so the resonances exhibit kinks and slopes around 10 meV/T (see figure 6.3(a)) without shifting uniformly in energy [40]. The number of peaks also roughly doubles and the average period in V_{SG} halves to around 5 mV. At 8 T the gap in source-drain bias shrinks leading to smaller Coulomb diamonds [figure 6.3(b)] and increase in the average conductance. Figure 6.3(c) plots the bias sweeps averaged across side-gate voltage at increasing magnetic fields and shows a softening of the gap for fields above 4 T and a shrinking of the gap to around 1 meV by 8 T. Such strong positive magnetoconductance is characteristic of GNRs and is associated with closing of both the transport and source-drain gaps [40]. This can be explained by an increase in the characteristic size L_c of the quantum dots and the consequent decrease in the energy required to hop between them. In GNRs there is strong evidence that quantum dots form due to potential fluctuations, which in SiC have been described using Gaussian statistics parameterised with the strength s $\approx$ 10 meV, a factor of 5 less than on SiO_2. Quantum dots form at MD when Fermi level E_F is within s, and tunnel barriers form between adjacent electron-hole puddles due to the quantum confinement gap Δ_{1D}. For a 100 nm wide GNR, the quantum confinement gap Δ_{1D} is comparable with the disorder potential s, which is depicted in figure 6.3(d). Transport is dominated by a few QDs and the conductance exhibits periodic transmission resonances (see figure 6.2(c)). When a magnetic field is applied, the density of states decreases in the bulk of the puddles while it increases at their edges. Electron transport through the GNR is therefore not confined to a particular puddle but can be delocalized in the GNR owing to chiral edge channels [10]. The consequent increase in the size L_c of the islands and reduction in charging energy provides a natural explanation for the shorter period and smaller source-drain bias gap in figure 6.3.

While the behaviour at MD fits within the original framework developed for potential/edge disorder-induced QDs in exfoliated monolayer GNRs [21], at LD the interpretation is more complicated due to presence of a vertical-field induced bandgap. It has been shown previously that the combined influence of charge transfer from a polymer and the buffer layer can open a gap of $\Delta_{BL} \approx 30meV$ in bilayer patches on SiC [42]. As implied already by the absence of peaks in the conductance at LD, resonant transmission through states at the band edges would be avoided as $s < \Delta_{BL}$. The magnetotransport at LD is shown in figure 6.4 proving that the source-drain gap does not shrink between 0 T and 8 T (see figure 6.4(a)), and changes non-monotonically as a function of increasing magnetic field (see figure 6.4(b)). When V_{SD} > 2 mV, the shard-like features do appear as a function of V_{SD}, indicating that transport still proceeds via localized states above this energy, but the presence of such states complicates unambiguous extraction of Δ_{BL} from bias spectroscopy.

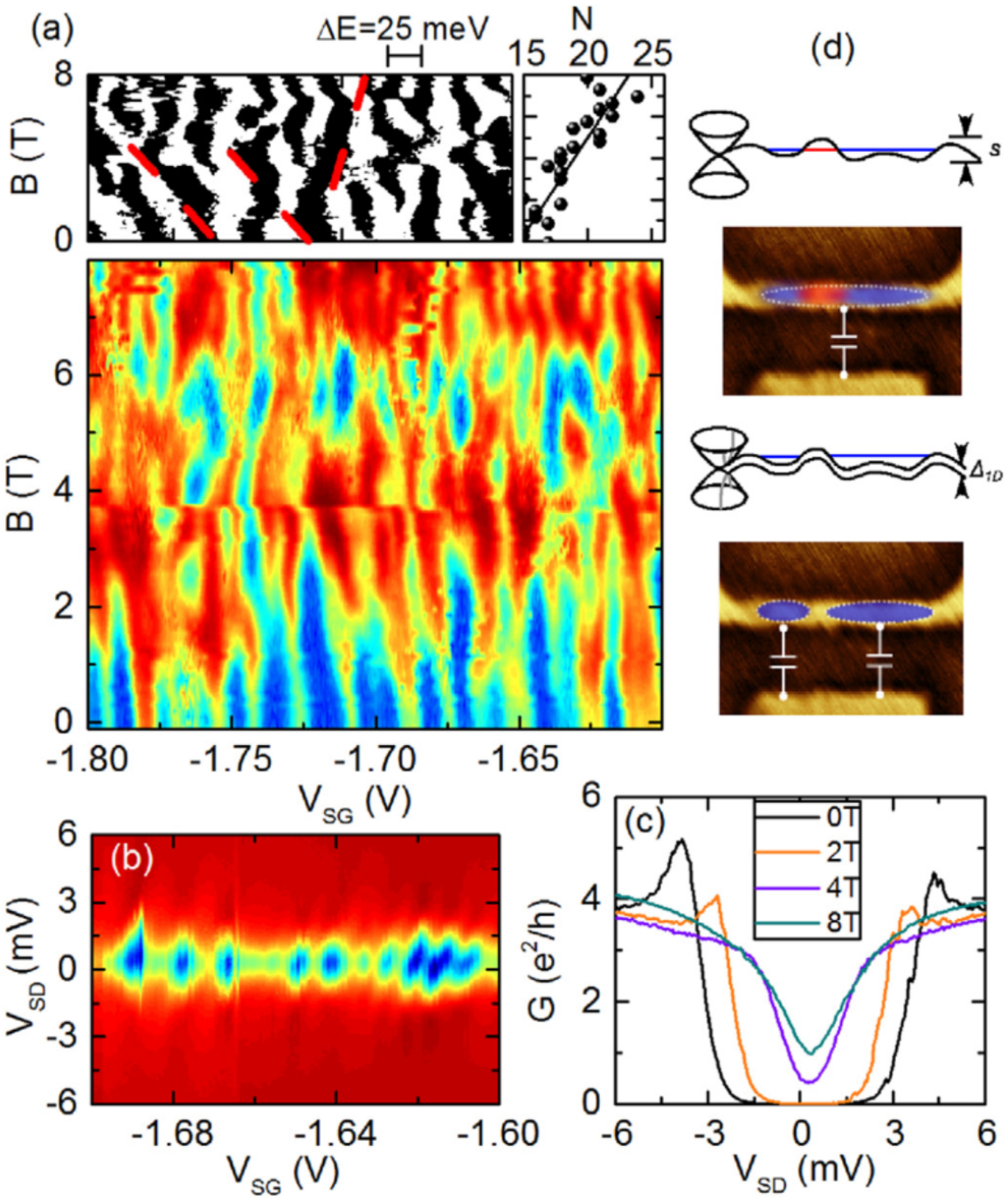

Fig. 6.3 (a) Conductance as a function of V_{SG} and B at MD (main panel). Raw data differentiated and segmented such that positive and negative slopes are white and black, respectively. Trajectories of peaks are highlighted by red lines (upper left). The number of peaks as a function of magnetic field is shown in upper right panel. (b) Conductance as a function of V_{SD} and V_{SG} at $8T$. (c) Plot of G as a function averaged across side gate voltage at 0, 2, 4 and 8 T. (d) Schematic diagrams showing a possible realization of the disorder potential and quantum confinement gap along the GNR at B = 0 T (lower) and B = 8 T (upper). (T = 1.4 K)

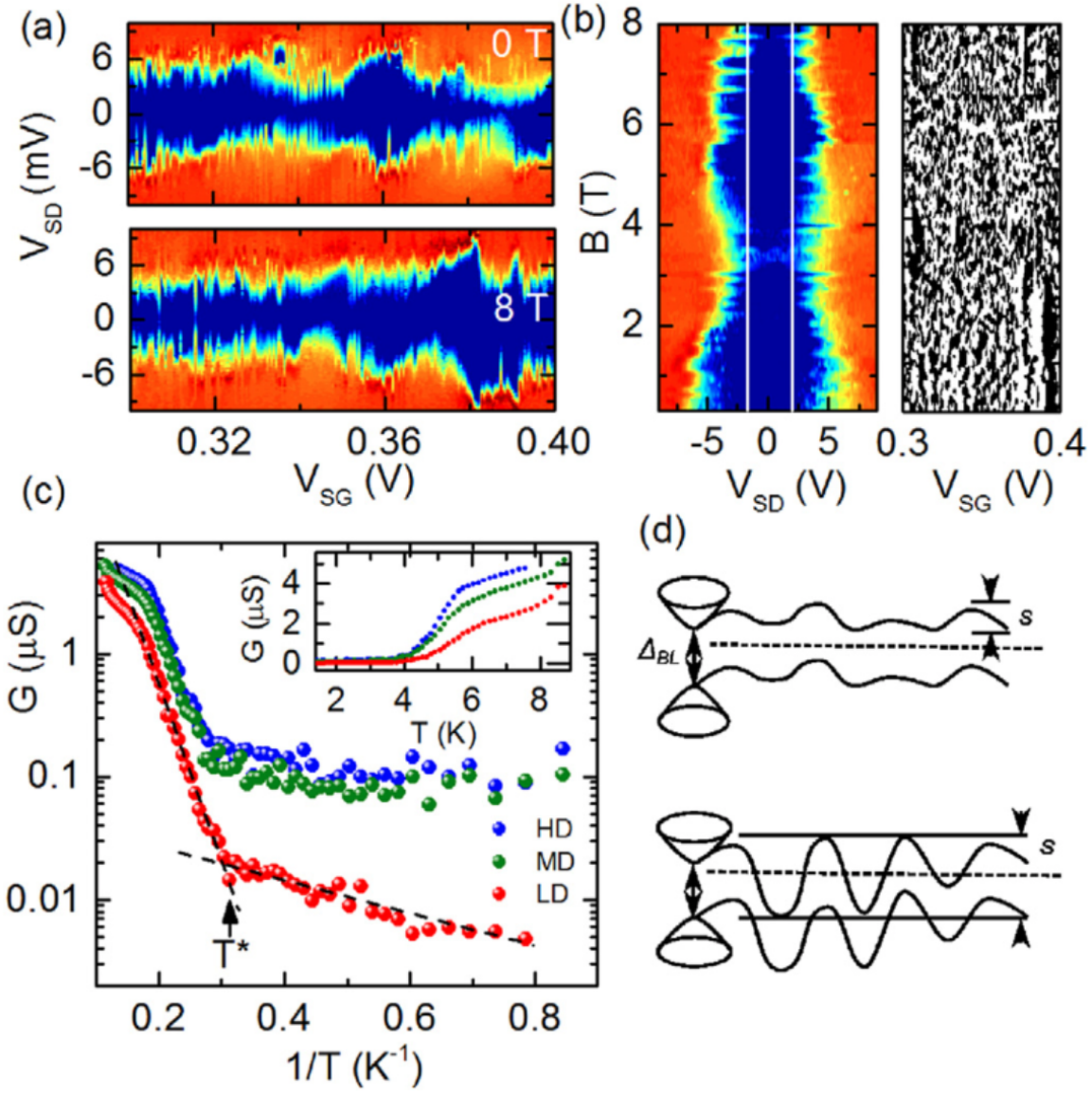

Fig. 6.4 (a) G as a function of V_{SD} and V_{SG} at 0 T and 8 T at LD. (b) Left: gap in $G(V_{SD})$ measured at fixed V_{SG} as a function of B. Right: side-gate sweeps as a function of magnetic field, differentiated and segmented in the same way as figure 6.3(a). (c) Dependence of the conductance as a function of inverse temperature for each doping level. Inset: Conductance as a function of temperature. (d) Schematic energy as a function of position along the GNR for the case $s < \Delta_{BL}$ (upper), where transport occurs via variable-range hopping, and for thermal activation above T^* if $s > \Delta_{BL}$ (lower).

The temperature dependence of the conductance is also investigated to probe gap formation in GNRs. Figure 6.4(c) presents the dependence of the conductance as a function of inverse temperature for the three different doping levels. In theory, at high temperature, thermal activation of electrons is described by

$$G \propto exp(E_a/2k_BT), \tag{6.2}$$

either between adjacent localized states ($E_a = E_c$) or via extended states above a uniformly gapped region ($E_a = \Delta_{BL}$ or Δ_{1D}). However at low temperature, variable-range hopping (VRH) leads to

$$G \propto exp(-(T_0/T)^{\gamma}), \tag{6.3}$$

where T_0 is the characteristic temperature for hopping, and $\gamma = 1/2$ for both 1D Mott and Efros-Shlovski VRH [168]. By fitting the data, we do observe a very clear change in behaviour at $T^* \approx 3.2$ K for LD and 3.6 K for MD and HD, with $E_a \approx 6$ meV for $T > T^*$ (see figure 6.4(c)). Figure 6.4(d) illustrates the energy as a function of position along the GNR for the case $s < \Delta_{BL}$ (upper), where transport occurs via variable-range hopping, and for thermal activation above T^* if $s > \Delta_{BL}$ (lower).

VRH is expected to dominate when the thermal energy drops to roughly $1/10$ of the activation energy of an individual island and our measured $E_a/kT^* \approx 5$ is in reasonable agreement. The similarity in the values of E_a suggests that it is set by the quantum confinement gap Δ_{1D}, rather than by Δ_{BL}, which is larger close to the Dirac Point.

6.1.3 Conclusion

In summary, we have studied electron transport in a SiC epitaxial bilayer graphene nanoribbon as a function of doping, magnetic field, and temperature. Away from charge neutrality, transport is only weakly modulated by changes in carrier concentration induced by a local side-gate. At medium doping close to charge neutrality, electron transport resembles that in exfoliated graphene nanoribbons and is well described by tunnelling of single electrons through a network of Coulomb-blockaded islands, with multiple quantum dots forming in series due to the interplay between disorder and quantum confinement. Under the influence of an external magnetic field, Coulomb blockade resonances fluctuate around an average energy and the gap shrinks as a function of magnetic field. At charge neutrality, however, conduction is less insensitive to external magnetic fields. Conduction resonances are absent and transport is suppressed even at high magnetic field, consistent with a bandgap induced by broken layer symmetry.

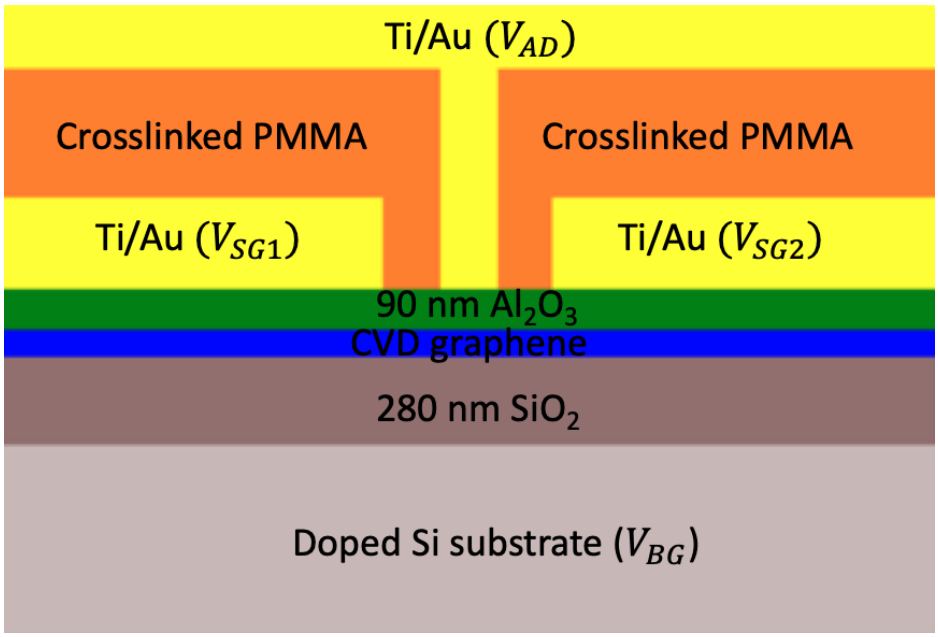

Fig. 6.5 Schematic diagram of side view layer structure of the CVD graphene antidot device.

6.2 Graphene Quantum Hall Antidots

Due to its exceptional electronic properties, graphene is an ideal material to develop single-electron devices such as spin qubits and quantized charge pumps. The key advantage with graphene is that tunnel barriers have a low capacitance, which makes it possible to transfer charge quickly and pump high currents at gigahertz frequency [45]. However, one drawback with etched dots is that spin-active edges and potential disorder lead to confined states (this has been discussed in the SiC GNRs) and short spin coherence times. Moreover, it is not possible to define quantum dots in monolayer graphene with electric fields because of the Dirac spectrum. In a strong perpendicular magnetic field, however, a Landau gap opens in the spectrum and it should be possible to confine charge in "antidots" with edges using electrostatic fields. Antidots form at potential hills and are well studied in III-V 2DEGs [63]. Using split gates it is possible to bring quantum Hall edge states into tunnel contact and to detect Coulomb blockade of localized states encircling the antidot. This section will discuss this type of graphene antidots (GADs) in quantum Hall regime.

6.2.1 Device Fabrication and Measurement

To scale up single-electron devices in graphene, we fabricate GADs devices based on CVD graphene Hall bars, which are patterned by optical lithography and have been discussed in chapter 4. With our fabrication method, each 10 mm^2 chip can produce 36 devices. The layer

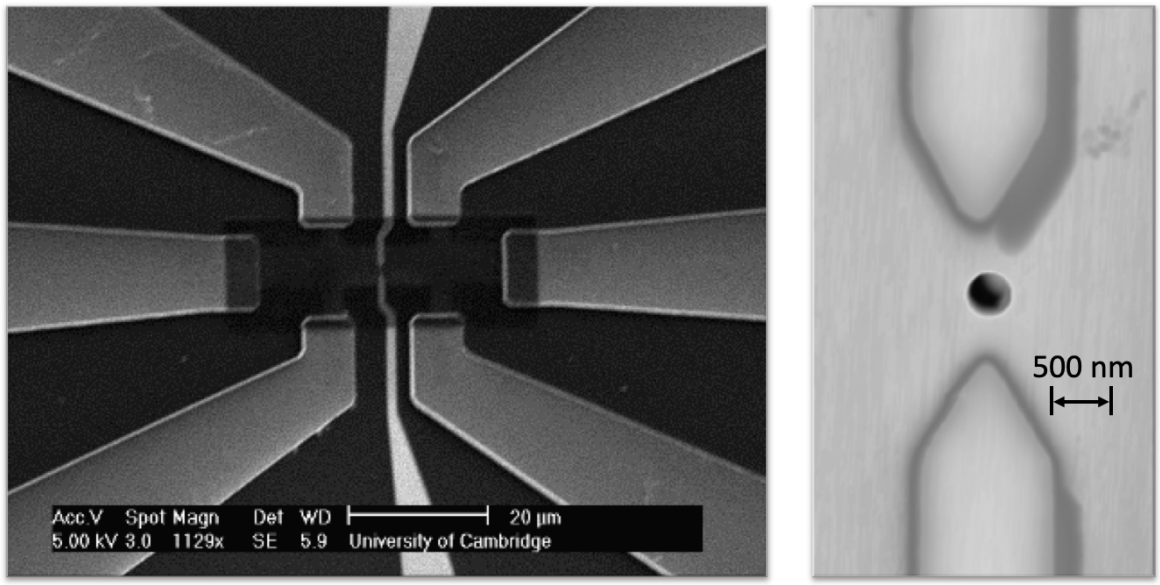

(a)

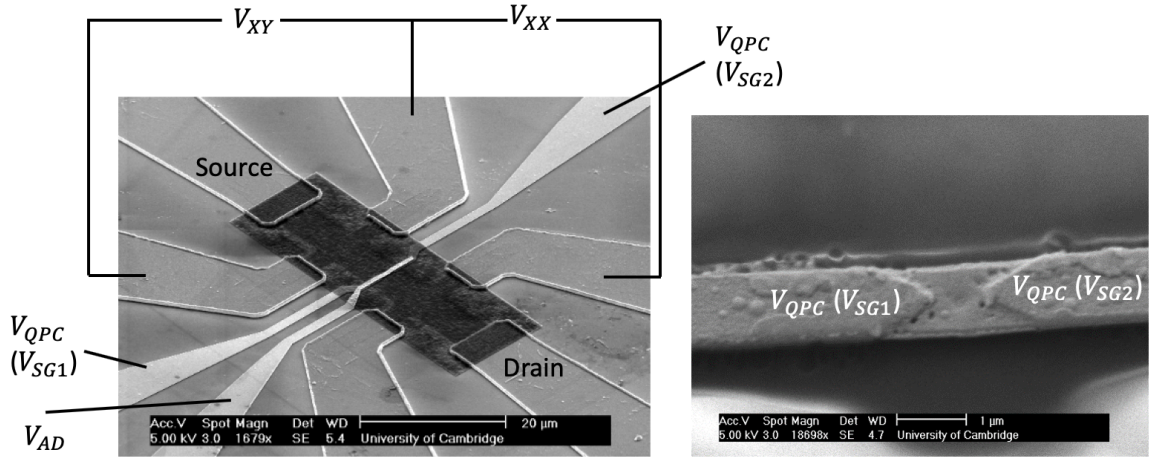

(b)

Fig. 6.6 (a) Left: SEM picture of a CVD graphene antidot device before top antidot gate V_{AD} deposition, with six contacts connected and a pair of split gates deposited in the centre. The dark rectangular area is crosslinked PMMA as the further antidot gate dielectric. Right: AFM picture of zoom-in of the central antidot hole region between a pair of split gates. (b) Left: SEM picture of a completed CVD graphene antidot device, with four-terminal measurement setup. Right: SEM picture of zoom-in of the central antidot region between a pair of split gates.

structure of the device is illustrated in 6.5. The CVD graphene is transferred onto the Si/SiO_2 substrate directly, after which we fabricate a Hall bar and encapsulate with 90 nm alumina dielectric layer by ALD [4]. In the middle of the Hall bar we define a pair of split gates with 1 μm width and around 600 nm separation by EBL. In order to deposit the antidot gate metal inside the QPC, another layer of crosslinked PMMA with thickness around 150 nm is used as the antidot gate dielectric with a small hole (diameter around 300 nm) patterned in the centre, which is shown in the scanning electron microscopy (SEM) picture of figure 6.2. Finally we put on the antidot gate metal through the hole.

The SEM picture of completed device is presented in figure 6.2, with a simple four-terminal measurement circuit. Electron transport measurements on GADs devices are performed using a four-terminal method with magnetic fields up to B = 8 T and temperatures down to T = 50 mK in the MX400 dilution refrigerator of the SP group. A 100 nA constant current is supplied by a Lock-in amplifier, which outputs 1 V voltage through a 10 MΩ resistor. V_{xx} and V_{xy} are recorded by another two Lock-ins. Back-gate V_{BG}, top antidot gate V_{AD}, and a pair of split gates V_{SG1} and V_{SG2} are applied by four SIM DC voltage sources.

6.2.2 Results and Discussion

We first characterize the device by measuring the resistance as a function of back-gate V_{BG} and a perpendicular magnetic field B, leading to a Landau fan diagram shown in figure 6.7(a), together with line-cuts of the back-gate sweeps at B = 0 T (figure 6.7(b)) and B = 8 T (figure 6.7(c)). Back-gate V_{BG} sweep at B = 0 T suggests that the sample is slightly n-type doped and the position of the Dirac point is $V_{Dirac} \approx$ -4 V. The mobility can be calculated $\mu \approx 2700$ $cm^2V^{-1}s^{-1}$ by the equation $\mu = |d\sigma/dV_{BG}|_{max}/C_G$, where C_G is the gate capacitance. When the perpendicular magnetic field is applied, Landau quantization forms with $E \propto \pm\sqrt{NB}$ $(N = 0, 1, 2, ...)$, where N is Landau level index [201]. This, in turn, gives rise to half-integer quantization of Hall conductance with filling factor $\nu = 4(N + 1/2)$. When the magnetic field is increasing from 0 T to 8 T, the Landau gaps become broader and broader. And when B reaches 8 T, the two Landau gaps closest to the charge neutrality point appear at V_{BG} = -0.6 V and V_{BG} = -11.5 V, corresponding to filling factor $\nu = 2$ and $\nu = -2$, respectively (see figure 6.7, the two dips closest to the Dirac point). Inside these Landau gaps, ballistic transport happens along the edge of the Hall bar and there is no electron states in the bulk. The quantum Hall antidots work in these edge states of quantum Hall regime.

As monolayer graphene is gapless, top-gates, such as quantum point contact (QPC) split gates applied on the Hall bar device can lead to the formation of a gate-controllable p-n junction [137]. Figure 6.8 exhibits a graphene Hall bar device with two types of top gates on it used for testing how top gates pinch off the Hall bar channel. This device is

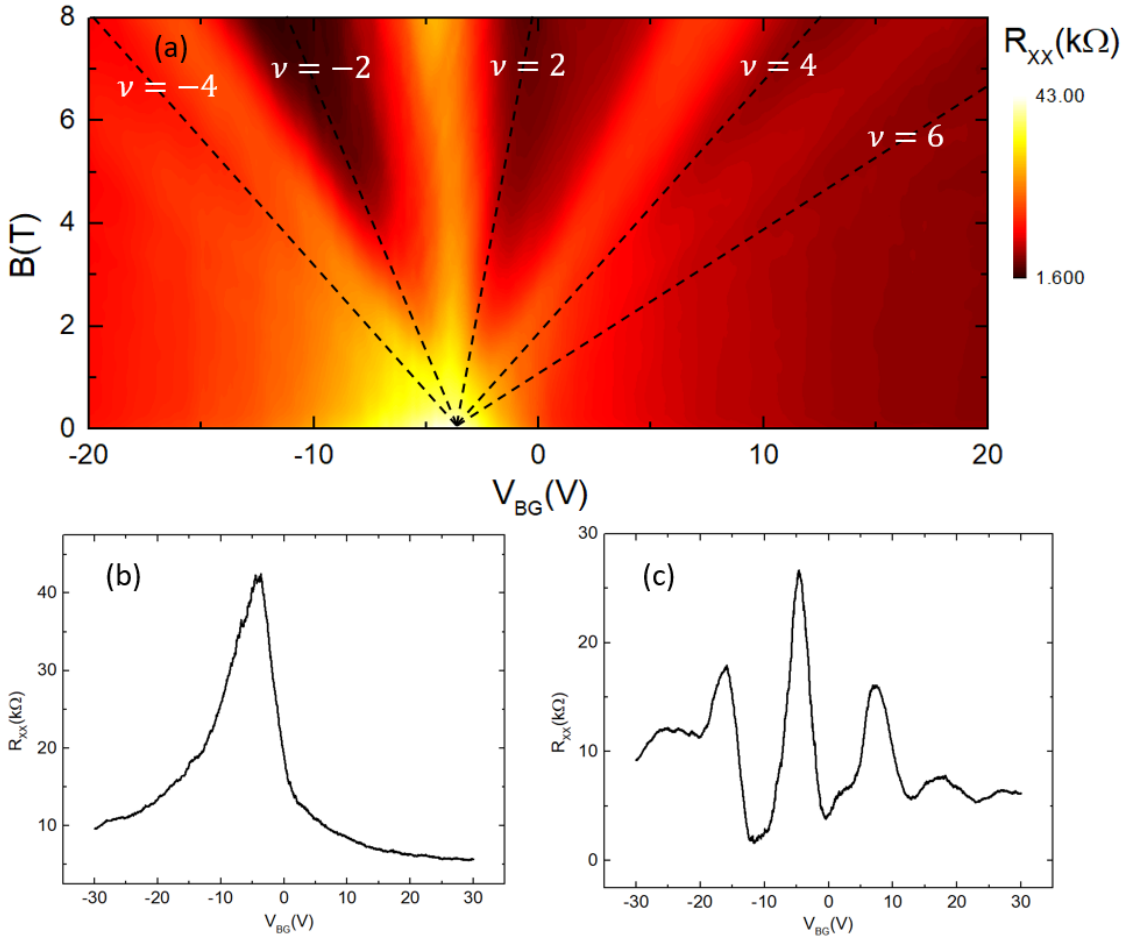

Fig. 6.7 (a) Landau fan diagram of a measured graphene Hall bar device, with black dashed lines indicating the regions at different filling factors. (b)(c) Linecuts of the back-gate sweeps at B = 0 T and B = 8 T, respectively. (T = 50 mK)

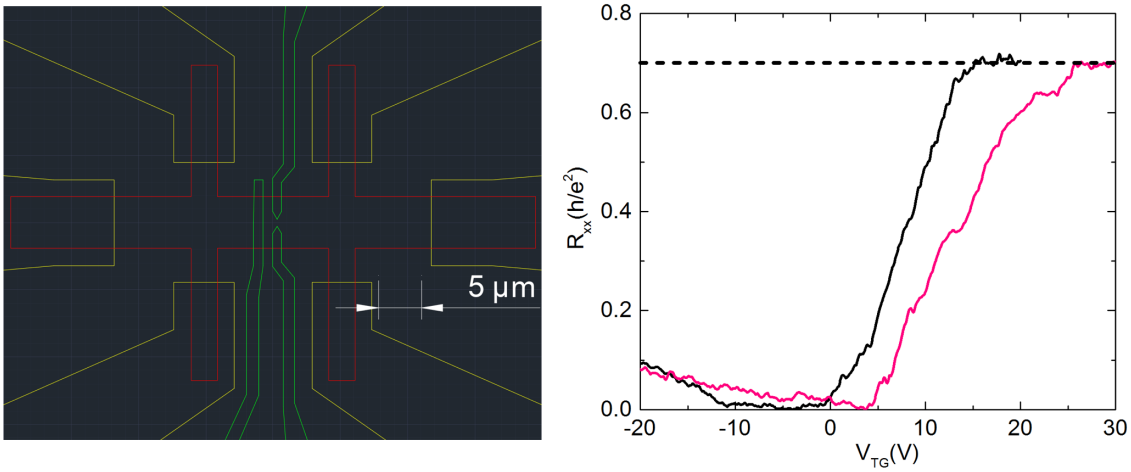

Fig. 6.8 Left: AutoCAD design of a graphene Hall bar device with two types of top gates (green layer). Right: Longitudinal resistance as a function of these two types top gates when the device is at quantum Hall edge states, with black curve showing the bar gate sweep and red curve the QPC split gates sweep (B = 6 T, T = 1.4 K).

fabricated in the same batch of the antidots device shown in figure 6.6 and investigated under a perpendicular magnetic field to form ballistic edge channels. Two types of top gates are studied separately, which are the top bar gate going cross the whole channel and a pair of QPC split gates. Both gates are shown in the green layer of the AutoCAD design of the left of figure 6.8. The right of figure 6.8 presents the longitudinal resistance R_{xx} as a function of these two types top gates when the device has quantum Hall edge states, with the black curve showing the bar gate sweep and the red curve the QPC split gates sweep. We can see that when the bar gate is over 15 V and QPC split gates over 25 V, a n-p-n junction forms along the Hall bar and the channel is depleted with a longitudinal resistance $R_{xx} \approx 0.7h/e^2$, which is different from that observed in exfoliated graphene QPC induced n-p-n junction reported in the reference [137], where they observed a $0.5h/e^2$ plateau with an explanation of chaotic mixing of edge channels. According to the Landauer–Buttiker formula [26], the coefficient 0.7 is the combination result of numbers of transmitted and reflected edge states.

We then focus back on our GADs device at a dilution fridge temperature 45 mK with B = 8 T. The back-gate is set at V_{BG} = -0.6 V, where the device is in the quantum Hall edge states regime and p-type doped with filling factor $\nu = 2$, and both QPC split gates V_{QPC} and antidot gate V_{AD} are applied negatively to the device to tune the channel conductivity. Figure 6.9 exhibits a mapping of longitudinal resistance as a function of both V_{QPC} and V_{AD}. This 2D plot consists of three regions, denoted with 1, 2, 3 in figure 6.9. In region 1, V_{QPC} and V_{AD} are not strong enough to interact with each other, therefore the channel is totally open without junctions being formed and the charge carrier can transport in a ballistic manner through it.

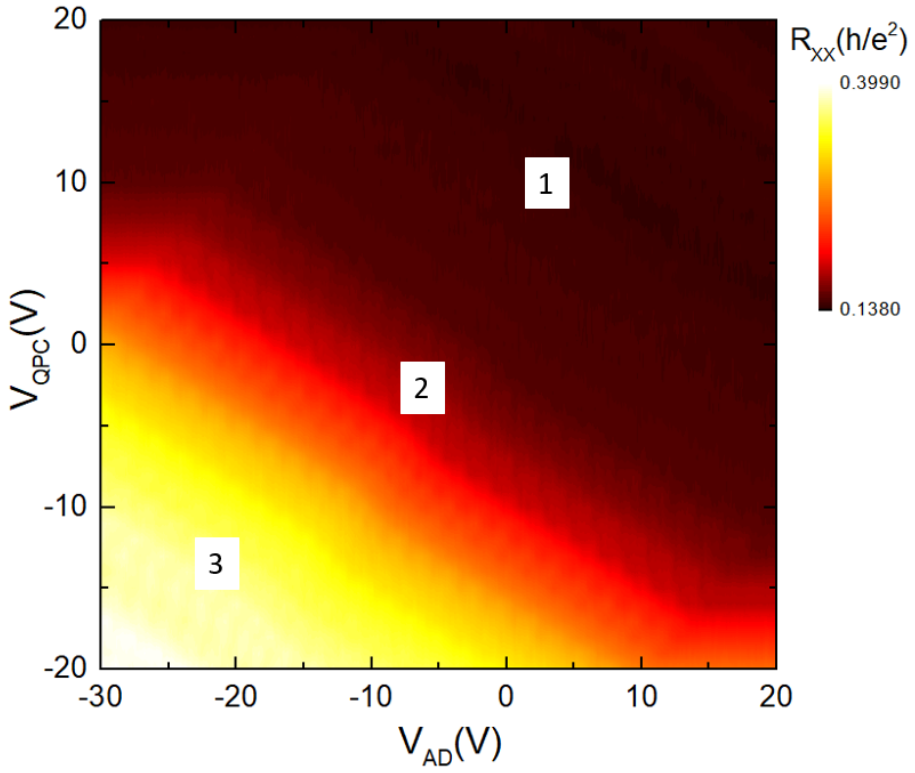

Fig. 6.9 2D mapping of longitudinal resistance as a function of both V_{QPC} and V_{AD} (B = 8T, T = 45 mK).

When V_{QPC} and V_{AD} increase to some value, interaction occurs between the antidot localised states and the extended quantum Hall edge states, which is the region 2 in 6.9. And in region 3, both V_{QPC} and V_{AD} are negative enough to reflect the edge state completely by forming a p-n-p junction along the Hall bar. Among these three regions, region 2 is of the most interest, as V_{AD} plays a role and the interaction between antidot localised states and the extended quantum Hall edge states allows us to better understand single-electron tunnelling effect in graphene.

Magnetotransport measurements are performed in region 2 to probe single-electron behaviours in the GADs device. Figure 6.10(a) shows a magnetotransport spectroscope against V_{AD}. Here, we also take the derivative of longitudinal resistance ΔR_{xx} with respect to V_{AD} in order to see more clearly how R_{xx} changes in a periodic manner. Aharonov-Bohm like oscillations can be observed and we get the the gradient of the slope $\Delta V_{AD}/\Delta B \sim 8$. In order to get insight into the period of V_{AD}, we plotted the line sweeps in 6.10(b), suggesting the period of antidot gate voltage in the Aharonov-Bohm oscillations is $\Delta V_{AD} \sim 0.7V$. Combining the gradient of the slope $\Delta V_{AD}/\Delta B \sim 8$, we can thus obtain the period of magnetic field in the Aharonov-Bohm oscillations $\Delta B \sim 0.0875T$. According to the following equation,

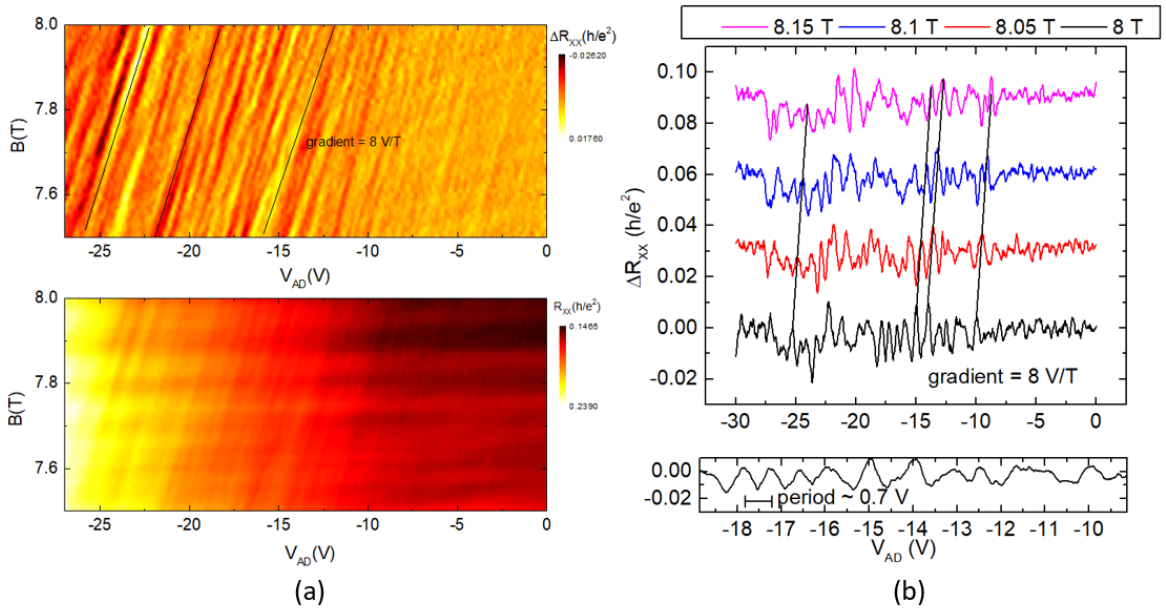

Fig. 6.10 (a) Magnetotransport spectroscope of both longitudinal resistance R_{xx} and its derivative ΔR_{xx} with respect to V_{AD} showing Aharonov-Bohm like oscillations. (b) Processed line plots suggesting the period of antidot gate voltage $\Delta V_{AD} \sim 0.7$ V.

$$\Delta B = \frac{1}{\nu_{AD}} \frac{h}{e\pi r_{AD}^2}, \tag{6.4}$$

where the the filling factor $\nu_{AD} = 2$, we can therefore calculate the radius of the real defined antidot $r_{AD} \approx 90$ nm, which is much smaller than the designed size r = 150 nm. This calculated result suggests that the antidot is not actually defined as designed. One possible reason is that the antidot top-gate metal may not be evaporated and deposited fully through the antidot hole. Another possibility might be that the antidot is induced by potential disorder instead due to impurities of the graphene material. This argument can be supported by the result in figure 6.7(c), where there is not a zero in the R_{xx} implying the mobility is not high enough or there is too much variation in doping over the sample. This will change the chances of observing Aharonov-Bohm oscillations in antidot devices by providing other back scattering mechanisms. In order to solve this problem, high quality graphene material such as hBN-graphene-hBN heterostructure, is needed and fabrication process needs to be improved to make the antidot gate contact better. However, due to the limited time of my PhD course, no further works are done to improve the performance of GADs devices.

We also investigated lever arm of different gates i.e. back-gate V_{BG}, QPC split gates V_{QPC} and antidot top-gate V_{AD} in the GADs device discussed above. Figure 6.11 demonstrates the

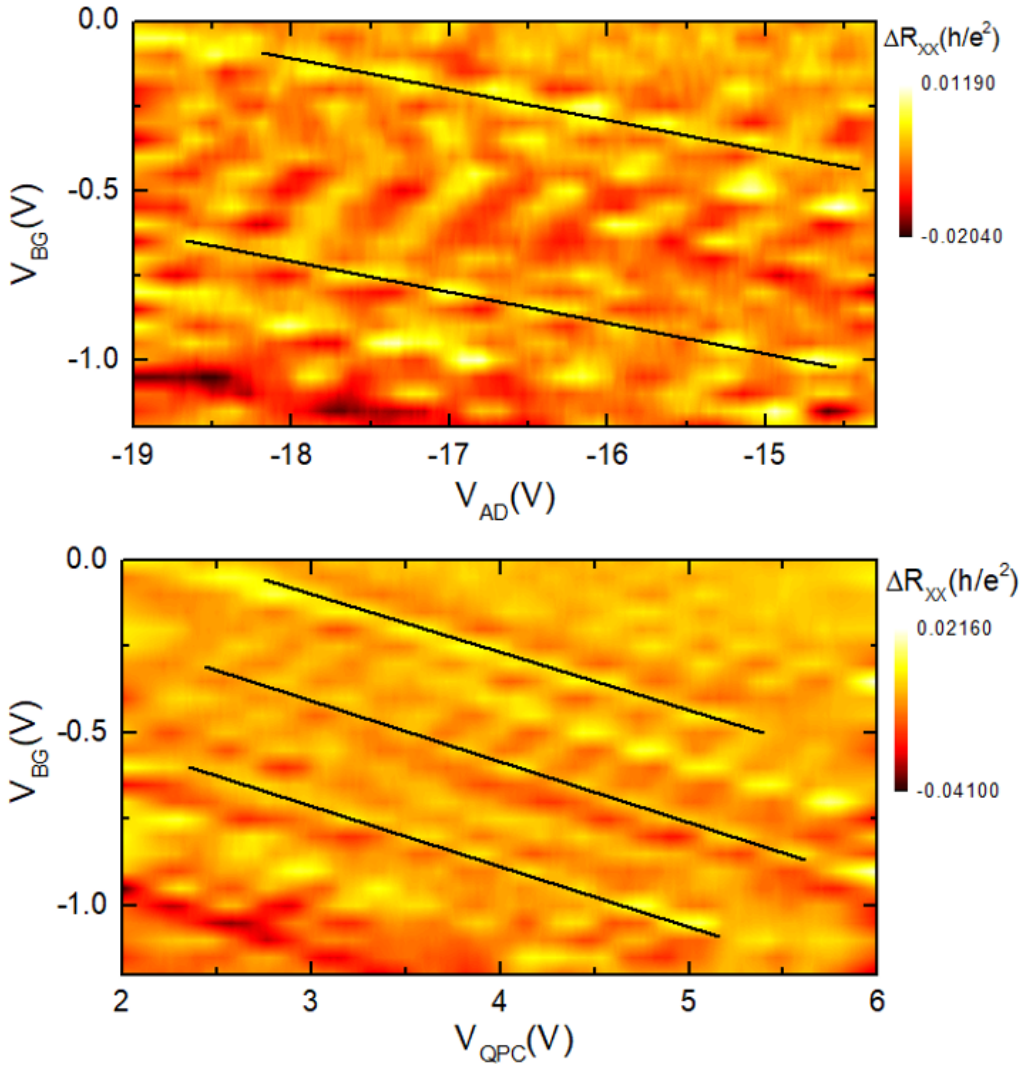

Fig. 6.11 Derivative of longitudinal resistance showing lever arms between different gates, i.e. back-gate V_{BG}, QPC split gates V_{QPC} and antidot top-gate V_{AD} in the GADs device.

Table 6.1 Gate parameters of the GADs device

Gate type	$A(\mu m^2)$	d(nm)	ε_r
V_{BG}	96	280	3.9
V_{QPC}	4.4	90	$9.3 \sim 11.5$
V_{AD}	0.07	90	$9.3 \sim 11.5$

comparison of the lever arms between V_{BG} and V_{QPC}, and V_{BG} and V_{AD}. We can thus obtain the following relationship:

$$V_{BG} : V_{QPC} : V_{AD} \approx 1 : 5 : 10. \tag{6.5}$$

Therefore, the capacitance relationship of these three gates can also be obtained:

$$C_{BG} : C_{QPC} : C_{AD} \approx 10 : 2 : 1. \tag{6.6}$$

However, from the geometry of the designed device, we can calculate the gate capacitance relationship using the equation $C = \varepsilon_r \varepsilon_0 A/d$ and the parameters from table 6.1:

$$C_{BG} : C_{QPC} : C_{AD} \approx 160 : 60 : 1. \tag{6.7}$$

The antidot gate capacitance is much bigger than that calculated from the designed geometry, which also suggests that the antidot is not well-defined. These gate oscillations due to Coulomb blockade are also the signatures of quantum dot formation in this system, suggesting that single-electron tunnelling occurs between the quantum Hall edge states and localized states encircling the antidot inside the pair of QPC split gates.

6.2.3 Conclusions and Future Work

Despite its unique properties, it is not possible to define quantum dots in monolayer graphene with electric fields because of the Dirac spectrum, and etched quantum dots in graphene shows confined states and short spin coherence times due to spin-active edges and potential disorder. Quantum Hall antidots stand out as an alternative way to create quantum dots by opening Landau gaps in graphene. We fabricated and measured the GADs devices in a perpendicular magnetic field. Although we routinely see the quantum Hall effect, Aharonov-Bohm effect and Coulomb blockade effect, signatures of the effective antidots have so far proved elusive, probably due to the disorder-broadening of the Landau levels. Calculations of both the quantum antidots size from the Aharonov-Bohm oscillations and quantum capacitance of the

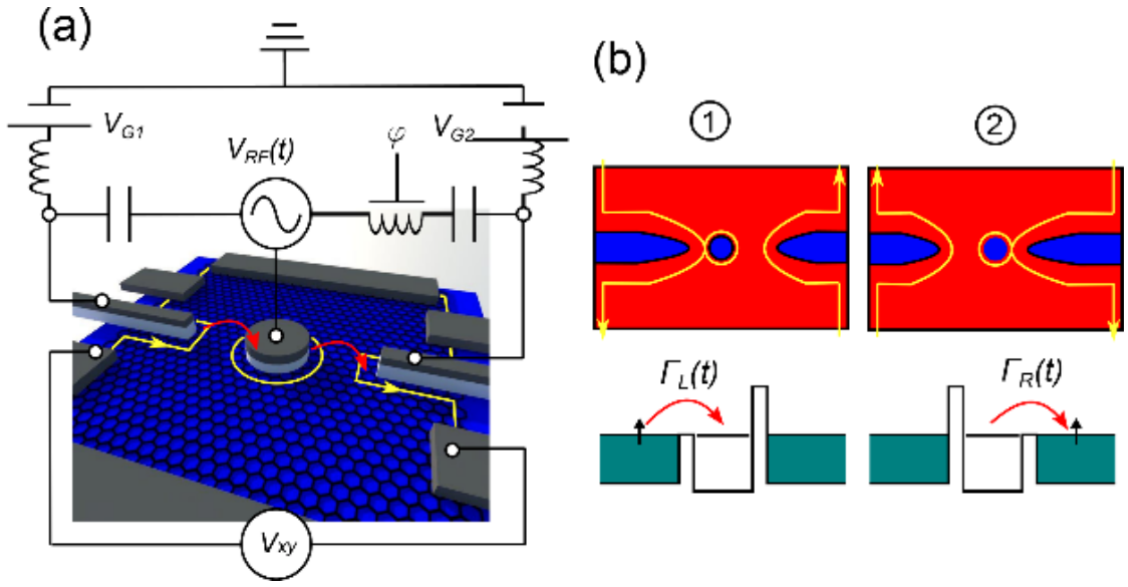

Fig. 6.12 (a) Circuit used to pump single electrons. Radio-frequency signals are applied to QPC split gates. (b) Illustration of the two main stages of pumping where individual charges are transferred. The QPC split gates modulate the separation between the edge states and the antidot tunnel rate.

antidot gate prove that the antidot in our GADs device is not well-defined and is probably defined by disorder in the system under the antidot.

For the future work in terms of GADs, high quality graphene material such as hBN-encapsulated graphene, is needed due to its clean surface and low potential disorder. Moreover, tunnel barriers in graphene have a low capacitance, which makes it possible to transfer charge quickly and pump high currents at radio-frequency. Therefore, quantum antidots provide a new idea for the realization of a fast and accurate quantized charge pumping technology in graphene. Figure 6.12 demonstrates a proposal for realizing charge pumping with GADs by applying radio-frequency signals to the QPC split gates. When driven by radio frequency electrodes, the coupling between edge states and the antidote localized states is adjusted and electrons can tunnel through the barriers between them one by one, creating a single electron pump. The QPC split gates modulate the separation between the edge states and the antidot tunnel rate. Compared with the charge pumping in etched double quantum dots [45], GADs is more suitable for the realization of fast and accurate quantized charge pumping due to the lack of the influence of edge disorder, and thus enables more accurate redefinition of Ampere in the single electron aspect, which could provide a powerful tool in the research of quantum metrology.

Chapter 7

Developing Radio-frequency Reflectometry in Quantum Dots

7.1 Introduction

The experiments discussed in the last three chapters were performed with conventional low frequency cryogenic transport measurements. However, the limited bandwidth caused by the high wiring capacitance and large sample resistance, as well as the large 1/f noise due to the motion of background charges, constrict the measurement sensitivity and accuracy. In order to overcome this obstacle, this chapter presents a radio-frequency (RF) reflectometry technique and applies this technique to two types of quantum dot systems, GaAs quantum antidots and graphene double quantum dots (DQDs). Using radio-frequency reflectometry we probe single-electron tunnelling behaviour in GaAs ADs and graphene DQDs with high sensitivity and at millikelvin temperatures.

The experiments in this chapter were carried out in a dilution refrigerator named MX400 in the Semiconductor Physics group at the Cavendish Laboratory. The high frequency wiring is shown in figure 3.4 adapted from Karl Petersson's PhD thesis. The RF reflectometry technique has been introduced in chapter 3. This chapter will discuss the development of the potential applications of RF reflectometry techniques in GaAs ADs and graphene DQDs, corresponding to capacitive and resistive couplings to the devices, respectively.

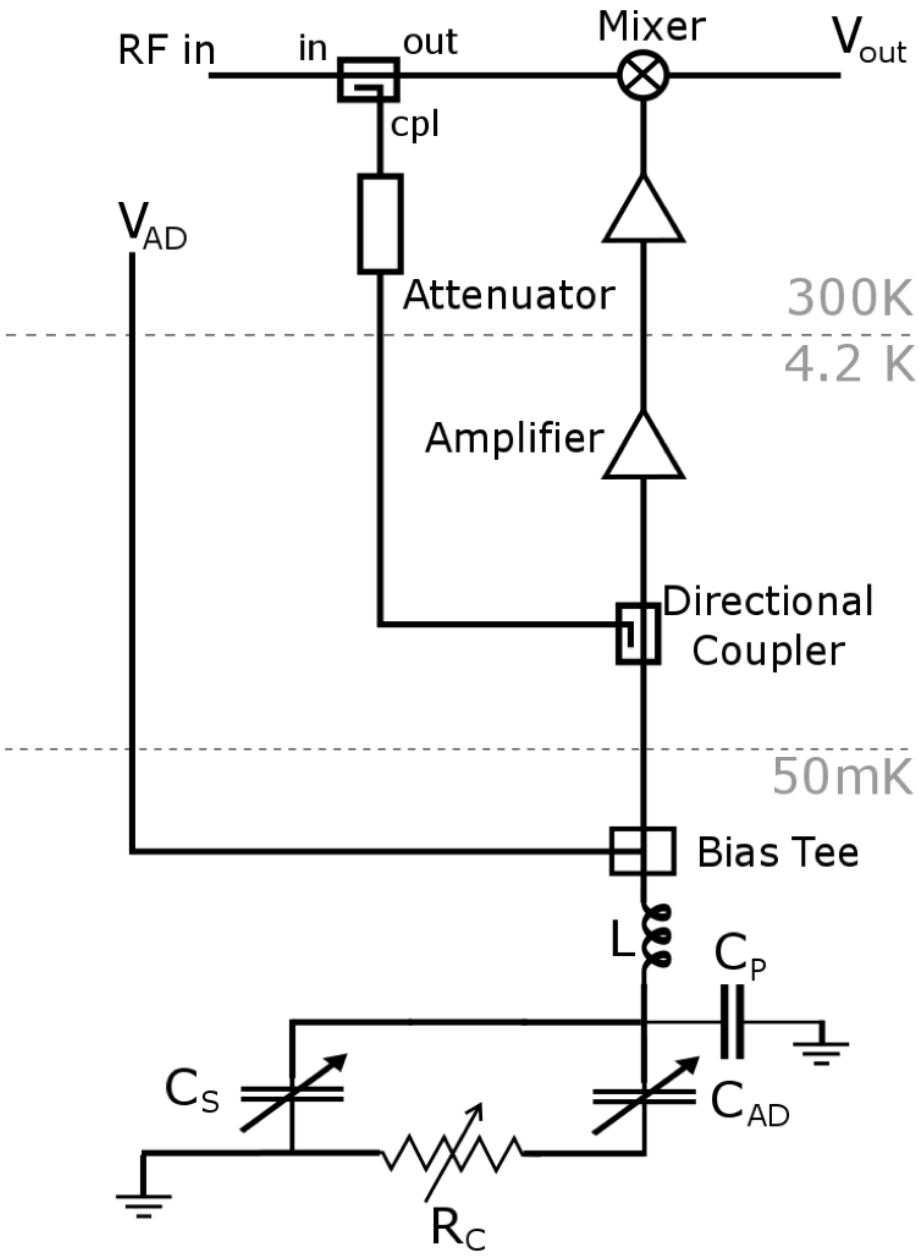

Fig. 7.1 Schematic of the radio-frequency reflectometry circuit.

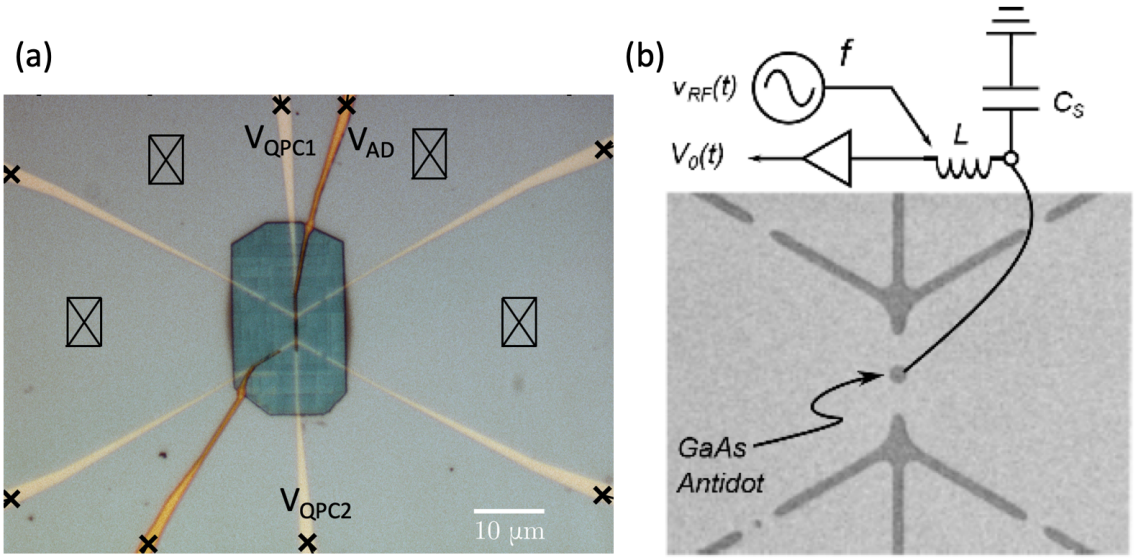

Fig. 7.2 (a) Optical microscope photograph of the GaAs antidots device measured in this chapter.(b) Radio-frequency voltage coupled to a tank circuit comprising an inductor and capacitor in series with the antidot. The reflected voltage is sensitive to charge transitions in the antidot and will allow state readout. Modified from Lee Bassett's PhD thesis.

7.2 GaAs Quantum Antidots

7.2.1 Device Description and Measurement Setup

The GaAs ADs samples measured in this chapter were fabricated by Lee Bassett, another previous PhD student in the SP group, who has investigated electron-electron interaction in GaAs ADs at low frequency. Figure 7.2(a) shows an optical microscope photograph of a measured antidot sample in this chapter. The sample was fabricated from a GaAs/AlGaAs quantum well structure containing a 2DEG situated 300 nm below the surface with a significantly reduced carrier density of $n_e = 1.1 \times 10^{11} cm^{-2}$. On top of the substrate, metal gates were patterned by EBL. A second metal layer was patterned on top of 350 nm of cross-linked PMMA in order to contact the central antidot gate so that voltages (V_{AD}, V_{QPC1}, and V_{QPC2}) could be applied independently. A negative voltage on the antidot gate creates an antidot by depleting the 2DEG underneath. The two split gates, which are used to bring the extended edge states close to the antidot, form parallel one-dimensional constrictions. The scanning electron micrograph photograph of the split gates and the antidot are shown in figure 7.2(b).

The measurements were performed using an RF reflectometry technique in the dilution refrigerator MX400 mentioned above with temperatures down to 40 mK, and magnetic fields up to 8 T. The RF tank circuit is applied capacitively to the antidot gate is shown in

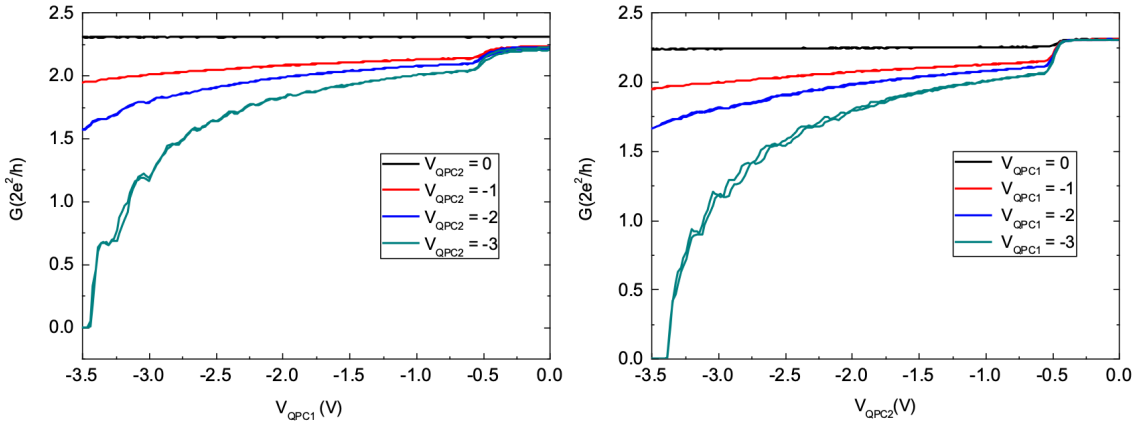

Fig. 7.3 The pinch-off effect of each single gate of the QPC split gates with the other gate voltage at a set value.

figure 7.2(b) as well. As introduced in chapter 3, the RF response is sensitive to the device impedance change, exhibiting resonant frequency change and corresponding phase shift. The idea of how the RF reflectometry works on the GaAs andidot can be understood from the schematic circuit in figure 7.1. The RF signal, which is created by a ultra high frequency lock-in (UHFLI) is attenuated at room temperature and transmitted to the sample via a directional coupler at 4.2 K. The RF signal then meets the DC signal via a Bias Tee at the mixing chamber, whose temperature is below 50 mK, before entering into the LC tank circuit and reaching the device. The reflected signal is then sent back to the cryogenic amplifier which is thermally anchored at 4.2 K. The signal is amplified again at room temperature before being demodulated and recorded by the UHFLI. Therefore, the reflected voltage (i.e. amplitude and phase) is sensitive to charge transitions in the antidot and will allow state readout.

7.2.2 Results and Discussion

We start with two-terminal low frequency transport measurements to test the pinch-off status of the one-dimensional channel created by the QPC split gates. The pinch-off effect of each single gate of the QPC split gates with the other gate voltage at a set value is demonstrated in figure 7.3. The channel can only be pinched off with both split gates working and the more negative the gate voltage that is applied, the further the pinch-off goes. Figure 7.4(a) shows the two-terminal conductance G of the one-dimensional channel as a function of both QPC split gates voltage V_{QPC}. The 2DEG underneath the gates starts to be depleted from $\sim$ -0.5 V and when $V_{QPC} < 2$ V, quantized conductance plateaus appear. When V_{QPC} reaches $\sim$ -3.25

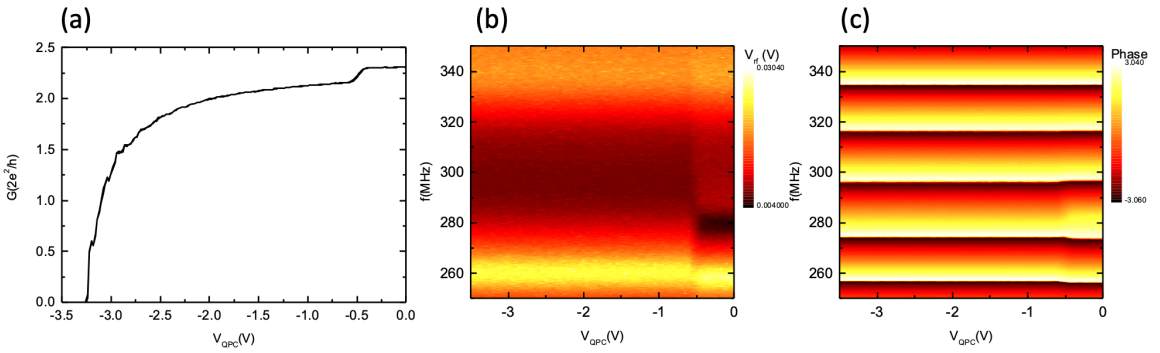

Fig. 7.4 (a) Two terminal conductance G of the one dimensional channel as a function of both QPC split gates voltage V_{QPC}. Measured reflected RF amplitude (b) and the corresponding phase change (c) as a function of V_{QPC}.

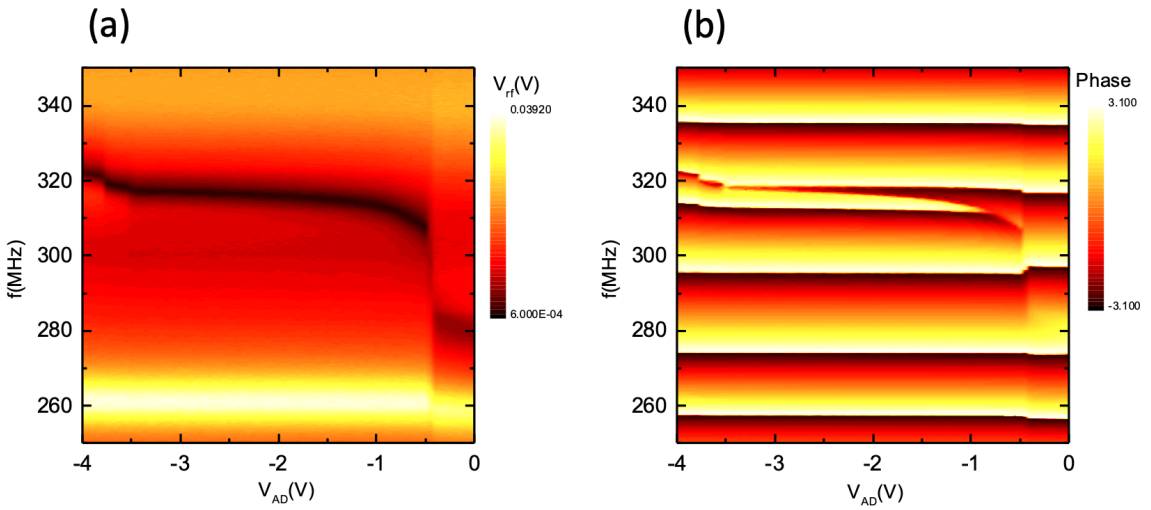

Fig. 7.5 Measured reflected RF amplitude (a) and the corresponding phase change (b) as a function of V_{AD}.

V, G = 0, the channel is completely pinched off. In the meanwhile, we also measured the reflected RF amplitude and the corresponding phase change as shown in 7.4(b) and 7.4(c). An obvious resonant frequency change from $\sim$ 280 MHz to $\sim$ 300 MHz occurs when $V_{QPC} \sim$ -0.5 V starts to deplete the 2DEG. The change in the carrier concentration of the depleted 2DEG leads to the change of the capacitance between the antidot gate and the 2DEG. And according to the equation $f_0 = 1/2\pi\sqrt{LC_s}$, the changed capacitance results in the resonant frequency shift.

Then we investigate the RF response when the antidot gate voltage V_{AD} is applied. A negative voltage starts to be applied to the antidot gate to deplete the 2DEG underneath the antidot area. The reflected RF amplitude and the corresponding phase shift are shown in 7.5(a) and 7.5(b). The antidot gate starts to deplete the 2DEG underneath when $V_{AD} \sim$ -0.45 V, where there is an obvious resonant frequency f_0 shifts from $\sim$ 280 MHz to $\sim$ 315 MHz, and then f_0 keeps stable until $V_{AD} \sim$ -3.5 V, where f_0 shifts again from $\sim$ 315 MHz to $\sim$ 320 MHz probably due to the depletion under the crosslinked regions caused by the large antidot gate voltage.

When a perpendicular magnetic field is applied to the GaAs antidot device, we can observe oscillations in the reflected RF voltage when magnetic field B is increasing, which is similar to the Aharonov–Bohm oscillations but the period is not fixed. Figure 7.6(a) presents the complex magnetoimpedance spectroscopy of the antidot. Modulation in the resistance of the 2DEG regions gives rise to periodic horizontal oscillations (vertical lines) highlighted by red arrows, while diagonal line (dashed) corresponds to the quantum capacitance of Landau levels under the antidot gate. We also measured the reflected RF voltage as a function of RF frequency and magnetic field B to see how the B effects resonant frequency. Figure 7.6(b) and (c) demonstrate the magentoimpedance spectroscopy of the meausred antidot device showing how resonant frequency changes against magnetic field with V_{AD} = 0 V and V_{AD} = -0.6 V, corresponding to non-depletion and depletion of the region under the antidot gate respectively.

7.2.3 Conclusion

This section presents the application of the RF reflectometry technique to the GaAs quantum antidot device. We study the RF response as a function of QPC split gates V_{QPC}, antidot gate V_{AD} and magnetic field B, suggesting the RF reflectometry technique is an useful and sensitive tool to probe quantum capacitance changes caused by the variation in the carrier concentration of the 2DEG. We observed some interesting oscillations in the complex magnetoimpedance spectroscopy of the antidot. However, these phenomena still need further investigation.

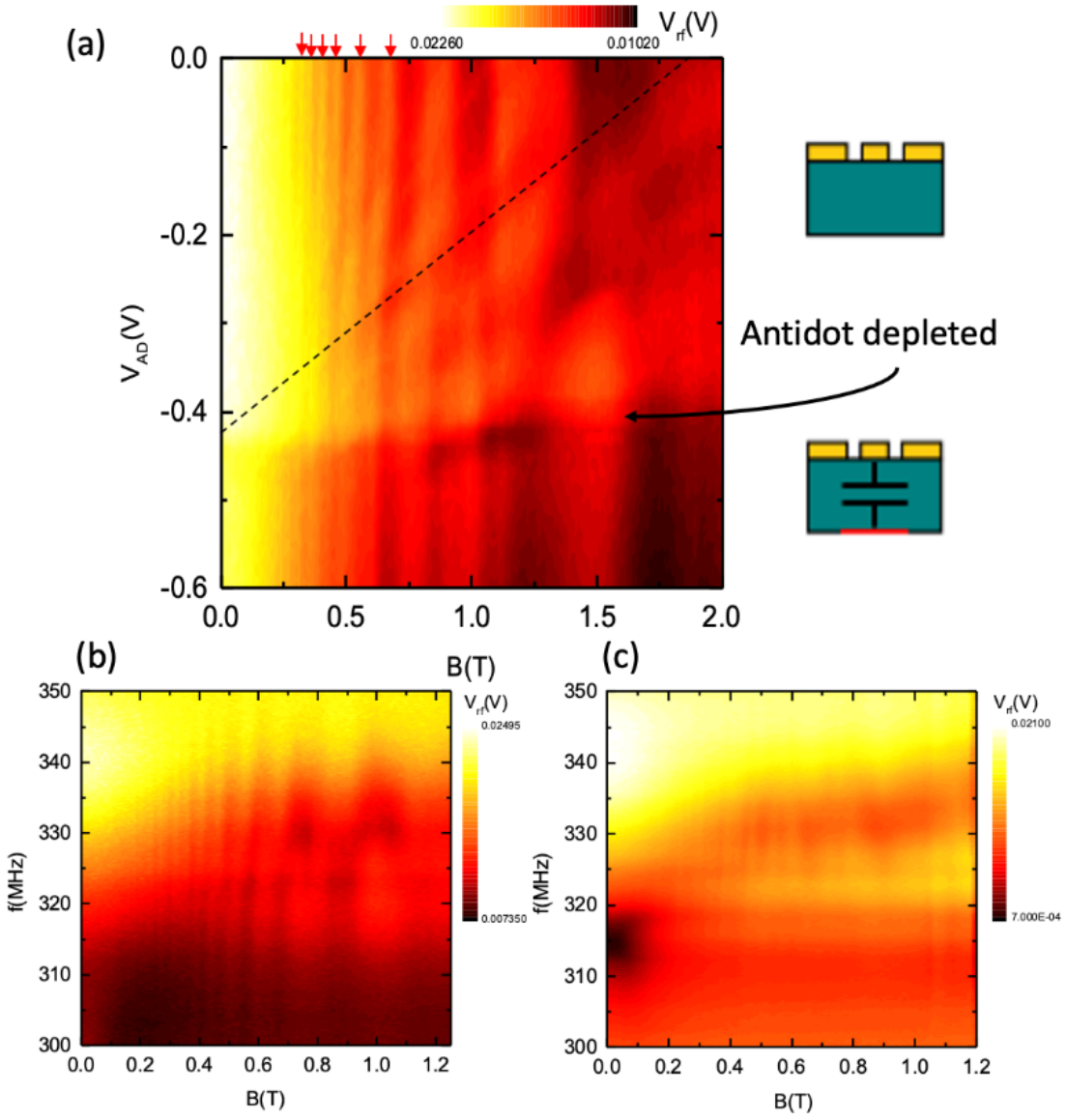

Fig. 7.6 (a) Complex magnetoimpedance spectroscopy of the antidot. Modulation in the resistance of the 2DEG regions gives rise to horizontal oscillations (vertical lines) highlighted by red arrows, while diagonal line (dashed) corresponds to the quantum capacitance of Landau levels under the antidot gate. (b)(c) Magentoimpedance spectroscopy of the antidot showing how resonant frequency changes against magnetic field with (b) V_{AD} = 0 V, and (c) V_{AD} = -0.6 V, corresponding to non-depletion and depletion of the region under the antidot gate respectively. (T = 50 mK)

7.3 Graphene Double Quantum Dots

The control of individual electrons and spins is of great interest in realizing quantum qubits for quantum computation application. A graphene double quantum dots (GDQDs) system [132] has been studied as a potential qubit with the additional possible benefit of increased spin coherence times [181]. In addition, GDQDs have also proved to be an ideal system to realize gigahertz charge pumping [45] for quantum metrology application, due to the low coupling capacitance of graphene. Transport through DQDs has been widely investigated in conventional semiconductor and exfoliated graphene [132]. This section will discuss scalable DQDs based on CVD graphene and RF reflectometry technique will be applied to probe single electron tunnelling in GDQDs.

7.3.1 Device Description

The CVD graphene used in fabricating DQDs is the same as that discussed in chapter 4 and each 10 mm $\times$ 10 mm chip can produce 36 GDQDs devices, which makes it possible to realize scalable single-electron devices in CVD graphene compared with exfoliated graphene. I designed and fabricated two kinds of GDQDs devices, straight and wrap-around. Figure 7.7(a) shows the AutoCAD designs of one of the two kinds of GDQDs devices respectively. The DQDs is connected with source and drain contacts via tunnel barriers, and one side gate V_{SG} and two plunger gates V_{PG1} and V_{PG2} are around 50 nm away from the DQDs. The side gate is used to tune the carrier concentration of the device while the two plunger gates are designed to change the Fermi energy on the two dots separately. The width of the tunnel barriers of the devices vary from 50 nm to 120 nm. This variation is designed for testing graphene etching by oxygen plasma, as if it is too narrow, the channel might be etched away from the side and it is too wide, we cannot observe quantum confinement effect. The actual width of the tunnel barriers of GDQDs is slightly less than the designed value due to the shrink during the etching process. Figure 7.7(b) exhibits the atomic force microscope (AFM) image of one of the measured straight GDQDs device in this thesis, as well as the connection to the RF reflectometry measurement circuit. The principle of how the RF reflectometry works on GDQDs is the same as that on the GaAs ADs, but the only difference lies in that it is coupled directly to the source of the device rather than through the gate.

The measurements are performed with a combination of a two-terminal circuit and RF reflectometry circuit via a bias-tee in the dilution refrigerator MX400. The RF reflectometry circuit has been described in the previous section. In terms of the DC two-terminal setup, a DC voltage (which can be adjusted according to the requirements) goes through a 10^{-3}

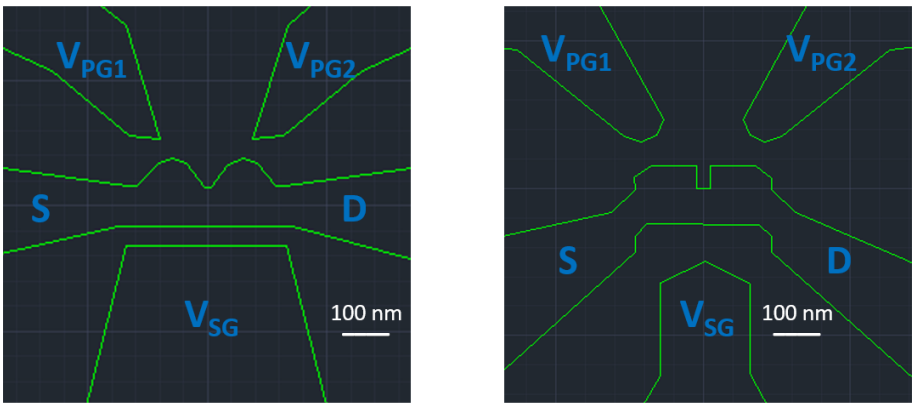

(a)

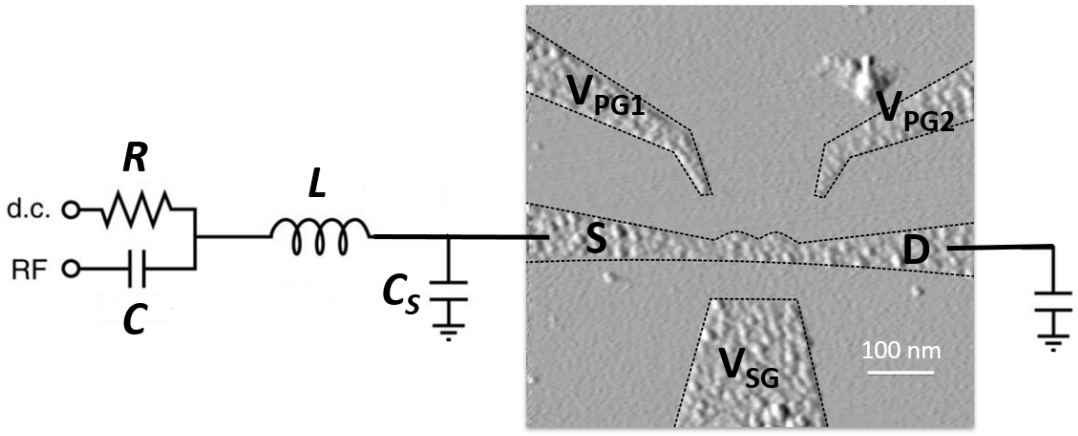

(b)

Fig. 7.7 (a) AutoCAD design of straight (left) and wrap-around (right) CVD graphene double quantum dots. (b) Atomic force microscope image of one of the measured straight GDQDs device in this thesis, with the connection to the RF reflectometry measurement circuit.

potential divider before getting into the device, and the current is pre-amplified by 10^8 before being received by Keithley 2000 DMM.

7.3.2 Results and Discussion

We first measured a straight GDQDs device as shown in the AFM image in figure 7.7(b). Before cooling the device down to fridge base temperature, we test the device at 4 K. Here, we supply a -15 dB RF signal using ultra high frequency lock-in (UHFLI), which goes through a 20 dB room temperature attenuator and a 35 dB low temperature attenuator and the RF signal is reduced down to -70 dB when it reaches the device. The two-terminal resistance of the device as a function of side-gate voltage V_{SG} and the corresponding reflected

RF voltage are shown in figure 7.8(a) and figure 7.8(b), respectively. We can see that the response of the reflected RF signal is consistent with the fluctuations of the resistance, which means the RF reflectometry technique is an useful alternative to probe the impedance changing non-invasively. The relationship between the reflected RF voltage and the two-terminal resistance of the device is plotted in figure 7.8(c). As described in chapter 3, the perfect matching occurs when the transformed impedance Z_t (changed by the variation in the device impedance) equals the characteristic impedance of the transmission line Z_0, where the reflection coefficient $\Gamma = (Z_t - Z_0)/(Z_t + Z_0) = 0$ and thus the reflected RF voltage is zero. Figure 7.8(c) suggests the best impedance match of this measurement happens at some point R < 150 kΩ. As the two-terminal resistance of the device is higher than 150 kΩ for the measured V_{SG} range, we cannot reach the perfect match point. However, we can still observe strong RF response in measuring this device. Figure 7.8(d) exhibits the frequency spectrum of the measured reflected RF voltage and corresponding phase at three different V_{SG}, with blue, yellow and pink denote V_{SG} = 0 V, 3 V and 6 V, respectively. Obvious changes in the depth of the dip at the resonant frequency $f_0 \approx 305$ MHz can be observed, while there is no observable frequency shift when V_{SG} tunes the carrier concentration of the device, suggesting only dissapative without dispersive processes happening. This is probably because the RF circuit is resistively and strongly coupled to the device, and the impedance change of the device comes mainly from the resistance change with almost no capacitance contribution.

Then the device is cooled down to the base temperature of 40 mK. Figure 7.9(a) presents the current I through the device as a function of source-drain bias V_{SD}. A source-drain gap can be observed of around 0.5 mV. Then we set V_{SD} = 1 mV and sweep the side-gate voltage V_{SG}. We obtain the current I through the device against V_{SG}, which is shown in figure 7.9(b), as well as the corresponding reflected RF voltage as a function of V_{SG} (see figure 7.9(c)). The combination of V_{SD} and V_{SG} sweeps suggests that Coulomb blockade effect can be observed resulting from quantum dots formation in the measured device.

To get a clear signature of the DQDs, we set V_{SG} = 2.1 V, where the current through the device is blocked, and tune the two plunger gates separately in order to see single-electron tunnelling effects. The results are shown in figure 7.9(d) and 7.9(e). The Coulomb gap in V_{PG2} is roughly double of that in V_{PG1}, which means that the two plunger gates might not be of the same distance away from dots as expected, or the dots might not be defined in the right place. In order to find the triple points as an evidence of the existence of double dots, we reduce the source-drain bias V_{SD} from 1 mV to 200 μV and plot a V_{PG1} - V_{PG2} 2D mapping, which is shown in figure 7.9(f). However, we are not able to see the triple points and honeycomb diagram as expected, so the double dots are not defined in this measured range. One possible reason for this is because of the designed geometry of the device. The

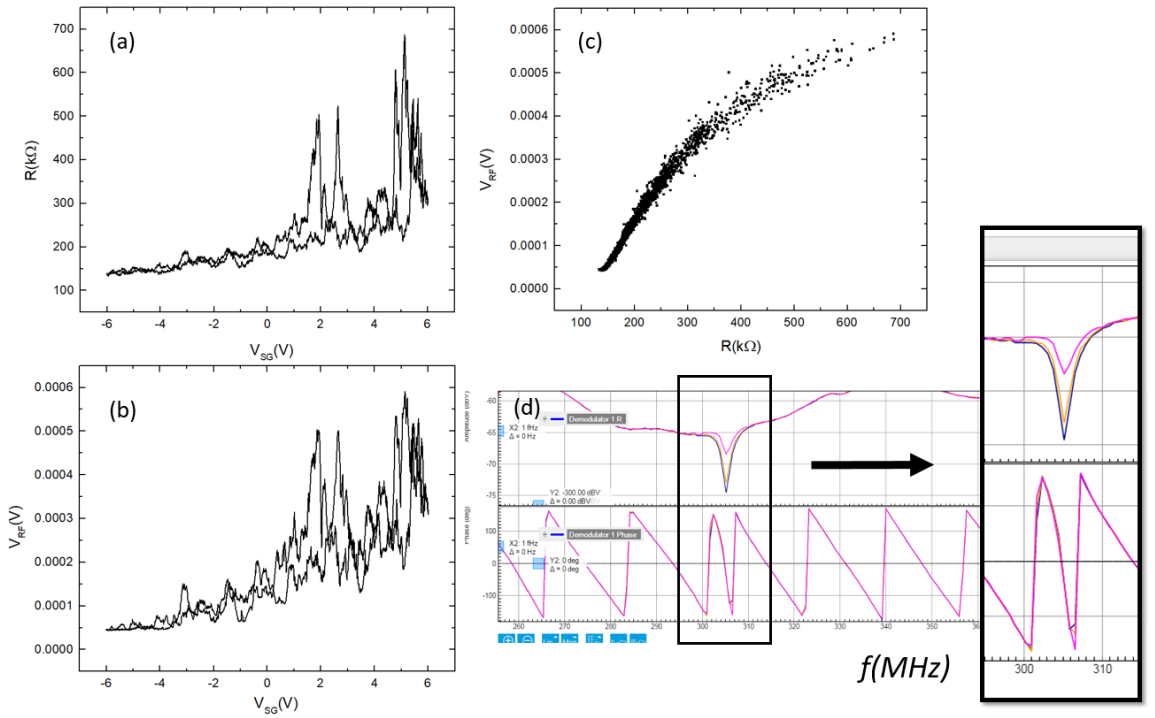

Fig. 7.8 (a) Two-terminal resistance of the measured GDQDs device as a function of side-gate voltage V_{SG}. (b) Corresponding reflected RF voltage as a function of V_{SG}. (c) Reflected RF voltage as a function of the two-terminal resistance of the device. (d) Frequency spectrum of the measured reflected RF voltage and corresponding phase at three different V_{SG}, with blue, yellow and pink denote V_{SG} = 0 V, 3 V and 6 V, respectively. (T = 4K)

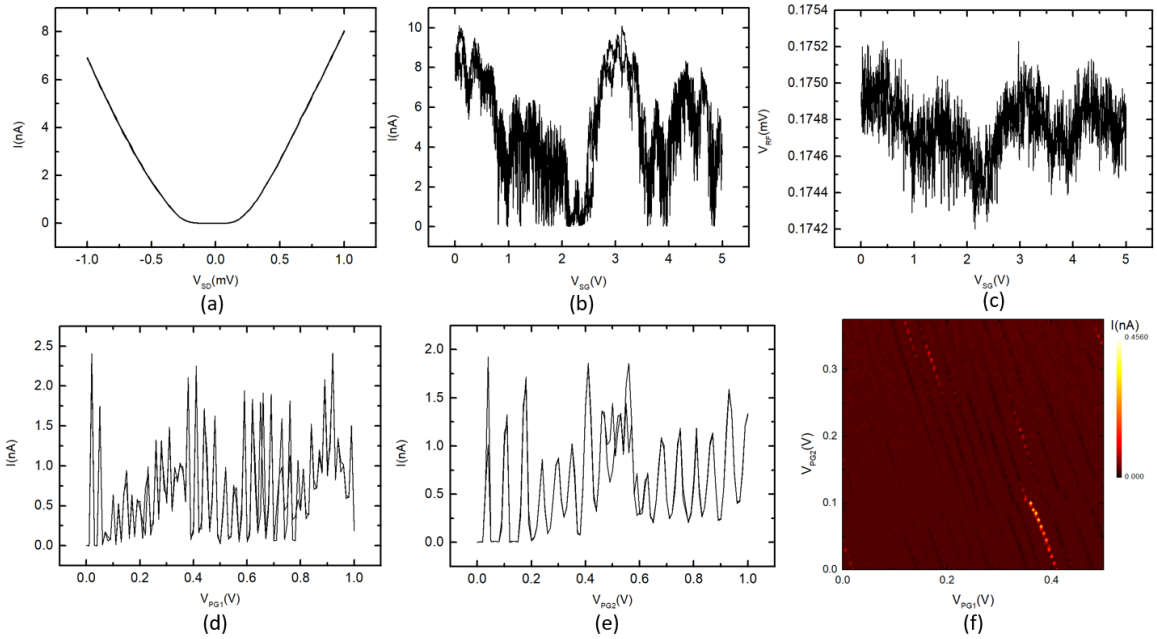

Fig. 7.9 (a) The measured current I through the GDQDs device as a function of source-drain bias V_{SD}. (b) The current as a function of side-gate voltage V_{SG}. (c) Corresponding reflected RF voltage as a function of V_{SG}. (d)(e) Two-terminal current through the GDQDs device as a function of two plunger gates V_{PG1} and V_{PG2}, when V_{SD} = 1 mV and V_{SG} = 2.1 V. (f) 2D mapping plot of the two plunger gates at V_{SD} = 200 μV and V_{SG} = 2.1 V. (T = 40 mK)

side-gate is far away from the other side of the dots, and thus it cannot tune the carrier concentration of both dots at the same level. Another reason might be that the tunnel barrier between the two dots is too weak to confine electrons in each single dot, so the device behaves like a single quantum dot rather than double dots. Noted that the mobility of the graphene material used for making the DQDs is around 1000 $cm^2V^{-1}s^{-1}$, which corresponds to mean free path around 50 nm, comparable to the smallest feature of the DQDs device, the high disorder level in the material will influence the DQDs formation as well.

Considering the geometry of the device, we attempt to push V_{SG} and V_{PG1}, V_{PG2} to high values and expect to see the transition from the single quantum dot regime to the double quantum dots regime. Figure 7.10(a) presents the measured two-terminal current through the GDQDs device as a function of side-gate voltage V_{SG} in a long range from 0 V to 20 V at V_{SD} = 1 mV. The trend of the variation of the current is going down when V_{SG} is increasing, and particularly the current is significantly reduced to around zero when V_{SG} is over 15 V. This tells us that during the previous measurements, we did not tune the graphene double dots device close to the Dirac point by using the side-gate. The Dirac point of this device might be located somewhere where $V_{SG} > 15$ V. Then we set V_{SG} = 18 V and reduce the source-drain bias down to V_{SD} = 100 μV and plot the V_{PG1} - V_{PG2} 2D mapping with high plunger gate values. The mapping is exhibited in figure 7.10(b), showing that some isolated triple points do exist, one of which is pointed out by a white dashed circle. Although we still cannot see the honeycomb diagram as a strong evidence of double dots regime in this plot due to the designed geometry of the device and possibly high disorder level in the material, some observable isolated triple points could be a signature of the double dots if all the gate parameters (V_{SG}, V_{PG1} and V_{PG2}) are tuned properly.

7.3.3 Conclusion

We fabricated and studied DQDs based on CVD graphene, and performed RF reflectometry experiments on them at 40 mK low temperatures. Using RF reflectometry technique we probe single-electron tunnelling in GDQDs, even though the signature of double dots is not strong due to the designed geometry of the measured device and possibly the poor quality of the CVD graphene. We show that the RF response is significantly dependant on the impedance variation of the device, which allows us to detect single-electron behaviours in a non-invasive manner.

To enhance the device performance, we plan to optimize the device designs by adjusting the device geometry, changing the etching method and adding a separate gate in the middle to tune the coupling between the two dots, as well as replacing the graphene gates with metal to increase the stability. Moveover, using CVD graphene, there is the potential to scale up

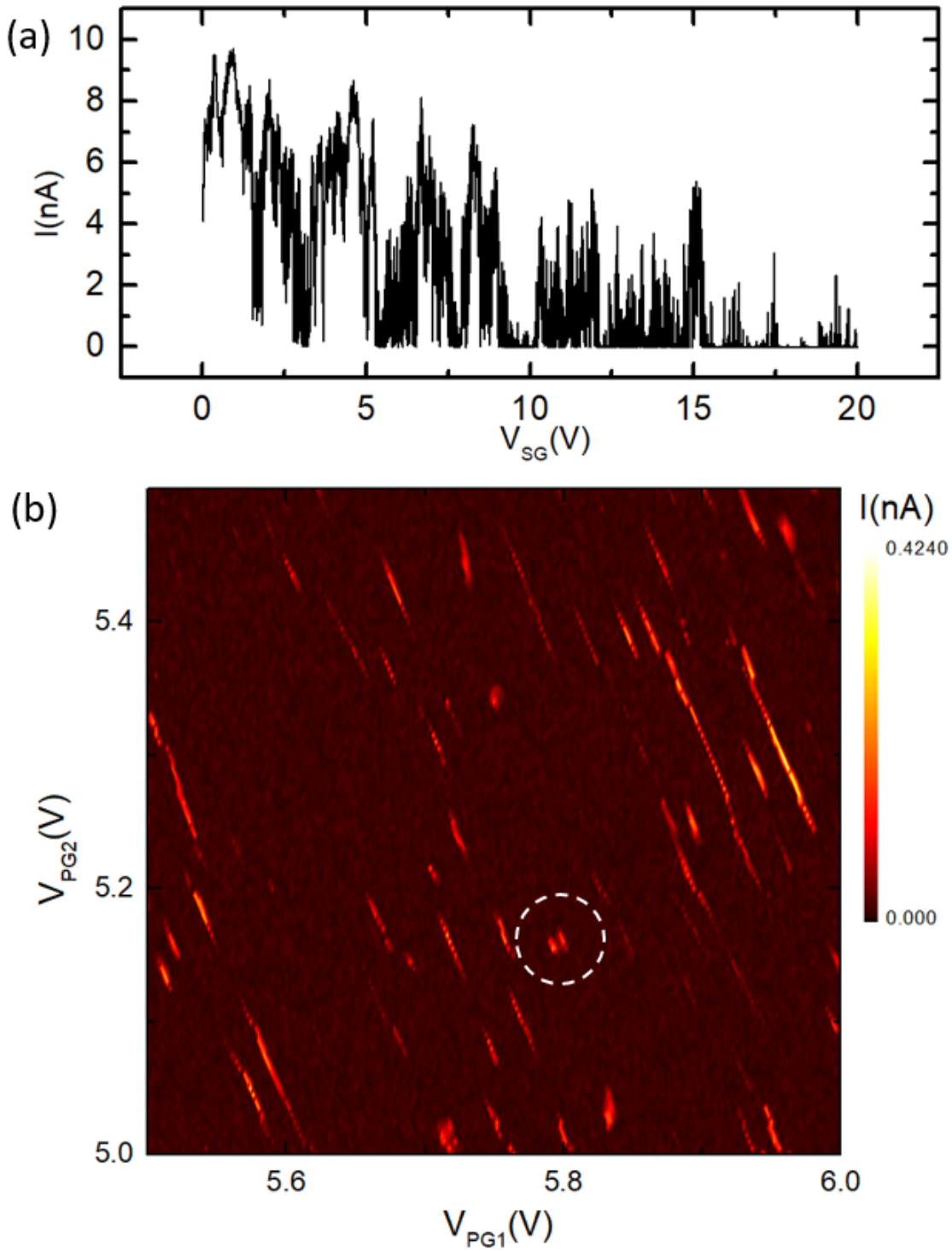

Fig. 7.10 (a) The two-terminal current through the GDQDs device as a function of side-gate voltage V_{SG} in a long range at $V_{SD} = 1mV$. (b) 2D mapping plot of the two plunger gates at $V_{SD} = 100\mu V$ and $V_{SG} = 18V$. One of the possible triple points is pointed out by a white dashed circle (T = 40 mK, B = 0 T).

graphene single-electron devices, such as charge pumps based on double dots [45], and even the parallel charge pumps leading to larger pumping currents, but this work shows that more work is needed improving the quality of CVD graphene before it can be reliably used for quantum devices.

7.4 Conclusion

This chapter discuss the development of the potential applications of the RF reflectometry technique in GaAs antidots and graphene double quantum dots, corresponding to capacitive and resistive couplings to the devices, respectively. Using radio-frequency reflectometry we non-invasively probe quantum capacitance changes and single-electron tunnelling behaviours in GaAs ADs and graphene DQDs with high sensitivity and at millikelvin temperatures. The physics of the complex magnetoimpedance spectroscopy of the GaAs antidot is still under discussion, and the design and the fabrication process of graphene double dots need to be optimized in the future work. Moreover, it is possible the mobility in CVD graphene is not high enough to us for nano scale quantum devices at present.

Chapter 8

Conclusions and Future Work

In this chapter I will briefly summarise the key results presented in this thesis and discuss the future plan for research in this area based on my results.

8.1 Conclusions

This thesis investigates electron transport properties in CVD graphene nanostructured devices. The two-dimensional character of graphene and its exceptional electronic properties make it a promising candidate to be used in the post-silicon electronics era. However, the lack of scalability and reproducibility of graphene devices fabricated from small exfoliated flakes and the high cost of epitaxial graphene on silicon carbide, remain the major obstacles for further commercialization of graphene electronics. In order to obtain large-scale high-quality graphene material at a reasonable cost, a CVD approach stands out as a possible technique of material production to provide a scalable route towards high electronic quality graphene, because its wafer-scale growth enables large scale production with a low cost.

Chapter 4 laid the foundation for the fabrication and operation of scalable graphene FETs. We have demonstrated a scalable and simple approach towards encapsulating and passivating high quality CVD graphene electronic devices by using a gaseous H_2O pretreatment to allow direct ALD of dense Al_2O_3 films on graphene. Based on this approach, by studying electrical characterisation and magnetotransport phenomena in encapsulated CVD grown Bernal stacked and large twist angle (30°) bilayer graphene FETs, as well as monolayer graphene FETs for reference, we show that electron scattering processes and hot electron effects can be tuned. It was found that the phase coherence length in AB stacked graphene is longer than that in monolayer but decays faster with temperature, while large twist angle bilayer graphene has the longest phase coherence length among them with enhanced inter-valley scattering. We have also found that the carrier temperature-dependent energy loss rates

of hot carriers in AB stacked CVD bilayer graphene follow closer to a T_e^3 power-law than a T_e^4 power-law, predicted in most previous graphene studies. This result has a significant impact on the study of CVD graphene and its further scalable device applications.

In order to enhance spin-orbit interaction in graphene for spintronics applications, chapter 5 investigated a graphene - TMD heterostructure with exfoliated WS_2 stacked on the top of CVD graphene. The material was patterned into a long Hall bar with half of its length having a graphene/WS_2 heterostructure and the other half being only graphene for reference. A reduced phase coherence length in the graphene/WS_2 heterostructure was found and a special transition from WL to WAL occurred around a certain carrier concentration possibly due to surface roughness-induced patches. It was also found that the dominant scattering mechanism in the heterostructure was only weakly temperature dependent up to 20 K, with phase coherence length value around 100 nm at low temperatures. This weak temperature dependence is probably due to induced spin-orbit coupling in Gr/WS_2 by a proximity effect. Although some physics in terms of electron scattering in Gr/WS_2 still requires further explanation, this attempt paves a way for further studies of scalable graphene spintronic devices.

To gain further insights into single electron phenomena as well as solve the lack of bandgap issues in graphene, graphene was studied by being patterned into various quantum dot structures, such as nanoribbon multiple quantum dots and quantum Hall antidots discussed in chapter 6, as well as double quantum dots in chapter 7. Electron tranport was studied in a SiC epitaxial bilayer graphene nanoribbon at three different carrier concentrations. Away from charge neutrality transport is only weakly modulated by a local side-gate, while at medium doping close to charge neutrality, electron transport resembles that in exfoliated graphene nanoribbons and is well described by tunnelling of single electrons through a network of Coulomb-blockaded islands, with multiple quantum dots formed in series due to the interplay between disorder and quantum confinement. Because the linear Dirac spectrum makes it impossible to define quantum dots in monolayer graphene by electric field, and the quality of etched quantum dots is influenced by edge disorders, antidots in the quantum Hall regime stand out as an alternative way to create quantum confinement by taking advantage of Landau gaps in graphene. Although we routinely see the quantum Hall effect, Aharonov-Bohm effect and Coulomb blockade effect, signatures of the effective antidots proved elusive, probably due to the disorder-broadening of the Landau levels. Due to its high sensitivity and accuracy, RF reflectometry provides a useful tool to detect single electron tunnelling in quantum dots, so that the time scale of the charge transfer [55] and spin dephasing [152] can be characterized. Chapter 7 was an attempt towards applying RF reflectometry technique in GaAs antidots and graphene double quantum dots, corresponding to capacitive and resistive

couplings to the devices, respectively. Using radio-frequency reflectometry we non-invasively probe the impedance change and single-electron tunnelling behaviours in GaAs antidots and graphene double dots with high sensitivity and at millikelvin temperatures. The physics of the complex magneto-impedance spectroscopy of the GaAs antidot is still under investigation, and the design and the fabrication process of graphene double dots need to be optimized. This work also shows that more efforts are needed to improve the quality of CVD graphene before it can be reliably used for quantum devices.

8.2 Future Work

In this thesis I have investigated the electron transport properties of various nanodevices fabricated from CVD grown graphene. Although many efforts have been made to optimize the growth and fabrication processes of CVD graphene during my PhD project, the mobility in CVD graphene is not yet high enough to us for nano-scale quantum devices at present. To further extend my work in the field of low-dimensional graphene research based on my results, I propose a few ideas which might be helpful to the goal of realizing scalale graphene FETs or quantum nanodevices.

In terms of scalable spintronics application, we plan to stack CVD grown TMD material on top of CVD graphene, in which case we can not only realize a more scalable route, but also expect to observe a strong induced spin-orbit coupling in graphene due to less surface ripples. Furthermore, since the impurities and interface quality constrain the performance of CVD graphene, we intend to combine hBN [48, 47] with CVD graphene to fabricate large-scale high-quality graphene quantum dots and antidots devices for the purpose of quantum metrology and quantum computation applications. In addition, gate-defined quantum dots have been realized by a simple perpendicular electric field leading to a tunable band gap in exfoliated graphene encapsulated with hBN [56, 13, 57]. It is also promising to produce scalable gate-defined quantum dots devices by using bilayer CVD graphene and hBN. Finally, once the quantum dot devices are optimized, we intend to perform RF experiments on them. Both double dots and quantum antidots are ideal systems to realize charge pumping when driven by fast gates. RF reflectometry technique can be combined with charge pumping via a QPC or SET [166, 32, 151, 155, 62] to read out charge and spin states, which is also imperative for further use in quantum computing.

Overall, this thesis presents a study of scalable nanostructured devices based on CVD produced graphene. The research in this thesis enables us to better understand the quantum physics in CVD graphene, and the fabrication and operation of CVD graphene nanostructures are highly promising for future electronics.

List of Publications

1. Alexander-Webber, J. A., Sagade, A. A., Aria, A. I., Van Veldhoven, Z. A., Braeuninger-Weimer, P., Wang, R., Cabrero-Vilatela, A., Martin, M.-B., **Sui, J.**, Connolly, M. R., and Hofmann, S. (2016). Encapsulation of graphene transistors and vertical device integrationby interface engineering with atomic layer deposited oxide. *2D Materials*, 4(1): 11008.

2. Chua, C., Lartsev, A., **Sui, J.**, Panchal, V., Puddy, R., Richardson, C., Smith, C. G.,Janssen, T., Tzalenchuk, A., Yakimova, R., Kubatkin, S., and Connolly, M. R. (2017). Observation of Coulomb blockade in nanostructured epitaxial bilayer graphene on SiC. *Carbon*, 119: 426–430.

3. **Sui, J.**, Fan, Y., Burton, O., Braeuninger-Weimer, P., Sagade, A. A., Smith, C. G., Hofmann, S., and Alexander-Webber, J. A. (2019). Twist angle dependent electron scattering in as-grown CVD bilayer graphene. *In preparation*.

4. **Sui, J.**, Alexander-Webber, J. A., Smith, C. G., Hofmann, S., and Fan, Y. (2019). Induced spin-orbit coupling in CVD graphene - transition metal dichalcogenide heterostructures. *In preparation*.

References

[1] Adam, S., Cho, S., Fuhrer, M. S., and Das Sarma, S. (2008). Density Inhomogeneity Driven Percolation Metal-Insulator Transition and Dimensional Crossover in Graphene Nanoribbons. *Physical Review Letters*, 101(4):46404.

[2] Alagha, S., Hernández, S. E., Blömers, C., Stoica, T., Calarco, R., and Schäpers, T. (2010). Universal conductance fluctuations and localization effects in InN nanowires connected in parallel. *Journal of Applied Physics*, 108(11):113704.

[3] Alencar, T. V., von Dreifus, D., Gabriela Cota Moreira, M., Eliel, G. S. N., Yeh, C.-H., Chiu, P.-W., Pimenta, M. A., Malard, L. M., and Maria de Paula, A. (2018). Twisted bilayer graphene photoluminescence emission peaks at van Hove singularities. *Journal of Physics: Condensed Matter*, 30(17):175302.

[4] Alexander-Webber, J. A., Sagade, A. A., Aria, A. I., Van Veldhoven, Z. A., Braeuninger-Weimer, P., Wang, R., Cabrero-Vilatela, A., Martin, M.-B., Sui, J., Connolly, M. R., and Hofmann, S. (2016). Encapsulation of graphene transistors and vertical device integration by interface engineering with atomic layer deposited oxide. *2D Materials*, 4(1):11008.

[5] Allen, M. J., Tung, V. C., and Kaner, R. B. (2010). Honeycomb Carbon: A Review of Graphene. *Chemical Reviews*, 110(1):132–145.

[6] Allen, M. T., Martin, J., and Yacoby, A. (2012). Gate-defined quantum confinement in suspended bilayer graphene. *Nature Communications*, 3:934.

[7] Altshuler, B. L., Aronov, A. G., and Khmelnitsky, D. E. (1982). Effects of electron-electron collisions with small energy transfers on quantum localisation. *Journal of Physics C: Solid State Physics*, 15(36):7367–7386.

[8] Appenzeller, J., Martel, R., Avouris, P., Stahl, H., Hunger, U. T., and Lengeler, B. (2001). Phase-coherent transport in ropes of single-wall carbon nanotubes. *Physical Review B*, 64(12):121404.

[9] Aria, A. I., Nakanishi, K., Xiao, L., Braeuninger-Weimer, P., Sagade, A. A., Alexander-Webber, J. A., and Hofmann, S. (2016). Parameter Space of Atomic Layer Deposition of Ultrathin Oxides on Graphene. *ACS Applied Materials & Interfaces*, 8(44):30564–30575.

[10] Bai, J., Cheng, R., Xiu, F., Liao, L., Wang, M., Shailos, A., Wang, K. L., Huang, Y., and Duan, X. (2010). Very large magnetoresistance in graphene nanoribbons. *Nature Nanotechnology*, 5:655.

[11] Baker, A. M. R., Alexander-Webber, J. A., Altebaeumer, T., McMullan, S. D., Janssen, T. J. B. M., Tzalenchuk, A., Lara-Avila, S., Kubatkin, S., Yakimova, R., Lin, C.-T., Li, L.-J., and Nicholas, R. J. (2013). Energy loss rates of hot Dirac fermions in epitaxial, exfoliated, and CVD graphene. *Physical Review B*, 87(4):45414.

[12] Baker, A. M. R., Alexander-Webber, J. A., Altebaeumer, T., and Nicholas, R. J. (2012). Energy relaxation for hot Dirac fermions in graphene and breakdown of the quantum Hall effect. *Physical Review B*, 85(11):115403.

[13] Banszerus, L., Frohn, B., Epping, A., Neumaier, D., Watanabe, K., Taniguchi, T., and Stampfer, C. (2018). Gate-Defined Electron–Hole Double Dots in Bilayer Graphene. *Nano Letters*, 18(8):4785–4790.

[14] Banszerus, L., Schmitz, M., Engels, S., Dauber, J., Oellers, M., Haupt, F., Watanabe, K., Taniguchi, T., Beschoten, B., and Stampfer, C. (2015). Ultrahigh-mobility graphene devices from chemical vapor deposition on reusable copper. *Science Advances*, 1(6):e1500222.

[15] Beenakker, C. W. J. and van Houten, H. (1991). Quantum Transport in Semiconductor Nanostructures. In Ehrenreich, H. and Turnbull, D. B. T. S. S. P., editors, *Semiconductor Heterostructures and Nanostructures*, volume 44, pages 1–228. Academic Press.

[16] Berger, C., Song, Z., Li, T., Li, X., Ogbazghi, A. Y., Feng, R., Dai, Z., Marchenkov, A. N., Conrad, E. H., First, P. N., and de Heer, W. A. (2004). Ultrathin Epitaxial Graphite: 2D Electron Gas Properties and a Route toward Graphene-based Nanoelectronics. *The Journal of Physical Chemistry B*, 108(52):19912–19916.

[17] Berger, C., Song, Z., Li, X., Wu, X., Brown, N., Naud, C., Mayou, D., Li, T., Hass, J., Marchenkov, A. N., Conrad, E. H., First, P. N., and de Heer, W. A. (2006). Electronic Confinement and Coherence in Patterned Epitaxial Graphene. *Science*, 312(5777):1191 LP – 1196.

[18] Bergmann, G. (1984). Weak localization in thin films: a time-of-flight experiment with conduction electrons. *Physics Reports*, 107(1):1–58.

[19] Bischoff, D., Krähenmann, T., Dröscher, S., Gruner, M. A., Barraud, C., Ihn, T., and Ensslin, K. (2012). Reactive-ion-etched graphene nanoribbons on a hexagonal boron nitride substrate. *Applied Physics Letters*, 101(20):203103.

[20] Bischoff, D., Libisch, F., Burgdörfer, J., Ihn, T., and Ensslin, K. (2014). Characterizing wave functions in graphene nanodevices: Electronic transport through ultrashort graphene constrictions on a boron nitride substrate. *Physical Review B*, 90(11):115405.

[21] Bischoff, D., Varlet, A., Simonet, P., Eich, M., Overweg, H. C., Ihn, T., and Ensslin, K. (2015). Localized charge carriers in graphene nanodevices. *Applied Physics Reviews*, 2(3):31301.

[22] Bolotin, K. I., Sikes, K. J., Jiang, Z., Klima, M., Fudenberg, G., Hone, J., Kim, P., and Stormer, H. L. (2008). Ultrahigh electron mobility in suspended graphene. *Solid State Communications*, 146(9):351–355.

[23] Braeuninger-Weimer, P., Brennan, B., Pollard, A. J., and Hofmann, S. (2016). Understanding and Controlling Cu-Catalyzed Graphene Nucleation: The Role of Impurities, Roughness, and Oxygen Scavenging. *Chemistry of Materials*, 28(24):8905–8915.

[24] Brey, L. and Fertig, H. A. (2006). Electronic states of graphene nanoribbons studied with the Dirac equation. *Physical Review B - Condensed Matter and Materials Physics*.

[25] Butler, S. Z., Hollen, S. M., Cao, L., Cui, Y., Gupta, J. A., Gutiérrez, H. R., Heinz, T. F., Hong, S. S., Huang, J., Ismach, A. F., Johnston-Halperin, E., Kuno, M., Plashnitsa, V. V., Robinson, R. D., Ruoff, R. S., Salahuddin, S., Shan, J., Shi, L., Spencer, M. G., Terrones, M., Windl, W., and Goldberger, J. E. (2013). Progress, Challenges, and Opportunities in Two-Dimensional Materials Beyond Graphene. *ACS Nano*, 7(4):2898–2926.

[26] Büttiker, M. (1986). Four-Terminal Phase-Coherent Conductance. *Physical Review Letters*, 57(14):1761–1764.

[27] Cao, Y., Fatemi, V., Demir, A., Fang, S., Tomarken, S. L., Luo, J. Y., Sanchez-Yamagishi, J. D., Watanabe, K., Taniguchi, T., Kaxiras, E., Ashoori, R. C., and Jarillo-Herrero, P. (2018a). Correlated insulator behaviour at half-filling in magic-angle graphene superlattices. *Nature*, 556:80.

[28] Cao, Y., Fatemi, V., Fang, S., Watanabe, K., Taniguchi, T., Kaxiras, E., and Jarillo-Herrero, P. (2018b). Unconventional superconductivity in magic-angle graphene superlattices. *Nature*, 556:43.

[29] Cao, Y.-Q., Cao, Z.-Y., Li, X., Wu, D., and Li, A.-D. (2014). A facile way to deposit conformal Al2O3 thin film on pristine graphene by atomic layer deposition. *Applied Surface Science*, 291:78–82.

[30] Carcia, P. F., McLean, R. S., Reilly, M. H., Groner, M. D., and George, S. M. (2006). Ca test of Al2O3 gas diffusion barriers grown by atomic layer deposition on polymers. *Applied Physics Letters*, 89(3):31915.

[31] Carrion, E. A., Serov, A. Y., Islam, S., Behnam, A., Malik, A., Xiong, F., Bianchi, M., Sordan, R., and Pop, E. (2014). Hysteresis-Free Nanosecond Pulsed Electrical Characterization of Top-Gated Graphene Transistors. *IEEE Transactions on Electron Devices*, 61(5):1583–1589.

[32] Cassidy, M. C., Dzurak, A. S., Clark, R. G., Petersson, K. D., Farrer, I., Ritchie, D. A., and Smith, C. G. (2007). Single shot charge detection using a radio-frequency quantum point contact. *Applied Physics Letters*, 91(22):222104.

[33] Castro, E. V., Peres, N. M. R., dos Santos, J. M. B. L., Guinea, F., and Neto, A. H. C. (2008). Bilayer graphene: gap tunability and edge properties. *Journal of Physics: Conference Series*, 129:12002.

[34] Castro Neto, A. H., Guinea, F., Peres, N. M. R., Novoselov, K. S., and Geim, A. K. (2009). The electronic properties of graphene. *Reviews of Modern Physics*, 81(1):109–162.

[35] Chen, F., Xia, J., Ferry, D. K., and Tao, N. (2009). Dielectric Screening Enhanced Performance in Graphene FET. *Nano Letters*, 9(7):2571–2574.

[36] Chen, J.-H., Jang, C., Xiao, S., Ishigami, M., and Fuhrer, M. S. (2008). Intrinsic and extrinsic performance limits of graphene devices on SiO2. *Nature Nanotechnology*, 3:206.

[37] Chen, X.-D., Xin, W., Jiang, W.-S., Liu, Z.-B., Chen, Y., and Tian, J.-G. (2016). High-Precision Twist-Controlled Bilayer and Trilayer Graphene. *Advanced Materials*, 28(13):2563–2570.

[38] Chen, Z., Lin, Y. M., Rooks, M. J., and Avouris, P. (2007). Graphene nano-ribbon electronics. *Physica E: Low-Dimensional Systems and Nanostructures*.

[39] Cheol Shin, W., Yong Kim, T., Sul, O., and Jin Cho, B. (2012). Seeding atomic layer deposition of high-k dielectric on graphene with ultrathin poly(4-vinylphenol) layer for enhanced device performance and reliability. *Applied Physics Letters*, 101(3):33507.

[40] Chiu, K. L., Connolly, M. R., Cresti, A., Chua, C., Chorley, S. J., Sfigakis, F., Milana, S., Ferrari, A. C., Griffiths, J. P., Jones, G. A. C., and Smith, C. G. (2012). Single-particle probing of edge-state formation in a graphene nanoribbon. *Physical Review B*, 85(20):205452.

[41] Choi, W., Choudhary, N., Han, G. H., Park, J., Akinwande, D., and Lee, Y. H. (2017). Recent development of two-dimensional transition metal dichalcogenides and their applications. *Materials Today*, 20(3):116–130.

[42] Chua, C., Connolly, M., Lartsev, A., Yager, T., Lara-Avila, S., Kubatkin, S., Kopylov, S., Fal'ko, V., Yakimova, R., Pearce, R., Janssen, T. J. B. M., Tzalenchuk, A., and Smith, C. G. (2014). Quantum Hall Effect and Quantum Point Contact in Bilayer-Patched Epitaxial Graphene. *Nano Letters*, 14(6):3369–3373.

[43] Chua, C., Lartsev, A., Sui, J., Panchal, V., Puddy, R., Richardson, C., Smith, C. G., Janssen, T., Tzalenchuk, A., Yakimova, R., Kubatkin, S., and Connolly, M. R. (2017). Observation of Coulomb blockade in nanostructured epitaxial bilayer graphene on SiC. *Carbon*, 119:426–430.

[44] Chuang, C., Lin, L.-H., Aoki, N., Ouchi, T., Mahjoub, A. M., Woo, T.-P., Puddy, R. K., Ochiai, Y., Smith, C. G., and Liang, C.-T. (2013). Mesoscopic conductance fluctuations in multi-layer graphene. *Applied Physics Letters*, 103(4):43117.

[45] Connolly, M. R., Chiu, K. L., Giblin, S. P., Kataoka, M., Fletcher, J. D., Chua, C., Griffiths, J. P., Jones, G. A. C., Fal'ko, V. I., Smith, C. G., and Janssen, T. J. B. M. (2013). Gigahertz quantized charge pumping in graphene quantum dots. *Nature Nanotechnology*, 8:417.

[46] Cooper, D., D'Anjou, B., Ghattamaneni, N., Harack, B., Hilke, M., Horth, A., Majlis, N., Massicotte, M., Vandsburger, L., Whiteway, E., and Yu, V. (2011). *Experimental Review of Graphene*, volume 2012.

[47] De Fazio, D., G. Purdie, D., Ott, A. K., Braeuninger, P., Khodkov, T., Goossens, S., Taniguchi, T., Watanabe, K., Livreri, P., H. L. Koppens, F., Hofmann, S., Goykhman, I., C. Ferrari, A., and Lombardo, A. (2019). *High-mobility, wet-transferred graphene grown by chemical vapor deposition*.

[48] Dean, C. R., Young, A. F., Meric, I., Lee, C., Wang, L., Sorgenfrei, S., Watanabe, K., Taniguchi, T., Kim, P., Shepard, K. L., and Hone, J. (2010). Boron nitride substrates for high-quality graphene electronics. *Nature Nanotechnology*, 5:722.

[49] Donnelly, V. M. and Kornblit, A. (2013). Plasma etching: Yesterday, today, and tomorrow. *Journal of Vacuum Science & Technology A*, 31(5):50825.

[50] Dröscher, S., Knowles, H., Meir, Y., Ensslin, K., and Ihn, T. (2011). Coulomb gap in graphene nanoribbons. *Physical Review B*, 84(7):73405.

[51] Du, X., Skachko, I., Barker, A., and Andrei, E. Y. (2008). Approaching ballistic transport in suspended graphene. *Nature Nanotechnology*, 3:491.

[52] Duan, X., Wang, C., Pan, A., Yu, R., and Duan, X. (2015). Two-dimensional transition metal dichalcogenides as atomically thin semiconductors: opportunities and challenges. *Chemical Society Reviews*, 44(24):8859–8876.

[53] Dugaev, V. K. and Katsnelson, M. I. (2013). Edge scattering of electrons in graphene: Boltzmann equation approach to the transport in graphene nanoribbons and nanodisks. *Physical Review B*, 88(23):235432.

[54] Dürkop, T., Getty, S. A., Cobas, E., and Fuhrer, M. S. (2004). Extraordinary Mobility in Semiconducting Carbon Nanotubes. *Nano Letters*, 4(1):35–39.

[55] Duty, T., Gunnarsson, D., Bladh, K., and Delsing, P. (2004). Coherent dynamics of a Josephson charge qubit. *Physical Review B*, 69(14):140503.

[56] Eich, M., Pisoni, R., Overweg, H., Kurzmann, A., Lee, Y., Rickhaus, P., Ihn, T., Ensslin, K., Herman, F., Sigrist, M., Watanabe, K., and Taniguchi, T. (2018a). Spin and Valley States in Gate-Defined Bilayer Graphene Quantum Dots. *Physical Review X*, 8(3):31023.

[57] Eich, M., Pisoni, R., Pally, A., Overweg, H., Kurzmann, A., Lee, Y., Rickhaus, P., Watanabe, K., Taniguchi, T., Ensslin, K., and Ihn, T. (2018b). Coupled Quantum Dots in Bilayer Graphene. *Nano Letters*, 18(8):5042–5048.

[58] Evaldsson, M., Zozoulenko, I. V., Xu, H., and Heinzel, T. (2008). Edge-disorder-induced Anderson localization and conduction gap in graphene nanoribbons. *Physical Review B - Condensed Matter and Materials Physics*.

[59] Ezawa, M. (2006). Peculiar width dependence of the electronic properties of carbon nanoribbons. *Physical Review B - Condensed Matter and Materials Physics*.

[60] Fang, W., Hsu, A. L., Song, Y., and Kong, J. (2015). A review of large-area bilayer graphene synthesis by chemical vapor deposition. *Nanoscale*, 7(48):20335–20351.

[61] Farmer, D. B., Chiu, H.-Y., Lin, Y.-M., Jenkins, K. A., Xia, F., and Avouris, P. (2009). Utilization of a Buffered Dielectric to Achieve High Field-Effect Carrier Mobility in Graphene Transistors. *Nano Letters*, 9(12):4474–4478.

[62] Field, M., Smith, C. G., Pepper, M., Ritchie, D. A., Frost, J. E. F., Jones, G. A. C., and Hasko, D. G. (1993). Measurements of Coulomb blockade with a noninvasive voltage probe. *Physical Review Letters*, 70(9):1311–1314.

[63] Ford, C. J. B., Simpson, P. J., Zailer, I., Mace, D. R., Yosefin, M., Pepper, M., Ritchie, D. A., Frost, J. E. F., Grimshaw, M. P., and Jones, G. A. C. (1994). Charging and double-frequency Aharonov-Bohm effects in an open system. *Physical Review B*, 49(24):17456–17459.

[64] Gallagher, P., Todd, K., and Goldhaber-Gordon, D. (2010). Disorder-induced gap behavior in graphene nanoribbons. *Physical Review B*, 81(11):115409.

[65] Garces, N. Y., Wheeler, V. D., Hite, J. K., Jernigan, G. G., Tedesco, J. L., Nepal, N., Eddy, C. R., and Gaskill, D. K. (2011). Epitaxial graphene surface preparation for atomic layer deposition of Al2O3. *Journal of Applied Physics*, 109(12):124304.

[66] Garcia, J. H., Vila, M., Cummings, A. W., and Roche, S. (2018). Spin transport in graphene/transition metal dichalcogenide heterostructures. *Chemical Society Reviews*, 47(9):3359–3379.

[67] Geim, A. K. and Novoselov, K. S. (2007). The rise of graphene. *Nature Materials*, 6:183.

[68] George, S. M. (2010). Atomic Layer Deposition: An Overview. *Chemical Reviews*, 110(1):111–131.

[69] Gershenson, M. E., Khavin, Y. B., Reuter, D., Schafmeister, P., and Wieck, A. D. (2000). Hot-Electron Effects in Two-Dimensional Hopping with a Large Localization Length. *Physical Review Letters*, 85(8):1718–1721.

[70] Gershenzon, M. E. (1982). JETP Lett.

[71] Giblin, S. P., Kataoka, M., Fletcher, J. D., See, P., Janssen, T., Griffiths, J. P., Jones, G. A. C., Farrer, I., and Ritchie, D. A. (2012). Towards a quantum representation of the ampere using single electron pumps. *Nature Communications*, 3:930.

[72] Gmitra, M., Konschuh, S., Ertler, C., Ambrosch-Draxl, C., and Fabian, J. (2009). Band-structure topologies of graphene: Spin-orbit coupling effects from first principles. *Physical Review B*, 80(23):235431.

[73] Goldman, V. J., Liu, J., and Zaslavsky, A. (2008). Electron tunneling spectroscopy of a quantum antidot in the integer quantum Hall regime. *Physical Review B*, 77(11):115328.

[74] Goldman, V. J. and Su, B. (1995). Resonant Tunneling in the Quantum Hall Regime: Measurement of Fractional Charge. *Science*, 267(5200):1010 LP – 1012.

[75] Goossens, A. S. M., Driessen, S. C. M., Baart, T. A., Watanabe, K., Taniguchi, T., and Vandersypen, L. M. K. (2012). Gate-Defined Confinement in Bilayer Graphene-Hexagonal Boron Nitride Hybrid Devices. *Nano Letters*, 12(9):4656–4660.

[76] Gorbachev, R. V., Tikhonenko, F. V., Mayorov, A. S., Horsell, D. W., and Savchenko, A. K. (2007). Weak Localization in Bilayer Graphene. *Physical Review Letters*, 98(17):176805.

[77] Gould, C., Sachrajda, A. S., Dharma-wardana, M. W. C., Feng, Y., and Coleridge, P. T. (1996). "Spectator" Modes and Antidot Molecules. *Physical Review Letters*, 77(26):5272–5275.

[78] Grabert, H., Devoret, M. H., and Kastner, M. (2008). Single Charge Tunneling: Coulomb Blockade Phenomena in Nanostructures . *Physics Today*.

[79] Güttinger, J., Stampfer, C., Libisch, F., Frey, T., Burgdörfer, J., Ihn, T., and Ensslin, K. (2009). Electron-Hole Crossover in Graphene Quantum Dots. *Physical Review Letters*, 103(4):46810.

[80] Han, M. Y., Özyilmaz, B., Zhang, Y., and Kim, P. (2007). Energy band-gap engineering of graphene nanoribbons. *Physical Review Letters*.

[81] Han, W., Kawakami, R. K., Gmitra, M., and Fabian, J. (2014). Graphene spintronics. *Nature Nanotechnology*, 9:794.

[82] Hanson, R., Kouwenhoven, L. P., Petta, J. R., Tarucha, S., and Vandersypen, L. M. K. (2007). Spins in few-electron quantum dots. *Reviews of Modern Physics*, 79(4):1217–1265.

[83] Havener, R. W., Zhuang, H., Brown, L., Hennig, R. G., and Park, J. (2012). Angle-Resolved Raman Imaging of Interlayer Rotations and Interactions in Twisted Bilayer Graphene. *Nano Letters*, 12(6):3162–3167.

[84] Hofmann, S., Braeuninger-Weimer, P., and Weatherup, R. S. (2015). CVD-Enabled Graphene Manufacture and Technology. *The Journal of Physical Chemistry Letters*, 6(14):2714–2721.

[85] Huang, J., Alexander-Webber, J. A., Janssen, T. J. B. M., Tzalenchuk, A., Yager, T., Lara-Avila, S., Kubatkin, S., Myers-Ward, R. L., Wheeler, V. D., Gaskill, D. K., and Nicholas, R. J. (2015). Hot carrier relaxation of Dirac fermions in bilayer epitaxial graphene. *Journal of Physics: Condensed Matter*, 27(16):164202.

[86] Huertas-Hernando, D., Guinea, F., and Brataas, A. (2006). Spin-orbit coupling in curved graphene, fullerenes, nanotubes, and nanotube caps. *Physical Review B*, 74(15):155426.

[87] Hwang, E. H. and Das Sarma, S. (2008). Acoustic phonon scattering limited carrier mobility in two-dimensional extrinsic graphene. *Physical Review B*, 77(11):115449.

[88] Jain, J. K. and Kivelson, S. A. (1988). Quantum Hall effect in quasi one-dimensional systems: Resistance fluctuations and breakdown. *Physical Review Letters*, 60(15):1542–1545.

[89] Jandhyala, S., Mordi, G., Lee, B., Lee, G., Floresca, C., Cha, P.-R., Ahn, J., Wallace, R. M., Chabal, Y. J., Kim, M. J., Colombo, L., Cho, K., and Kim, J. (2012). Atomic Layer Deposition of Dielectrics on Graphene Using Reversibly Physisorbed Ozone. *ACS Nano*, 6(3):2722–2730.

[90] Janssen, T. J. B. M., Tzalenchuk, A., Yakimova, R., Kubatkin, S., Lara-Avila, S., Kopylov, S., and Fal'ko, V. I. (2011). Anomalously strong pinning of the filling factor $\nu = 2$ in epitaxial graphene. *Physical Review B*, 83(23):233402.

[91] Jariwala, D., Sangwan, V. K., Lauhon, L. J., Marks, T. J., and Hersam, M. C. (2014). Emerging Device Applications for Semiconducting Two-Dimensional Transition Metal Dichalcogenides. *ACS Nano*, 8(2):1102–1120.

[92] Jauregui, L. A., Cao, H., Wu, W., Yu, Q., and Chen, Y. P. (2011). Electronic properties of grains and grain boundaries in graphene grown by chemical vapor deposition. *Solid State Communications*, 151(16):1100–1104.

[93] Jeong, S.-J., Kim, H. W., Heo, J., Lee, M.-H., Song, H. J., Ku, J., Lee, Y., Cho, Y., Jeon, W., Suh, H., Hwang, S., and Park, S. (2016). Physisorbed-precursor-assisted atomic layer deposition of reliable ultrathin dielectric films on inert graphene surfaces for low-power electronics. *2D Materials*, 3(3):35027.

[94] Jiang, Z., Zhang, Y., Tan, Y.-W., Stormer, H. L., and Kim, P. (2007). Quantum Hall effect in graphene. *Solid State Communications*, 143(1):14–19.

[95] John, G. (2005). The quantum electrical triangle. *Philosophical Transactions of the Royal Society A: Mathematical, Physical and Engineering Sciences*, 363(1834):2221–2247.

[96] Joshi, P., Romero, H. E., Neal, A. T., Toutam, V. K., and Tadigadapa, S. A. (2010). Intrinsic doping and gate hysteresis in graphene field effect devices fabricated on SiO2substrates. *Journal of Physics: Condensed Matter*, 22(33):334214.

[97] Ju, L., Shi, Z., Nair, N., Lv, Y., Jin, C., Velasco Jr, J., Ojeda-Aristizabal, C., Bechtel, H. A., Martin, M. C., Zettl, A., Analytis, J., and Wang, F. (2015). Topological valley transport at bilayer graphene domain walls. *Nature*, 520:650.

[98] Kataoka, M., Ford, C. J. B., Faini, G., Mailly, D., Simmons, M. Y., Mace, D. R., Liang, C.-T., and Ritchie, D. A. (1999). Detection of Coulomb Charging around an Antidot in the Quantum Hall Regime. *Physical Review Letters*, 83(1):160–163.

[99] Kataoka, M., Ford, C. J. B., Faini, G., Mailly, D., Simmons, M. Y., and Ritchie, D. A. (2000). Coulomb blockade of tunneling through compressible rings formed around an antidot: An explanation for $h/2e$ Aharonov-Bohm oscillations. *Physical Review B*, 62(8):R4817–R4820.

[100] Kataoka, M., Ford, C. J. B., Simmons, M. Y., and Ritchie, D. A. (2002). Kondo Effect in a Quantum Antidot. *Physical Review Letters*, 89(22):226803.

[101] Katsnelson, M. I. (2007). Graphene: carbon in two dimensions. *Materials Today*, 10(1):20–27.

[102] Katsnelson, M. I., Novoselov, K. S., and Geim, A. K. (2006). Chiral tunnelling and the Klein paradox in graphene. *Nature Physics*, 2:620.

[103] Kechedzhi, K., Fal'ko, V. I., McCann, E., and Altshuler, B. L. (2007). Influence of Trigonal Warping on Interference Effects in Bilayer Graphene. *Physical Review Letters*, 98(17):176806.

[104] Kim, K., Coh, S., Tan, L. Z., Regan, W., Yuk, J. M., Chatterjee, E., Crommie, M. F., Cohen, M. L., Louie, S. G., and Zettl, A. (2012). Raman Spectroscopy Study of Rotated Double-Layer Graphene: Misorientation-Angle Dependence of Electronic Structure. *Physical Review Letters*, 108(24):246103.

[105] Kim, S., Nah, J., Jo, I., Shahrjerdi, D., Colombo, L., Yao, Z., Tutuc, E., and Banerjee, S. K. (2009). Realization of a high mobility dual-gated graphene field-effect transistor with Al2O3 dielectric. *Applied Physics Letters*, 94(6):62107.

[106] Kitzmann, J., Göritz, A., Fraschke, M., Lukosius, M., Wenger, C., Wolff, A., and Lupina, G. (2016). Perfluorodecyltrichlorosilane-based seed-layer for improved chemical vapour deposition of ultrathin hafnium dioxide films on graphene. *Scientific Reports*, 6:29223.

[107] Klitzing, K. v., Dorda, G., and Pepper, M. (1980). New Method for High-Accuracy Determination of the Fine-Structure Constant Based on Quantized Hall Resistance. *Physical Review Letters*, 45(6):494–497.

[108] Kobayashi, Y., Fukui, K. I., Enoki, T., Kusakabe, K., and Kaburagi, Y. (2005). Observation of zigzag and armchair edges of graphite using scanning tunneling microscopy and spectroscopy. *Physical Review B - Condensed Matter and Materials Physics*.

[109] Konar, A., Fang, T., and Jena, D. (2010). Effect of high-κ gate dielectrics on charge transport in graphene-based field effect transistors. *Physical Review B*, 82(11):115452.

[110] Konschuh, S., Gmitra, M., and Fabian, J. (2010). Tight-binding theory of the spin-orbit coupling in graphene. *Physical Review B*, 82(24):245412.

[111] Kopylov, S., Tzalenchuk, A., Kubatkin, S., and Fal'ko, V. I. (2010). Charge transfer between epitaxial graphene and silicon carbide. *Applied Physics Letters*, 97(11):112109.

[112] Kubakaddi, S. S. (2009). Interaction of massless Dirac electrons with acoustic phonons in graphene at low temperatures. *Physical Review B*, 79(7):75417.

[113] Kuc, A., Zibouche, N., and Heine, T. (2011). Influence of quantum confinement on the electronic structure of the transition metal sulfide TS${}_{2}$. *Physical Review B*, 83(24):245213.

[114] Lartsev, A., Yager, T., Bergsten, T., Tzalenchuk, A., Janssen, T. J. B. M., Yakimova, R., Lara-Avila, S., and Kubatkin, S. (2014). Tuning carrier density across Dirac point in epitaxial graphene on SiC by corona discharge. *Applied Physics Letters*, 105(6):63106.

[115] Leadley, D. R., Nicholas, R. J., Harris, J. J., and Foxon, C. T. (1989). Cyclotron phonon emission and electron energy loss rates in GaAs-GaAlAs heterojunctions. *Semiconductor Science and Technology*, 4(10):879–884.

[116] Lee, B., Mordi, G., Kim, M. J., Chabal, Y. J., Vogel, E. M., Wallace, R. M., Cho, K. J., Colombo, L., and Kim, J. (2010). Characteristics of high-k Al2O3 dielectric using ozone-based atomic layer deposition for dual-gated graphene devices. *Applied Physics Letters*, 97(4):43107.

[117] Lee, B., Park, S.-Y., Kim, H.-C., Cho, K., Vogel, E. M., Kim, M. J., Wallace, R. M., and Kim, J. (2008). Conformal Al2O3 dielectric layer deposited by atomic layer deposition for graphene-based nanoelectronics. *Applied Physics Letters*, 92(20):203102.

[118] Lee, Y. G., Kang, C. G., Cho, C., Kim, Y., Hwang, H. J., and Lee, B. H. (2013). Quantitative analysis of hysteretic reactions at the interface of graphene and SiO2 using the short pulse I–V method. *Carbon*, 60:453–460.

[119] Leturcq, R., L'Hôte, D., Tourbot, R., Senz, V., Gennser, U., Ihn, T., Ensslin, K., Dehlinger, G., and Grützmacher, D. (2003). Hot-hole effects in a dilute two-dimensional gas in SiGe. *Europhysics Letters (EPL)*, 61(4):499–505.

[120] Li, X., Wu, X., Sprinkle, M., Ming, F., Ruan, M., Hu, Y., Berger, C., and de Heer, W. A. (2010). Top- and side-gated epitaxial graphene field effect transistors. *physica status solidi (a)*, 207(2):286–290.

[121] Libisch, F., Rotter, S., Güttinger, J., Stampfer, C., and Burgdörfer, J. (2010). Transition to Landau levels in graphene quantum dots. *Physical Review B*, 81(24):245411.

[122] llqhe (2015). https://physicsresearchinbeijing.files.wordpress.com/2011/07/llqhe.gif.

[123] Lu, C.-C., Lin, Y.-C., Liu, Z., Yeh, C.-H., Suenaga, K., and Chiu, P.-W. (2013). Twisting Bilayer Graphene Superlattices. *ACS Nano*, 7(3):2587–2594.

[124] Maasilta, I. J. and Goldman, V. J. (1998). Energetics of quantum antidot states in the quantum Hall regime. *Physical Review B*, 57(8):R4273–R4276.

[125] Manzeli, S., Ovchinnikov, D., Pasquier, D., Yazyev, O. V., and Kis, A. (2017). 2D transition metal dichalcogenides. *Nature Reviews Materials*, 2:17033.

[126] Martin, M.-B., Dlubak, B., Weatherup, R. S., Yang, H., Deranlot, C., Bouzehouane, K., Petroff, F., Anane, A., Hofmann, S., Robertson, J., Fert, A., and Seneor, P. (2014). Sub-nanometer Atomic Layer Deposition for Spintronics in Magnetic Tunnel Junctions Based on Graphene Spin-Filtering Membranes. *ACS Nano*, 8(8):7890–7895.

[127] McCann, E. (2006). Asymmetry gap in the electronic band structure of bilayer graphene. *Physical Review B*, 74(16):161403.

[128] McCann, E. and Fal'ko, V. I. (2006). Landau-Level Degeneracy and Quantum Hall Effect in a Graphite Bilayer. *Physical Review Letters*, 96(8):86805.

[129] McCann, E. and Koshino, M. (2013). The electronic properties of bilayer graphene. *Reports on Progress in Physics*, 76(5):56503.

[130] Miller, J. B., Zumbühl, D. M., Marcus, C. M., Lyanda-Geller, Y. B., Goldhaber-Gordon, D., Campman, K., and Gossard, A. C. (2003). Gate-Controlled Spin-Orbit Quantum Interference Effects in Lateral Transport. *Physical Review Letters*, 90(7):76807.

[131] Minke, S., Bundesmann, J., Weiss, D., and Eroms, J. (2012). Phase coherent transport in graphene nanoribbons and graphene nanoribbon arrays. *Physical Review B - Condensed Matter and Materials Physics*.

[132] Molitor, F., Dröscher, S., Güttinger, J., Jacobsen, A., Stampfer, C., Ihn, T., and Ensslin, K. (2009). Transport through graphene double dots. *Applied Physics Letters*, 94(22):222107.

[133] Moore, G. E. (2006). Cramming more components onto integrated circuits, Reprinted from Electronics, volume 38, number 8, April 19, 1965, pp.114 ff. *IEEE Solid-State Circuits Society Newsletter*, 11(3):33–35.

[134] Morozov, S. V., Novoselov, K. S., Katsnelson, M. I., Schedin, F., Ponomarenko, L. A., Jiang, D., and Geim, A. K. (2006). Strong Suppression of Weak Localization in Graphene. *Physical Review Letters*, 97(1):16801.

[135] Morpurgo, A. F. and Guinea, F. (2006). Intervalley Scattering, Long-Range Disorder, and Effective Time-Reversal Symmetry Breaking in Graphene. *Physical Review Letters*, 97(19):196804.

[136] Mucciolo, E. R., Castro Neto, A. H., and Lewenkopf, C. H. (2009). Conductance quantization and transport gaps in disordered graphene nanoribbons. *Physical Review B - Condensed Matter and Materials Physics*.

[137] Nakaharai, S., Williams, J. R., and Marcus, C. M. (2011). Gate-Defined Graphene Quantum Point Contact in the Quantum Hall Regime. *Physical Review Letters*, 107(3):36602.

[138] Narozhny, B. N., Zala, G., and Aleiner, I. L. (2002). Interaction corrections at intermediate temperatures: Dephasing time. *Physical Review B*, 65(18):180202.

[139] Novoselov, K. S., Falko, V. I., Colombo, L., Gellert, P. R., Schwab, M. G., and Kim, K. (2012). A roadmap for graphene. *Nature*, 490:192.

[140] Novoselov, K. S., Geim, A. K., Morozov, S. V., Jiang, D., Katsnelson, M. I., Grigorieva, I. V., Dubonos, S. V., and Firsov, A. A. (2005). Two-dimensional gas of massless Dirac fermions in graphene. *Nature*, 438:197.

[141] Novoselov, K. S., Geim, A. K., Morozov, S. V., Jiang, D., Zhang, Y., Dubonos, S. V., Grigorieva, I. V., and Firsov, A. A. (2004). Electric Field Effect in Atomically Thin Carbon Films. *Science*, 306(5696):666–669.

[142] Novoselov, K. S., Jiang, Z., Zhang, Y., Morozov, S. V., Stormer, H. L., Zeitler, U., Maan, J. C., Boebinger, G. S., Kim, P., and Geim, A. K. (2007). Room-Temperature Quantum Hall Effect in Graphene. *Science*, 315(5817):1379 LP – 1379.

[143] Novoselov, K. S., McCann, E., Morozov, S. V., Fal'ko, V. I., Katsnelson, M. I., Zeitler, U., Jiang, D., Schedin, F., and Geim, A. K. (2006). Unconventional quantum Hall effect and Berry's phase of 2π in bilayer graphene. *Nature Physics*, 2:177.

[144] Ohta, T., Bostwick, A., Seyller, T., Horn, K., and Rotenberg, E. (2006). Controlling the Electronic Structure of Bilayer Graphene. *Science*, 313(5789):951 LP – 954.

[145] Oostinga, J. B., Heersche, H. B., Liu, X., Morpurgo, A. F., and Vandersypen, L. M. K. (2007). Gate-induced insulating state in bilayer graphene devices. *Nature Materials*, 7:151.

[146] Panchal, V., Lartsev, A., Manzin, A., Yakimova, R., Tzalenchuk, A., and Kazakova, O. (2014). Visualisation of edge effects in side-gated graphene nanodevices. *Scientific Reports*, 4:5881.

[147] Panchal, V., Pearce, R., Yakimova, R., Tzalenchuk, A., and Kazakova, O. (2013). Standardization of surface potential measurements of graphene domains. *Scientific Reports*, 3:2597.

[148] Patel, H., Havener, R. W., Brown, L., Liang, Y., Yang, L., Park, J., and Graham, M. W. (2015). Tunable Optical Excitations in Twisted Bilayer Graphene Form Strongly Bound Excitons. *Nano Letters*, 15(9):5932–5937.

[149] Pekola, J. P., Saira, O.-P., Maisi, V. F., Kemppinen, A., Möttönen, M., Pashkin, Y. A., and Averin, D. V. (2013). Single-electron current sources: Toward a refined definition of the ampere. *Reviews of Modern Physics*, 85(4):1421–1472.

[150] Penfold-Fitch, Z., Sfigakis, F., and Buitelaar, M. (2017). Microwave Spectroscopy of a Carbon Nanotube Charge Qubit. *Physical Review Applied*, 7(5):54017.

[151] Petersson, K. D., Smith, C. G., Anderson, D., Atkinson, P., Jones, G. A. C., and Ritchie, D. A. (2010). Charge and Spin State Readout of a Double Quantum Dot Coupled to a Resonator. *Nano Letters*, 10(8):2789–2793.

[152] Petta, J. R., Johnson, A. C., Taylor, J. M., Laird, E. A., Yacoby, A., Lukin, M. D., Marcus, C. M., Hanson, M. P., and Gossard, A. C. (2005). Coherent Manipulation of Coupled Electron Spins in Semiconductor Quantum Dots. *Science*, 309(5744):2180 LP – 2184.

[153] Pham, V. P., Jang, H.-S., Whang, D., and Choi, J.-Y. (2017). Direct growth of graphene on rigid and flexible substrates: progress, applications, and challenges. *Chemical Society Reviews*, 46(20):6276–6300.

[154] Pirkle, A., Chan, J., Venugopal, A., Hinojos, D., Magnuson, C. W., McDonnell, S., Colombo, L., Vogel, E. M., Ruoff, R. S., and Wallace, R. M. (2011). The effect of chemical residues on the physical and electrical properties of chemical vapor deposited graphene transferred to SiO2. *Applied Physics Letters*, 99(12):122108.

[155] Reilly, D. J., Marcus, C. M., Hanson, M. P., and Gossard, A. C. (2007). Fast single-charge sensing with a rf quantum point contact. *Applied Physics Letters*, 91(16):162101.

[156] Reina, A., Jia, X., Ho, J., Nezich, D., Son, H., Bulovic, V., Dresselhaus, M. S., and Kong, J. (2009). Large Area, Few-Layer Graphene Films on Arbitrary Substrates by Chemical Vapor Deposition. *Nano Letters*, 9(1):30–35.

[157] Rickhaus, P., Wallbank, J., Slizovskiy, S., Pisoni, R., Overweg, H., Lee, Y., Eich, M., Liu, M.-H., Watanabe, K., Taniguchi, T., Ihn, T., and Ensslin, K. (2018). Transport Through a Network of Topological Channels in Twisted Bilayer Graphene. *Nano Letters*, 18(11):6725–6730.

[158] Robinson, J. A., LaBella, M., Trumbull, K. A., Weng, X., Cavelero, R., Daniels, T., Hughes, Z., Hollander, M., Fanton, M., and Snyder, D. (2010). Epitaxial Graphene Materials Integration: Effects of Dielectric Overlayers on Structural and Electronic Properties. *ACS Nano*, 4(5):2667–2672.

[159] Rode, D. L. (1971). Electron Transport in InSb, InAs, and InP. *Physical Review B*, 3(10):3287–3299.

[160] Roschier, L., Hakonen, P., Bladh, K., Delsing, P., Lehnert, K. W., Spietz, L., and Schoelkopf, R. J. (2004). Noise performance of the radio-frequency single-electron transistor. *Journal of Applied Physics*, 95(3):1274–1286.

[161] Ryu, S., Liu, L., Berciaud, S., Yu, Y.-J., Liu, H., Kim, P., Flynn, G. W., and Brus, L. E. (2010). Atmospheric Oxygen Binding and Hole Doping in Deformed Graphene on a SiO2 Substrate. *Nano Letters*, 10(12):4944–4951.

[162] Sachrajda, A. S., Feng, Y., Taylor, R. P., Kirczenow, G., Henning, L., Wang, J., Zawadzki, P., and Coleridge, P. T. (1994). Magnetoconductance of a nanoscale antidot. *Physical Review B*, 50(15):10856–10863.

[163] Sagade, A. A., Neumaier, D., Schall, D., Otto, M., Pesquera, A., Centeno, A., Elorza, A. Z., and Kurz, H. (2015). Highly air stable passivation of graphene based field effect devices. *Nanoscale*, 7(8):3558–3564.

[164] Schedin, F., Geim, A. K., Morozov, S. V., Hill, E. W., Blake, P., Katsnelson, M. I., and Novoselov, K. S. (2007). Detection of individual gas molecules adsorbed on graphene. *Nature Materials*, 6:652.

[165] Schnez, S., Ensslin, K., Sigrist, M., and Ihn, T. (2008). Analytic model of the energy spectrum of a graphene quantum dot in a perpendicular magnetic field. *Physical Review B*, 78(19):195427.

[166] Schoelkopf, R. J., Wahlgren, P., Kozhevnikov, A. A., Delsing, P., and Prober, D. E. (1998). The Radio-Frequency Single-Electron Transistor (RF-SET): A Fast and Ultrasensitive Electrometer. *Science*, 280(5367):1238–1242.

[167] Shimazaki, Y., Yamamoto, M., Borzenets, I. V., Watanabe, K., Taniguchi, T., and Tarucha, S. (2015). Generation and detection of pure valley current by electrically induced Berry curvature in bilayer graphene. *Nature Physics*, 11:1032.

[168] Shklovskii, B. I. and Efros, A. L. (2013). *Electronic properties of doped semiconductors*, volume 45. Springer Science & Business Media.

[169] Sim, H.-S., Kataoka, M., and Ford, C. J. B. (2008). Electron interactions in an antidot in the integer quantum Hall regime. *Physics Reports*, 456(4):127–165.

[170] Sim, H.-S., Kataoka, M., Yi, H., Hwang, N. Y., Choi, M.-S., and Yang, S.-R. E. (2003). Coulomb Blockade and Kondo Effect in a Quantum Hall Antidot. *Physical Review Letters*, 91(26):266801.

[171] Smith, C. G., Pepper, M., Newbury, R., Ahmed, H., Hasko, D. G., Peacock, D. C., Frost, J. E. F., Ritchie, D. A., Jones, G. A. C., and Hill, G. (1989). One-dimensional quantised ballistic resistors in parallel configuration. *Journal of Physics: Condensed Matter*, 1(37):6763–6770.

[172] Sols, F., Guinea, F., and Neto, A. H. (2007). Coulomb blockade in graphene nanoribbons. *Physical Review Letters*.

[173] Song, J. C. W., Reizer, M. Y., and Levitov, L. S. (2012). Disorder-Assisted Electron-Phonon Scattering and Cooling Pathways in Graphene. *Physical Review Letters*, 109(10):106602.

[174] Stampfer, C., Güttinger, J., Hellmüller, S., Molitor, F., Ensslin, K., and Ihn, T. (2009). Energy gaps in etched graphene nanoribbons. *Physical Review Letters*.

[175] Suzuura, H. and Ando, T. (2002). Crossover from Symplectic to Orthogonal Class in a Two-Dimensional Honeycomb Lattice. *Physical Review Letters*, 89(26):266603.

[176] Taskinen, L. J., Starrett, R. P., Martin, T. P., Micolich, A. P., Hamilton, A. R., Simmons, M. Y., Ritchie, D. A., and Pepper, M. (2008). Radio-frequency reflectometry on large gated two-dimensional systems. *Review of Scientific Instruments*, 79(12):123901.

[177] Teh, W. H., Liang, C.-T., Graham, M., and Smith, C. G. (2003). Cross-linked PMMA as a low-dimensional dielectric sacrificial layer. *Journal of Microelectromechanical Systems*, 12(5):641–648.

[178] Tikhonenko, F. V., Horsell, D. W., Gorbachev, R. V., and Savchenko, A. K. (2008). Weak Localization in Graphene Flakes. *Physical Review Letters*, 100(5):56802.

[179] Tikhonenko, F. V., Kozikov, A. A., Savchenko, A. K., and Gorbachev, R. V. (2009). Transition between Electron Localization and Antilocalization in Graphene. *Physical Review Letters*, 103(22):226801.

[180] Timp, G., Chang, A. M., Mankiewich, P., Behringer, R., Cunningham, J. E., Chang, T. Y., and Howard, R. E. (1987). Quantum transport in an electron-wave guide. *Physical Review Letters*, 59(6):732–735.

[181] Trauzettel, B., Bulaev, D. V., Loss, D., and Burkard, G. (2007). Spin qubits in graphene quantum dots. *Nature Physics*, 3:192.

[182] Tse, W.-K. and Das Sarma, S. (2009). Energy relaxation of hot Dirac fermions in graphene. *Physical Review B*, 79(23):235406.

[183] Tzalenchuk, A., Lara-Avila, S., Kalaboukhov, A., Paolillo, S., Syväjärvi, M., Yakimova, R., Kazakova, O., Janssen, T. J. B. M., Fal'ko, V., and Kubatkin, S. (2010). Towards a quantum resistance standard based on epitaxial graphene. *Nature Nanotechnology*, 5:186.

[184] Van der Wiel, W. G., De Franceschi, S., Elzerman, J. M., Fujisawa, T., Tarucha, S., and Kouwenhoven, L. P. (2003). Electron transport through double quantum dots.

[185] Virojanadara, C., Syväjarvi, M., Yakimova, R., Johansson, L. I., Zakharov, A. A., and Balasubramanian, T. (2008). Homogeneous large-area graphene layer growth on $6H$-SiC(0001). *Physical Review B*, 78(24):245403.

[186] von Klitzing, K. (2006). 25 Years of Quantum Hall Effect (QHE) A Personal View on the Discovery, Physics and Applications of this Quantum Effect. pages 1–21.

[187] Wallace, P. R. (1947). The Band Theory of Graphite. *Physical Review*, 71(9):622–634.

[188] Wang, H., Wu, Y., Cong, C., Shang, J., and Yu, T. (2010). Hysteresis of Electronic Transport in Graphene Transistors. *ACS Nano*, 4(12):7221–7228.

[189] Wang, X., Tabakman, S. M., and Dai, H. (2008). Atomic Layer Deposition of Metal Oxides on Pristine and Functionalized Graphene. *Journal of the American Chemical Society*, 130(26):8152–8153.

[190] Wojtaszek, M. and Jonkman, H. (2009). Graphene: a two type charge carrier system.

[191] Wojtaszek, M., Vera-Marun, I. J., Whiteway, E., Hilke, M., and van Wees, B. J. (2014). Absence of hyperfine effects in ^{13}C-graphene spin-valve devices. *Physical Review B*, 89(3):35417.

[192] Xiao, D., Chang, M.-C., and Niu, Q. (2010). Berry phase effects on electronic properties. *Reviews of Modern Physics*, 82(3):1959–2007.

[193] Xu, H. and Heinzel, T. (2012). Impurity and edge roughness scattering in graphene nanoribbons: the Boltzmann approach. *Journal of Physics: Condensed Matter*, 24(45):455303.

[194] Yan, Z., Peng, Z., and Tour, J. M. (2014). Chemical Vapor Deposition of Graphene Single Crystals. *Accounts of Chemical Research*, 47(4):1327–1337.

[195] Yang, Y., Brenner, K., and Murali, R. (2012). The influence of atmosphere on electrical transport in graphene. *Carbon*, 50(5):1727–1733.

[196] Yao, W., Wang, E., Bao, C., Zhang, Y., Zhang, K., Bao, K., Chan, C. K., Chen, C., Avila, J., Asensio, M. C., Zhu, J., and Zhou, S. (2018). Quasicrystalline 30° twisted bilayer graphene as an incommensurate superlattice with strong interlayer coupling. *Proceedings of the National Academy of Sciences*, 115(27):6928 LP – 6933.

[197] Yin, J., Wang, H., Peng, H., Tan, Z., Liao, L., Lin, L., Sun, X., Koh, A. L., Chen, Y., Peng, H., and Liu, Z. (2016). Selectively enhanced photocurrent generation in twisted bilayer graphene with van Hove singularity. *Nature Communications*, 7:10699.

[198] Zhang, Y., Tan, Y.-W., Stormer, H. L., and Kim, P. (2005). Experimental observation of the quantum Hall effect and Berry's phase in graphene. *Nature*, 438:201.

[199] Zhang, Y., Tang, T.-T., Girit, C., Hao, Z., Martin, M. C., Zettl, A., Crommie, M. F., Shen, Y. R., and Wang, F. (2009). Direct observation of a widely tunable bandgap in bilayer graphene. *Nature*, 459:820.

[200] Zheng, L., Cheng, X., Cao, D., Wang, G., Wang, Z., Xu, D., Xia, C., Shen, L., Yu, Y., and Shen, D. (2014). Improvement of Al2O3 Films on Graphene Grown by Atomic Layer Deposition with Pre-H2O Treatment. *ACS Applied Materials & Interfaces*, 6(10):7014–7019.

[201] Zheng, Y. and Ando, T. (2002). Hall conductivity of a two-dimensional graphite system. *Physical Review B*, 65(24):245420.

[202] Zimmerli, G., Eiles, T. M., Kautz, R. L., and Martinis, J. M. (1992). Noise in the Coulomb blockade electrometer. *Applied Physics Letters*, 61(2):237–239.

Appendix A

Fabrication Processing Steps of the CVD Graphene Nano-devices

This appendix summarizes the fabrication processing steps of CVD graphene nanostructured devices, including graphene Hall bar, graphene antidots and graphene double quantum dots studied in this thesis. The details about the experimental techniques of each step can be referred to chapter 3. The aim of this appendix is to provide reference for other researchers working on this field.

Graphene Hall bar

1. Transfer CVD graphene onto a pre-cleaned silicon substrate using PMMA;
2. Pattern alignment markers and bond pads using optical lithography followed by oxygen plasma etch and Ti/Au (5 nm/50 nm) deposition by thermal evaporation;
3. Define graphene Hall bar mesa using optical lithography followed by oxygen plasma etch;
4. Pattern contacts using optical lithography followed by depositing Ti/Au (10 nm/120 nm) by thermal evaporation;
5. Encapsulate 90 nm Al_2O_3 dielectric films using a gaseous H_2O pretreatment and atomic layer deposition growing method;
6. The devices are then ready for packaging, bonding and measurements.

Graphene Antidots

1. Transfer CVD graphene onto a pre-cleaned silicon substrate using PMMA;
2. Pattern alignment markers and bond pads using optical lithography followed by oxygen plasma etch and Ti/Au (5 nm/50 nm) deposition by thermal evaporation;
3. Define graphene Hall bar mesa using optical lithography followed by oxygen plasma etch;
4. Pattern contacts using optical lithography followed by depositing Ti/Au (10 nm/120 nm) by thermal evaporation;
5. Encapsulate 90 nm Al_2O_3 dielectric films using a gaseous H_2O pretreatment and atomic layer deposition growing method;
6. Define quantum point contact split gates using electron beam lithography followed by evaporating Ti/Au (10 nm/80 nm) and lift-off processing;
7. Deposit a thick layer of PMMA ($\sim$ 200 nm) followed by opening up an antidot hole through the middle of the split gates using electron beam lithography;
8. Crosslink PMMA on a big square covering the Hall bar mesa using electron beam lithography to form a dielectric layer;
9. Define antidot top gates and deposit Ti/Au (10 nm/80 nm) through the hole by thermal evaporation using a rotary sample holder plate with an inclined angle (45°) to ensure the deposited metal can climb over the edge of the thick crosslinked PMMA dielectric layer;
10. The devices are then ready for packaging, bonding and measurements.

Graphene Double Quantum Dots

1. Transfer CVD graphene onto a pre-cleaned silicon substrate using PMMA;
2. Pattern alignment markers and bond pads using optical lithography followed by oxygen plasma etch and Ti/Au (5 nm/50 nm) deposition by thermal evaporation;

3. Pattern big graphene square mesa using optical lithography followed by oxygen plasma etch;

4. Pattern contact tracks using optical lithography followed by depositing Ti/Au (10 nm/120 nm) by thermal evaporation;

5. Define the mesa of graphene double dots and side gates using electron beam lithography followed by oxygen plasma etch;

6. Encapsulate 90 nm Al_2O_3 dielectric films using a gaseous H_2O pretreatment and atomic layer deposition growing method;

7. The devices are then ready for packaging, bonding and measurements.